SELF-COMPACTING CONCRETE: MIX PROPORTIONING, PROPERTIES AND ITS FLOW SIMULATION IN THE V-FUNNEL

Wajde Shober Saheb Alyhya

B.Sc., M.Sc.

A thesis submitted to Cardiff University for the degree of

Doctor of Philosophy

School of Engineering

Cardiff University

United Kingdom

November 2016

In the name of God

The most compassionate and the most merciful

DEDICATION

For all those people who sacrifice themselves for our sake, without them, I would not have been able to study and succeed

Wajde Alyhya

DECLARATION AND STATEMENTS

DECLARATION

This work has not previously been accepted in substance for any degree and is not concurrently submitted in candidature for any degree.

Signed ……..…... (**Wajde S. S. Alyhya**) Date…….…….

STATEMENT 1

This thesis is being submitted in partial fulfillment of the requirements for the degree of Doctor of Philosophy (PhD).

Signed ……..…. (**Wajde S. S. Alyhya**) Date…….…….

STATEMENT 2

This thesis is the result of my own independent work/investigation, except where otherwise stated. Other sources are acknowledged by explicit references.

Signed ……..… (**Wajde S. S. Alyhya**) Date…….…….

STATEMENT 3

I hereby give consent for my thesis, if accepted, to be available for photocopying and inter-library loan, and for the title and summary to be made available to outside organizations.

Signed ……..…. (**Wajde S. S. Alyhya**) Date…….…….

ACKNOWLEDGEMENT

The work outlined in this thesis was conducted at Cardiff University, School of Engineering. I greatly appreciate the opportunity to have a research position and to start such an interesting project. Of course, this thesis would not exist at all without the generous financial support of my beloved country, Iraq represented by the Ministry of Higher Education and Scientific Research. You sponsored my study and gave me this opportunity; I wish you peace and progress.

I would also like to express my appreciation to the Iraqi Cultural Attaché in London for their support and help to strive towards my goal.

My special appreciation and thanks go to my supervisor Professor Karihaloo; you have been a tremendous mentor for me. I would especially like to thank you for encouraging me and for allowing me to grow as a researcher. Your advice has always been priceless. I will be indebted to you for sparing your precious time.

My heartfelt thanks are also due to Dr Kulasegaram for his support, encouragement and for providing the opportunity to work with him.

I would like to thank the members of research office and laboratory at Cardiff University for taking time out from their busy schedule to help me.

It is evident that this thesis required far more than just my own personal efforts, and I must express my thanks to all authors and co-authors listed in the references of my thesis. Without their work and the work of others before them, this thesis would be impossible.

Special thanks to my family for their endless support and patience during study years. Words cannot express how grateful I am to my beloved wife and children for all of the sacrifices that they have made on my behalf, especially during the final stage of the study.

In addition, I extend my warm thanks to my father, mother, brothers and sisters. Your constant prayer for me was what sustained me thus far.

I would also like to express my appreciation to all my friends, especially my office members who supported me to strive towards my goal.

SYNOPSIS

Self-compacting concrete (SCC) is a type of concrete, which flows under the sole influence of gravity up to leveling, air out and consolidates itself without any external compaction energy. It was a response to the lack of qualified skilled workers at the construction sites and a solution for the accomplishment of durable concrete structures.

Self-compactability of a concrete mix is widely affected by the characteristics of ingredients and their proportions. Thus, it becomes necessary to develop a successful procedure for mix proportioning of SCC. The heuristic nature of the early mix proportioning methods motivated researchers to carry out extensive research on the rheological properties of SCC that has significantly improved the proportioning of SCC mixes. A rigorous proportioning method for SCC based on sound physical principles was proposed. However, such a method produces a bewildering array of mixes that reach the target plastic viscosity but does not give any practical guidelines on how to choose the most appropriate mix and does not explicitly impose compressive strength as a design criterion. These shortcomings were overcome in this work by developing a new mix proportioning method. Indeed, practical guidelines in the form of design charts were provided for choosing the mix proportions that achieve a target plastic viscosity in the range 3 to 15Pa s (the lower limit varies with target cube compressive strength) and a target cube compressive strength in the range 30 to 80MPa.

To verify the proposed mix design method, an experimental validation was performed on a series of SCC mixes in both the fresh and hardened states. Three sets of SCC mixes were prepared jointly with other two PhD students (Abo Dhaheer, 2016; Al-Rubaye, 2016). These mixes are designated A, B, and C for the low, medium and high paste to solids ratios, respectively. (Note that mixes designated A and C were contributed by the other two named PhD students). Tests on these mixes conclusively proved the validity of the mix design approach in the sense that all the mixes met the self-compactability criteria and achieved the desired target plastic viscosity and cube compressive strength.

Although SCC has passed from the research phase into the real application, the differences in its composition (i.e. higher paste volume and lower coarse aggregate volume) from normal vibrated concrete (NVC) raise concerns among researchers about its fracture behaviour. Thus, an experimental study has been carried out to investigate in detail the role of several composition parameters of SCC mixes on their fracture behaviour differing by the coarse aggregate volume, paste to solids ratio (p/s) and water to cementitious material (*w/cm*) ratio. The specific fracture energy and the tension-softening diagram of a concrete mix are the most critical parameters that describe its fracture behaviour as they form a basis for the evaluation of the load carrying capacity of cracked concrete. First, the size-dependent fracture energy (G_f) has been determined using the RILEM work-of-fracture test on three point bend specimens of a single size, half of which contained a shallow starter notch (notch to depth ratio=0.1), while the other half contained a deep notch (notch to depth ratio=0.6). Then the specific size-independent fracture energy (G_F) was calculated using the simplified boundary effect formalism in which a bilinear diagram approximates the variation in the fracture energy along the unbroken specimen ligament. Finally, the bilinear approximation of the tension softening diagram corresponding to G_F has been obtained using the non-linear hinge model.

Predicting the flow behaviour in the formwork and linking the required rheological parameters to flow tests conducted on the site will help to optimise the casting process. A Lagrangian particle-based method, the smooth particle hydrodynamics (SPH) is used to model the flow of SCC mixes in the V-funnel. An incompressible SPH method was employed to simulate the flow of such a non-Newtonian fluid whose behaviour is best described by a Bingham-type model, in which the kink in the shear stress versus shear strain rate diagram is first appropriately smoothed out. The basic equations solved in the SPH are the incompressible mass conservation and momentum equations. The simulation of the SCC mixes emphasised the distribution of larger aggregates particles of different sizes throughout the flow in the 3-dimensional V-funnel configuration. The capabilities of this methodology were validated by comparing the simulation results with the V-funnel tests carried out in the laboratory.

NOTATIONS

SCC	Self-compacting concrete
NVC	Normal vibrated concrete
a	Notch depth, mm
a_l	Transition ligament length, mm
CA	Coarse aggregate ≤ 20 mm
CBM	Crack band model
c_f	Coefficient of kinematic friction, N s/m
cm	Cementitious materials
CRMs	Cement replacement materials
E	Modulus of elasticity, GPa
FA	Fine aggregate ≤2 mm
FBZ	Fracture process zone
FCM	Factious crack model
f_{ct}	Direct tensile strength, MPa
f_{cu}	Cube compressive strength, MPa
f_{st}	Splitting (indirect) tensile strength, MPa
g	Coarse aggregate size range, mm
g	Gravitational acceleration, m/s^2
G_f	Size-dependent fracture energy, N/m
G_F	Size-independent fracture energy, N/m
ggbs	Ground granulated blast furnace slag
ITZ	Interfacial transition zone
l_{ch}	Characteristic length, mm
LEFM	Linear elastic fracture mechanics
LP	Limestone powder ≤ 125μm
NLEFM	Nonlinear elastic fracture mechanics
Np	Number of particles
P	Pressure, Pa
p/s	Paste to solids, %
SBE	Simplified boundary effect formalism
SP	Super-plasticizer
SPH	Smooth particle hydrodynamic method
Δt	Time step, s
t_{200}	Time taken for SCC to reach the distance of 200mm from the gate in the L-box test, s
t_{400}	Time taken for SCC to reach the distance of 400mm from the gate in the L-box test, s
t_{500}	Time taken for SCC to spread 500mm in the flow test, s
$t_{500\,j}$	Time taken for SCC to spread 500mm in the J-ring test, s
TPB	Three-point bending test
TSD	Tension softening diagram
$t_{v\text{-}funnel}$	Time taken to see the light in the bottom of the V-funnel test, s
v^*_{n+1}	Intermediate particle velocity at time step n+1, m/s
Va	Assigned volume per particle, mm^3
VMAs	Viscosity modifying agents

v_n	Normal component of velocity, m/s
v_{n+1}	Particle velocity at time step n+1, m/s
v_t	The tangential component of velocity, m/s
W	Beam depth, mm
w/cm	Water to cementitious materials, %
W/P	Water to powder, %
x_n	Particle position at time step n
x_{n+1}	Particle position at time step n+1
α	Notch to depth, %
η	Plastic viscosity of SCC mixes, Pa s
τ	Shear stress, Pa
τ_y	Yield stress of SCC mix, Pa
ϕ_i	Volume fraction of solids, mm^3
ρ	Fluid particle density, kg/m^3
$\dot{\gamma}$	Shear strain rate, s^{-1}
∇^2	Laplacian

Contents

Chapter 1

Introduction

1.1 Introduction

This Chapter provides an introduction to the research that has been conducted during the PhD program; it sets out the research background, aims, objectives and thesis outline.

1.2 Research background

Concrete is the most plentiful of all man-made composite materials and is among the most essential construction materials. It is likely by far to consider it as the most common building material and continue to have the same significance in the future due to its countless merits, such as low cost, worldwide availability, high durability, and ability to withstand extreme environments. However, this construction material has to meet highly challenging demands of modern day concrete structures, represented by advances in architectural concepts, the complexity of construction, problematic reinforcement details. These needs together with the decline in the number of skilled operatives, particularly in Japan, led to producing poorly compacted concrete and consequently non-durable concrete structures.

In the late 1980s, there was a surge of interest based on Japanese thinking and exactly on that of Prof. Okamura in 1986 at Tokyo University, Japan (Okamura and Ouchi, 2003; Ouchi, 2001) to conceptualise a solution for the aggravated problems related to the poorly compacted cast concrete. The direction of this evolution was towards the creation of a new vibration-free concrete with which durable and reliable structures could be easily constructed. This was the motivation for developing self-compacting concrete (SCC), a modified cement-based material that, without any external compaction energy, flows, passes, fills and compacts under the influence of its dead weight alone. Such concrete can be used for casting members of heavy reinforcement, places where it is very limited or no access to vibrators and highly complicated shapes of formwork. In such cases, SCC provides a far superior solution than normally vibrated concrete (NVC).

Since its inception, SCC offers a high degree of automation of concrete industry and many other advantages. It will not only enhance the performance and working conditions (i.e. reduce the hazardous tasks for workers), it can also minimise the

special costs of in situ cast concrete constructions due to improved casting cycle, quality, surface finish, durability and reliability of concrete structures and eliminate some of the potential human errors.

SCC is a sensitive mix, strongly dependent on the composition and the characteristics of its constituents. It, like other types of concrete, has a heterogeneous nature as it consists of various graded materials (i.e. cementitious materials, filler, fine and coarse aggregate). The successful design of SCC mix must ensure a right balance between its competing properties of deformability (i.e. high flow-ability) and stability (i.e. segregation resistance). Thus, and due to its non-homogeneous composition, i.e. different specific gravities of its ingredients, the balance between high deformability and stability becomes a very complex issue, as it is tough to maintain its constituents in a cohesive form where higher mass particles (large aggregates) tend to settle down. Thus, it becomes essential to develop a proper mix design procedure for SCC.

A Bingham-type model, whose main parameters are plastic viscosity and yield stress, best describes the basic behaviour of the non-Newtonian viscous SCC. SCC has to possess a relatively low yield stress (τ_y) (the minimum energy required to initiate flow) to ensure high flow-ability, an adequate plastic viscosity (η) (a measure of a fluid's resistance to flow) to resist segregation and bleeding and must maintain its homogeneity during transportation and placing to ensure high structural performance and long-term durability (Chai, 1998). SCC constituents are of a broad range of size particles and densities. Thus, the prediction of an SCC flow behaviour becomes very challenging, especially in heavily reinforced structural members and in the presence of large size of coarse aggregate. The numerical modelling can provide an efficient tool for evaluating the flow behaviour in the fresh state. Importantly, it can determine whether an SCC mix is met the self-compactibility criteria. Moreover, modelling the flow of SCC in different formwork geometries may present an important way to control a proper casting process and ensure matching the rheological properties (i.e. yield stress and plastic viscosity) of the concrete.

It is well-known that fracture process is a fundamental phenomenon in quasi-brittle materials like concrete (Karihaloo, 1995; Bažant and Planas, 1997; Lilliu and van Mier, 2003). It can be considered as a primary reason for their damage under mechanical loading contributing to a significant degradation of material strength

(Tejchman and Bobinski, 2012). Fracture behaviour of a quasi-brittle SCC is an important aspect to be considered for analysis and design of engineering structures especially large-scale members, which consequently provides a basis for the evaluation of the strength of cracked structures (Bažant and Planas, 1997). Therefore, a realistic description of the fracture mechanism is crucial to ensure the safety of the structure. For a successful SCC, a reduction in coarse aggregate volume fraction and hence a high fine material content is required (Zhu and Gibbs, 2005). Such changes can increase cost and cause a temperature rise during hydration, and they possibly affect concrete properties such as shrinkage and creep. Other consequential effects of the mix composition are the potential changes in the pore structure and hardened properties especially fracture behaviour and consequently different cracking mechanisms in SCC in comparison with NVC. Still today, there are significant concerns among researchers that SCC may have different fracture behaviour compared to NVC, and this needs further research.

These are all the questions that deserve answers to which this thesis is dedicated.

1.3 Aims and objectives

As with any primary research program, there are profound questions, which drive the research. However, the size and complexity of research questions for a PhD program require division into a number of separate objectives. It is the findings from these objectives that, when combined, will satisfy the research aims.

1.3.1 Aims

To produce a successful SCC, it is essential to understand how the constituents affect the concrete fresh and hardened properties. This can be achieved by a proper mix design procedure. Moreover, the fracture behaviour of SCC mix of different composition needs to be addressed. It is also very useful to develop numerical simulation tools to avoid repeated and time-consuming laboratory work.

1.3.2 Research objectives

A number of distinct experimental objectives were set together with the modelling objectives to fulfil the final research aims and to provide a structure for the research processes, and these are as follows:

- **To develop a rational SCC mix design method based on target plastic viscosity and compressive strength**

SCC mix design methods have been developed by Karihaloo and Ghanbari (2012) and Deeb and Karihaloo (2013). They exploited the micromechanical expression used to estimate the plastic viscosity of an SCC mix from the known viscosity of the paste used in it. While such methods are rigorous and based on sound physical principles, they produce a bewildering array of mixes that reach the target plastic viscosity, but they do not give any practical guidelines on how to choose the most appropriate mix. Moreover, they are based on reference mixes of a range of known cube compressive strengths, but the latter was not explicitly imposed as a design criterion. The development in this thesis has been done by providing straightforward mix design charts and explicitly imposing the target cube compressive strength criterion.

- **To validate the developed rational SCC mix design method by proportioning SCC mixes of varying strengths and performances**

By using the improved rational mix design procedure, a number of SCC mixes have been developed and verified for self-compactibility by using four current SCC tests namely, slump flow, J-ring, L-box, and V-funnel.

- **To investigate the fracture behaviour of the developed SCC mixes of different composition**

For selected developed SCC mixes, the effect of different SCC composition (i.e. different coarse aggregate volume fractions, different paste to solids (p/s) ratios and different water to cementitious materials (*w/cm*) ratio on their fracture behaviour has been studied in detail.

- **To determine the SCC Bingham parameters (η and τ_y) that are needed for the modelling process by**

1. Estimating the plastic viscosity of the developed SCC mixes using the micromechanical procedure (Ghanbari and Karihaloo, 2009);
2. Predicting the yield stress by an inverse manner of the developed SCC mixes (Badry, 2015).

- **To simulate the 3-dimentional flow of the non-Newtonian viscous SCC mixes in the V-funnel**

The constitutive equation has been coupled with the mass and momentum conservation equations to simulate the 3-dimentional flow of the non-Newtonian viscous SCC mixes in the V-funnel test configuration using the smooth particle hydrodynamic approach (SPH).

- **To identify and monitor the distribution of larger aggregate particles of different sizes during the flow in the V-funnel and after the flow has stopped by**

Monitoring the distribution of larger aggregate particles process in various time steps and for all the developed SCC mixes to reveal whether or not they are homogeneously distributed.

1.4 Thesis outline

This thesis is organised into eight Chapters, which are further divided into sections and sub-sections for the clarity of presentation, followed by bibliographical references and Appendices.

Chapter 2 aims to provide a background knowledge of SCC. First, it provides a general overview of SCC, its properties, the materials used in its production and their effects on SCC characteristics in the fresh and hardened states. Second, it gives a summary of the tests available for SCC in its fresh state. Finally, previous mix design approaches have briefly been described.

Chapters 3 describes various computational methods used to model the flow of SCC mixes treating them as homogeneous or non-homogeneous masses. A brief overview of smooth particle hydrodynamic approach, its concept, particle interpolation, kernel functions will also be given. The three-dimensional Lagrangian form of the governing

equations of flow used to model the flow of SCC, namely the mass and momentum conservation equations are reported in this Chapter.

Chapter 4 describes the steps followed to develop an SCC mix design procedure based on target plastic viscosity and cube compressive strength.

Chapter 5 explains the validation process of the proposed mix design procedure. A series of SCC mixes were developed with different target plastic viscosity (3-15Pa s) and strength grades (30-80MPa).

Chapter 6 devotes to the study of the effect of three selected composition parameters of SCC mixes on their fracture behaviour by conducting three-point bend (TPB) tests on shallow (10mm), and deep (60mm) notched beams. The composition parameters are the coarse aggregate volume fractions, paste to solids (p/s) ratio and water to cementitious material (*w/cm*) ratio. The Chapter also describes an inverse procedure based on the non-linear hinge concept for identifying the parameters of the tension softening diagram (TSD) corresponding to the true specific fracture energy (G_F). It is worth to mention that in order to provide a broad picture of the effect of all the above parameters, this experimental work was carried out jointly with two other PhD students. These mixes, designated by A, B, and C, have different volumetric ratios of paste (cementitious materials, filler, super-plasticiser, and water), and solids (fine and coarse aggregate) as well as different strength grades.

Chapter 7 summarises the results of the three-dimensional incompressible Lagrangian modelling of the non-Newtonian viscous SCC mixes in the V-funnel. The formulation relating to incompressible SPH has been coupled with a suitable Bingham-type model to represent the rheological behaviour of SCC. The basic equations solved in SPH are the incompressible mass and momentum conservation equations. The simulation of SCC has also revealed the distribution of larger aggregates ($g \geq 8$mm) during the flow throughout the V-funnel mould at different time increments.

Chapter 8 ends the thesis with general conclusions embodied in Chapters 4 to 7 and also recommendations for future research.

The thesis concludes with an alphabetical list of references to the work in the literature, referred to in the text, and several appendices. A portion of the work described in this

thesis has been published or is in the publication process. For easy reference, the publications are listed below:

[1] Alyhya, W.S., Abo Dhaheer, M.S., Al-Rubaye, M.M., Karihaloo, B.L. and Kulasegaram, S. 2015. A rational method for the design of self-compacting concrete mixes based on target plastic viscosity and compressive strength. *35th Cement and Concrete Science Conference (CCSC35),* Aberdeen, UK.

[2] Alyhya, W.S., Abo Dhaheer, M.S., Al-Rubaye, M.M. and Karihaloo, B.L. 2016. Influence of mix composition and strength on the fracture properties of self-compacting concrete. *Construction and Building Materials 110, pp. 312–322*.

[3] Alyhya, W.S., Karihaloo, B.L. and Kulasegaram, S. 2016. Simulation of self-compacting concrete in V-funnel test by SPH. In: *24th Proceedings Conference of the Association for Computational Mechanics in Engineering (ACME),* Cardiff, UK.

[4] Alyhya, W.S., Abo Dhaheer, M.S., Al-Rubaye M. M., Karihaloo, B.L. and Kulasegaram, S. 2016. A rational method for the design of self-compacting concrete mixes based on target compressive strength. In: Khayat, K. H. ed. *8th International RILEM Symposium on Self-Compacting Concrete. RILEM Publications SARL*, Washington DC, USA.

[5] Alyhya, W.S., Kulasegaram, S. and Karihaloo, B.L. 2016. Simulation of the flow of self-compacting concrete in the V-funnel by SPH. (Revision s*ubmitted to the Cement and Concrete Research journal*).

[6] Abo Dhaheer, M.S., Al-Rubaye, M.M., Alyhya, W.S., Karihaloo, B.L. and Kulasegaram, S. 2016. Proportioning of self-compacting concrete mixes based on target plastic viscosity and compressive strength: Mix design procedure. *Journal of Sustainable Cement-Based Materials 5(4), pp. 199–216.*

[7] Abo Dhaheer, M.S., Al-Rubaye, M.M., Alyhya, W.S., Karihaloo, B.L. and Kulasegaram, S. 2016. Proportioning of self-compacting concrete mixes based on target plastic viscosity and compressive strength: Experimental validation. *Journal of Sustainable Cement-Based Materials 5(4), pp. 217–232.*

[8] Al-Rubaye, M.M., Alyhya, W.S., Abo Dhaheer, M.S. and Karihaloo, B.L. 2016. Influence of composition variations on the fracture behaviour of self-compacting concrete. In: *21st European Conference on Fracture (ECF21)*, Catania, Italy.

Chapter 2

Self-compacting concrete (SCC)

2.1 Introduction

Concrete is the most widely utilized construction material in the world for infrastructure and civil engineering applications, followed by wood, steel, and other materials. Interestingly, over ten billion tons of concrete are globally produced each year (Mehta, 2002). According to the Cement Sustainability Initiative, CSI (2009) the manufactured concrete is roughly estimated to be equal to 25 billion tons per year, which means 3.8 tons per person per year in the world. Nevertheless, the casting of such concrete, which is known traditionally as normal vibrated concrete (NVC) involves placing and subsequent vibration process that is necessary for better-hardened concrete in the real structure (Neville and Brooks, 2010). The vibration process is often carried out by vibrators, usually operated by unskilled labour with inherently difficult supervision (Frandsen and Schultz, 1997; Neville and Brooks, 2010).

In the early1980s and particularly in Japan, the NVC has been criticised for its durability issues. This was due to the poor compaction resulting from a decline in the numbers of skilled workers in the construction industry, with subsequent effects on construction quality and durability. Such problems might also occur when concrete does not properly surround reinforcement resulting in honeycombing (Frandsen and Schultz, 1997). Indeed, and especially in heavily reinforced members, it is often not an easy task to ensure a fully compacted concrete where there is limited or no access for vibrators. In such cases, there are no practical means by which full compaction of concrete on a site can ever be completely ensured.

The best answer towards overcoming and solving such issues was by developing self-compacting concrete (SCC), which is a concrete that can achieve impressive deformability and homogeneity in its fresh state, filling every nook and corner around the reinforcement, and forming a compact, uniform, void-free mass under its own weight without any external vibration (Okamura and Ouchi, 2003). Since its development at the early 1990s, SCC is gradually becoming the preferred formulation globally for members in numerous civil engineering applications, where it is hard or impossible to pour and vibrate NVC.

SCC with its exceptional fresh properties (i.e. filling ability, passing ability and segregation resistance) provides the opportunity to exploit several potential benefits.

It can give designers and architects more freedom of creativity that was not previously possible. Lighter and thinner members can be produced, bigger span bridges can be developed, and marine structures can be built, making SCC an extremely promising material for the future of the in-situ and precast construction industries. These benefits and others, which will be discussed further, later on, cover various important areas in the building field.

This Chapter will give a short introduction and historical background to the development of SCC as well as its definition. The merits and demerits of SCC application and its key properties will also be summarised. A brief overview of the common methods used to measure SCC properties will be provided. Also, a general summary of the materials used to produce SCC will be given, highlighting their main effects on its characteristics in the fresh and hardened states. Furthermore, the most popular mix design approaches for SCC will also be briefly reviewed. Hence, this Chapter outlines the overarching research used to address the objectives, as set out in Chapter 1.

2.2 History of SCC development

Okamura was the first who proposed SCC in 1986. The first SCC mix was completed in 1988 at the University of Tokyo, using the same constituent materials as in NVC (Ouchi, 2001). The fundamental reasons behind the employment of SCC were to shorten construction time, to avoid vibrating confined zones, which are rather difficult to access, and to eliminate noise caused by vibration (Okamura and Ouchi, 2003). In the last two decades, SCC has been developed further by utilizing various new constituents such as pulverized fuel ash (PFA), condensed silica fume (CSF) and ground granulated blast-furnace slag (ggbs). What is more, the development of highly active water-reducing admixtures (super-plasticisers) combined with high powder contents has been boosting the use of SCC much further. Consequently, SCC has gained a wide interest, especially for structures with complex shapes, complicated casting processes, and very congested reinforcements.

2.3 Definition of SCC

There are various definitions of SCC in the literature. SCC can be defined, to a great extent, by its workability. It is an advanced type of concrete (also known as a super workable concrete) that sees the addition of super-plasticiser and a stabiliser significantly increase the ease and rate of flow and pass through complex geometrical configurations under its own weight without vibration maintaining homogeneity.

The BS EN 206-9 (2010) defines SCC as "concrete that is able to flow and compact under its own weight, fill the formwork with its reinforcement, ducts, boxouts, etc., whilst maintaining homogeneity". The American Concrete Institute (ACI) (2007) defines SCC as "a highly flowable, non-segregating concrete that can spread into place, fill the formwork, and encapsulate the reinforcement without any mechanical consolidation".

The essential fresh properties of SCC, which will be enumerated later, have been satisfied in these definitions and met the SCC' requirements resulting in high-quality hardened concrete (Figure 2.1), independently of the workmanship during placing.

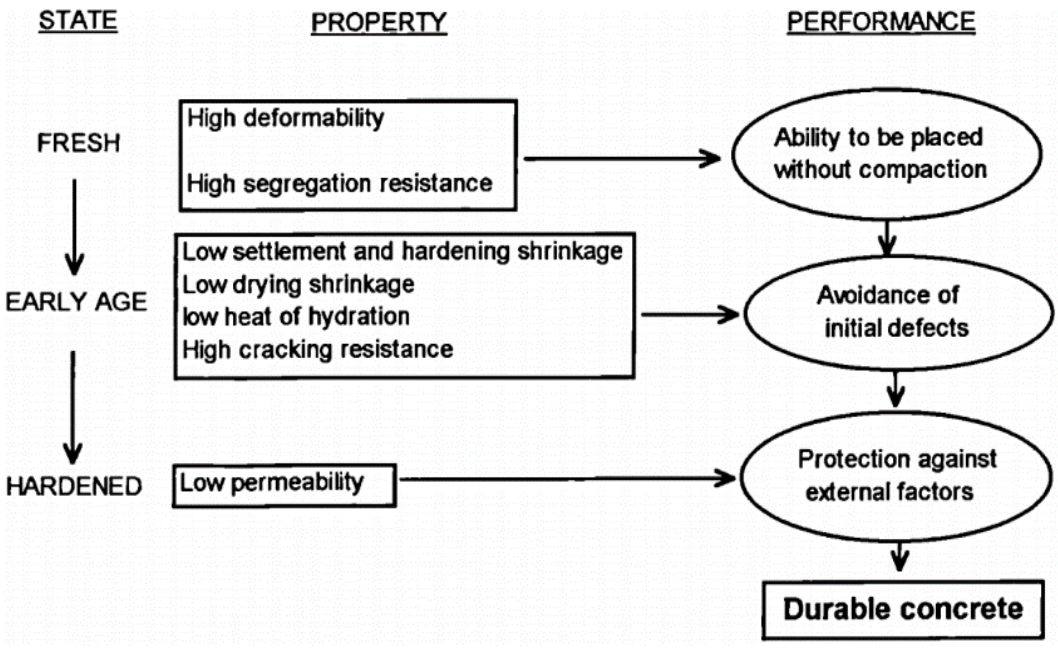

Figure 2. 1 Definition of self-compacting high-performance concrete (After Okamura, 1992)

2.4 Properties of fresh SCC

The properties of significance for any discussion of fresh SCC are those that affect its placement and compaction. It is in these properties that SCC shines and differentiates itself from other concrete types. Characteristics of SCC are literally linked to its fresh properties. SCC has three key fresh properties: filling ability, passing ability and segregation resistance and they should be secured during transporting and after placing (The Concrete Society (BRE), 2005; Pade, 2005; Anon, 2005). These properties are interdependent and related to each other. Any change in one property will normally result in a change in the others. In other words, poor filling ability and/or high segregation resistance can cause insufficient passing ability, i.e. blocking. Hence, SCC can be basically considered as a trade-off between filling ability and segregation resistance as illustrated in Figure 2.2.

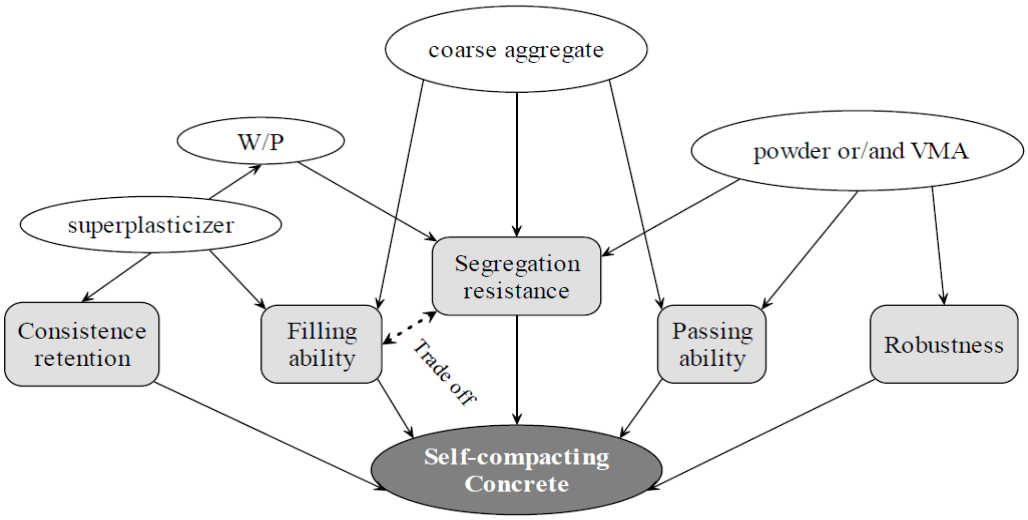

Figure 2. 2 Schematic of approaches for achieving SCC (After Liu, 2009)

2.4.1 Filling ability

Filling ability is the ability of fresh SCC to flow into and fill formwork under the action of gravity. It reflects the changes in SCC's deformability, i.e. the ability of fresh SCC to change its shape driven by its own weight and casting energy (Khayat, 1999a). The deformability consists of two primary aspects: the deformation capacity, which is the maximum ability to deform i.e. how far concrete can flow; and the deformation

velocity, which refers to the time needed by concrete to stop flowing, i.e. how fast concrete can flow. Filling ability is a harmony between capacity and velocity of deformation. For example, an SCC of high deformation capacity and low deformation velocity tends to be very viscous and would take a long time to fill the formwork.

The inter-particle friction between solid particles (powder, fine aggregate, and coarse aggregate) should be reduced to attain SCC with high filling ability. This can be achieved by utilizing additional water, which is not the optimal option as it can cause segregation due to its adverse effect on viscosity and yield stress. Too much water also has undesirable consequences for strength and durability. Unlike water addition, the incorporation of high range water reducing admixtures (super-plasticisers) can not only reduce the inter-particle friction by dispersing cement particles but also maintain the filling ability (Figure 2.2) (Khayat, 1999a; Sonebi and Bartos, 2002). It also has less or no adverse effect on hardened properties than water. On the other hand, coarse aggregate content and its particle size distribution also affect filling ability as less amount and/or continuously graded coarse aggregate reduce the inter-particle friction (Khayat, 1999a; Sonebi et al., 2001).

2.4.2 Passing ability

Passing ability, which is a property unique to SCC determines and guarantees how well an SCC mix will flow through restricted spaces and tight openings without blocking, which consequently secures its specific applications in densely reinforced structures, such as bridge decks, tunnel linings or tubing segments. Passing ability relates to the risk of blocking, which results from the interaction between aggregate particles and also between aggregate particles and the restricted space. When SCC approaches a tight space, the different flowing velocities of the aggregate and mortar cause a local increase in the content of coarse aggregate. Thus, some aggregates may bridge or arch at the narrow openings preventing the rest of concrete from passing, as shown in Figure 2.3 (Noguchi et al., 1999; Okamura and Ouchi, 2003).

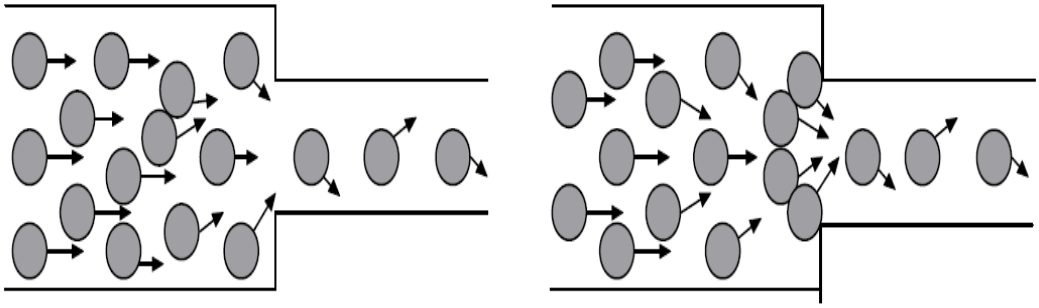

Figure 2. 3 Blocking mechanism (After RILEM TC174, 2000)

The property of passing ability is significant in any situation where the aggregate particles in an SCC have to rearrange themselves to go through a tight opening (Figure 2.4) (Daczko, 2012).

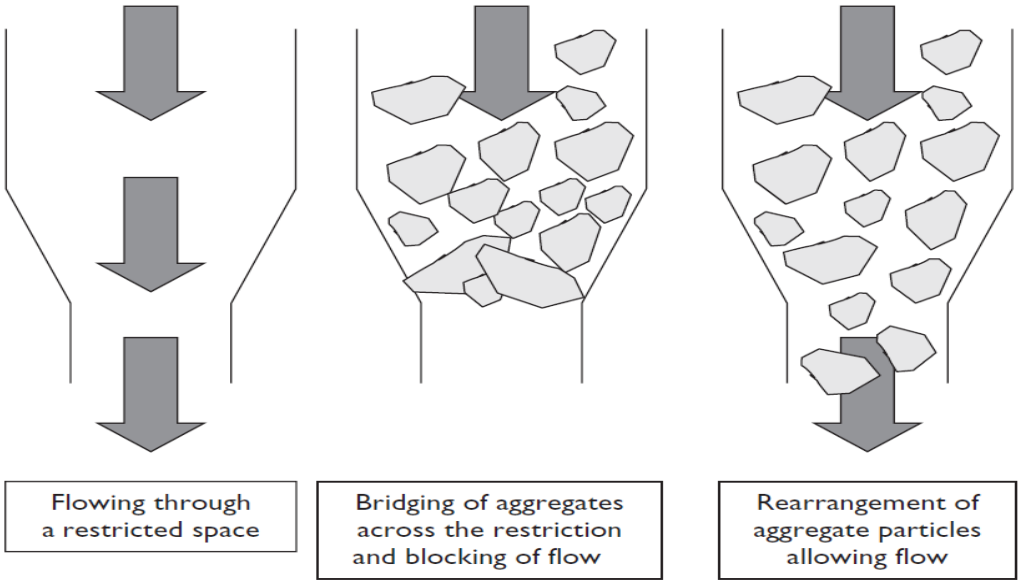

Figure 2. 4 Aggregate blocking and flowing through a tight opening (After Daczko, 2012)

The risk of blocking depends mainly on the size, shape, and content of coarse aggregate. Lower size and content of coarse aggregate as well as high paste volume are very effective factors in inhibiting the blocking risk (Billberg et al., 2004). Billberg et al. (2004) also concluded that the ability of SCC to pass depends primarily on yield stress rather than viscosity. However, a paste with sufficient viscosity can also prevent

local increases in coarse aggregate and hence avoid blocking. The viscosity increases when incorporating powder materials such as fly ash, ggbs, and limestone filler as better distribution and particle packing will be achieved (Edamatsu and Nishida, 1998). Another efficient approach to ensure sufficient viscosity is the use of viscosity modifying agents (VMAs), which will be discussed further in a later section.

2.4.3 Segregation resistance

The segregation resistance (i.e. stability) is the strength of the SCC' components to migration or separation. Since SCC' components are of various sizes and densities, it is highly susceptible to segregation. The component particles, which have a relatively high density or a low surface-volume ratio, are more prone to separation. The segregation includes that between water and solid (free water detaches from solid particles and freely moves, which is known as bleeding), or between paste and aggregate or between mortar and coarse aggregate (RILEM TC174, 2000). The segregation is determined under two conditions: dynamic and static. The former is the one happens during transport, placement, and up to the point where the latter takes over (i.e. when SCC mix sits undisturbed). The segregation can cause harmful effects on SCC properties such as surface defects (e.g. cracking and weak surface layer) and nonhomogeneous structure of hardened concrete. The effective technique to enhance the stability of SCC is by ensuring an appropriate viscosity. This can be accomplished by binding additional free water by reducing the water to powder ratio (W/P) by utilizing high volumes of powder materials or viscosity modifying agents (VMAs). Reducing the size and lowering the content of coarse aggregate are also an effective technique in inhibiting segregation.

2.5 Self-compactability criteria

To secure self-compactability, it is necessary to maintain superior filling ability, real obstacle passing ability, and sufficient segregation resistance. In other words, SCC must be as fluid as possible in its fresh state to fill, under its own weight, all the far-reaching corners of the formwork and pass smoothly through heavy reinforcement without blocking or segregation. The methodology of selecting the right amount of

materials and admixtures is essential in achieving the self-compactability goal. Okamura and Ouchi (2003) have proposed the following three main rules (Figure 2.5).

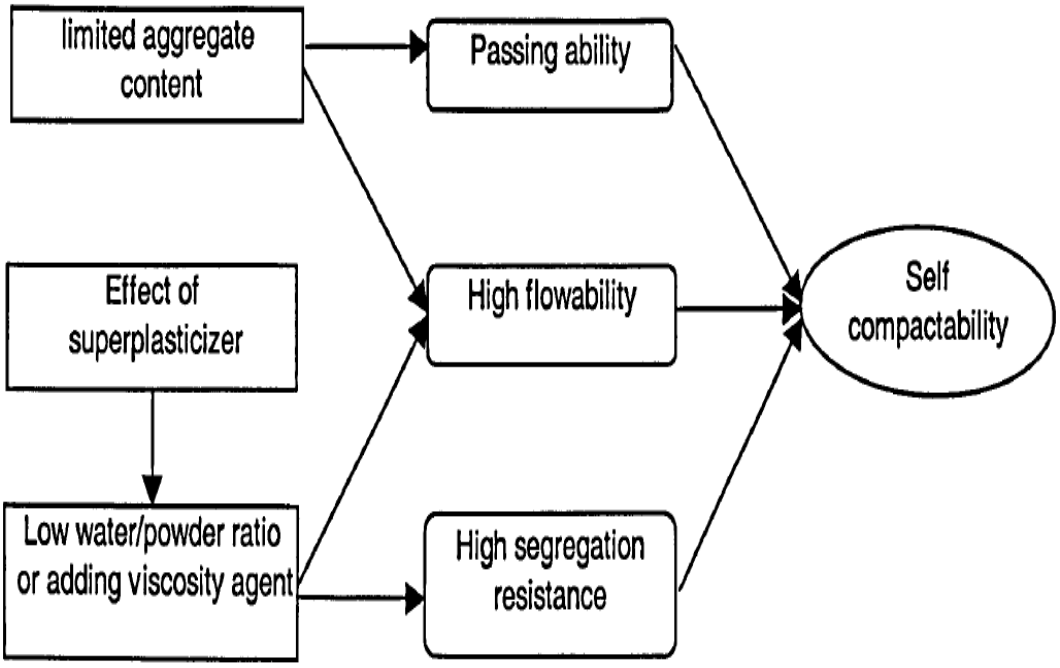

Figure 2. 5 The three core rules for obtaining self-compacting concrete (After Jin, 2002)

2.5.1 Limited aggregate content

The properties of SCC, especially the passing ability, are highly affected by the friction between the aggregates particles. In densely reinforced areas, the passing ability can be enhanced by reducing the volume and the maximum size of coarse aggregate and/or using round aggregate instead of crushed one. In other words, when the relative distance between aggregate particles reduces, the frequency of collision as well as the contact between them will increase (Okumara and Ouchi, 1999), causing high internal stress, particularly when concrete gets deformed near obstacles resulting in blocking of aggregate particles (Figure 2.6). Thus, limiting the coarse aggregate content, whose energy consumption is particularly intense to a level lower than normal proportions is very effective in avoiding any blocking.

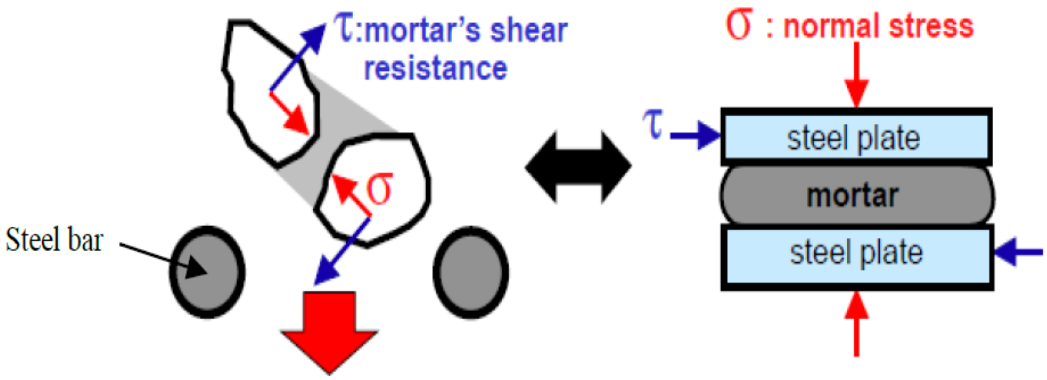

Figure 2. 6 Normal stress generated in mortar due to approaching coarse aggregate particles near reinforcing bars (After Okamura et al., 2003)

2.5.2 Low water to powder ratio

Highly viscous SCC is often required to be able to carry coarse aggregate particles and prevent segregation. Such a goal can be secured by the incorporation of high amounts of powder materials, which also have a positive influence on filling ability (Khayat, 2000). Using additions such as ggbs, silica fume, fly ash and limestone filler are the best solution to be included within the significant amount of the powder materials to avoid the subsequent adverse effect of using only Portland cement. Another effective alternative for increasing the paste volume is by using viscosity modifying agents (VMAs), which give the same effect in minimising the tendency of coarse aggregate to segregation by thickening the paste and keeping the water in the skeleton. VMAs are assumed to make SCC less sensitive to water variations. However, the small quantities of VMAs used cause difficulties in achieving an accurate dosage.

2.5.3 Effect of super-plasticiser

High deformability (i.e. filling ability) can be effectively attained by the use of a super-plasticiser, which disperses flocculated cement particles, reducing the attractive forces among them and keeping the water to powder ratio at very low value. However, it has been stated that a highly fluid SCC, which results from low viscous SCC due to the use of high super-plasticiser dosage could be more prone to have its coarsest particles

segregated (Roussel et al., 2009; Desnerck et al., 2011). Low viscous SCC can cause an increase in the coarse aggregate local volume fraction near obstacles and nonhomogeneous concrete (Figure 2.7). Therefore, it is necessary to employ an optimum dosage of super-plasticiser as low resistance to segregation might result when higher dosage is used.

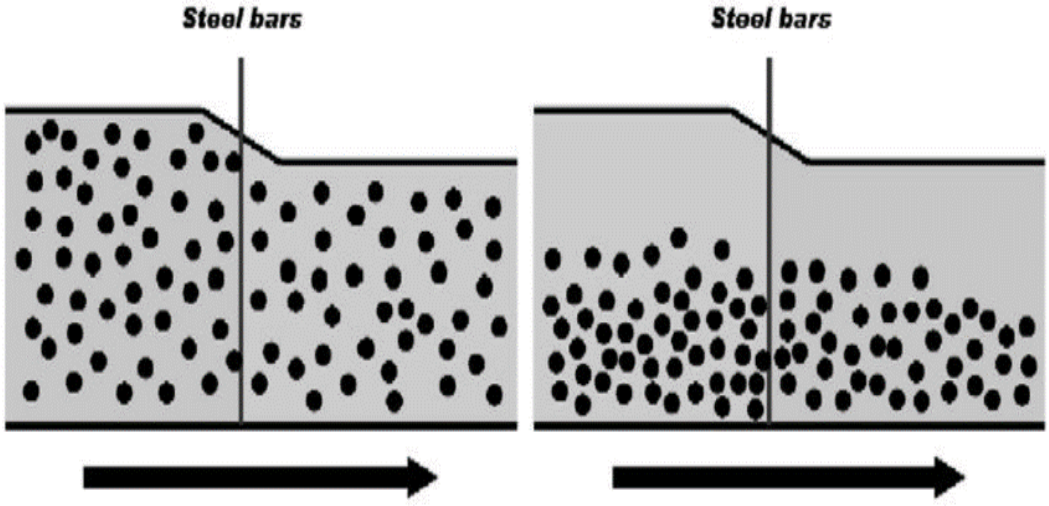

Figure 2. 7 Low viscosity SCC is more prone to separation (After Roussel et al., 2009)

2.6 Approaches to achieving SCC

According to the original conception of Okamura and Ozawa (2003), SCC is broadly obtained by three approaches based on the technique followed in achieving the adequate viscosity (Dehn et al., 2000; Holschmacher and Klug, 2002) as follows:

1. SCC based on increased powder content (powder type): SCC is characterized by a low water to powder ratio (i.e. a high powder content), which is required to limit the free moisture content and increase the viscosity. This was the first generated prototype of SCC. SCC mixes of this approach are sensitive to changes in constituent materials because of the high powder content. Due to the low W/P ratio, such concrete is anticipated to have a high strength and shrinkage and low permeability. Usually, additions such as cement replacement materials (CRMs) and fillers are used to replace Portland cement to control the heat of hydration.

2. SCC based on viscosity modifying agents (VMAs) (VMAs type): This approach is characterized by using viscosity modifying agents (VMAs), which are added primarily to provide the appropriate viscosity. Compared with the powder type SCC, this requires greater super-plasticiser dosage or high W/P ratio to achieve the filling ability requirements.

3. SCC based on both VMAs and powder (combined type): This approach of SCC was developed to improve the stability of the powder type SCC by adding a small amount of VMAs. In such SCC mixes, the content of VMAs is less than that in the VMAs type SCC; the content of powders and W/P ratio are less than those in the powder type SCC. The VMAs contributes to the viscosity along with the powder. SCC based on this type reported having high filling ability and strong segregation resistance (Khayat, 1998). Typical powder contents according to JSCE recommendations (Uomoto and Ozawa, 1999) are shown in Table 2.1.

Table 2. 1 Typical powder contents according to JSCE recommendations

SCC approach	Powder content %	Mass* kg/m^3
SCC based on increased powder content	16-19	500-600
SCC based on viscosity modifying agents (VMAs)	9.5-16	300-500
SCC based on both VMAs and powder	>13	>410

*based on Portland cement only

2.7 Merits and demerits of using SCC

Any new technology must have significant advantages over existing technology for it to be applied. This section will briefly describe the merits and demerits of using SCC.

2.7.1 Merits

Using SCC produces several benefits over NVC. Some of the significant benefits are summarized below:

1. Health and environmental protection

A noisy environment is no doubt harmful to the health of people, particularly when it lasts for a long time. Thus, the use of SCC can eliminate the health problems related to the use of vibration equipment such as blood circulation that causing "white fingers" and deafness (RILEM TC174, 2000). All these are the reasons behind considering SCC as 'the quiet revolution in concrete construction (The Concrete Society (BRE), 2005). Furthermore, SCC makes not only concrete work less difficult but can also improve workplace environment by reducing noise pollution. Using SCC can also offer a reduction in sound level at sites, precast factories, and neighbourhoods; hence, it provides a quieter construction environment (that is why it is sometimes called as silent concrete) and makes construction activities more acceptable to residents.

2. Economy and time-saving

Labour cost in the developed countries is the main expenditure of concrete work, and modern construction management always has the aims of lowering cost and shortening construction schedules, especially in massive concrete structures where compaction is very labour intensive. Using SCC can not only significantly reduce the labour cost but can also lessen the time of construction by accelerating construction process, especially in precast industry. The ease of placement of SCC increases productivity and cost saving by reducing required equipment, labour and wear and tear of forms. It can also lessen the number of workers and save material consumption. Because of its high fluidity, SCC allows saving energy and ensures reasonable cost in place due to eliminating vibration process. Furthermore, SCC can also enable the supplier to provide better consistency in delivering concrete, which reduces interventions at the plants or job sites.

3. Enhanced quality

The quality of hardened concrete will be enhanced as high attention is required to the quality control before placing SCC (Desnerck et al., 2014). High level of homogeneity and minimal SCC voids can be yielded in sites of intricate castings (i.e. congested

reinforcement and limited or no access for vibrators) providing the potential for superior durability. Furthermore, SCC is often produced with low water-binder ratio, thus providing higher early strength, earlier demoulding and faster use of elements and structures. Moreover, the filling ability merit of SCC makes it very suitable for exceptional and technically challenging structures such as tunnel linings, as the likelihood to compact the concrete is limited in such closed spaces.

4. Innovations in construction system
NVC restricts construction work in many ways due to the need for vibration during placing. Among these restrictions are the limitation on the height of placing lift, the necessity for scaffolding construction for consolidation work, and the need to separate placing of bases and walls of box-section members. As SCC eliminates vibration, the construction system can be significantly improved and rationalised.

5. SCC gives a broad opportunity for the use of high volumes of by-product materials such as silica fume, fly ash, limestone powder, and others since higher volumes of powder material are required to enhance the cohesiveness (Yahia et al. 2005).
6. The use of SCC at construction sites reduces the risk of accidents by decreasing the number of cables required for the operation of compacting equipment, thus decreases workers compensation premiums.
7. Construction with SCC does not require skilled employees and is not affected by the shape of framework and arrangement of reinforcement in the structures.

2.7.2 Demerits

Everything has two sides, and some disadvantages often accompany advantages. Despite all the above advantages, following are some of the potential disadvantages:

1. Production of SCC places very strict requirements on the selection of materials in comparison with NVC. An uncontrolled variation of moisture content in fine aggregate and overdosing of super-plasticiser will have a much greater effect on the properties of SCC, especially at very low *w/c* ratio. The high powder content and the use of admixture also lead to high sensitivity of SCC to any variation in material content than that of NVC.

2. Proper stockpiling of aggregate, uniformity of moisture in the batching process, and good sampling practice are essential for SCC mix. A change in SCC properties could be a warning sign for its quality control.

3. High standard quality control needs to be enforced when producing SCC. However, the quality control is easier to carry out in a factory than on site, and generally, SCC makes things harder for the concrete suppliers, but easier for the site workers.

4. Development of an SCC requires a significant number of laboratory trial batches in addition to the field size trial batches to simulate typical production conditions.

5. Higher lateral pressure on the formwork due to the inherent low yield stress of SCC. The real lateral pressure depends on the pouring and hardening rates of concrete. This adverse effect compromises profitability and increases liability due to the need for building expensive and robust formwork.

6. SCC is initially costlier than NVC based on material cost due to the higher powder content and the use of admixture, particularly super-plasticisers (The Concrete Society (BRE), 2005; Nehdi and Rahman, 2004). However, in large structures, the increase in material cost can be easily outweighed by the enhancement in productivity, the elimination of vibration expense and maintenance, and the employment of by-product materials.

7. Conventional equipment can be used to pump SCC, and possibilities of blocking in bent and tapered pipes are low due to low segregation and excellent deformability. However, the pumping resistance in straight pipes is higher than that of NVC. Since frictional resistance increases as standard pressure on concrete increases, pumping vertically upward and pumping rate increase lead to a greater increase in pumping resistance compared with NVC. Hence, it is recommended to place SCC slowly and continuously, and pipes of 125mm in diameter are recommended instead of pipes of 100mm for pumping NVC.

2.8 Self-compactability tests

The conventional methods for testing the workability of NVC cannot be used for SCC because they are not sufficiently sensitive to detect a tendency to segregation. Different tests are described below (§ 2.8.1) to assess the essential properties of fresh SCC.

Tattersall (2003) proposed three categories of tests that are useful for workability evaluation of SCC mix:

- Qualitative assessment tests provide a general description of self-compactability behaviour with no attempt to quantify such properties as filling ability, passing ability and segregation resistance (stability), which have been discussed previously in § 2.4.
- Quantitative assessment and empirical tests provide a simple description of the behaviour of SCC such as slump flow test, L-box test…etc., which will be discussed further later on (BS EN 206-9, 2010).
- Quantitative principal assessment tests provide a description related to rheological properties of SCC such as plastic viscosity, yield stress…etc., which will be described briefly in Chapter 3.

2.8.1 Slump flow test

This test was first developed to assess underwater concrete in Japan. It evaluates the ability of concrete to deform (horizontal free flow) under its own weight against the friction of the base with no other external restraint or obstructions present. This test, however, cannot check whether SCC will pass through spaces between reinforcement bars, but may be useful as a routine control test, to detect the tendency for the paste to separate from the mix. The spread diameter is a measure of filling ability of SCC while the time needed for SCC mix to reach 500mm flow (t_{500}) is a measure of viscosity. It can be conducted on-site as it is a rapid and straightforward test procedure, though the base plate size is somewhat unwieldy, level ground is essential, and two people are required if the t_{500} time is to be determined. It can be debated that the completely free flow unrestricted by any boundaries, is not representative of the practice in concrete construction, but the test can be used to evaluate the consistency of ready-mixed concrete supply to a site from load to load. The EFNARC (2005) suggest three classes for the slump flow according to the final spread (Table 2.2).

Table 2. 2 Slump flow classes according to EFNARC (2005)

SCC class	Slump spread mm
SF1	550-650
SF2	660-750
SF3	760-850

Test apparatus

Truncated cone (Abram's cone) is used in this test with internal dimensions of 100mm diameter at the top, 200mm at the base, and a 300mm height, conforming to EN12350-2 (2010) (Figure 2.8). A base plate is of a stiff non-absorbing material, at least 700mm square, marked with a circle that marking the central location for the slump cone, and a further concentric circle of 500mm diameter.

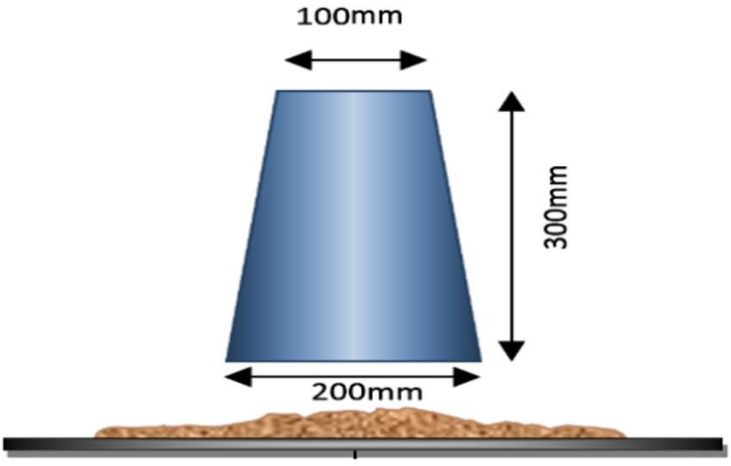

Figure 2. 8 Apparatus for the slump flow test

2.8.2 V-funnel test

The test was first developed in Japan (Ouchi, 2003). It is used to evaluate the filling ability of SCC with a maximum aggregate size of 20mm. It is also useful for adjusting the powder content, water content and admixture dosage. Apart from the above uses,

the V-funnel can provide the practitioner with a relative indication of the plastic viscosity. The V-funnel is filled with about 12 litres of SCC and the time taken for it to flow through the apparatus is measured and recorded as the discharge time ($t_{v\text{-}funnel}$). The inverted cone shape will cause any liability of SCC for blocking to be reflected in the result i.e. when there is too much content of coarse aggregate or high viscosity mix. Low flow time can be associated with high filling ability due to low paste viscosity and low inter-particle friction. The EFNARC guidelines (2005) suggest two classes according to the V-funnel time (Table 2.3). The dimensions of V-funnel are shown in Figure 2.9 (BS EN 12350-9, 2010).

Table 2. 3 Viscosity classes

SCC class	500mm spread time t_{500}, s	V-funnel time $t_{v\text{-}funnel}$, s
VS1/VF1	≤ 2	≤ 8
VS2/VF2	> 2	9-25

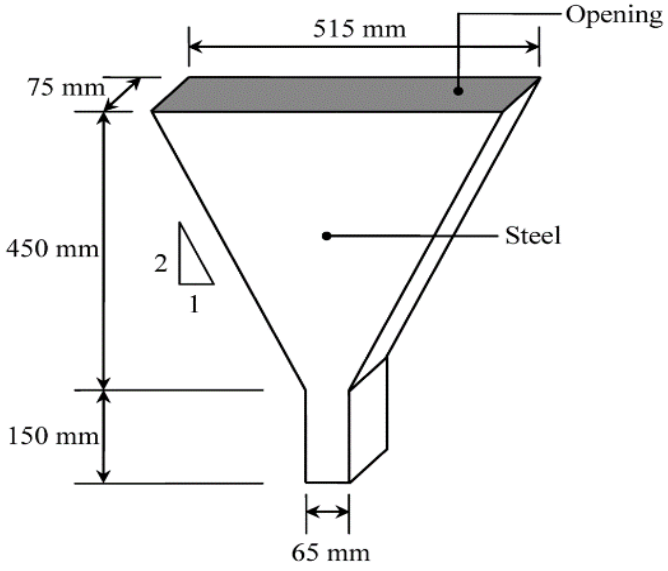

Figure 2. 9 V-funnel test apparatus

2.8.3 J-ring test

This test can determine the ability of SCC to pass through tight openings including spaces between reinforcing bars. The J-ring can be used in conjunction with the slump flow or even with the V-funnel. These combinations can check the filling and passing abilities of SCC. The spacing between J-ring bars can be adjusted. After the test, the time needed for the flow to reach 500mm diameter is recorded as t_{500J}, and the flow is allowed to stop before recording the measurements. The height difference between the concrete inside and that just outside the J-ring is also measured. This will provide an indication of the passing ability or the degree to which the passage of SCC through the gaps in bars is restricted.

Test apparatus

A truncated cone mould, without foot pieces with internal dimensions 100mm diameter at the top, 200mm diameter at the base, and a 300mm height are used. The base plate of a stiff none absorbing material, at least, 700mm square, marked with a circle showing the central location of the slump cone, and a further concentric circle of 500mm diameter. The equipment also consists of a (30mm×25mm) open steel ring, drilled vertically with holes to accept threaded sections of reinforcing bars. These sections can be of different diameters and spaced at different intervals by normal reinforcement consideration - three times the maximum aggregate size might be adequate. The diameter of the ring of vertical bars is 300mm and the height 100mm. The apparatus is shown in the Figure 2.10.

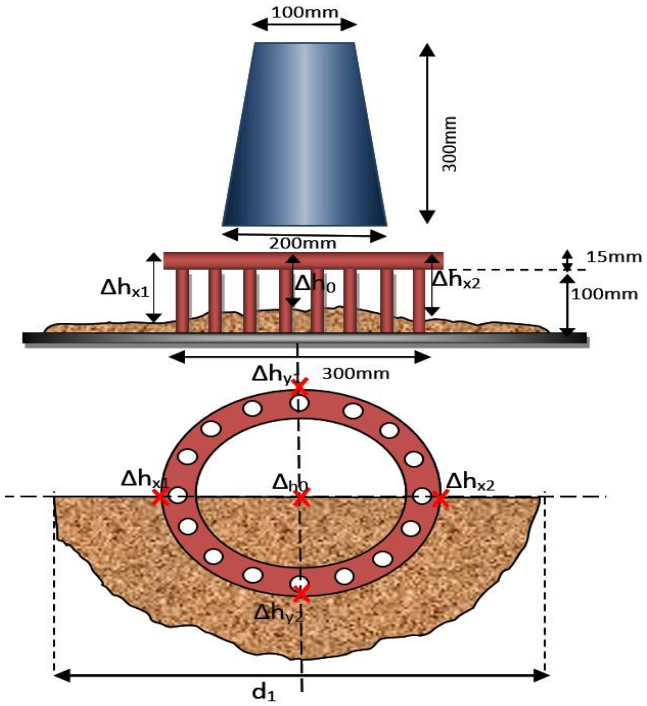

Figure 2. 10 J-ring test apparatus

2.8.4 L-box test

This test evaluates the filling ability of SCC and the capacity to pass through narrow openings including spaces between reinforcement and other obstacles without blocking. The segregation (lack of stability) can also be revealed visually or by subsequently sawing and inspecting various sections of the concrete in the horizontal section. The reinforcement bars can be set at two optional spacings to impose a more or less ultimate test of the passing ability of the concrete.

Test apparatus

The apparatus has a rectangular section box in the shape of an 'L', with a horizontal and vertical section separated by a sliding gate in front of which vertical reinforcement bars are fitted. The vertical part is filled with SCC, and then the gate lifted vertically to let the concrete flow into the horizontal section. When the flow has stopped, the height at the end of the horizontal section is expressed as a ratio of that remaining in the vertical section (H_2/H_1). It is an indication to the slope of the concrete when at rest, (i.e. an indication of passing ability) or a reveal of the degree to which the passage of

concrete through the bars is restricted. The EFNARC (2005) suggest two classes according to H_2/H_1 ratio (Table 2.4).

Table 2. 4 Passing ability classes for SCC

SCC class	Passing ability
PA1	≥ 0.80 with 2 bars
PA2	≥ 0.80 with 3 bars

The horizontal part of the box can be marked at 200mm and 400mm from the gate and the times took to reach these points are recorded. These are known as t_{200} and t_{400} times and are an indication of the filling ability. L-box shape and dimensions as shown in Figure 2.11.

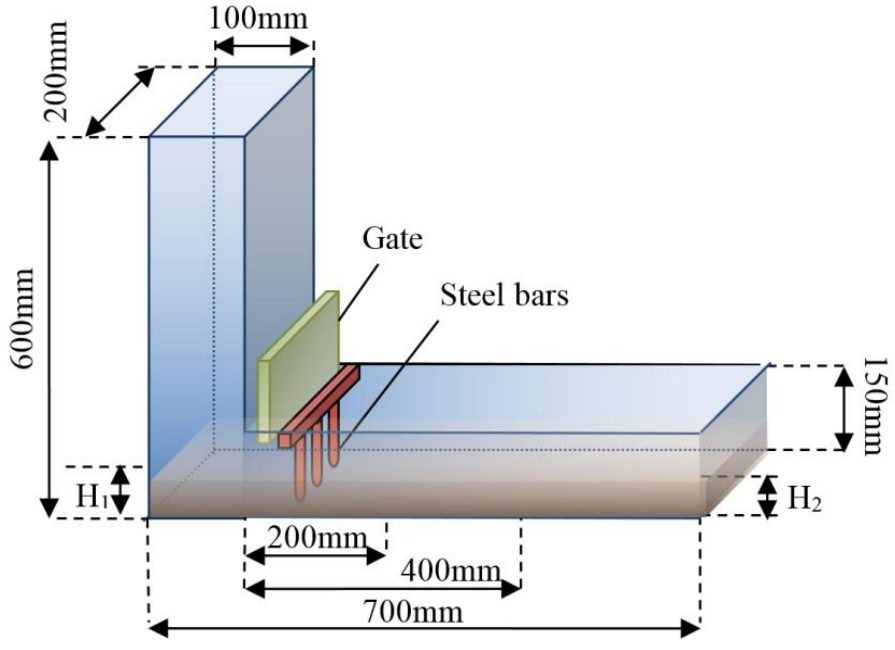

Figure 2. 11 L-box test apparatus

2.9 Constituent materials used in SCC

SCC can be made from ingredients, which are almost the same as used in producing NVC but it has to meet special requirements, which cannot always be attainable by using common ingredients and normal design procedure. Figure 2.12 shows typical volume percentages of constituent materials in SCC and NVC.

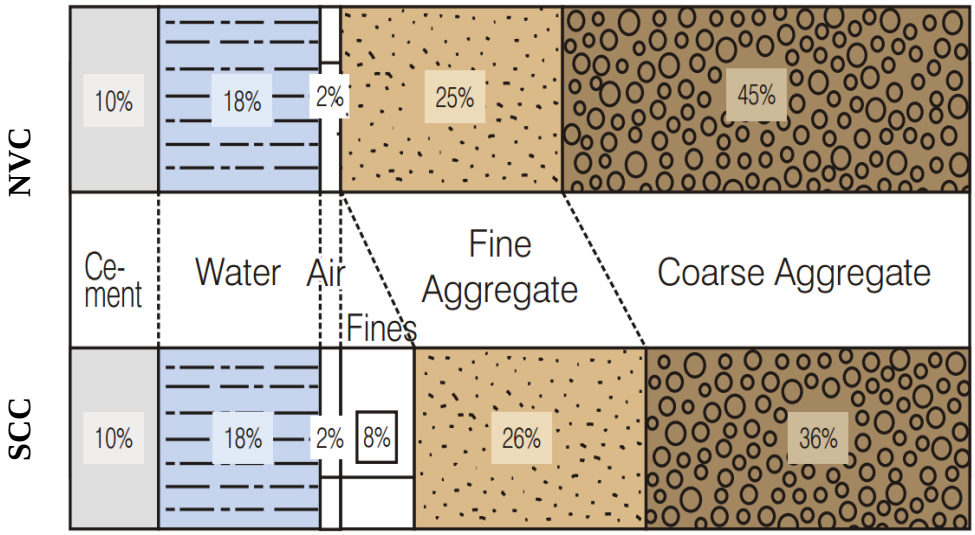

Figure 2. 12 Typical volume fractions of constituents in SCC (After Kosmatka et al., 2003)

The component materials in SCC and their roles on the fresh and hardened properties are reviewed in the next section.

2.9.1 Cement

Portland cement concrete is foremost among the construction materials used in civil engineering projects around the world. The reasons behind its common use are varied, but among the most important are the commercial and widespread availability of its ingredients, its versatility, and adaptability and the minimal maintenance requirements during service (Mindess et al., 2003). All types of Portland cement have been effectively used in the production of SCC, such as CEM I, blast furnace slag cement and sulphate resisting cement (ASTM C151, type III). Indeed, the European guidelines for SCC (2005) state that all cement, which conforms to EN 197-1 can be used in producing SCC (BS EN 197-1, 2011). The performance of SCC can be highly affected by the chemical composition of cement such as C_3A and C_4AF as they initially adsorb

super-plasticiser during mixing and consequently affect its dispersion efficiency and consistency retention. C_3A and C_4AF have a rapid initial hydration (Collepardi, 1998), which is the reason behind the preference for low heat Portland cement (low C_3A and C_4AF) in the early development of SCC in Japan.

2.9.2 Additions

High powder contents are usually required to produce SCC. When only Portland cement is used, SCC will be expensive and susceptible to high thermal shrinkage. It is, therefore, necessary to substitute some of the Portland cement by other ultra-fines materials known as additions such as fly ash, ggbs or limestone powder. Additions are 'finely divided materials used in concrete to improve certain properties or to achieve specific properties' including two types: nearly inert or semi-inert additions (Type I) and pozzolanic or latent hydraulic additions (Type II) (BS 8500-1, 2006). The inert or semi-inert additions are known as fillers, while pozzolanic or latent hydraulic additions are known as cement replacement materials (CRMs).

2.9.2.1 Fillers

These materials, apart from any chemical influence, can help in realizing a change in the microstructure of the SCC matrix associated with their small size particles. They can provide an enhancement in packing density, an increase in the stability of fresh SCC and a reduction in voids thus decreasing entrapped water in the system (Bosiljkov, 2003). The shape, size and surface characteristics of filler particles are highly important as they affect their behaviour during mixing and after placing as well. Limestone powder and chalk powder are the most common filler materials used in SCC

1. Limestone powder is only a filler material in the SCC mix, and it does not participate in cement hydration (Ye et al., 2007). However, it has been stated that although limestone powder is not a pozzolanic material, it can still contribute to the strength (Edamatsu and Nishida, 1998; Péra et al., 1999; Sonebi et al., 2005). This is because finely ground limestone particles act as nucleation sites for cement hydration, which accelerate early age strength

development. Limestone powder can decrease the water absorption and may reduce drying shrinkage of SCC (Felekoğlu and Sarikahya, 2008). It has been stated that limestone powder has little effect on viscosity but can increase yield stress (Carlsward et al., 2003).

2. A few SCCs incorporating chalk powder in the range of 25~55% of powder content was reported (Zhu and Gibbs, 2005). Higher amount of super-plasticiser is required to produce SCC mixes with chalk powder than those produced with limestone powder of the same filling ability.

As well as the above-mentioned common filler additions, SCC was successfully produced with fine sawdust ash with satisfactory self-compactibility and compressive strength (Elinwa et al., 2008). Crushed tyre rubber (Bignozzi and Sandrolini, 2006), quarry fines (Ho et al., 2002) and fines of sand (Felekoğlu, 2008) have also been used in SCC with careful attention to mix design. There is no doubt that using such materials can reduce the cost of SCC.

2.9.2.2 Cement replacement materials (CRMs)

Cement replacement materials (also known as pozzolana) are special types of industrial waste products or naturally occurring materials that can be used in concrete mixes to replace some of the Portland cement to improve or achieve certain properties (BS 8500-1, 2006). A pozzolana is a siliceous or siliceous and aluminous material that possesses no or little cementitious value but will, in the presence of water and when it is in finely divided form, react chemically with calcium hydroxide to produce compounds possessing cementitious properties (Ramezanianpour, 2014; Bosiljkov, 2003). A standard pozzolanic material is characterised by:

- High amorphous silica content of varied pozzolanic activity.
- Large surface area in which fine particles react faster than coarse particles resulting in higher early strength.

The main chemical ingredients in CRMs are SiO_2 and Al_2O_3, and they may respond slowly with portlandite ($Ca(OH)_2$), which is a cement hydration product, leading to the formation of calcium silicate and aluminate hydrates (pozzolanic reaction). These will supplement those produced by the Portland cement hydration and fill the voids, improving long-term durability by reducing shrinkage, creep, permeability, chloride

ingress, and sulphate attack. The pozzolanic reaction can also lessen the porosity of the interfacial zone thus improving the bond strength between aggregate and paste (Kuroda et al., 2000; Wong et al., 1999). The contribution of CRMs to the strength is primarily related to their pozzolanic reactivity, which depends on the replacement ratios and their inherent properties. CRMs of fine particles, for example, can act as nucleation sites for crystallization of hydration products thus improving the strength and durability (Kuroda et al., 2000; Ping and Beaudoin, 1992).

Almost all SCC include either a binary or ternary blend cement with CRM additions to improve rheological or fresh properties, control strength, reduce temperature rise and improve hardened properties (Domone, 2006). The successful incorporation of CRMs into SCC turns waste (by-products) or low-value materials into a valuable resource, thus reducing costs, saving natural resources and reducing CO_2 emissions. The commonly used CRMs and their effects on the fresh and hardened properties of SCC are summarised below:

1. Pulverised fly ash (PFA) is useful for the enhancement of the rheological properties of SCC because of its spherical particle shape, thus improving filling ability and stability. It can also reduce sensitivity to any variance in water content. However, an ultra-pulverised fly ash of Blaine surface area 500~600 m^2/kg may produce a cohesive paste that resists easy flow. Fly ash contributes to the late age strength due to its pozzolanic activity (The Concrete Society (BRE), 2005).
2. Ground granulated blast-furnace slag (ggbs) can increase concrete viscosity; contribute to the higher late strength; provide excellent chemical resistance; provide significant efficacy in controlling alkali-aggregate reactions and superior resistance to salt corrosion as it is inherently hydraulic (Ramezanianpour, 2014). It can substitute up to 70% of the Portland cement by weight (Dinakar et al., 2013b). Ground granulated blast-furnace slag may cause an increase in the setting time by 30 minutes and slightly decrease water demand (The Concrete Society (BRE), 2005). SCC with ggbs, in comparison with PFA, is more robust to water variation.
3. Silica fume (SF) which is also known as a micro silica is a highly fine and expensive practically spherical shape powder. It increases viscosity and shear

stress (i.e. yield stress), thus significantly decreases slump flow and resistance to segregation (Carlsward et al., 2003; EFNARC, 2005; Memon et al., 2013). It can improve the hardened properties and durability of SCC. Up to 5%, have been utilised in SCC as a modest quantity (Memon et al., 2013).

4. Metakaolin is produced by heating china clay, and its particle size is smaller than cement particles, but not as fine as silica fume. It is of high-quality than other by-products industry and more stable than other additions. Portland cement can be replaced by a normal percent of 5~10%, which can positively affect the concrete bleeding while replacement of up to 20% in SCC can improve resistance to permeability (The Concrete Society (BRE), 2005).

Among the above, PFA is widely available in most countries as an industrial by-product and has been proved to improve the fresh and hardened properties of concrete significantly (Neville and Brooks, 2010).

2.9.3 Water

Water is an essential constituent of SCC as it actively participates in the chemical reaction with Portland cement and profoundly influences fresh and hardened properties of SCC. It can reduce both viscosity and yield stress. SCC becomes much more susceptible to segregation when using only water to improve filling ability. For this reason, SCC could not be developed until powerful super-plasticisers became available. Water in fresh SCC includes that retained by powder materials (cement and additions) and a free one, which mainly controls self-compactibility and performance of SCC (Kasemchaisiri and Tangtermsirikul, 2008). The moisture content of coarse and fine aggregates also has a significant impact on the free water content (Persson, 2000). That is why the humidity of aggregate should be kept more than the saturated surface dry level (SSD) (Aarre and Domone, 2001). The *w/c* is also another important factor that is necessary to maintain consistency retention alongside with the types of super-plasticiser. That is the higher the *w/c* ratio, the lower the consistency loss for the same initial consistency (Felekoğlu and Sarikahya, 2008).

2.9.4 Admixtures

An admixture can be defined as a material added in small quantities before or during mixing process to modify one or more properties of a concrete mix (Dransfield, 2003). Many admixtures have been reported to be used in producing SCC, but super-plasticisers are the essential ones.

2.9.4.1 Super-plasticisers

One of the primary tasks when producing SCC is to keep the water content low and simultaneously have an outstandingly fluid concrete, which can be achieved by using super-plasticisers. The superb workability cannot allow the separation of fresh SCC components. Cement particles always flocculate and agglomerate when they mix with water, which is due to Van der Waals and attractive electrostatic forces that are generated by the electric charge on the surface of the particles. A significant amount of free water will be trapped in the flocculation process causing a reduction in the consistency of concrete. The use of super-plasticisers or water reducing agents impart a negative surface charge on the cement particles, and thus causing electrostatic repulsion, which in turn prevents the flocculation and agglomeration, and liberates the trapped free water as shown in Figure 2.13. Super-plasticisers, in comparison with water reducing agents, can provide a greater performance and a longer retention for consistency as they induce higher electrostatic and/or steric repulsive forces (Bonen and Shah, 2005; Uchikawa et al., 1995).

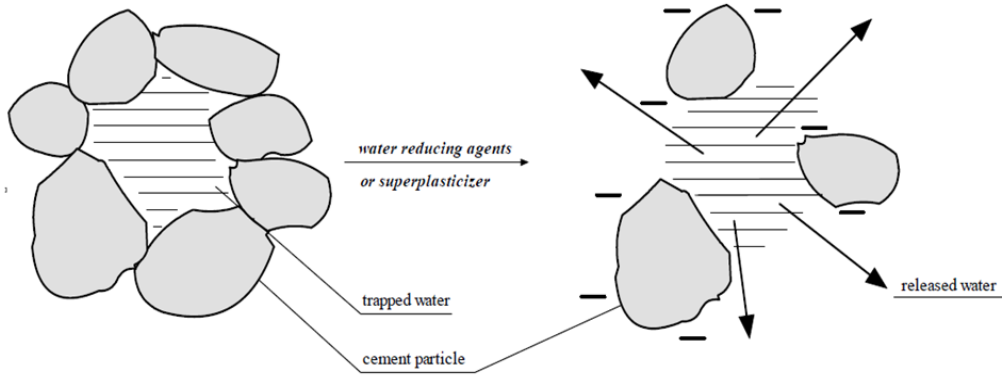

Figure 2. 13 Flocculation of cement particles entrapping water and the dispersion effect by water reducing agents or super-plasticisers

Mechanism of action

Super-plasticisers employed in SCC can be classified according to their dispersion mechanism:

- Electrostatic repulsion
- Steric repulsion.

Super-plasticisers mainly based on repulsive electrostatic forces include naphthalene sulfonate (NF), melamine sulfonate (MF) and amino sulfonate-based agents. All of them impart a negative charge on the cement particles, thus causing dispersion (Kim et al., 2000). On the other hand, those mainly based on steric repulsive forces include poly-carboxylate-based agents. They absorb water and produce a thick layer on the cement particle surface, thus generating effective steric repulsion (Yamada et al., 2000). Also, the carboxyl group in the molecule imparts a negative charge to cement particles, which produce a weaker electrostatic particle repulsion than that of the sulfonic group (Uchikawa et al., 1995). The carboxyl group is the newly developed super-plasticiser and has the ability to provide a high consistency, a proper viscosity, and a long consistency retention even when using small amounts and at low *w/c* ratio (Collepardi et al., 2007).

2.9.4.2 Viscosity modifying agents (VMAs)

These products are mostly cellulose derivatives, polysaccharides or colloidal suspensions. They are used to enhance viscosity and increase stability (i.e. segregation resistance) (Koehler and Fowler, 2007). VMAs can be divided into two types based on the mechanism of action (Yammamuro et al., 1997):

- Adsorptive
- Non-adsorptive

The adsorptive VMAs act on cement particles. After addition, they adsorb onto cement particle surfaces and form a bridge structure, thus imparting viscosity to SCC. While the non-adsorptive VMAs act on water. They increase concrete viscosity by either their water-soluble polymer chains using some free water or through their molecule linking (Khayat, 1999a).

2.9.5 Aggregates

Aggregates, in general, occupy around two-thirds of the total volume of SCC and have a significant effect on its properties. They are granular materials, derived mostly from natural rock (crushed stone, or natural gravels) and sands, although synthetic materials such as slags and expanded clay or shale are used to some extent, mostly in lightweight concretes (Mindess et al., 2003). Aggregates, in addition to their use as economical fillers, can enhance concrete dimensional stability and wear resistance (Neville and Brooks, 2010).

2.9.5.1 Fine aggregate

Fine aggregate is a naturally occurring granular material composed of finely divided rock and mineral particles. The composition of fine aggregate is highly variable, depending on the local rock sources and conditions, but an essential constituent of sand is silica (SiO_2), often in the form of quartz. Fine aggregate with a spherical shape, well-distributed grading, and low absorption are preferable for SCC than angular crushed one as they can help in achieving self-compactibility. It was found by Emborg (2000) that the moisture variation in sand affects the performance of SCC. Therefore, it is crucial to control the moisture content of sand when producing SCC as an error of 0.5% will cause a change in water content of $8kg/m^3$ in concrete. This could cause a modification in the slump spread by around 45mm. Therefore, it is recommended to keep the minimum moisture content of aggregates above the SSD level. Furthermore, the proportion of fine particles (less than 125μm) in the fine aggregate has a more obvious influence on SCC than NVC as it may help in increasing cohesion, and thereby segregation resistance (Felekoğlu, 2008; Topçu and Uğurlu, 2003).

2.9.5.2 Coarse aggregate

For SCC, coarse aggregate content should be limited to reduce inter-particle friction and prevent blocking. The shape of the aggregate particle will affect performance, as will variations in moisture content. A naturally rounded aggregate might be preferable to crush angular aggregate for SCC as it provides better filling ability because of the minimal expected inter-particle friction. Furthermore, a better deformation capacity

can be achieved in SCC when using a continuous grading of aggregates. On the other hand, blocking can mostly happen if the size of coarse aggregate is larger than the bar spacing. Most SCC applications have used a maximum size of coarse aggregate within the range of 16~20mm based on local availability and practice (Domone, 2006), although SCC has been produced successfully with coarse aggregate up to 40mm (Jones and Holton, 2003). Okamura and Ouchi (2003) reported that an increase in coarse aggregate content leads to a decrease in the resulting filling ability regardless of its shape.

2.9.6 Other materials

Entrapped air admixture reduces viscosity and increases slump flow (Carlsward et al., 2003). Since air voids trap only a small amount of water and cannot prevent aggregate particles from colliding and contacting with each other, they can be considered simply as a filling material in SCC. Other materials are successfully used to improve the ductility/toughness of hardened SCC such as carbon fibre, steel fibre, and glass fibre. However, they all cause a reduction in filling ability and an increase in the risk of blocking.

2.10 Hardened properties of SCC

Significant engineering properties such as strength, dimensional changes, and durability mainly depend on the void systems, such as the total void volume, the void distribution, and connectivity (Neville and Brooks, 2010). Concrete is a complicated system, which develops with time including a wide range of void sizes. Numerous papers have been published on all aspects of hardened properties of SCC, usually in comparison with NVC. A brief review is given in the following sections.

2.10.1 Hydration

SCC has a same mechanism of hydration to that in NVC (RILEM TC174, 2000). However, the hydration development is influenced by the higher content of powder materials and admixtures. For example, incorporation of limestone powder in SCC leads to an increase in hydration reaction (Poppe and De Schutter, 2005). Fine powder

particles act like heterogeneous nucleation sites that boost the hydration process (Kadri and Duval, 2002).

2.10.2 Microstructure

As vibration makes water accumulate on the surfaces of coarse aggregate particles, NVC tends to contain a porous matrix and poor interfacial zones, which weaken hardened properties. Elimination of the vibration process and the incorporation of high amounts of powder lead to a denser cement matrix and an improved interface between aggregates and paste in SCC (Tragardh, 1999).

2.10.3 Strength

Strength is one of the most critical properties of concrete since it is a direct reflection of the structure's capacity to carrying loads and a reasonable indicator of other properties.

2.10.3.1 Compressive strength

The compressive strength is regarded as representative of all mechanical properties. It is also, in general, the characteristic material parameter used for the classification of concrete in national and international standard codes. The compressive strength of SCC and NVC of similar composition does not differ significantly in the majority of the published test results. Also, the comparison of hardening processes indicates that the strength development of SCC and NVC is similar (Dehn et al., 2000; Domone, 2007; Gibbs and Zhu, 1999; Holschmacher and Klug, 2002; RILEM TC174, 2000; Sonebi and Bartos, 2002).

2.10.3.2 Tensile strength

All factors, which affect the characteristics of cement matrix microstructure and interfacial transition zone (ITZ) are of decisive importance in the tensile behaviour. When the water to powder (W/P) ratios are similar, the splitting tensile strength of SCC will be higher than that of NVC (Holschmacher and Klug, 2002; Zhu et al., 2004).

The tensile to compressive strength ratio of SCC was 10~30% higher than that of NVC (Gibbs and Zhu, 1999; Gram and Piiparinen, 1999). This probably results from the better microstructure, especially the minimal porosity (i.e. denser cement matrix is present) within the ITZ of SCC due to the use of high amounts of powder. The development of tensile strength with time of SCC and NVC follow a similar trend.

2.10.4 Modulus of elasticity

The modulus of elasticity is used to calculate the elastic deflection, which is a controlling parameter in the design of slabs, pre-stressed and post-tensioned structures. For concrete, the stress-strain curve is non-linear from which different modulus of elasticity can be determined. Static modulus (E_s) is the slope of the tangent to the curve at a particular stress while dynamic modulus (E_d) is the slope of the tangent to the curves at the origin. E_s is usually 0.8~0.85 of E_d depending on the compressive strength and other factors (Domone and Illston, 2010).

It is well-known that the modulus of elasticity of concrete depends on Young´s moduli of the individual components and their volume percentages. Thus, the SCC modulus of elasticity increases with high contents of aggregates of high rigidity. Relatively, the elastic modulus of SCC might be anticipated to be lower due to the high content of fines materials as dominating factors as well as the low content of coarse aggregate in SCC in comparison with NVC. This was confirmed by (Dehn et al., 2000; Domone, 2007; Holschmacher and Klug, 2002). Indeed, it was illustrated that the modulus of elasticity of SCC could be up to 20% lower compared with NVC having the same compressive strength and made from the same aggregates (Dehn et al., 2000; Domone, 2007; Holschmacher and Klug, 2002).

2.10.5 Bond properties

The bond between reinforcement and concrete is essential considering the broad applications of reinforcement in concrete. Thus, effective bond strength can improve structural performance and protect the reinforcement bars from corrosion.

Poor bond often results from bleeding or segregation of SCC. Water and air rise are trapped under reinforcement bars, which lead to an uneven bond strength along the

bars. Bond strength is lower in the lower parts of concrete in comparison with higher levels. Better homogeneity of SCC eliminates the top bar effect and make it less distinctive (Domone, 2007; Holschmacher and Klug, 2002). However, it was also stated that the bond to steel of SCC was similar to or better than that of NVC (Chan et al., 2003; Dehn et al., 2000; Domone, 2007). Moreover, the bond strength of SCC with the same strength grade 35 and 60MPa was 10~40% higher than that of NVC for bar diameters of 12 and 20mm (Zhu et al., 2004).

2.10.6 Shrinkage

Evaluating volume changes such as shrinkage is necessary for SCC as it produces tensile stress within the concrete leading to adverse cracks, which enable harmful materials to penetrate into the concrete and cause further durability problems. Shrinkage is necessary for prestressed concrete because it relaxes the prestressing force, thus reducing structural capacity (Atiş, 2003). It is a time-dependent deformation, including autogenous and drying shrinkage. Autogenous shrinkage, on the one hand, occurs because the volume of the hydration products is less than that of water and cement. It depends on the *w/c* ratio, and the age of the concrete, and it increases if the *w/c* ratio decreases (Persson, 1997). Drying shrinkage, on the other hand, results from the water loss from cement paste to atmosphere. Water held by capillary tension is one of the important factors affecting the drying shrinkage. The use of higher contents of powder and super-plasticiser in SCC may contribute to higher shrinkage than in NVC. The drying shrinkage of SCC was found to be 10~50% higher than that of NVC (Holschmacher and Klug, 2002; Suksawang et al., 2006). However, it was reported that denser microstructure of SCC suppresses drying shrinkage (The Concrete Society (BRE), 2005; Bouzoubaa and Lachemi, 2001; Sonebi et al., 2000). Indeed, use of limestone powder in SCC was found to reduce shrinkage (Bui and Montgomery, 1999). Other studies reported that the amount of shrinkage of SCC did not differ from that of NVC when the compressive strength was the same (Persson, 2001). The above contradictions may be the result of different experimental procedures, specimen sizes, and material properties being used.

2.10.7 Creep

Creep is defined as the time-dependent gradual increase in strain for a constant applied stress, which usually happens in cement paste. The creep decreases as cement hydrates, which result in lower porosity. Also, aggregates restrain the creep of paste. For this reason, a higher amount of aggregates of higher modulus of elasticity will reduce creep. Persson (2001) confirmed that the creep is influenced by cement paste porosity and it reduces with the strength increase in the same way for both SCC and NVC. The creep of SCC is anticipated to be higher than NVC due to its higher cement paste. However, no general statement about the creep of SCC can be made due to the lack and contradictory nature of existing data (Holschmacher and Klug, 2002). Nevertheless, creep of SCC is influenced by the water to powder (W/P) ratio and curing methods in the same way as for NVC.

2.10.8 Fracture behaviour

Fracture mechanics, in a broad sense, is a theory of failure and the propagation of that failure through the structure, based on energy criteria in conjunction with strength criteria. Physically, the fracture is the local separation of material into at least two pieces when sufficient stress is applied on the atomic level to break the bonds that hold atoms together. Fracture failure can result for many reasons, including uncertainties in the loading or environment, imperfections in the materials, and deficiencies in design, construction or maintenance.

All concrete structures are full of flaws such as water-filled pores, air voids, and shrinkage cracks that already exist even prior to loading. Failure of concrete structures typically involves the stable growth of these cracks (micro-cracks), until significant cracking zones are formed under external loading and prior to the maximum load is reached. When a crack reaches a certain critical size due to the high-stress concentrations around it, it can propagate catastrophically through the structure, despite the total stress being considerably less than would typically cause failure in a tensile specimen.

Fracture researchers have now no doubt that the introduction of fracture mechanics into the criteria of design for all brittle failures of reinforced concrete structures (such

as punching shear, diagonal shear, pull out or torsion, or for concrete dams) can achieve considerable advantages. It will help to increase uniform safety margins, particularly for structures of various sizes. This, in turn, will enhance economy and assessment procedures as well, which in turn improves the reliability of structure. It will also make it possible to present innovative designs and utilise new concrete materials to improve structural durability and integrity. Furthermore, it will provide rational explanations for the many empirical provisions in the current design codes. Fracture mechanics will be in particular useful for high strength concrete structures, fiber-reinforced concrete structures, concrete structures of unusually large sizes, and for pre-stressed structures. Indeed, fracture mechanics is of urgent necessity for concrete dams, and nuclear reactor containment vessels in which the safety concerns are particularly very high as consequences of a potential disaster are enormous (Karihaloo, 1995).

2.10.8.1 Linear elastic fracture mechanics (LEFM)

The tensile fracture strength of an elastic-brittle material, such as glass, is significantly affected by the presence of discontinuities or flaws (e.g. micro-cracks) and other impurities in the material (Karihaloo, 1995). These micro-cracks could be present before the application of any load or may form during the load application. Linear elastic fracture mechanics (LEFM) of Griffith (Karihaloo, 1995) is based on the assumption that fracture processes initiate at the defects and introduce high-stress concentrations near their tips and therefore, the material tensile strength is exceeded earlier and before the stress is uniformly distributed in the material. In other words, LEFM allows stress to reach huge value (theoretically infinite) at the crack tip.

The main features of LEFM described above can be summarised as follows (Karihaloo, 1995):

1. The brittle fracture involves only one additional material parameter in addition to the usual two elastic constants E and v.
2. The stresses and strains in the neighbourhood of a sharp crack tip are enormous, and they tend to infinity at the sharp crack tip itself.

3. The entire body remains elastic during the fracture process, and the dissipated energy is only at a point (sharp crack tip).

The second and third features of LEFM contravene the basic principles of the linear theory of elasticity concerning small strains and Hooke's law. Griffith (Karihaloo, 1995) had observed the inconsistency between the linear elastic fracture model and the real physical situation prevailing at the sharp crack tip. He, therefore, proposed that the crack faces should be allowed to close smoothly under the influence of the main cohesive forces.

Generally, the literature distinguishes three possible modes of deformation at a crack tip, termed Mode I, II and III, which are also known as the opening mode, the in-plane shear mode, and the anti-plane (out of plane) shear mode respectively; as illustrated in Figure 2.14 (Karihaloo, 1995; Roylance, 2001).

- The opening mode (Mode I) is the common type of fracture mode, and the crack surfaces move in the y-direction while the forces are perpendicular to the crack (Figure 2.14a).
- The sliding mode (Mode II) is the in-plane shear mode, and the crack surfaces move horizontally in the x-direction while the forces are acting parallel to the crack (Figure 2.14b).
- The tearing mode (Mode III) is also called as anti-plane (out of plane) shear mode, and the crack surfaces move across each other in the z-direction while the forces are parallel to the crack (Figure 2.14c).

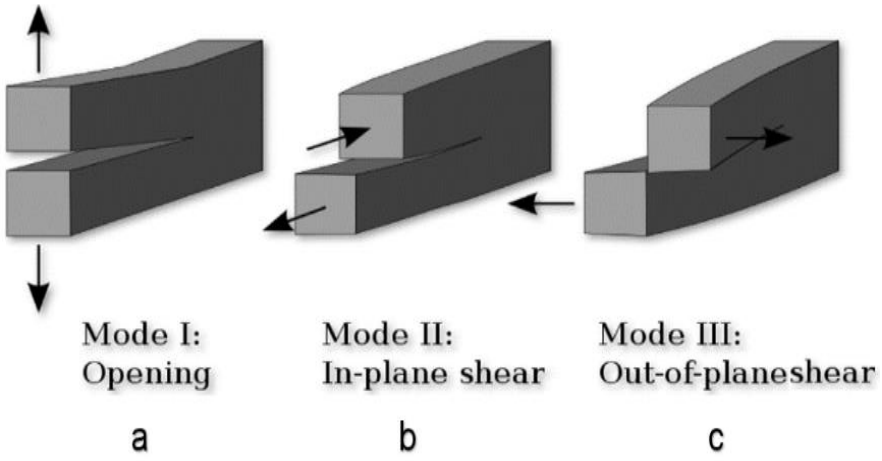

Figure 2. 14 Modes of crack propagation

From the fracture point of view, Mode I is the most severe mode as the growth of a crack in the real material under pure Mode II and III conditions needs an enormous amount of energy, due to friction between the crack faces.

Applicability of LEFM to SCC

Attempts were made to apply LEFM to SCC, which was thought to be a brittle material, but these proved unsuccessful since SCC exhibit an entirely different response. Intense research in this field revealed that all cement-based materials that were traditionally regarded to be a brittle exhibit, in reality, a different response. Figure 2.15 shows the typical load-deformation curve for a quasi-brittle material in tension/flexure. For any quasi-brittle material such as SCC, a substantial non-linearity exists before the maximum stress is reached (AB), which represents the strain hardening response of the material. After that, a region of tension softening (i.e. an increase in deformation with decreasing tension carrying capacity) will exist due primarily to the randomly formed micro-cracks. The aggregate interlock and other frictional effects cause the tail region of tension softening (CD). The pre-peak non-linearity has only a minor influence on the SCC fracture behaviour. The main influence, in fact, comes from the tension softening response as it reduces the energy flux that can be released into the crack tip and thus leads to an increase in the surface area of the fracture. Therefore, the application of LEFM to SCC structures is limited, due to the existence of the tension softening response. In other words, the fracture behaviour of SCC is influenced by the formation of an extensive fracture process zone ahead of the pre-existing notch/crack, as illustrated in Figure 2.15.

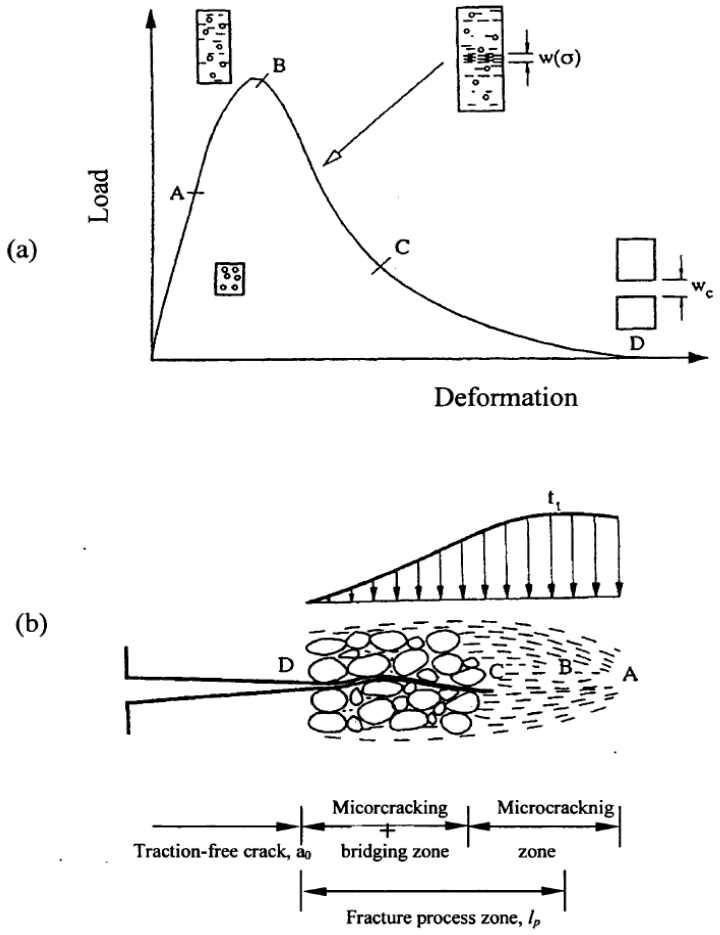

Figure 2. 15 (a) Typical load-deformation response in tension/flexure of a quasi-brittle material (b) The fracture process zone ahead of the real traction-free crack (After Karihaloo, 1995)

Fracture process zone (FPZ)

A certain inelastic zone of some finite size must exist around the crack tip because of the very high stresses there. There is evidence of the existence of intermediate inelastic zone between cracked and uncracked area, which is known as the fracture process zone (FPZ). FPZ can be defined as the area in which the material undergoes strain-softening, i.e., the stress normal to the plane of crack decreases with increasing strain. FPZ consists of micro-cracks, which are individual small cracks very close to crack tip. When the crack propagates, these micro-cracks coalesce and become a single structure to provide continuity to the already existing crack. FPZ also acts as a bridging zone between cracked and uncracked portions. The ductile materials like steel have a tiny FPZ, which makes strain hardening dominate over strain softening. The presence of the FPZ zone hinders the application of LEFM to cement-based materials. It is worth

to pay attention to the analysis of this zone as it is very helpful in the prediction of crack propagation and the ultimate failure of concrete. Many mechanisms that are responsible for fracture process in concrete are related to the development of the FPZ. Some of these mechanisms are indicated in Figure 2.16 such as micro-cracking at aggregate due to the presence of a macro-crack, de-bonding, and micro-cracking, coalescence of debonding crack with a macro-crack and the crack bridging, de-bonding, branching and micro-cracking.

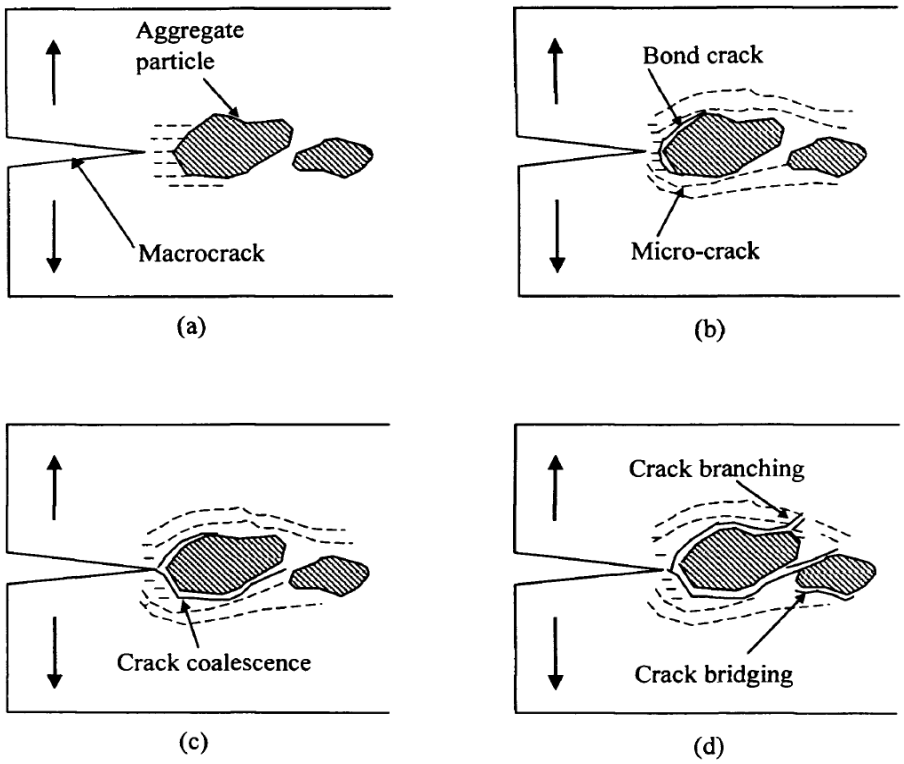

Figure 2. 16 Schematic representation of the fracture process zone (a) micro-cracking at aggregate, (b) debonding and micro-cracking, (c) coalescence of debonding crack with macro-crack, and micro-cracking,(d) crack bridging, debonding, crack branching and microcracking (After Karihaloo, 1995)

The size of FPZ depends on the microstructure of the material and the stress field existing ahead of an introduced macro-crack (Karihaloo, 1995). Since the FPZ consumes a substantial amount of the energy supplied by the applied load, a crack can propagate steadily before the peak load. Some parts of crack surfaces may remain in contact after cracking, which will prevent the catastrophic failure of concrete structures when immediately past the peak load.

2.10.8.2 Nonlinear fracture mechanics with softening zone

As mentioned above, the existence of the inelastic zone (i.e. FPZ) is the reason behind the deviation of concrete fracture behaviour from LEFM, which undergoes progressive softening damage due to micro-cracking. Therefore, a fracture theory is able to describe the material softening process that takes place in the fracture process zone must be a non-linear fracture theory. Hillerborg et al., (1976) proposed the first non-linear theory of fracture mechanics for quasi-brittle materials like concrete, while the second theory proposed by Bažant (1984). The two non-linear theories are briefly described in the next section.

The non-linear fracture theory applicable to ductile materials such as metals is different from that applicable to quasi-brittle materials like concrete or rock. This is because the fracture process zone in ductile materials, despite its small size, is surrounded by a large nonlinear plastic zone, whereas the fracture process zone in quasi-brittle materials occupies nearly the entire zone of nonlinear deformation. In comparison, the nonlinear zone is almost absent in brittle materials as illustrated in Figure 2.17.

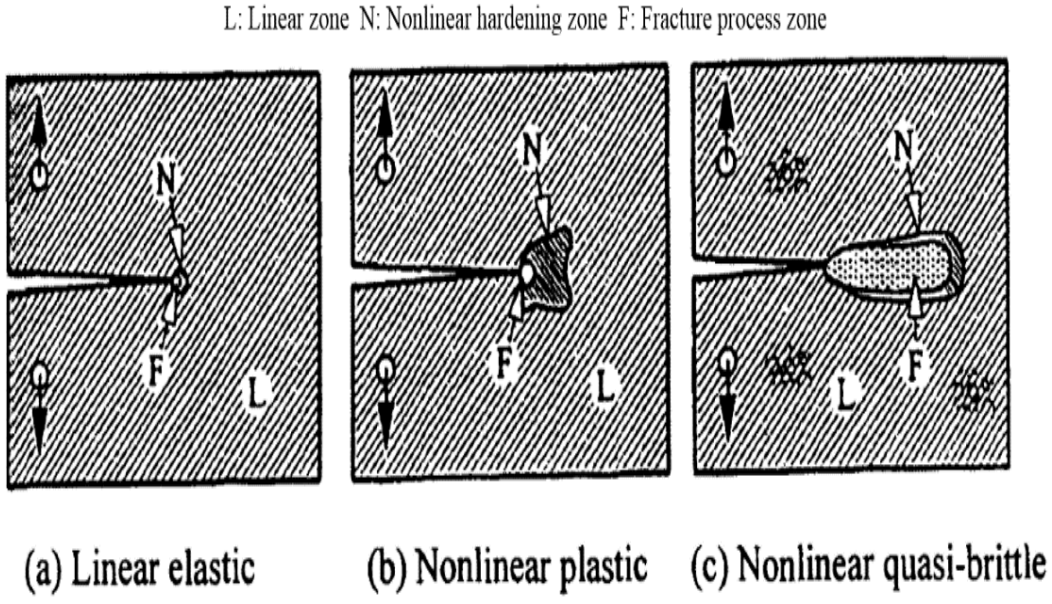

Figure 2. 17 Distinguishing features of fracture in (a) a brittle material, (b) a ductile material, (c) a quasi-brittle material (After Karihaloo, 1995)

Fictitious crack model (FCM)

The first nonlinear theory of fracture mechanics of concrete is the so-called Fictitious Crack Model (FCM) proposed by Hillerborg et al., (1976). It includes the tension softening fracture process zone through a fictitious crack ahead of the pre-existing crack whose faces are acted upon by certain closing stresses such that there is no concentration of stress at the tip of this extended crack (Figure 2.18). In this model, the crack is composed of two crack regions namely; a real traction-free crack, (the visible crack in which no stress or displacement can be transmitted) and a fictitious crack of negligible thickness ahead of the physical crack (along the FPZ in which the stress can be transmitted but not the displacement). The FCM is used when the cracks are few and isolated, which is the reason for this method to be known as the discrete crack model.

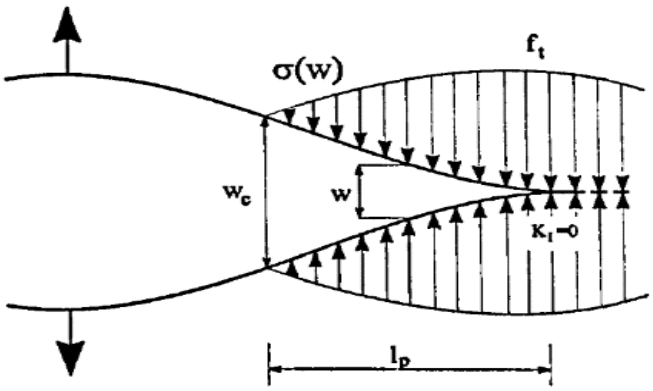

Figure 2. 18 A real traction-free crack terminating in a fictitious crack of length l_p (After Karihaloo, 1995)

Crack band model (CBM)

In the FCM described above, the fracture process zone is assumed to be a line crack with negligible width. Bažant and Oh (1983) modelled the FPZ by a band of uniformly and continuously distributed (smeared) micro-cracks with a fixed width of h_b (Figure 2.19a). This is the so-called Crack Band Model (CBM). Stable crack propagation is then simulated by progressively micro-cracking within this band, which is described by a stress-strain relationship (Figure 2.19b). The crack opening displacement (w) is equal to the product of the strain and the width of the crack band (h_b). The CBM is

used when the cracks are diffuse and numerous. That is why it is known as the smeared crack model.

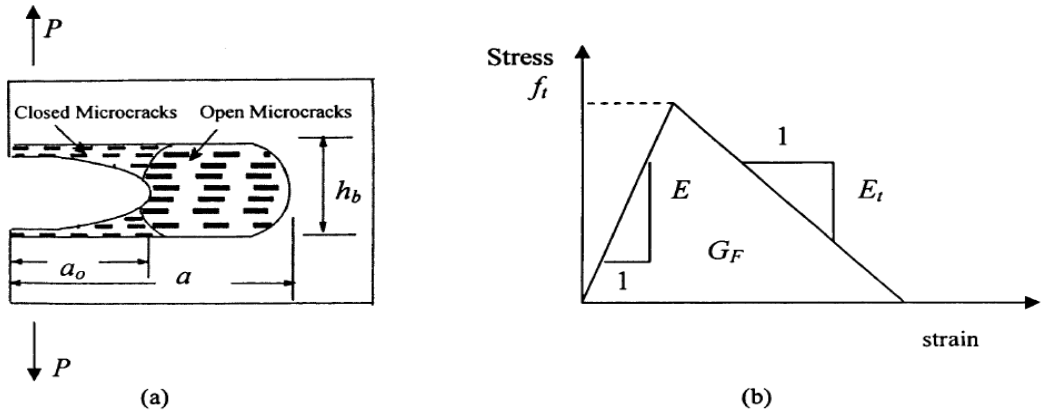

Figure 2. 19 (a) Crack band model for fracture of concrete (b) stress-strain curve for the micro-crack band (After Karihaloo, 1995)

The FCM is a widely accepted model to describe the non-linear fracture behaviour of concrete (Most and Bucher, 2003). In order to apply this model to SCC mix, two main parameters are required: the size-independent fracture energy (G_F) and the tension softening diagram $\sigma(w)$. These parameters form the basis for the load carrying capacity assessment of cracked concrete structures (Karihaloo, 1995; Bažant and Planas, 1997).

The simplified boundary effect formalism (Abdalla and Karihaloo, 2003) can be simply used to calculate G_F from previously notched three-point bend tests of identical size specimens with only two distinctly different notches to depth ratios. On the other hand, implementing the direct tension test could ideally obtain the $\sigma(w)$, which is, however, not a simple task. Thus, it is usually approximated by a bilinear relationship whose parameters are determined in an inverse manner by matching the experimental and theoretical load-displacement curves of the notched beams. For unnecessary duplication, detailed information about the above parameters will be given and examined further with all relevant results in Chapter 6.

2.11 Mix proportioning of SCC

The tight control on the two conflicting physical properties of SCC (i.e. deformability and stability) represent the stem of any favourable mix proportioning. Deformability, which is related to low yield stress, is essential to secure easy pour and high-quality finish with minimal labour. Simultaneously, the resulting SCC can possess low segregation resistance, which causes irregular hardened concrete with flaws. On the other hand, stability, which is related to adequate viscosity, is necessary to reduce the risk of segregation but relatively high viscosity may result in a poor placement ability. Thus, reconciling these two naturally contradictory requirements is a further challenge. In addition to the above self-compactability requirements, designed SCC should also achieve the demand of strength and durability of hardened SCC (Shi et al., 2015). Thus, successful mix proportioning for SCC should be widely applicable; technically satisfy all requirements, and be sustainable and economic (Viramgama et al., 2016).

Although numerous mix proportioning methods have been proposed for SCC based on different principles or control parameters, till date, no "standard" SCC mix fully meets the above requirements. A lack of uniform criteria and specific design parameters that are necessary to assess the SCC design process hinders the determination of the effectiveness of the available design methods. The following sections will briefly describe the various published approaches for mix design of SCC after been arranged into five categories according to their design principles (Shi et al., 2015). The principle, most distinguished merits, and limitations of each category are presented.

2.11.1 Empirical design category

The empirical design category determines the initial mix proportions based on empirical data involving coarse and fine aggregates contents, water and cementitious material contents and super-plasticiser dosage (Shi et al., 2015). Several trial mixes and adjustments are conducted for the best estimation of mix proportioning of ingredients that produce properties in demand. Based on experience, Okamura and Ouchi (1998) proposed a design procedure involving a fixed 50% of the solid volume as coarse aggregate content and a fixed 40% of the mortar volume as fine aggregate content. To ensure self-compactability, trials are made to the super-plasticiser dosage

and the water/powder ratio within 0.9 and 1.0 by volume based on the powder properties. Simplicity is the significant merit of this approach. However, there is a need for intensive laboratory testing to obtain cooperative behaviour for available constituents and satisfactory mix proportions. Indeed, intensive re-testing and adjustments are necessary in the case of any changes in raw materials. Moreover, no parameters that describe the properties of aggregate, such as grading and maximum size appear in this approach. Other examples of mix design methods that follow this approach are given by (Edamatsu and Nishida, 1998; Domone, 2010).

2.11.2 Compressive strength category

This category of methods determines cement, additions, water and aggregate contents based on required compressive strength. Kheder and Al Jadiri (2010) built a mix proportion approach based on combining the requirements of the ACI 211.1 (1991) used for proportioning NVC and the EFNARC (2005) by increasing the upper limit of the original compressive strength in the ACI 211.1 from 40 to 75MPa. This category can provide a simple and accurate procedure to obtain specific amounts of ingredients and reduces the need for trial mixes. Also, methods of this category take into account the effect of fine and coarse aggregates grading or the contributions of CRMs on the properties of SCC. However, amendments to all SCC mix ingredients are necessary to achieve an optimal mix proportion, which is one of its shortcomings. The method of Dinakar et al., (2013b) is another example of mix proportioning methods that are within this category.

2.11.3 Close aggregate packing category

This class of mix design determines mix proportions by initially obtaining ‘‘the least void’’ between aggregates based on different packing models, then fill the void between aggregates by applying pastes (Shi et al., 2015). In other words, this method mainly takes into account the relationships between paste and aggregate mix phases. Simplicity and consumption for a few binders are the main strong points of this category. However, its principal issue, especially in the construction field is SCC tends to segregate. Methods with their concepts within this category can be found in (Sedran and Larrard, 1999; Su et al., 2001; Sebaibi et al., 2013; Kanadasan and Razak, 2014).

2.11.4 Statistical factorial category

The influence of different key parameters such as contents of cement and CRMs, water to powder ratio, the volume of coarse aggregate and the dosage of super-plasticiser on fresh and hardened properties of SCC are considered in establishing the mix proportioning methods of this category. Based on the mix design of NVC, mix proportion is calculated accordingly by determining cognitive domains for each parameter (Shi et al., 2015). Khayat et al., (1999b) proposed a mix design procedure that includes five main mix parameters: coarse aggregate volume, cementitious materials content, water to cementitious materials ratio, VMAs dosage, and super-plasticiser dosage in addition to a varied fine aggregate content to fulfil the total volume. All these parameters, in a statistically sound manner, were evaluated and fitted to the results of each measured property (slump flow, filling ability, v-funnel time and compressive strength). This mix design approach is applicable for a broad range and provides an effective means to determine the impact of key variables on SCC properties. The most significant weakness of this approach is the establishment of statistical relationships, which requires much laboratory testing on available raw materials. Examples of such mix design method can also be found in (Ozbay et al., 2009; Bouziani, 2013).

2.11.5 Rheology of paste category

This category proposed that segregation resistance and workability of fresh concrete can be highly dictated by the rheology of cement paste matrix for a given particle size distribution and volume fraction of aggregate (Shi et al., 2015). Moreover, this approach required a minimum yield stress and viscosity of paste that must be exceeded to avoid segregation under both static (rest) and dynamic (flow) conditions, respectively. Deeb and Karihaloo (2013) recently extended a rigorous mix proportioning that are proposed by Karihaloo and Ghanbari (2012) for proportioning high strength SCC mixes with and without steel fibres exploiting the plastic viscosity expression (Ghanbari and Karihaloo, 2009). The extension performed by widening the range of SCC mixes with a traditional coarse aggregate of varying characteristic cube strength ranges between 35 and 100MPa. Nevertheless, the method did not provide any practical guidelines on how to choose the most appropriate mix. Indeed, the

compressive strength was not explicitly imposed as a design criterion in this method. The main advantage of this category is its ability to reduce laboratory work and material consumption and provide the basis for quality control and further development of new mineral and chemical admixtures. The methods proposed in (Saak et al., 2001; Bui et al., 2002; Ferrara et al., 2007) are also based on this category concept.

2.12 Concluding remarks

For several years beginning in the eighties, concrete has been criticised due to its durability problems, which became a noteworthy topic of interest in Japan. Structures of durable concrete require adequate compaction by skilled employees. However, the gradual decline in the number of skilled workers in Japan's construction industry had caused a deterioration in the quality of the construction work. One effective solution for the achievement of durable concrete structures independent of the quality of construction work or the skill of workers was the employment of self-compacting concrete. Self-compacting or self-consolidating concrete, (SCC) has been defined as a relatively high-performance concrete that can flow purely under its own weight and pass freely around obstacles, filling every nook and corner of a formwork between reinforcement, without the need for external vibration. Nevertheless, SCC is not a new concrete, but rather a sophisticated and evolving technology.

Since it was developed, SCC has become one of the most desirable types of concrete due to its outstanding fresh properties. Fresh SCC ought to meet three criteria: superior flowing ability, good obstruction-passing ability and sufficient resistance to segregation, which gives the opportunity to exploit several potential advantages. It can give designers and architects more freedom of creativity that was not previously possible. Lighter and thinner members can be produced, bigger span bridges can be developed, and marine structures can be built, making SCC an extremely promising material for the future of the in-situ and precast construction industries.

The distinguishing feature of SCC is its self-compactibility properties, and many tests have been suggested on these, which can be drawn up by flowing and passing abilities tests. The former can be investigated by slump flow and V-funnel while the latter uses

the J-ring and L-box for verification. The slump flow test is straightforward and easy to operate, which make it preferable in the laboratory and on sites. It is widely used to examine the flow capacity by measuring the average final spread diameter deforming under self-weight, and the flow velocity by measuring the time to a spread of 500mm. The V-funnel flow test, on the other hand, is most popular for testing flow velocity when passing through narrow space between reinforcements. Indeed, it can also involve an indication of the passing ability and the viscosity of fresh SCC. Unlike the V-funnel test, the L-box and the J-ring tests measure the passing ability through a mesh of bars. An advantage of such tests is the ease and visual assessment of any tendency to block or segregation.

It has also been stated that conventional materials used for NVC can also be used for SCC, although some substances or blends of powder may be preferable. No particular specification is needed for the selection of materials, and therefore, SCC should not be treated as special concrete regarding materials. The use of relatively high amounts of reactive and non-reactive natural fillers or/and manufacturing by-products as a partial replacement of Portland cement can be considered as one of the most latest potential developments that could contribute effectively to accomplishing minimal cost and sustainable SCC construction. What is more, an improvement can be attained by such replacement in both the mechanical and durability characteristics of concrete generally, and SCC specifically.

It has been revealed from the literature review of hardened properties that SCC mixes usually, but not always, offer better results in such properties due to the microstructure's improvement. Numerous investigations have been carried out for NVC to predict the test results of compressive and tensile strength from each other. However, it is still not quite clear whether such prediction is valid for SCC and therefore, more experimental results are crucial to finding a solution to such issue.

According to the results obtained from the literature, questions have been raised by researchers whether the high paste volume and low coarse aggregate contents in SCC produce lower fracture energy when compared with NVC. A limited number of studies has dealt with compositional parameters that affecting the SCC fracture behaviour such as coarse aggregate volume fractions, paste volume, and strength grade. Moreover, very few of these studies investigated the true fracture energy (size-

independent fracture energy,G_F. Therefore, research is required to investigate the G_F of SCC mixes with varied compositional parameters.

Several of mix proportioning methods have been developed, based on different approaches. Every individual method possesses its own distinguishing features and inherent limitations, and has been drawn up for its own specific conditions and environment, which causes difficulty in comparison. However, in most of the reviewed approaches, excessive attention has primarily been paid to the fresh properties of SCC, rather than hardened properties. Therefore, hardened properties together with fresh properties need to be imposed as design criteria to produce SCC mixes successfully. This necessitates further study to set up a mix proportioning method, which can be easily followed and widely used in various environments.

In the next Chapter, the rheology of SCC and in particular the Bingham model for describing its constitutive behaviour will be reviewed. We shall also examine the computational techniques and in particular, the smooth particles hydrodynamic (SPH) that are used to simulate the flow of the non-Newtonian SCC in the V-funnel.

Chapter 3

Rheology and modelling of SCC flow

3.1 Introduction

High workability is the most important and complex characteristic of SCC where Tattersall (2003) adopted a number of ways to interpret it. Two of these ways, which are highly operator dependent, were discussed in details in the previous Chapter. The third way that based on fundamental physical quantities assessment, which is in no way reliant on a particular operator, will be the first part to be discussed in this Chapter. This will be useful in achieving the second part, which will devote to a discussion on, and classification of the simulation approaches to model SCC flow with a considerable emphasis on the smooth particle hydrodynamics (SPH) methodology.

3.2 Rheology of fresh SCC

Cementitious materials such as SCC are of a significant technological importance and, according to (Banfill, 2006), their performance is satisfactory if one can successfully perform all casting processes in the freshly mixed state. The processes such as transporting, pumping, pouring, injection, spraying, spreading, self-levelling, moulding and compaction are based on the rheological characteristic of SCC. Rheology is the theory studying the properties of matter that determining its flow behaviour under applied stress. The rheological properties of liquid materials have fundamentally described the relation between shear stress (Pa) and shear rate (s^{-1}). The former is related to the force or pressure applied to the material while the latter is linked to the velocity distribution of the test equipment (Macosko, 1994).

The basic parameters of the rheology are yield stress and plastic viscosity, which are necessary to describe the flow properties of SCC. These two parameters provide more stable results than other conventional tests in describing the workability of SCC (Yen et al., 1999). They can directly reflect the ability of SCC in compacting and casting and help in understanding SCC behaviour concerning interactions in the fresh state. Thus, an adequate attention for those two parameters that lead to an SCC able to fill all the formwork, pass through heavy reinforcement without showing any blockage and segregation is required (Papanastasiou, 1987).

The plastic viscosity (η) can be considered as the internal friction of the fluid. In other words, it reflects the resistance of the fluid to flow, which is mainly due to the

interaction between fluid particles after the yield stress (τ_y) has been surpassed. On the other hand, in the physical sense, the yield stress is assumed to act as a switch between the flow and the no-flow region, i.e. between liquid-like and solid-like behaviour (Heymann and Aksel, 2007). In other words, stress has to be applied to the material to initiate flow. Below this stress, the material behaves as elastic solid. When the applied stress is higher than the yield value, the material flows and behaves as a viscous fluid. The yield stress of SCC has been reported to have a very low value (tens of Pascal) in comparison with normal concretes (thousands of Pascal) and remain nearly constant over a wide range of plastic viscosities as shown in Figure 3.1.

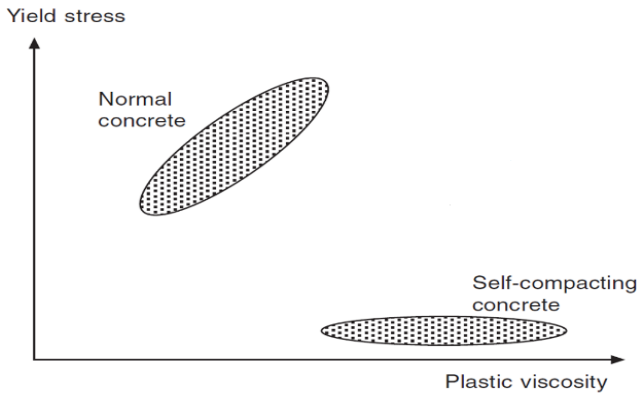

Figure 3. 1 Parameters of rheology for two types of concrete (Domone, 2003)

From a physical point of view, fresh SCC, which is dominated by its fluid-like, can be considered as a suspension of various sizes of particles in a continuous fluid phase. When flowing, particles interactions occur and modify the rheological behaviour. This is the reason behind not describing rheological behaviour of fresh SCC with the simplest Newtonian viscosity function of the flow behaviour of liquids. Instead, the bi-linear Bingham-type rheological model, which is the simplest form of the non-Newtonian model, is most frequently used. The flow curve of such model is as linear as the Newtonian one, but it intercepts the shear stress axis instead of passing through the origin. This intercept shows that there is stress, i.e. yield stress, which is needed for flow to occur.

3.3 Common rheological models

Fresh SCC is a suspension, and rheological equations typical for suspension flows are used to describe material flow behaviour mathematically. These equations give the evolution of stresses and deformations in the material. Fresh SCC exhibits complex non-Newtonian flow behaviour (Macosko, 1994). Most authors use the Bingham or Herschel-Bulkley models, which follow Eqs. 3.1-3.2 and 3.3-3.4 respectively. The Bingham equation is the most commonly used equation, which assumes the occurrence of yield stress and linear behaviour at the shear stresses higher than the yield value. The reasons for the widespread acceptance of this model are mostly practical: the model parameters can be measured independently, and the flow of real SCC seems to follow this equation fairly well in most cases (Ferraris, 1999). The overview of different rheological equations that describe suspension flows can be found in (Macosko, 1994), and those used for cementitious materials are given in (Ferraris, 1999; Banfill, 2006).

Bingham plastic model

The simplest Bingham plastic model or the Bingham model is written as;

$$\boldsymbol{\tau} = \tau_y + \eta\dot{\gamma} \qquad \boldsymbol{\tau} > \tau_y \tag{3. 1}$$

$$\dot{\gamma} = 0 \qquad \boldsymbol{\tau} \leq \tau_y \tag{3. 2}$$

Herschel-Bulkley model

This model is a generalisation of the Bingham model in such a way that, upon deformation, the viscosity can be shear thinning (viscosity decreases with shear rate) or shear thickening (viscosity increases with the shear rate) and it is written as;

$$\boldsymbol{\tau} = \tau_y + \eta\dot{\gamma}^n \qquad \boldsymbol{\tau} > \tau_y \tag{3. 3}$$

$$\dot{\gamma} = 0 \qquad \boldsymbol{\tau} \leq \tau_y \tag{3. 4}$$

For n <1, the fluid exhibits shear thinning properties

n =1; the fluid shows Bingham behaviour

n >1, the fluid shows shear thickening behaviour

In Eq. 3.3, n is an empirical curve-fitting parameter known as the flow behaviour index. For a shear thinning fluid, the index, n may have a value between 0 and 1. The greater degree of shear thinning can be achieved from the smaller value of n and vice versa. For a shear thickening fluid, the index n will be greater than unity.

3.4 Measuring Bingham parameters

A rheometer is commonly used to measure the Bingham parameters of general viscous liquids (such as cement pastes) and solid-liquid suspensions (such as SCC). When choosing rheometers, it should take into consideration the small size of aggregate used in SCC compared with conventional vibrated concrete, the presence of yield stress, moderate plastic viscosity, the potential of segregation and the high sensitivity to small changes in materials and their proportions. Basically, two types of rheometer can be used, namely, those that impose a controlled shear rate on SCC and measure its shear stress, and those that do the opposite (Domone, 2003).

Domone (2003) has reported that for a given SCC mix, different rheometers can give different fundamental rheological parameters (Figure 3.2). This was indeed proved by Banfill et al. (2001) using a series of comparative tests in which three instruments were taken to the same laboratory and used simultaneously to test a series of fresh SCC mixes with a different wide range of rheological characteristics. There were more consistent results for the yield stress values than those of the plastic viscosity. This implies that there is still no reliable technique to be applied to determine material properties (particularly plastic viscosity) from concrete rheometers, and there is a necessity to develop a universal tool for parameter determination (Vasilić, 2015). These unreliable results, which no doubt have a significant scatter with mixes containing long fibres, have triggered research into alternative prediction techniques for plastic viscosity (Krieger and Dougherty, 1959; Struble and Sun, 1995).

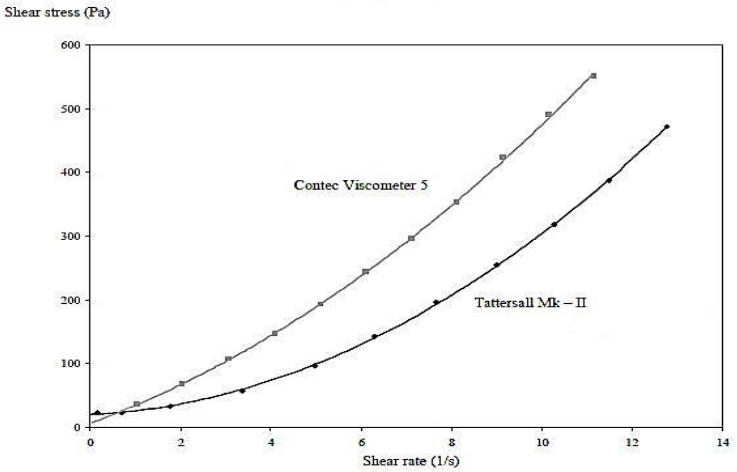

Figure 3. 2 Two different responses for a single SCC mix tested by two rheometers (Feys et al. 2007)

Ghanbari and Karihaloo (2009) have therefore developed a micromechanical procedure for estimating the plastic viscosity of SCC with or without steel fibres from the known plastic viscosity of cement paste alone or of the cement paste with SP and/or VMAs. This procedure has been proved to be able to predict the plastic viscosity of SCC mixes with or without fibres that agree very well with the measured values. Details about this micromechanical procedure will be explained in Chapter 4. The yield stress, on the other hand, has been predicted through inverse parameter fitting using the SPH simulation methodology of the slump flow test by matching the measured and simulated t_{500}, and the final spread diameter as well (Badry et al., 2016).

3.5 Why simulate the flow of SCC?

Prior using on a construction site, SCC should be approved through initial testing, which are simple experiments conducted to verify if the SCC fulfils its key properties, namely filling ability, passing ability and resistance to segregation. Lots of standardised tests were developed to evaluate the fresh properties of SCC (Ferraris and Martys, 2012). Additionally, some simple tests (such as slump flow test) are usually conducted directly at the construction site giving a qualitative information about the workability of SCC (BS EN 12350-8, 2010). Nevertheless, even when SCC is positively proved in initial tests, problems like bleeding, segregation or incomplete form filling can still occur. Moreover, improper filling of complex and heavily

reinforced members can occur even when a stable, robust, non-segregating SCC with well-adjusted flow properties is used. This means that the tests mentioned above are not always sufficient to characterise SCC properly and to predict its behaviour on the construction site. Furthermore, the characterization of cementitious materials such as SCC is a challenging task due to their diverse and complex rheological behaviour. High requirements of SCC leave no place for trial and error or correction of material properties through utilisation and has to be approved previously. All these issues set the need for the use of numerical modelling in SCC technology. This can be achieved by following a scientific-based approach where rheological and numerical investigations are employed together with the goal to take over control of casting process (Ferraris and Martys, 2012). Simulations can be an aid in complex situations and may help to avoid expensive mistakes on the site. Furthermore, simulations can provide insight into flow patterns that are difficult, costly or impossible to reveal using experimental techniques (Kuzmin, 2006). Table 3.1 shows a general comparison of experimental measurements and numerical simulations and outlines some other advantages in using numerical simulations.

Table 3. 1 Comparison of the experimental measurements and numerical techniques to predict material flow behaviour (Kuzmin, 2006)

Experimental measurements	Numerical simulations
Quantitative description of flow phenomena	Quantitative prediction of flow phenomena
For one quantity at a time	For all desired quantities
At a set number of points and time moments	With high resolution in space and time
For a laboratory-scale model	For the actual flow domain
For a restricted scope of issues and working conditions	For virtually any problem and realistic operating conditions
Expensive, slow, sequential, single-purpose	Cheap(er), fast(er), parallel, multiple-purpose

3.6 Numerical simulation

Recent developments in the field of SCC technology go towards a scientifically based approach to a concrete casting where both experimental studies and numerical simulations are utilised to achieve an optimal mix design and an efficient casting. The numerical simulation using modern computers has increasingly become an important approach for solving complicated engineering problems and replacing expensive experimental tests to save time, effort and materials. It plays a valuable tool in providing tests and examinations for theories, offering insights to complex physics, and helping in the interpretation and even the discovery of new phenomena.

The fresh properties of SCC have a direct influence on its strength and durability in the hardened state. SCC, which is not properly cast and consolidated, may be prone to defects such as honeycombs, air voids and segregation (Patzák and Bittnar, 2009) causing a major durability problem. For aesthetic reasons, the defective surfaces can be repaired after the casting if the cost of repair is not prohibitive, but detecting problems that occur inside the formwork can be tough (Dufour and Pijaudier-Cabot, 2005). Additionally, since complex material behaviour disallows the rheological characterisation of SCC using traditional rheometers, the use of numerical simulations is useful in determining the unknown material parameters.

Therefore, computational modelling the flow of SCC in its fresh form can significantly contribute to the durability and strength of a structure and can be a tool for both understanding and measuring the rheological behaviour of SCC and for mix proportioning as well.

The computational modelling allows us to predict:

- Whether or not the formwork is filled;

- The blocking and passing behaviour as SCC particles migrate through reinforcements, especially when fibres and/or large aggregates are present;

- The minimum workability of the fresh SCC that could ensure the proper filling of a given formwork, thus avoiding the use of highly flowable mixes of high tendency to static and dynamic segregation;

- The rheological behaviour of SCC is a potential tool for improving mix proportioning;

- The distribution of large aggregates during the flow of SCC and therefore avoiding segregation and ensuring the homogeneity of the mix;

- The distribution of fibres and their orientation in the formwork, therefore optimising the durability and strength of SCC.

The SCC flow simulation problem to be modelled is quite complex; one deals here with a free-surface flow of a dense suspension with a broad range of particle sizes. SCC is a suspension of coarse aggregates in a mortar. Mortar is yet again a suspension of dispersed sand particles in cement paste. Cement paste is not a simple homogeneous liquid, but it is a suspension of cement grains in water. All these particles have different shapes and a wide range of sizes varying from tenths of nanometres (the smallest cement grains) to several centimetres (the largest coarse aggregates) (see Figure 3.2) (Banfill, 2006). A comprehensive overview of the previous and current numerical studies on concrete flow can be found in (Ferraris and Martys, 2012; Roussel et al. 2007; Gram and Silfwerbrand, 2011) and most recently in (Mechtcherine et al., 2014).

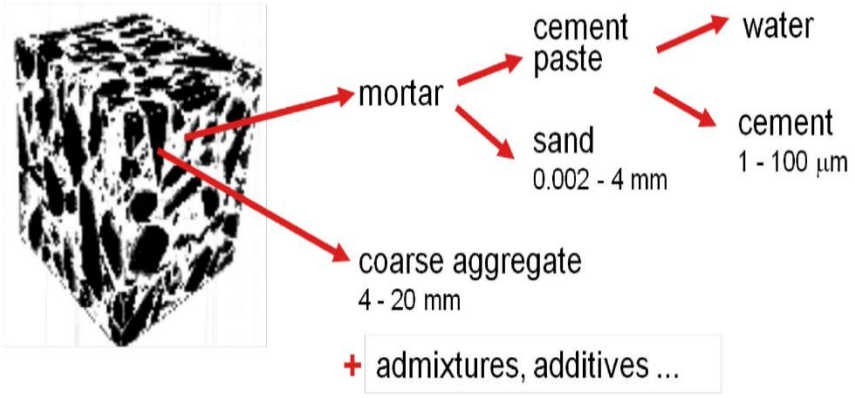

Figure 3. 3 A computer tomography image of concrete sample with particles from micro to centimetre scale (After Garboczi, 2002)

3.7 Simulation approaches

Many attempts have been made to simulate the flow of fresh SCC. From a computational point of view, two main categories are available for the modelling of SCC flow. Of the first type are methods that treat SCC as a homogeneous medium while SCC as a heterogeneous medium lies in the second category. Choosing the suitable technique depends on the purpose of the simulation and the scale of observation in which the solid components of SCC are considered as separate particles or are embedded in the matrix (Ferraris and Martys, 2012). It is common in concrete technology field to consider SCC as a two-phase suspension: "liquid phase" made of either cement paste or mortar and dispersed phase made of the coarser particles.

3.7.1 Simulation SCC as a homogeneous

The one-phase approach considers SCC as a viscous fluid without particle inclusions. It is the easiest and fastest way to predict casting of fresh SCC to some extent. According to Roussel et al. (2010), from a physical and modelling point of view, fresh SCC can be considered as a fluid when the granular nature of the material can be ignored in comparison with the hydrodynamic interactions within the material. The limitation of this approach is that the blocking of particles and segregation cannot be predicted (Roussel, 2007). This approach has been followed by many researchers (Thrane et al., 2004; Roussel and Coussot, 2005; Roussel 2006a; Patzák and Bittnar, 2009; and Gao and Fourie, 2015).

3.7.2 Simulation SCC as a heterogeneous

SCC in the fresh state can exhibit a fluid-like or a granular medium-like behaviour based on the volume fraction of coarse aggregates in the viscous suspension. The multiphase approach tries to capture the suspension nature of SCC (particles in a matrix phase) (Ferraris and Martys, 2012). It is worth mentioning that when solving multiphase flows, numerical solutions require a substantial amount of computation even for simple cases. This model is efficient and robust allowing simulations of tens of thousands of particles. Some examples of multiphase modelling can be found in

(Gram 2009; Martys, 2005; Dufour and Pijaudier-Cabot, 2005; Švec et al., 2012). The recent overview can be found in (Ferraris and Martys, 2012).

3.8 Solution procedure of the numerical simulations

All numerical simulations follow an identical procedure to serve a practical purpose. There are in principle some basic steps in the procedure of numerical simulation. From the observed physical phenomena, mathematical models are firstly built with some possible simplifications and assumptions. The form of governing equations with appropriate boundary conditions generally drives these models. Boundary and/or initial conditions are necessary for determining the field variables in space and/or time. The next step to numerically solve the governing equations involves dividing the continuum problem domain into a discrete number of elements or components. This will form the computational frame for the numerical approximation, which is based on a theory of function approximations and includes discrete representation of the governing equations according to the discretization technique used before coding or translating the decomposed domain and numerical algorithms into a computer code in one of the programming languages. A typical numerical simulation procedure of any problem involves the following parameters shown in Figure 3.3 (Liu and Liu, 2003).

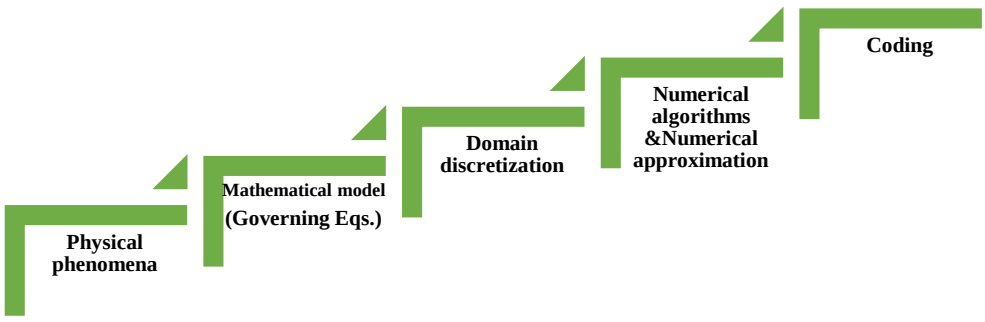

Figure 3. 4 The numerical strategy of simulation technique

3.8.1 Mathematical model (governing equations)

The first step of the numerical strategy will focus on the observed physical phenomenon, which represents here the simulation of SCC flow. The second step is to identify the mathematical model of the studied phenomenon. As mentioned above, the flow of SCC can be best described as a non-Newtonian liquid. Due to its high fluidity, the behaviour of fresh SCC is driven by using the governing equations of fluid. Fluid dynamics uses the concept of fluid particles whose motion is described by Newton's second law of motion. The basic governing equations of the flow of fluids are the mathematical statements for the following three physical laws: continuity, momentum and energy equations, which are based on the fundamental physical laws of conservation. However, in the absence of heat flux in a continuum, the energy can be assumed to be identically conserved. In the case of incompressible flow when the viscosity and density are not affected by the temperature, energy conservation equations can, therefore, be ignored:

- **Continuity equation (the mass conservation)**

The continuity equation or the mass conservation equation in the Lagrangian form is:

$$\frac{1}{\rho}\frac{D\rho}{Dt} + \nabla.\mathbf{v} = 0 \qquad (3.\ 5)$$

The first term in Eq. 3.5 vanishes since the density is constant due to the incompressible flow assumption. Therefore, it becomes

$$\nabla.\mathbf{v} = 0 \qquad (3.\ 6)$$

Here ρ, t, and $\mathbf{v}$ the fluid particle density, time, and particle velocity respectively. D denotes the substantial or material derivative.

- **Momentum conservation equations**

If gravity (g) is the only body force acting on the continuum the momentum conservation equations in the Lagrangian form can be written in the compact vectorial form as

$$\frac{D\mathbf{v}}{Dt} = -\frac{1}{\rho}\nabla P + \frac{1}{\rho}\nabla.\boldsymbol{\tau} + \mathrm{g} \qquad (3.\ 7)$$

where $\rho, t, \mathbf{v}, P, \boldsymbol{\tau}$ and g represent the fluid particle density, time, particle velocity, pressure, shear stress tensor and gravitational acceleration, respectively.

3.8.2 Domain discretization

Domain discretization represents the third step in the numerical strategy reported above. In this step, the continuum problem domain is divided into a finite number of discrete components to solve the governing equations numerically. This technique is different according to the numerical method used. From a graphical point of view, computational modelling can be divided into two broad categories, grid (Mesh-based) and particle-based (Mesh-less) methods. Figure 3.4 illustrates the two different discretizations of the same geometrical domain.

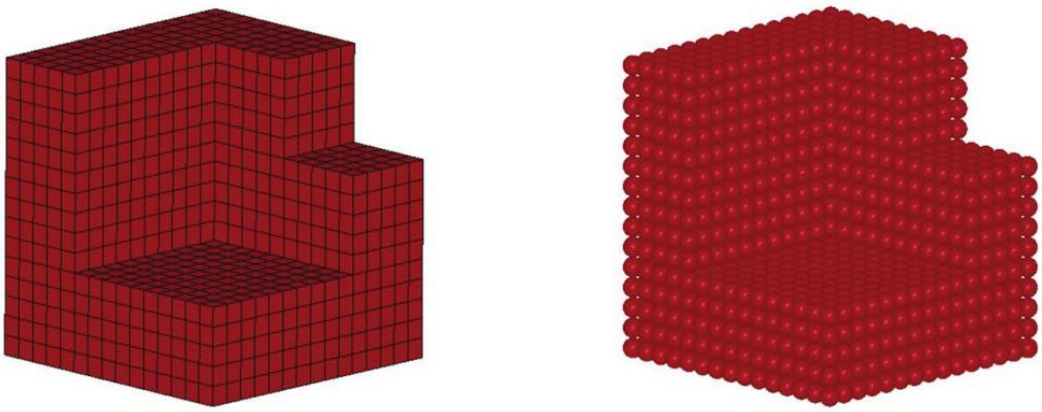

Figure 3. 5 Comparison between grid method (left) and particle method (right) for the same geometry (After Vesenjak and Ren, 2007)

3.8.2.1 Grid based method (Mesh-based method)

In the grid or mesh-based method, the discretization of the problem domain is performed by dividing the continuum domain into small discrete domains called the mesh or grid, which are connected to each other by nodes. The accuracy of the numerical approximation is closely related to the mesh topography (i.e. shape, size..., etc.). Although grid based methods, such as the finite element method (FEM), the finite

difference method (FDM) are very commonly used, the difficulty in solving complicated problems namely free surfaces, large deformability, moving interfaces, difficult boundary conditions and complex geometries make them computationally costly and time-consuming (Liu and Liu, 2003). As the generation of the mesh for a grid method is a prerequisite for complicated problems, it can be harder than solving the problem itself since all the formulation, and their results are based on the quality of the mesh (Vesenjak and Ren, 2007). Therefore, mesh-less methods become more attractive to treat problems where it is hard to used grid based methods.

3.8.2.2 Particle based method (Mesh-less based method)

In particle (or mesh-less) methods, the analysis domain is represented by a set of nodal points or particles without using any mesh that provides the connectivity between those nodes. Here, it is easy to handle large deformations, moving interfaces, difficult boundary conditions and complex geometries, since the connectivity among nodes is generated as part of the computation. Moreover, it is easy to control accuracy by simply adding more particles and adjusting the shape function. A number of meshfree methods have been proposed for the analysis of fluid flow, such as the smooth particle hydrodynamics (SPH) (Kulasegaram and Karihaloo, 2013), Element Free Galerkin Method (Yang, 2013), Reproducing Kernel Particle Method (Xiong et al., 2005) and Cloud Method (Burke et al., 2010). These methods share some common features but are different in the means of function approximation and the implementation process (Liu and Liu, 2003).

Eulerian and Lagrangian approaches

Eulerian and Lagrangian are the fundamental ways that describe the physical governing equations.

The Eulerian approach is a spatial description, and it is used to track a certain fixed place in the flow field and follows the change in properties, as different materials pass through this place (Figure 3.5).

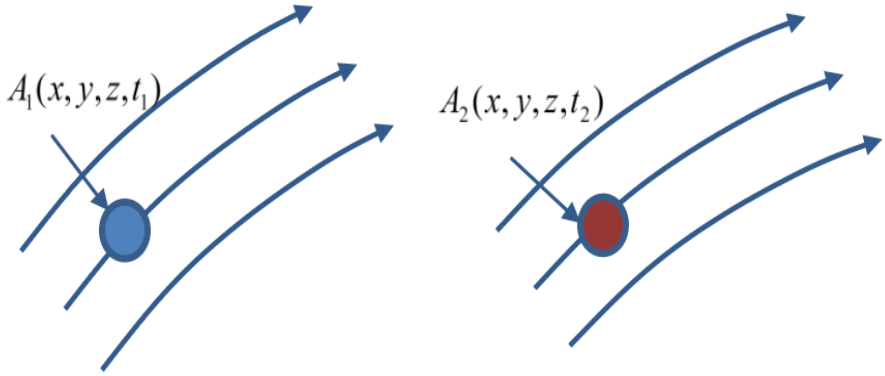

Figure 3. 6 Eulerian approaches: various fluid elements at different times at a fixed location in the fluid flow

The Lagrangian approach is used to track a material element of the fluid as it moves, and the changes in its properties, e.g. velocity are monitored (Figure 3.6).

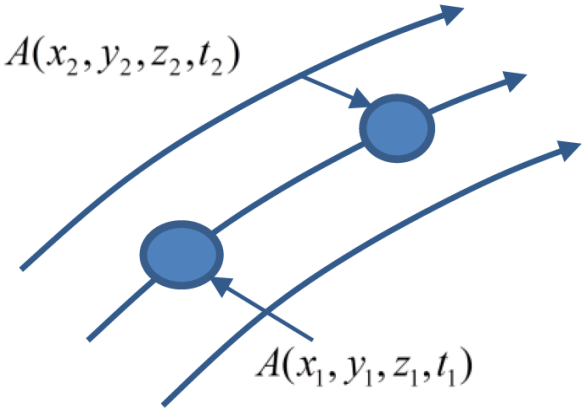

Figure 3. 7 Lagrangian approaches: fluid particle motion from time t_1 to time t_2

3.8.3 Numerical approximation

The fourth step in the numerical strategy is the numerical approximation, which can be performed using different numerical methods. Despite the fact that mesh-based numerical methods are the primary computational methodology in computational engineering mechanics, its limited application efficiency in many complex problems (e.g. free surface problems and large deformations) have encouraged researchers to

develop other computational methods, able to avoid the mesh dependence. One of the attractive mesh-free formulations is the smooth particle hydrodynamics (SPH).

The next section will briefly report an overview of the smooth particle hydrodynamics (SPH) as a mesh-free computational method, which will be used in the present research. It can take into account special features of SCC flow such as large deformations, large heterogeneity (i.e. particles of different sizes) and free surfaces flow, as these features pose significant challenges to the mesh-based methods. Unlike the mesh-based methods, SPH as a particle-based method does not require re-meshing. This method has been tested and proved to be efficient and accurate in modelling SCC with and without fibres by many researchers (Kulasegaram et al., 2011; Kulasegaram and Karihaloo, 2013; Badry, 2015).

3.9 Smooth particle hydrodynamics (SPH)

The SPH is a Lagrangian particle-based numerical approach, which was first independently pioneered by Lucy (1977) and Gingold and Monaghan (1977) to solve particular astrophysical problems in three-dimensional open space. As the collective movement of those particles is similar to the flow of a liquid or gas, it can be modelled by the governing equations of the hydrodynamics. The SPH was firstly conceived for compressible flow problems in confined flow simulations until later Monaghan et al. (1994) proposed and developed a modified SPH formulation to model free surface liquid flow. Several other researchers have since contributed to the method and solved various engineering problems including multi-phase problems (Monaghan and Kocharyan, 1995), quasi-incompressible flow (Monaghan, 1994; Morris et al., 1997), incompressible fluid flow (Shao and Lo, 2003; Solenthaler and Pajarola, 2009), flow through porous media (Zhu et al., 1999), viscous fluid flow (Takeda et al., 1994), gravity currents (Monaghan, 1996), heat transfer (Chaniotis et al. 2002; Cleary et al. 2002), turbulent flows (Welton, 1998), interfacial flows, discontinuity and large deformability (Bui et al., 2008; Colagrossi and Landrini, 2003) and sloshing problems (Kelecy and Pletcher, 1997). The interaction between fluids, free surfaces and many other applications can also be simulated using SPH (Amini et al., 2011).

Benz and Asphaug (1994) extended the application of SPH to cover the fracture of brittle solids. Bonet and Kulasegaram (2000) applied SPH to simulate the metal forming. Libersky et al. (1993) introduced an approximation of the full stress tensor into the "classical" SPH formulation. This was a pilot application of the SPH method to the dynamics of elastic-plastic solids, and its success resulted in some applications in related fields. One of the drawbacks associated with the simulation of elastic problems was the tensile instability, which is the instability of the numerical solution that occurs when simulating material undergoing substantial tensile deformations. Several correcting techniques were proposed to overcome the problem of tensile or spatial instability (Chen et al., 1999; Dyka et al., 1997; Monaghan, 2000), including other notable modifications or corrections to the SPH method (Bonet and Kulasegaram, 2000b; Dilts, 1998). The tensile instability problem rarely occurs in fluid dynamics simulations, but can be very severe in solid body computations. Further information on these improvements, as well as the basics of SPH, can be found in the reviews of (Price, 2012; Rosswog, 2009; Rosswog, 2015; Monaghan, 1992; Monaghan, 2005; Springel, 2010).

SPH is gaining more and more popularity, and with the continuing improvement and modifications, the accuracy, stability, and adaptability of the method have reached an acceptable level for practical engineering applications. Moreover, "the harmonious combination between the Lagrangian formulation and particle approximation" (Liu and Liu, 2003) allowed particles to carry material properties. Therefore, it becomes easier to model flow with complex geometry, free surfaces, discontinuity and significant deformation. The Lagrangian nature of SPH allows the grid to be embedded in the material, which reduces some of the material interface problems associated with Eulerian techniques. Nevertheless, as mentioned before because the motion of SPH particles is similar to liquid or gas flow, therefore those particles can be simulated using the governing equations of hydrodynamics (Liu and Liu, 2003).

As every numerical method, SPH comes with its own set of benefits and pitfalls. Some, but certainly not all of these, are highlighted below in particular in comparison to grid-based methods (Pettitt, 2014);

Advantages

- SPH is usually boundless, so no matter is lost or forced back into the simulation at domain boundaries thereby inherently conserving the mass of the system.
- The code spends its time evolving only the regions with a non-zero density field, so no time is wasted modelling empty space as in grid codes.
- The adaptive resolution (both spatially and temporally) are relatively easy to implement, i.e. no need to re-create/adapt meshes as in grid-based codes.
- The fluid evolution history is intrinsically simple to trace due to the particle-like nature. This would require the inclusion of tracer particles in grid-based codes to follow the fluid flow.
- SPH is comparatively straightforward and easy to model complex physics and geometries in 3D due to free/moving material boundaries.
- Particle nature makes coupling to N-body or self-gravity physics relatively straightforward.
- The distribution of mass between particles ensures exact conservation of mass as the mass of each particle is constant throughout time.

Disadvantages

- Need to build and constantly update neighbour lists (by link-lists or binary trees) to evaluate particle summations.
- The initial conditions can be influential on the eventual outcome. Need to decide on whether to set particles on a cubic, hexagonal or random lattice arrangement initially.
- Resolution is limited by particle number, which is fixed at the start of the simulation, whereas in theory, a grid can be subdivided indefinitely.
- Radiative transfer and magnetohydrodynamics can be harder to implement than the cell structured nature of grid-based codes.

3.9.1 SPH concept

SPH is an integral interpolation method to approximate values and derivatives of continuous field quantities by using discrete sample points (Gingold and Monaghan,

1977). The key characteristics employed to solve problems in SPH as reported by Liu and Liu (2003) are:

Domain discretisation

The entire problem domain in the physical space is discretized into a finite number of macroscopic volumes of fluid. A particle in SPH represents each macroscopic volume fluid. These particles possess individual material properties and move according to the governing conservation equations.

SPH support domain

The support domain for a particle '*a*' is the domain where all the information for all particles inside this domain is used to determine the information at the point '*a*' (see Figure 3.7). This means that any physical property of a particle '*a*' can be obtained by summing the same property of particles that lie in the support domain (Ω) within a smoothing radius (*ch*) of the observed particle '*a*' and multiplying the sum by a smoothing function, where *c* is a scaling constant related to the smoothing function. The smoothing length (*h*) is generally small for a high-density region and large for a low-density one; on average the support domain should have 30-80 neighbouring particles within the smoothing volume (Deeb, 2013).

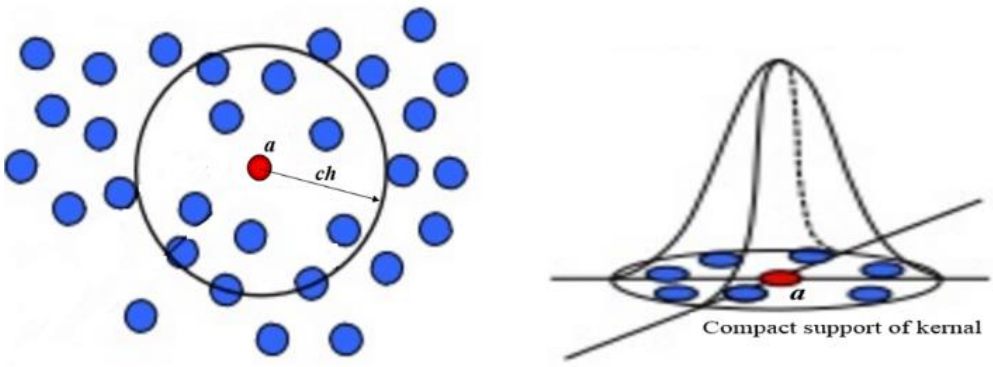

Figure 3. 8 Particle approximations using neighbouring particles within support domain of smoothing kernel for particle *a*

The smoothing radius (*ch*) is a key parameter in the SPH approximation. It defines the distance within which particles interact with each other or, in other words, the distance

with a non-zero value of the smoothing kernel (the so-called support domain of the kernel). The value of the constant *c* is determined by choice of the smoothing kernel. For a common case with *c* equal to two, particles separated at a distance greater than two smoothing radii will have no influence on the parameters at the current particle (Vorobyev, 2012). This is exactly correct when the value of the smoothing function is zero if the distance to the neighbouring particle is greater than or equal to *2h*. Figure 3.7 also shows the support domain of particle '*a*' and all the neighbouring particles that lie in the support domain. Particles which are closer to the centre (i.e. particle *a*) have a greater contribution to the property of *a* unlike particles outside the influence domain that have no contribution at all. The influence area of each particle will be, therefore, defined using the kernel function. There are two main steps in the SPH formulation: kernel approximation, which includes the integral representation of a function and its derivatives and particle interpolation or approximation.

Kernel approximation

Each particle, say particle '*a*' as illustrated in Figure 3.7, carries the field variables such as the mass (m_a), density (ρ_a), pressure (P_a), velocity (v_a), position (a), temperature (T_a), internal energy (ϵ_a) and any other quantities. All physical quantities are updated every time step. These field variables are represented by integral functions, the so-called kernel functions. SPH provides a concept to approximate the spatial derivative using particles, which therefore makes computing the spatial derivatives in the particle-based method as easy as in the grid-based methods. SPH is based on integral interpolation; for instance, a continuous quantity, $f(x)$ over a space Ω can be written as the convolution of the amount and Delta function:

$$f(x) = \int_{\Omega} f(x')\delta(x - x')dx' \tag{3. 8}$$

where Ω is the volume of the domain, dx' an elementary volume, and $\delta(x - x')$ is the Dirac Delta function i.e.

$$\delta(x - x') = \begin{cases} 1 & x = x' \\ 0 & x \neq x' \end{cases} \tag{3. 9}$$

The Dirac Delta function is approximated with the so-called smoothing kernel function, *W* of limited support, *h*;

$$f(x) \approx \int_{\Omega} f(x')\, W(x - x', h) dx' \quad (3.\ 10)$$

W should be differentiable, normalised and should converge to the Delta function. The SPH approximation is highly dependent on the choice of the kernel function. The most common kernels are Gaussian, cubic spline and quartic spline (Liu and Liu, 2003).

Particle approximation

Particle approximation in SPH involves discretizing the entire domain problem into a limited number of particles (N) and then approximately determining all the field variables on these particles. First, the infinitesimal volume (dx') at the location of particle (b) can be approximately replaced by the finite volume of the particle (V_b). This inclusion of density (ρ_b) and mass (m_b) makes SPH the ideal numerical solution to simulate dynamic fluid flow applications such as the flow of SCC. Then, the continuous integral in Eq. 3.10 can be converted to a discretized form of summation over all the particles (N) in the support domain (Ω). A quantity $f(x)$ at an arbitrary position (x) is approximated using quantities (f_b) at sample positions (x_b). The kernel function (W) realises a diminishing influence of particles at larger distances. Therefore, the continuous integral in Eq. 3.10 can be expressed in the equivalent forms of discretized particle approximation

$$f(x) = \sum_{b=1}^{N} m_b \frac{f(x_b)}{\rho_b} W(x - x_b, h) \quad (3.\ 11)$$

$$f(x) = \sum_{b=1}^{N} V_b\, f(x_b) W_b(x) \quad (3.\ 12)$$

The differential of this function is given by

$$\nabla f(x) = \sum_{b=1}^{N} V_b\, f(x_b) \nabla W_b(x) \quad (3.\ 13)$$

where the quantity $\nabla W_b(x)$ denotes the gradient of the kernel, which is taken as centred on the position of particle *a* (Figure 3.8). Eqs. 3.12 and 3.13 state that the value of any function (or its differential) at any position is approximated using the average of the values of the function at all the particles within the support domain (particles *b=1,2,…N*) of that particle weighted by the smoothing function $W_b(x)$.

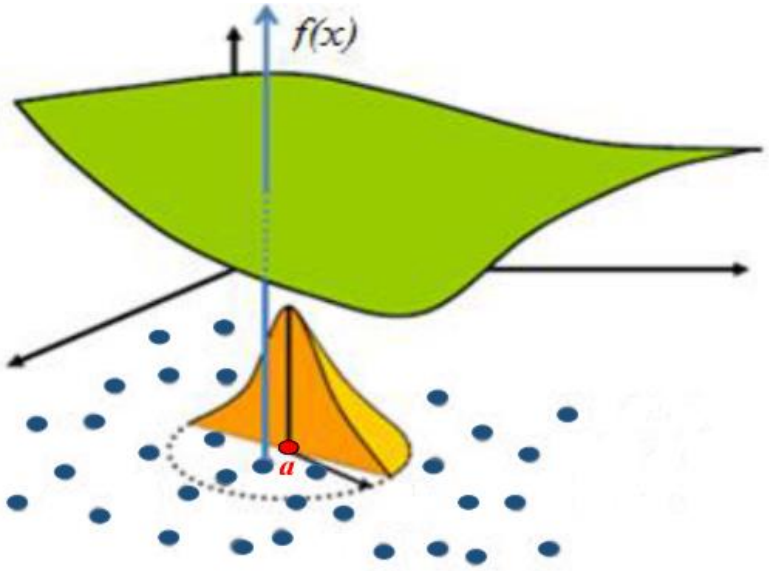

Figure 3. 9 Particle approximation of function *f(x)*

The application of Eq. 3.12 to compute the approximate value for the density of a continuum leads to the classical SPH equation:

$$\rho(x) = \sum_{b=1}^{N} m_b \, W_b(x) \qquad (3.\ 14)$$

Adaptive

The particle approximation is performed every time step, and the contributions of the particles depend on their current locations.

Lagrangian

The particle approximation is made on all terms related to field variables to produce a set of ordinary differential equations (ODEs) in a discretized form with respect to time.

3.9.2 Nearest neighbour search

In SPH, it is vital to know relevant particles that interact with each other. In other words, when dealing with a specific particle '*a'*, a list of the entire neighbourhood particles should be defined at each time step (i.e. the relevant *b*'s for which to calculate the properties of '*a'*). This neighbour particle search is the most computationally expensive part of the simulation (Bayraktar et al., 2009). Thus, special care should be

taken to reduce the time needed at this step. Many methods have been implemented to ensure an adequate way for neighbourhood search. The simply loop over all particles would be the most obvious way to do so, but this would be a very computationally expensive scaling. Two such options that are frequently used in SPH codes are "Link lists" and "Tree codes". Both are offering an improvement on the basic neighbour search (Liu and Liu, 2003). The method adopted in the present work is the "Tree codes", which is used by Bonet and Peraire (1991) and shown to be efficient for 3D problems.

3.9.3 Treatment of boundary conditions

In SPH, boundary conditions should be imposed to ensure balancing the inner particle forces, which preventing those particles from penetrating the wall. A range of methods is available in the literature to impose boundary conditions in SPH method. These are, for example, repulsive forces (Monaghan, 1994), mirror particles (Takeda et al. 1994; Cummins and Rudman 1999) and dummy particles (Dalrymple and Rogers, 2006; Shao and Lo, 2003; Lee et al., 2008; Amini et al., 2011). The dummy particle approach will be used in this thesis (see Chapter 7).

3.10 Concluding remarks

SCC is a suspension of different particles (aggregate, sand, cement) dispersed in a liquid at very high concentrations. Understanding the rheology of SCC is crucial for the successful casting process. Mix design, testing and casting of SCC leave plenty of room for improvement, and the key for further progress lays in the integration of experimental tests and numerical simulations. The recent developments go towards the scientific approach in SCC technology, where one utilises both numerical simulations and experimental measurement as an aid in the following areas:

- to optimise the mix design;
- to determine unknown material properties from rheometer measurements;
- to predict casting behaviour, where a numerical simulation of casting should be able to analyse defects such as improper filling, segregation or blocking;
- to optimise casting process.

This Chapter has described the present status regarding computational modelling of fresh concrete flow. A succinct summary of SPH as a suitable method to model the SCC flow has been given. The adaptability of SPH, its simplicity, and Lagrangian nature make it more attractive to deal with the heterogeneous flow of SCC as compared with any other method. Thus, such a computational strategy will be presented in Chapter 7 to simulate the flow behaviour of SCC in the V-funnel shape.

Chapter 4

Proportioning of SCC mixes:

Mix design procedure

4.1 Introduction

Designing SCC mix necessitates finding a compromise between two factors: flow-ability and passing ability and segregation resistance (Kim et al., 2012; Corinaldesi and Moriconi, 2004; Wu and An, 2014; Okamura and Ouchi, 2003). The former is achieved by using super-plasticisers and/or viscosity modifying agents (VMAs), while the latter is achieved through the selection of the proper amount and type of powders i.e. cement replacement materials (CRMs). To produce a successful SCC, the major work includes designing proper mix proportions and examining whether the properties of the resulting SCC mix meet the desired requirements (Su and Miao, 2003). Moreover, the flow behaviour of SCC in its fresh state, which is significantly affected by the combinations and features of its ingredients, has a significant impact on its properties in the hardened state (Heirman et al., 2009; Petit et al., 2007).

The early mix proportioning approaches proposed by Okumara and Ouchi (1999), Domone (2000) and Okamura et al. (2000) and later developed by others (Ouchi et al., 1998) were all heuristic in nature requiring many trial mixes. However, the extensive research work carried out on the rheological properties of SCC (Roussel, 2006b; Tregger et al., 2012; Saak et al., 2001; Chidiac and Mahmoodzadeh, 2009; Figueiras et al., 2014; Wallevik and Wallevik, 2011; Petersson and Billberg, 1999; Li and Kwan, 2011; Li and Kwan, 2013) has significantly improved the proportioning of SCC mixes. Over the last two decades, researchers around the world have proposed a significant number of different mix design methods (Shi et al., 2015). However, it remains a tough procedure as it involves many variables and understanding their effects on concrete performance in fresh and hardened states. The European Federation of National Trade Associations (EFNARC) guidelines (2005) give typical ranges of primary ingredients (Table 4.1); the actual amounts depend on the desired strength and other performance requirements. Thus, the mix proportioning still involves considerable trial and error.

Table 4. 1 Typical range of SCC mix compositions according to EFNARC(2005)

Ingredients	Typical range by mass kg/m^3	Typical range by volume, *l*/m^3
Powder (cementitious materials + filler)	380–600	–
Water	150–210	150–210
Coarse aggregate	750–1000	270–360
Water to powder ratio by volume	0.85–1.10	
Fine aggregate	Typically 48–55% of the total aggregate	

The methods for proportioning self-compacting concrete (SCC) mixes have not kept pace with their production techniques. A rigorous method for proportioning normal and high strength SCC mixes based on their plastic viscosity has been proposed by Karihaloo and Ghanbari (2012) and Deeb and Karihaloo (2013). It exploits the expression for the plastic viscosity of an SCC mix developed by Ghanbari and Karihaloo (2009) using micromechanical principles. This expression shows how the known plastic viscosity of the paste is increased by the addition of solid phase particles, i.e. filler, fine and coarse aggregates. The contribution of each of the solid phases to the overall increase depends on its volume fraction and shape of its particles. As a result, the final expression for the plastic viscosity of an SCC mix is the product of the known plastic viscosity of its paste and the contributions of each of the solid phases. Whilst the method for proportioning SCC mixes proposed in (Karihaloo and Ghanbari, 2012; Deeb and Karihaloo, 2013) is rigorous, and based on sound physical principles, it produces a bewildering array of mixes that reach the target plastic viscosity but does not give any practical guidelines on how to choose the most appropriate mix. Moreover, the method was developed on the basis of reference mixes of a range of known cube compressive strength, but the latter was not explicitly imposed as a design criterion.

This Chapter aims to overcome the above shortcomings of such method and develop a method for proportioning SCC mixes based on the desired target plastic viscosity and compressive strength of the mix. Practical guidelines in the form of design charts are provided for choosing mix proportions that achieve target cube compressive strength in the range of 30 to 80MPa and target plastic viscosity of 15Pa s as an upper limit for all SCC grades and 3, 4, 5, 6, 7 and 8Pa s for mix grade 30, 40, 50, 60, 70 and 80MPa as lower limits, respectively. Several examples on the use of the design charts

are given. The contents of this Chapter have been published as a journal paper in 'Sustainable Cement-Based Materials' (see publications list in Chapter 1).

4.2 Target compressive strength

The compressive strength of a concrete mix is mostly determined by the ratio of water to cementitious material (*w/cm*) under given curing conditions. A regression analysis was performed on the data collected from many published sources (Deeb and Karihaloo, 2013; Beygi et al., 2013a; Dinakar et al., 2013a; Panesar and Shindman, 2011; Felekoğlu et al., 2007; Rozière et al., 2007; Nikbin et al., 2014a; Boukendakdji et al., 2012; Persson, 2001; Dinakar et al., 2013b; Hoffmann and Leemann, 2005; Parra et al., 2011; Beygi et al., 2013b; Nuruddin et al., 2014; Zhu and Gibbs, 2005; Carpinteri and Brighenti, 2010; Rabehi et al., 2013; Beygi et al., 2014a; Dinakar et al., 2008; Collepardi et al., 2007; Nikbin et al., 2014b; Khaloo et al., 2014; Bui et al., 2002; Domone, 2007; Ferrara et al., 2007) and on the data obtained in various studies in Cardiff University (Figure 4.1). It was found that the compressive strength of SCC (MPa) could be best fitted by an Abrams-type relation (R^2 =0.94):

$$f_{cu} = \frac{195}{12.65^{(w/cm)}} \quad (4.1)$$

where f_{cu} is the 28–day equivalent cube compressive strength (MPa) and *w/cm* is the ratio of water to cementitious materials (i.e. cement + cement replacement material, e.g. ggbs). The large scatter in the surveyed data is no doubt a reflection of the differences in the curing conditions, the cement type, the type of cement replacement materials and replacement levels up to 30%, the amount of coarse aggregate and the maximum size of coarse aggregate. The values have been adjusted for the size of the cube test specimens to that of 100mm cubes. It was found, however, that formula (4.1) overestimates the cube compressive strength of low strength (30 and 40MPa) SCC mixes. This is perhaps a result of the presence of high powder content in these mixes, as has also been stated in (Nanthagopalan and Santhanam, 2009). For 30MPa mix, the *w/cm* predicted by (4.1) needs to be decreased by approximately 14% and that for 40MPa mix by 8%.

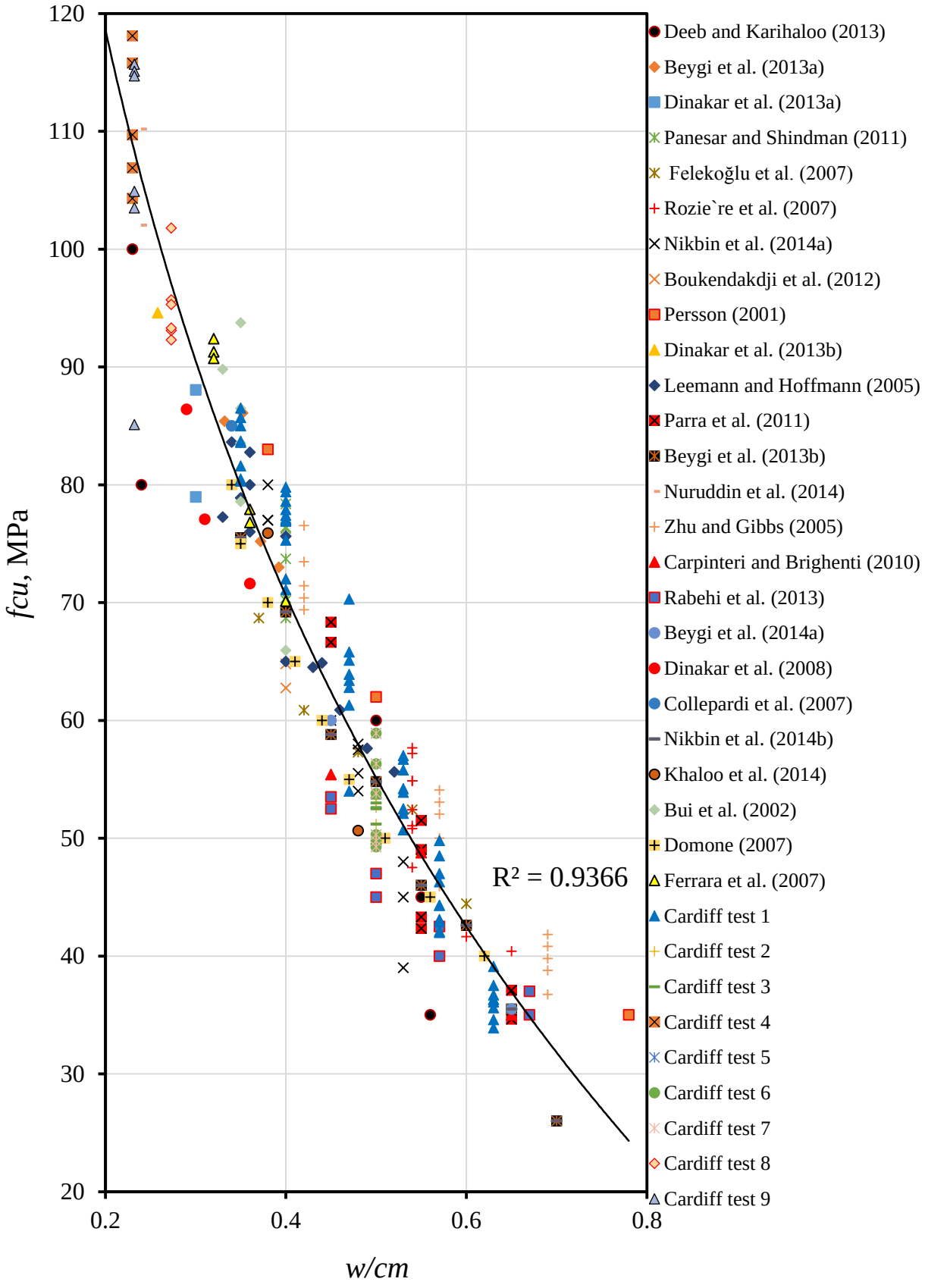

Figure 4. 1 Compressive strength and water to cementitious materials ratio relationship

4.3 Target plastic viscosity

Fresh SCC is a non-Newtonian fluid best described by a Bingham-type model. This model contains two rheological parameters of SCC namely its yield stress and plastic viscosity (Dransfield, 2003). It is known, however, that the yield stress of SCC mix is low (in the order of tens of Pa) in comparison with vibrated concrete mix, and it remains so over a wide range of plastic viscosity (Dransfield, 2003). Thus, the most important parameter is the plastic viscosity, which changes with the plastic viscosity of the paste and the mix composition.

The plastic viscosity of a homogeneous viscous fluid such as a paste (a mixture of cement, cement replacement material, water and super-plasticiser) can be measured rather accurately with a viscometer, which is not possible for a nonhomogeneous viscous fluid such as an SCC mix. There is a large scatter in the plastic viscosity of the same SCC mix measured with different rheometers, as has been reported by many researchers (Wallevik and Wallevik, 2011; Banfill et al., 2001; Feys et al., 2007). Ghanbari and Karihaloo (2009) have therefore proposed a micromechanical procedure for estimating the plastic viscosity of an SCC mix knowing the plastic viscosity of the paste used in it. In this procedure, SCC is regarded as a two-phase suspension in which the solid phase is suspended in a viscous liquid phase. The increase in the plastic viscosity of the liquid phase because of the addition of the solid phase (filler, fine and coarse aggregates) is estimated in a stepwise manner from the two-phase suspension model. In the first step, the solid phase is the finest solid material, for example, the filler in the viscous fluid phase i.e. the paste. In the next step, the finest solid i.e. fine aggregate is the solid phase suspended in the viscous fluid phase now formed by the two-phase suspension from the first step. This procedure is continued until all the solid phase ingredients have been added. The plastic viscosity of the *i*-th liquid-solid suspension can be estimated from the plastic viscosity of the preceding (*i*-1) th phase as

$$\eta_{ci} = \eta_{ci-1} \times f_i(\phi_i) \qquad (4.\ 2)$$

Here,

η_{ci} = plastic viscosity of the *i*-th liquid-solid suspension;

η_{ci-1}= plastic viscosity of the preceding (i-1) th phase. In the first step i = 1, η_{c0} is the known plastic viscosity of the paste;

$f_i(\phi_i)$= a factor larger than unity that predicts the increase in the plastic viscosity induced the solid phase with a volume fraction ϕ_i.

Figure 4.2 shows the hierarchy of these two-phase suspensions used in the estimation of the plastic viscosity of all mixes developed in this work based on the viscosity of the cement paste used in them.

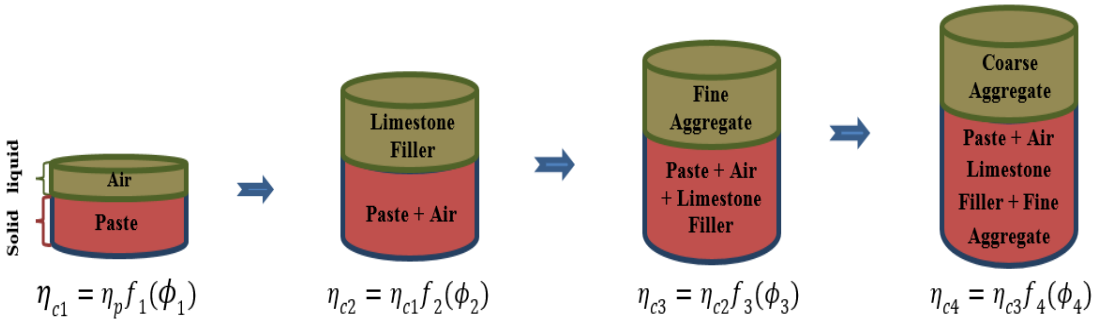

Figure 4. 2 Hierarchy of two-phase liquid-solid suspensions constituting an SCC mix

According to this procedure, the plastic viscosity of an SCC mix is given by:

$$\eta_{mix} = \eta_{paste} \times f_1(\phi_1) \times f_2(\phi_2) \ldots \times f_n(\phi_n) \quad (4.\ 3)$$

where n is the total number of solid phases in the mix. Besides the filler, fine and coarse aggregates, air voids can also be treated as a second phase in a viscous suspension. Einstein was the first to develop an expression $f_i(\phi_i)$ for dilute suspensions (second phase volume fraction less than 10%), containing randomly distributed rigid or hollow spheres with no hydrodynamic interactions:

$$f_i(\phi_i) = 1 + [\eta]\phi_i \quad (4.\ 4)$$

The numerical factor $[\eta]$ is equal to 2.5 for rigid spherical particles and to 1 for spherical air bubbles that are packed randomly in a hexagonal arrangement. Subsequent investigations have proved that the numerical factor 2.5 is quite accurate even for rigid ellipsoidal particles with an aspect ratio less than 3.

However, at higher concentrations of the solid phase (volume fraction >10% up to the maximum possible volume fraction, ϕ_m), the hydrodynamic interactions between the particles and the Brownian motions cannot be ignored. In this situation, Krieger–Dougherty (1959) formula (Eq. 4.5) has been found to be appropriate for cement–based suspensions. The value of ϕ_m is 0.74 for hexagonal close packing, 0.63 for random hexagonal packing, and 0.524 for cubic packing.

$$f_i(\phi_i) = (1 - \frac{\phi_i}{\phi_m})^{-[\eta]\phi_m} \quad (4.5)$$

The particle size distribution significantly affects ϕ_m. Furthermore, the numerical factor $[\eta]$ and ϕ_m depend on the shear rate; the former tends to decrease with increasing shear rate, whereas the latter shows the opposite trend. However, $[\eta]$ and ϕ_m change in such a way that a decrease in the first leads to an increase in the second, but the product of the both changes remains practically the same and equal, on average, to 1.9 (de Kruif et al., 1985). In most SCC mixes, the volume fractions of the filler, fine and coarse aggregates generally exceed 10%, so that their contribution to the increase in the known plastic viscosity of the paste is given by Eq. 4.5. The volume fraction of the trapped air bubbles is however low, around 2%, such that Eq. 4.4 with the numerical factor equal to 1.0 is appropriate. For simplicity, this 2% increase due to trapped air is included in the plastic viscosity of the paste in Eq. 4.6:

$$\eta_{mix} = \eta_{paste} \times \left(1 - \frac{\phi_{Filler}}{\phi_m}\right)^{-1.9} \times \left(1 - \frac{\phi_{Fine\ Agg.}}{\phi_m}\right)^{-1.9} \times \left(1 - \frac{\phi_{Coarse\ Agg.}}{\phi_m}\right)^{-1.9} \quad (4.6)$$

Note that the packing density (i.e. the maximum volume fraction, ϕ_m) increases with the addition of solid phases. When the first solid phase is added to the paste, the packing is loose so that it is appropriate to assume cubic packing. When however, the last solid phase is added to the suspension, the packing is very dense and it is appropriate to assume hexagonal close packing.

4.4 Calculation the plastic viscosity of SCC mixes

The calculation of the plastic viscosity using the above micromechanical model proposed by Ghanbari and Karihaloo (2009) will be demonstrated on a mix 50B,

(Table 4.2 (see Table 5.1 in Chapter 5 for other SCC mixes details)) as an example, and it is the same procedure for all the developed SCC mixes.

Table 4. 2 Mix proportion and details of 50MPa SCC mix

Ingredients		Weight, kg/m^3	Volume, m^3	ϕ	$f(\phi)$
Cementitious materials	cement	281.2	0.095	–	–
	ggbs	93.80	0.039	–	–
Water		198.8	0.199	–	–
Limestone powder		139	0.058	0.140	1.805
Fine Aggregate		760	0.287	0.410	7.360
Coarse Aggregate		840	0.300	0.300	2.685

Step 1: The plastic viscosity estimation of the liquid phase (η_{paste});

The plastic viscosity of the cement paste (cement+ggbs+SP+water+air) is estimated from published data that based on *w/cm* ratio of the mix (Grezeszczyk and Lipowski, 1997; Nehdi and Rahman, 2004; Sun et al., 2006) and it equals to 0.23Pa s (Table 4.3).

Step 2: The first solid phase addition is the filler i.e. limestone powder (*LP*) as shown in Figure 4.3.

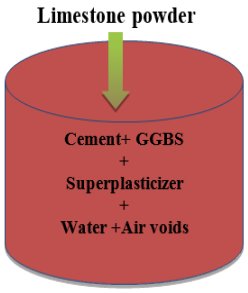

Figure 4. 3 First solid phase (limestone powder) added to the previous liquid phase (paste)

In this case, limestone powder (*LP*) is considered the solid phase and (cement+ggbs +SP+water+air) is the liquid phase. The volume fraction of the solid phase is determined using Eq. 4.7;

$$\phi_{LP} = \frac{v_{LP}}{v_{LP}+v_{paste}} \qquad (4.7)$$

Here, v_{LP} is the volume fraction of the solid phase (limestone powder), v_{paste} is the volume of the continuous matrix phase (paste volume) in which the solid phase is suspended. After calculating the volume of each ingredient in the mix, the volume of paste (v_p) is equal to 0.355 m^3 (see Table 5.1 in the next Chapter), limestone powder is considered the solid phase and the components within the container are the liquid phase. The volume fraction of *LP* is:

$$\phi_{LP} = \frac{0.058}{0.058+0.355} = 0.140 > 0.10;$$

Using Eq. 4.5, $\phi_m = 0.524$ (cubic packing) gives;

$$f_{LP}(\phi_{LP}) = (1 - \frac{0.140}{0.524})^{-1.9} = 1.805;$$

Based on Eq. 4.2; the plastic viscosity of the two-phase suspension is;

$$\eta(\phi_{LP+air+paste}) = \eta_{paste} \times f_{LP}(\phi_{LP});$$

$$\eta(\phi_{LP+air+paste}) = 0.23 \times 1.805 = 0.415 \text{ Pa s};$$

Step 3: The second solid phase addition i.e. fine aggregate (*FA*) (Figure 4.4);

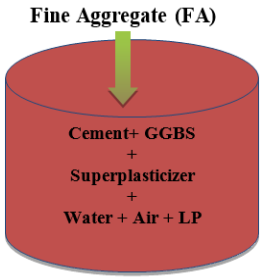

Figure 4. 4 Second solid phase (fine aggregate) added to the previous liquid phase (paste + LP)

Fine aggregate (*FA*) are now considered as the solid phase and the ingredients in the container as the liquid phase. The volume fraction of *FA* is;

ϕ_{FA}=0.410 > 0.10.

Using Eq. 4.5; ϕ_m= 0.630 (random hexagonal packing) gives;

$f_{FA}(\phi_{FA}) = (1 - \frac{0.410}{0.630})^{-1.9}$;

$f_{FA}(\phi_{FA}) = 7.360$.

Based on Eq. 4.2; the plastic viscosity of the two-phase suspension is

$\eta(\phi_{FA+LP+air+paste}) = \eta_{paste} \times f_{LP}(\phi_{LP}) \times f_{FA}(\phi_{FA})$;

$\eta(\phi_{FA+LP+air+paste}) = 0.23 \times 1.805 \times 7.360 = 3.06$ Pa s.

Step 4: The third solid phase addition i.e. coarse aggregates (*CA*) (Figure 4.5);

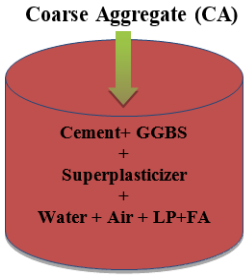

Figure 4. 5 Third solid phase (coarse aggregate) added to the previous liquid phase (paste + LP+ FA)

Coarse aggregate is now considered as the solid phase and the ingredients in the container as the liquid phase. The volume fraction of *CA* is;

ϕ_{CA}=0.300 > 0.10;

Using Eq. 4.5; $\phi_m = 0.740$ (hexagonal close packing) gives;

$f_{CA}(\phi_{CA}) = (1 - \frac{0.300}{0.740})^{-1.9}$; $f_{CA}(\phi_{CA}) = 2.685$;

Based on Eq. 4.2, the plastic viscosity of the mix is finally

$\eta\left(\phi_{CA+FA+LP+air+paste}\right) = \eta_{paste} \times f_{LP}(\phi_{LP}) \times f_{FA}(\phi_{FA}) \times f_{CA}(\phi_{CA})$;

$\eta(\phi_{CA+FA+LP+air+paste}) = 0.23 \times 1.805 \times 7.360 \times 2.685 = 8.13$ Pa s

4.5 Basic steps of the proposed mix design method

The basic steps of the proposed mix design method are summarised below and illustrated as a flowchart in Figure 4.6.

1. Select the desired plastic viscosity of the mix within the range of 3-15Pa s, remembering that the slump flow time (t_{500}) increases with increasing plastic viscosity of the mix. The EFNARC guidelines (2005) may be helpful in the choice of the desired plastic viscosity depending on the applications;

2. Calculate the ratio of water to cementitious materials (*w/cm*) that produces the target cube characteristic strength from Eq. 4.1;

3. Choose the water content in the range of 150-210kg/m^3, following EFNARC guidelines (2005), and calculate the mass of the cementitious materials (*cm*) in kg/m^3. The amount of ggbs is assumed to be 25% of the cementitious material (*cm*). It is known (Nehdi and Rahman, 2004) that the replacement of 25% the Portland cement (*c*) by ggbs has little or no effect on the paste viscosity;

4. Assume a trial super-plasticiser dosage (SP) as a percent of the cementitious material mass in the range of 0.4-0.8% for the MasterGlenium super-plasticiser used in this work. For this super-plasticiser, the manufacturer's recommended dosage is 0.2-1.2kg per 100kg of cementitious material (BASF, 2014);

5. Estimate the plastic viscosity of the paste from the *w/cm* and *SP/cm* ratios (Sun et al., 2006)(see Table 4.3). It is known that *SP/cm* has little impact on the paste viscosity; the major impact is on the yield stress (Domone, 2003);

6. Calculate the mass of the solid phase ingredients (filler, fine aggregate, and coarse aggregate) according to their volume fractions as explained in the examples below;

7. Check if the total volume of the produced mix is equal to 1m^3. If not, scale the ingredient masses to achieve a total volume of 1m^3;

8. Calculate the plastic viscosity of the mix using Eq. 4.6 and compare it with the desired one (step 1). If the difference is within ± 5%, adopt the mix proportions. If not, choose a different combination of the volume fractions of the solid phase ingredients (step 6) and repeat steps 7–8.

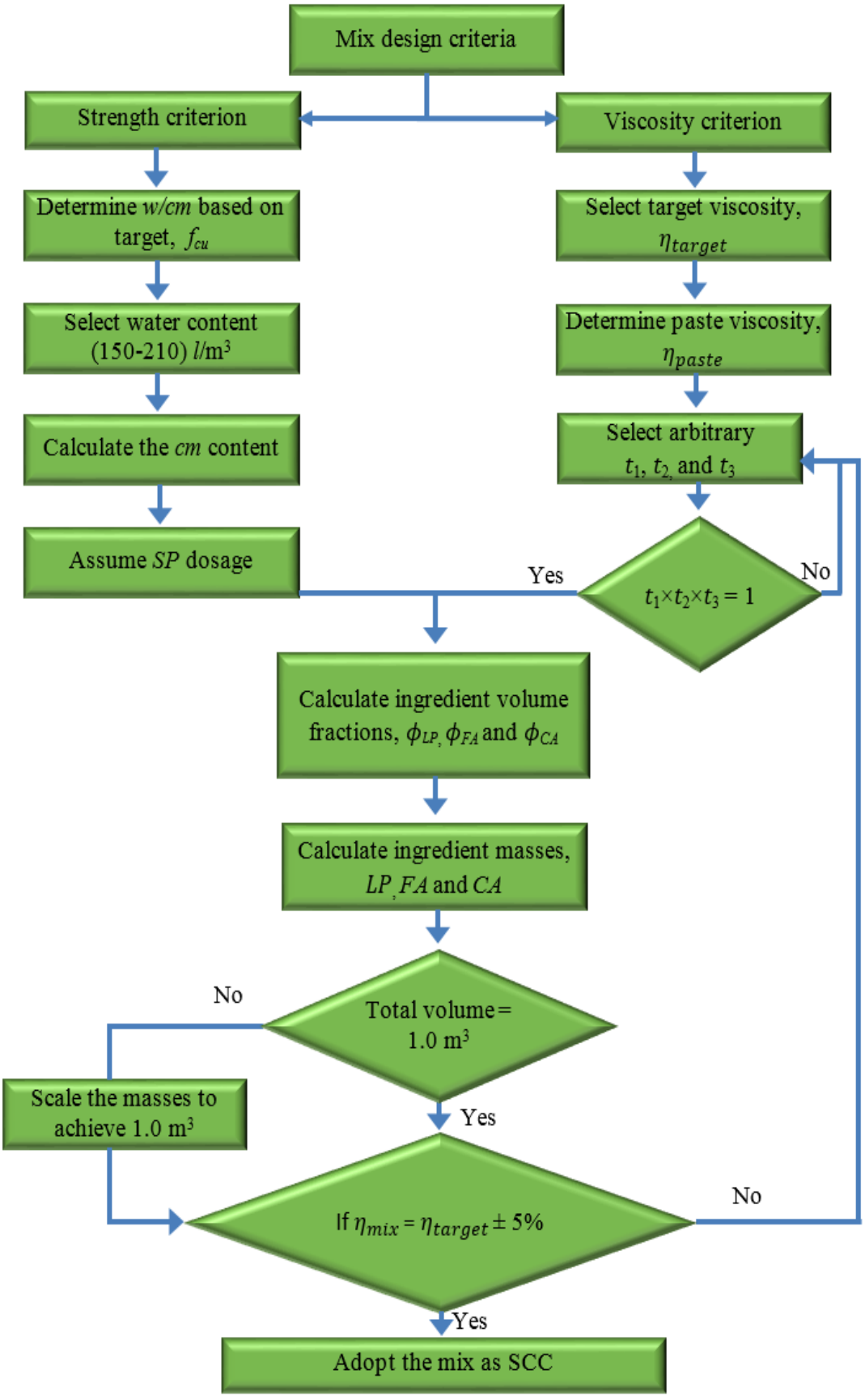

Figure 4. 6 Mix design procedure flowchart

Table 4. 3 Estimated plastic viscosity of the paste (cement+ggbs+SP+water+air)

w/cm	η_{paste}, Pa s	$\eta_{paste+air\ voids}$, Pa s
0.63	0.104	0.11
0.57	0.176	0.18
0.53	0.224	0.23
0.47	0.286	0.29
0.40	0.330	0.34
0.35	0.365	0.37

4.6 Examples of mix proportioning

As an example, let us proportion the mix of an SCC having a 28-day target cube compressive strength of 60MPa. The procedure is as follows:

1. Suppose that the desired target plastic viscosity of the mix is equal to 9Pa s;

2. Calculate the *w/cm* ratio from Eq. 4.1 corresponding to grade strength C60. It works out to be 0.47;

3. Assume the water content (w) to be 190kg/m^3, then the mass of cementitious materials (cm);

$cm = \frac{w}{(w/cm)} = \frac{190}{0.47}$ =404.3kg/m^3;

4. Assume a trial super-plasticiser dosage (SP) as a percent of mass of cementitious materials (say 0.65%), which equals 2.63kg/m^3;

5. Estimate the plastic viscosity of the paste; η_{paste} = 0.29Pa s (Table 4.3);

6. To estimate the volume fractions of limestone powder (LP), fine aggregate (FA) and coarse aggregate (CA), we first rewrite Eq. 4.6 as (note the use of different packing densities, as explained above)

$$\eta_{mix} = \eta_{paste} \times \left(1 - \frac{\phi_{LP}}{0.524}\right)^{-1.9} \times \left(1 - \frac{\phi_{FA}}{0.63}\right)^{-1.9} \times \left(1 - \frac{\phi_{CA}}{0.74}\right)^{-1.9}$$

Let $u = \left(\frac{\eta_{mix}}{\eta_{paste}} \times 0.524^{-1.9} \times 0.63^{-1.9} \times 0.74^{-1.9}\right)^{\frac{1}{-1.9}}$

so that the above equation becomes

$u = (0.524 - \phi_{LP}) \times (0.63 - \phi_{FA}) \times (0.74 - \phi_{CA})$

Substituting η_{mix} = 9Pa s and η_{paste} = 0.29Pa s, gives

u = 0.040 =$(0.524 - \phi_{LP})\times (0.63 - \phi_{FA})\times (0.74 - \phi_{CA})$

Let $x = \sqrt[3]{u} = 0.3422$,

then the values of ϕ_{LP}, ϕ_{FA} and ϕ_{CA} are given by

ϕ_{LP}= $0.524 - t_1 \times x$

ϕ_{FA}= $0.63 - t_2 \times x$

ϕ_{CA}= $0.74 - t_3 \times x$

where, t_1, t_2, and t_3 are arbitrarily chosen factors such that $t_1 \times t_2 \times t_3 = 1$.

Let us choose t_1 = 1, t_2 = 1 and t_3= 1, in the first instance.

For this choice of t_1, t_2, and t_3, the volume fractions of solid phases will be;

ϕ_{LP}= $0.524 - t_1 \times x$ = 0.524 – 1 × 0.3422 = 0.1818

ϕ_{FA}= $0.630 - t_2 \times x$ = 0.630 – 1 × 0.3422 = 0.2878

ϕ_{CA}= $0.740 - t_3 \times x$ = 0.740 – 1 × 0.3422 = 0.3978

The amounts of solid phases, i.e. limestone powder (*LP*), fine aggregate (*FA*), and coarse aggregate (CA) that are suspended in the liquid paste are calculated according to their volume fractions, ϕ_i knowing that the densities of cement, ggbs, water, super-plasticiser, limestone powder, fine aggregate and, coarse aggregate are 2950, 2400, 1000, 1070, 2400, 2650 and 2800kg/m^3, respectively;

$$\phi_{LP} = \frac{\frac{LP}{\rho_{LP}}}{\left(\frac{c}{\rho_c} + \frac{ggbs}{\rho_{ggbs}} + \frac{w}{\rho_w} + \frac{SP}{\rho_{SP}} + 0.02\right) + \frac{LP}{\rho_{LP}}} \quad \rightarrow \quad LP = 190.6\ kg/m^3$$

$$\phi_{FA} = \frac{\frac{FA}{\rho_{FA}}}{\left(\frac{c}{\rho_c} + \frac{ggbs}{\rho_{ggbs}} + \frac{w}{\rho_w} + \frac{SP}{\rho_{SP}} + \frac{LP}{\rho_{LP}} + 0.02\right) + \frac{FA}{\rho_{FA}}} \quad \rightarrow \quad FA = 467.8\ \text{kg/m}^3$$

$$\phi_{CA} = \frac{\frac{CA}{\rho_{CA}}}{\left(\frac{c}{\rho_c} + \frac{ggbs}{\rho_{ggbs}} + \frac{w}{\rho_w} + \frac{SP}{\rho_{SP}} + \frac{LP}{\rho_{LP}} + \frac{FA}{\rho_{FA}} + 0.02\right) + \frac{CA}{\rho_{CA}}} \rightarrow \quad CA = 1134 \text{ kg/m}^3$$

7. The total volume of the SCC mix that the above ingredients will yield (including the volume occupied by trapped air bubbles, 0.02)

$$\text{Total Volume} = \frac{c}{\rho_c} + \frac{ggbs}{\rho_{ggbs}} + \frac{w}{\rho_w} + \frac{SP}{\rho_{SP}} + \frac{LP}{\rho_{LP}} + \frac{FA}{\rho_{FA}} + \frac{CA}{\rho_{CA}} + 0.02$$

$$\text{Total Volume} = \frac{404.3 \times 0.75}{2950} + \frac{404.3 \times 0.25}{2400} + \frac{190}{1000} + \frac{2.63}{1070} + \frac{190.6}{2400} + \frac{467.8}{2650} + \frac{1134}{2800} + 0.02 = 1.018 \text{ m}^3$$

As the yield does not equal 1m^3, the amounts of materials are adjusted;

cm = 404.3 / 1.018 = 396.9kg/m^3

w = 190 / 1.018 = 186.6kg/m^3

SP = 2.63 / 1.018 = 2.58kg/m^3

LP = 190.6 / 1.018= 187.1kg/m^3

FA = 467.8 / 1.018= 459.3kg/m^3

CA = 1134 / 1.018= 1114kg/m^3

$$\text{Total Volume} = \frac{c}{\rho_c} + \frac{ggbs}{\rho_{ggbs}} + \frac{w}{\rho_w} + \frac{SP}{\rho_{SP}} + \frac{LP}{\rho_{LP}} + \frac{FA}{\rho_{FA}} + \frac{CA}{\rho_{CA}} + 0.02 = \ 1.000 \text{ m}^3$$

8. Check the plastic viscosity of the mix using Eq. 4.6;

$$\eta_{mix} = \eta_{paste} \times \left(1 - \frac{\phi_{LP}}{\phi_m}\right)^{-1.9} \times \left(1 - \frac{\phi_{FA}}{\phi_m}\right)^{-1.9} \times \left(1 - \frac{\phi_{CA}}{\phi_m}\right)^{-1.9}$$

$$\eta_{mix} = 0.34 \times \left(1 - \frac{0.1817}{0.524}\right)^{-1.9} \times \left(1 - \frac{0.2877}{0.63}\right)^{-1.9} \times \left(1 - \frac{0.3977}{0.74}\right)^{-1.9} = 8.97\text{Pa s}$$

The mix masses before and after scaling to 1.0 m^3 are given in Table 4.4, together with the difference between the actual and target plastic viscosities.

Table 4. 4 Mix constituents and plastic viscosity of an SCC mix

	Ingredient, kg/m^3							η, Pa s	Difference
	cement	ggbs	*w*	*SP*	*LP*	*FA*	*CA*		
Before adjust.	303.2	101.1	190	2.63	190.6	467.8	1134	–	
After adjust.	297.7	99.2	186.6	2.58	187.1	459.3	1114	8.977	– 0.3%
Density	2950	2400	1000	1070	2400	2650	2800	–	

As the difference of 0.3% in the plastic viscosity is well within the acceptable range, the mix would seem to be acceptable.

However, the amount of coarse aggregate exceeds the limit of the EFNARC guidelines (2005), so it is necessary to adjust the mix proportions, choosing different arbitrary values of t_1, t_2 and t_3 for the same target plastic viscosity and strength:

Steps 1-5 are the same as described above.

6. To calculate the volume fractions of solid phases, let choose values of t_1, t_2, and t_3 different from those used above. Let t_1 = 1.2, t_2 = 0.7 and t_3 = 1.2 such that $t_1 \times t_2 \times t_3$ = 1.0. Accordingly, the volume fractions of solid phases work out to be ϕ_{LP} = 0.1134, ϕ_{FA} = 0.3905 and ϕ_{CA} = 0.3294. The amounts of solid phases, i.e. limestone powder LP, fine aggregate FA and coarse aggregate CA that are suspended in the liquid paste are calculated according to their volume fractions ϕ_i;

$$\phi_{LP} = \frac{\frac{LP}{\rho_{LP}}}{\left(\frac{c}{\rho_c} + \frac{ggbs}{\rho_{ggbs}} + \frac{w}{\rho_w} + \frac{SP}{\rho_{SP}} + 0.02\right) + \frac{LP}{\rho_{LP}}} \quad \rightarrow \quad LP = 190.7\ kg/m^3$$

$$\phi_{FA} = \frac{\frac{FA}{\rho_{FA}}}{\left(\frac{c}{\rho_c} + \frac{ggbs}{\rho_{ggbs}} + \frac{w}{\rho_w} + \frac{SP}{\rho_{SP}} + \frac{LP}{\rho_{LP}} + 0.02\right) + \frac{FA}{\rho_{FA}}} \quad \rightarrow \quad FA = 684.3\ \text{kg/m}^3$$

$$\phi_{CA} = \frac{\frac{CA}{\rho_{CA}}}{\left(\frac{c}{\rho_c} + \frac{ggbs}{\rho_{ggbs}} + \frac{w}{\rho_w} + \frac{SP}{\rho_{SP}} + \frac{LP}{\rho_{LP}} + \frac{FA}{\rho_{FA}} + 0.02\right) + \frac{CA}{\rho_{CA}}} \rightarrow CA = 909.5 \text{ kg/m}^3$$

The total volume of the SCC mix that the above ingredients will yield (including the volume occupied by trapped air bubbles, 0.02);

$$\text{Total Volume} = \frac{c}{\rho_c} + \frac{ggbs}{\rho_{ggbs}} + \frac{w}{\rho_w} + \frac{SP}{\rho_{SP}} + \frac{LP}{\rho_{LP}} + \frac{FA}{\rho_{FA}} + \frac{CA}{\rho_{CA}} + 0.02 = 0.986 \text{ m}^3$$

As the yield does not equal to 1.0 m^3, the amounts of ingredients are adjusted. The results are shown in Table 4.5.

The mix plastic viscosity is calculated by using Eq. 4.6. As the difference between the target plastic viscosity and the original mix plastic viscosity is within ± 5%, the mix proportions after adjustment are acceptable.

Table 4. 5 Mix constituents and plastic viscosity of an SCC mix

	Ingredient, kg/m^3							η, Pa s	Difference
	cement	ggbs	*w*	*SP*	*LP*	*FA*	*CA*		
Before adjust.	303.2	101.1	190	2.63	109.7	684.3	909.5	–	
									–1.3 %
After adjust.	307.5	102.5	192.7	2.67	111.2	693.9	922.3	8.883	
Density	2950	2400	1000	1070	2400	2650	2800	–	

Given that the choice of t_i is somewhat arbitary, it is clear that there are many (theoretically infinite) combinations of the volume fractions of the solid phases that can be chosen for an SCC mix and still reach the target cube compressive strength and mix plastic viscosity. It is however possible that some of these combinations may not yield a satisfactory SCC mix. It is therefore necessary to use other sources of information based on accumulated knowledge of SCC mixes, e.g. the EFNARC guidelines (2005) and survey report (Domone, 2006), as was done above. To aid the user in making a knowledgeable choice, a software program was developed (Appendix A) from which design charts were constructed which are presented below.

4.7 Design charts for mix proportioning of normal and high strength SCC mixes

Thousands of solid phase volume fraction combinations (i.e. t_1, t_2, and t_3) were produced using a software program. These combinations covered wide ranges of target cube compressive strength and mix plastic viscosity. They have been collected in groups according to the target strength for ease of SCC mix proportioning. It was found convenient for presentation of a huge body of data to normalise the amounts of dry phases by the plastic viscosity and to present the amounts in separate plots, beginning with the cementitious materials (*cm*), and ending with the content of all dry phases (*cm + LP + FA + CA*). These design charts are given in Figures 4.7-4.12. The scatter reflects the multiplicity of combinations. It is however interesting to note that the scatter is the least in the bottom (*cm*) and the top (*cm + LP + FA + CA*) curves. This is because the amount of *cm* calculated from the target compressive strength is according to the water content, which varies in the narrow range of 150-210*l*/m^3 and the amounts of all dry ingredients contribute to the target plastic viscosity of the mix. It is necessary to clarify that the design charts have varying starting target plastic viscosity within a range of 3-15Pa s; the upper bound for all mix grades was 15Pa s, whereas the lower bound started from 3Pa s for the low strength mix grade (i.e. 30MPa) and 8Pa s for high strength mix grade (i.e. 80MPa). The limitations on several parameters (the amount of cement replacement materials, the dosage of super-plasticiser and flow spread**)** that dominate the mix proportioning is behind these differences in the lower plastic viscosity.

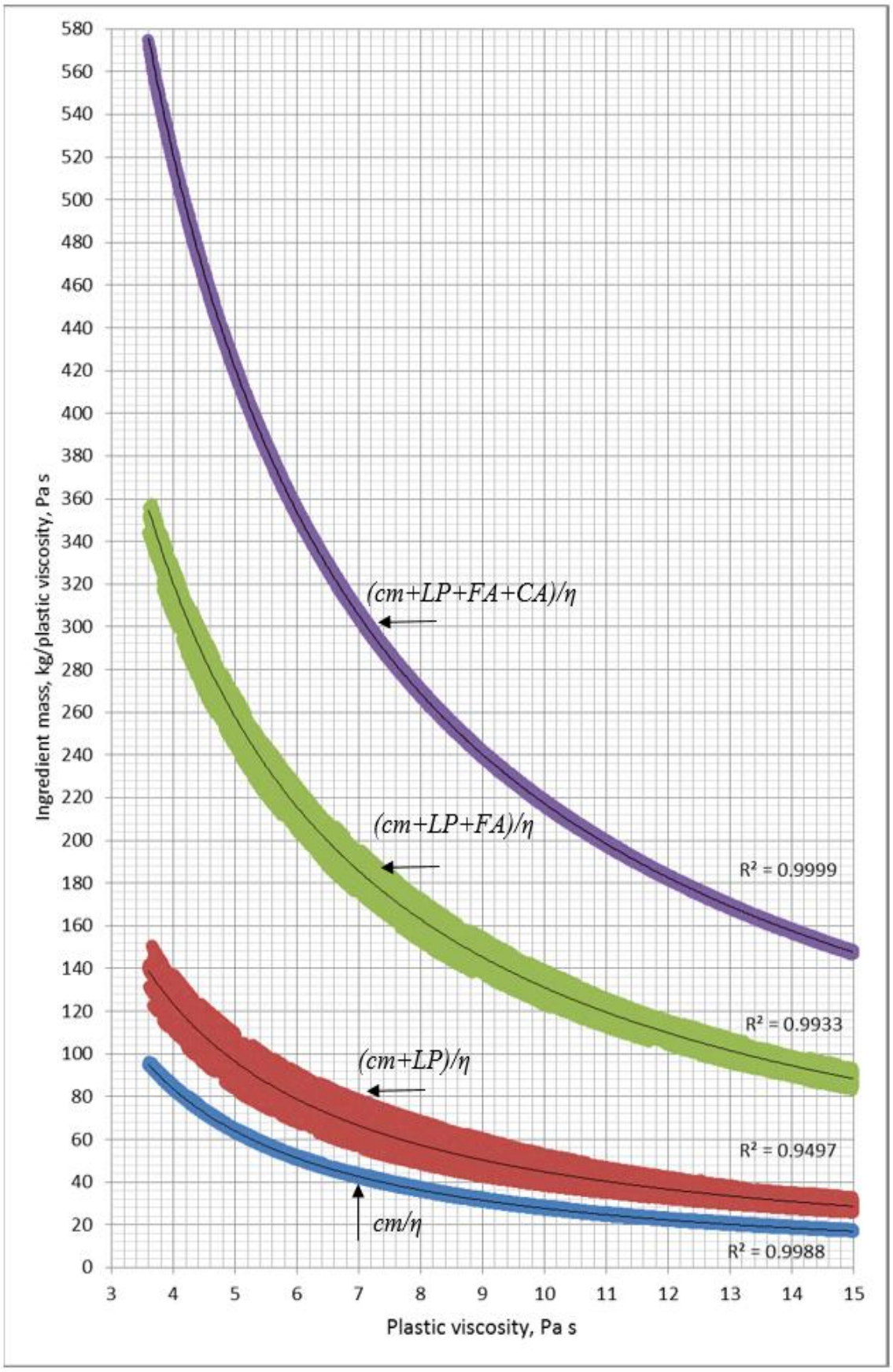

Figure 4. 7 Ingredient mass (kg) normalised by mix plastic viscosity vs. plastic viscosity for 30MPa mix

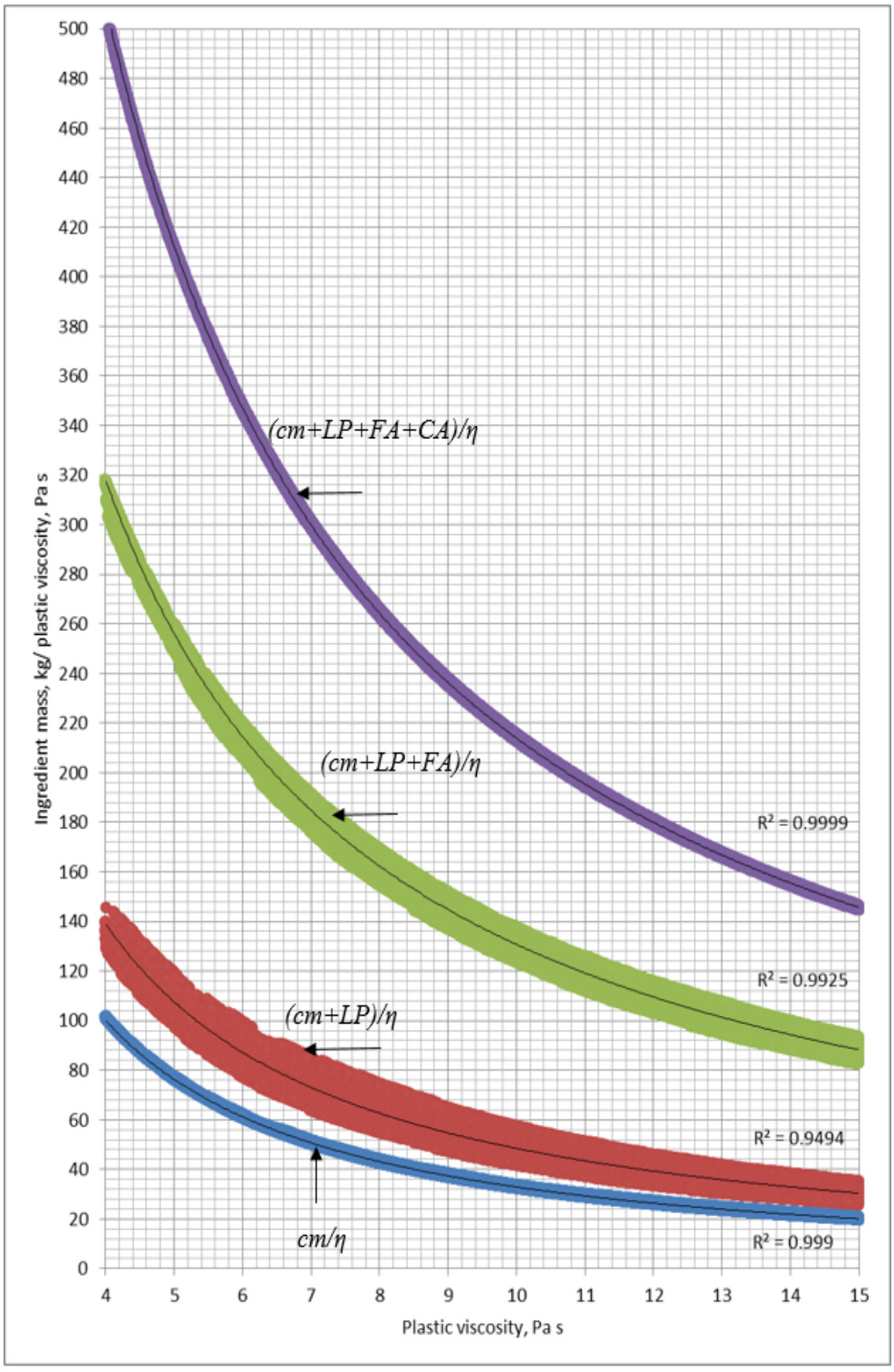

Figure 4. 8 Ingredient mass (kg) normalised by mix plastic viscosity vs. plastic viscosity for 40MPa mix

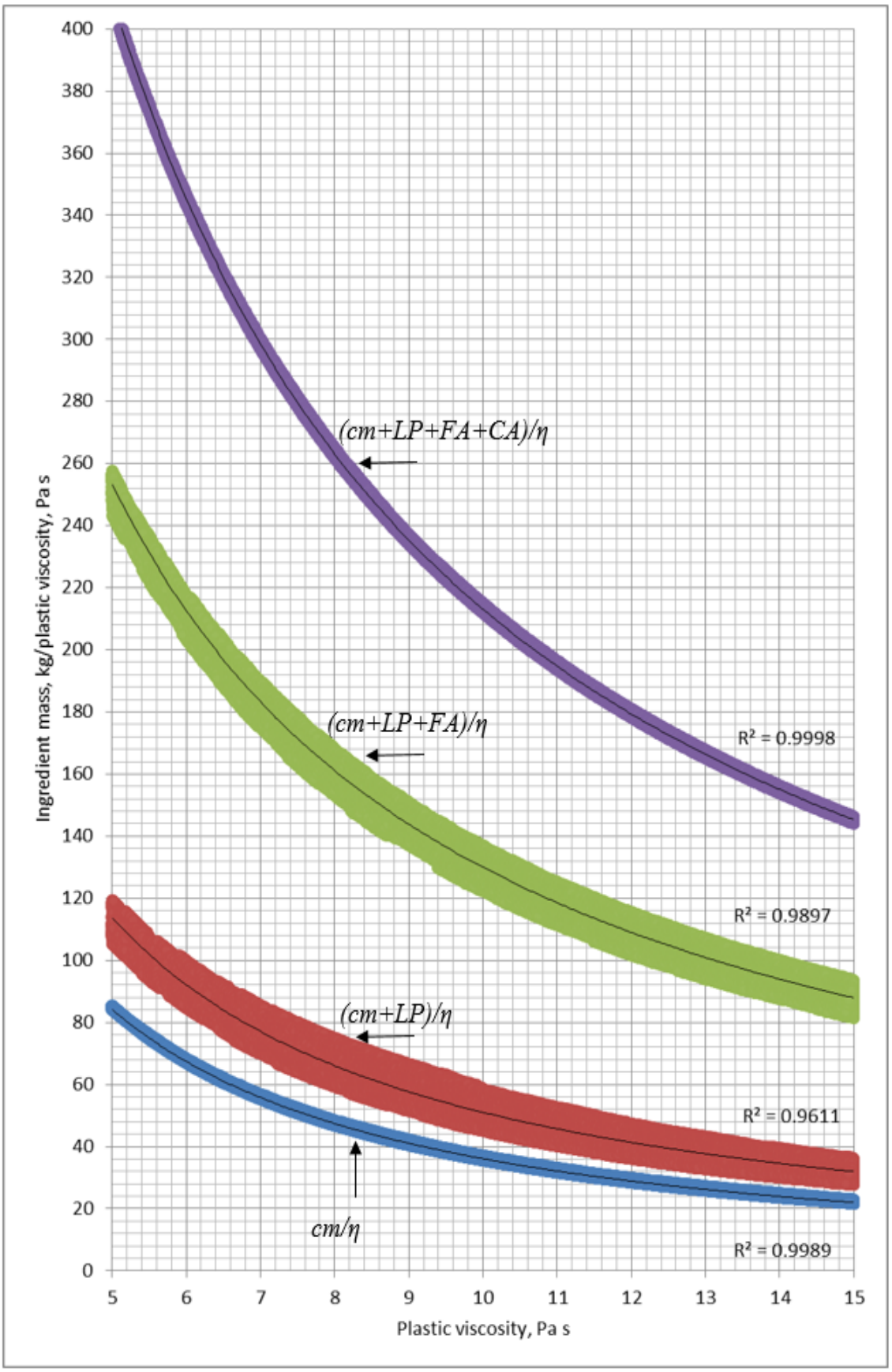

Figure 4. 9 Ingredient mass (kg) normalised by mix plastic viscosity vs. plastic viscosity for 50MPa mix

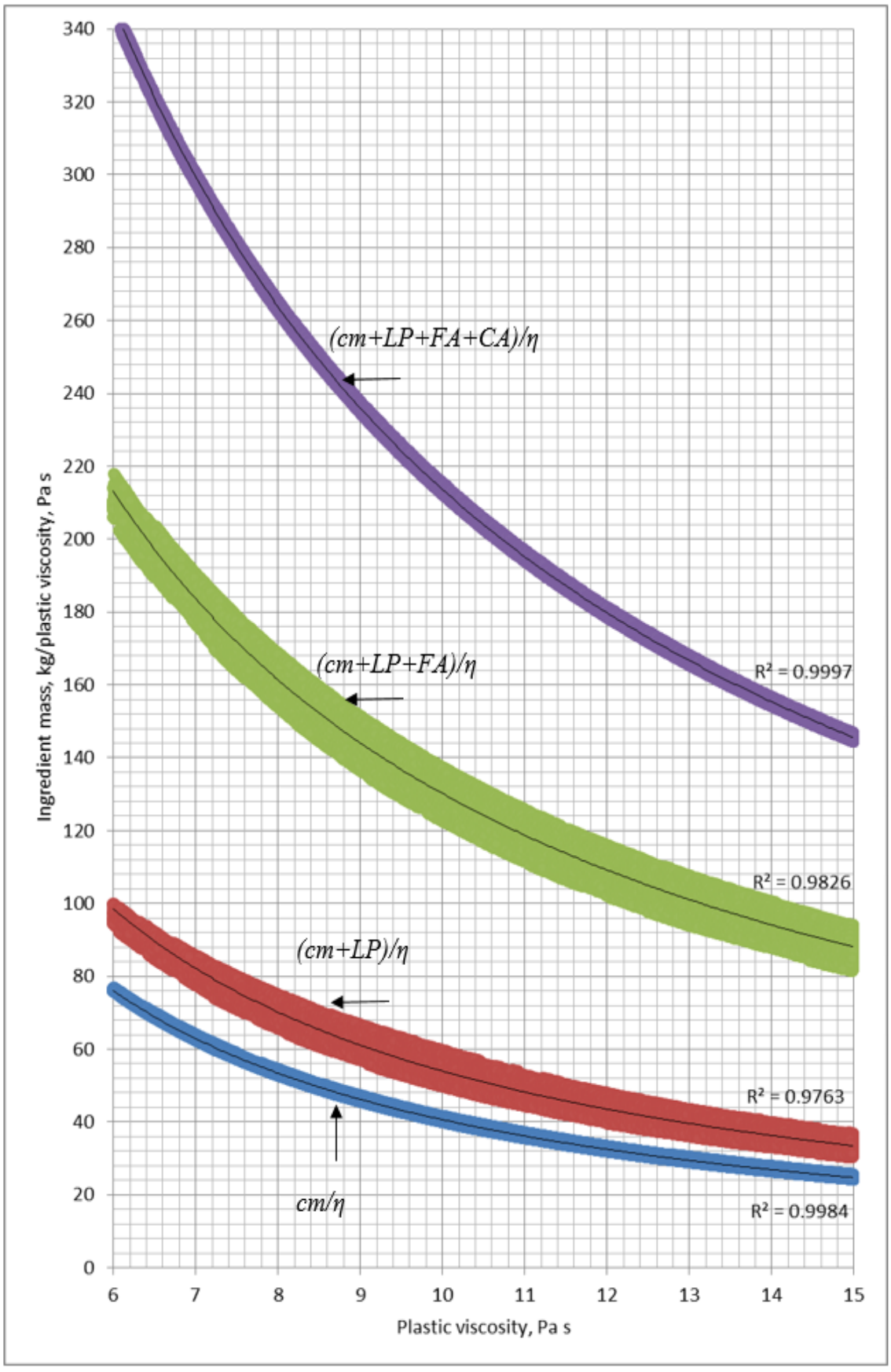

Figure 4. 10 Ingredient mass (kg) normalised by mix plastic viscosity vs. plastic viscosity for 60MPa mix

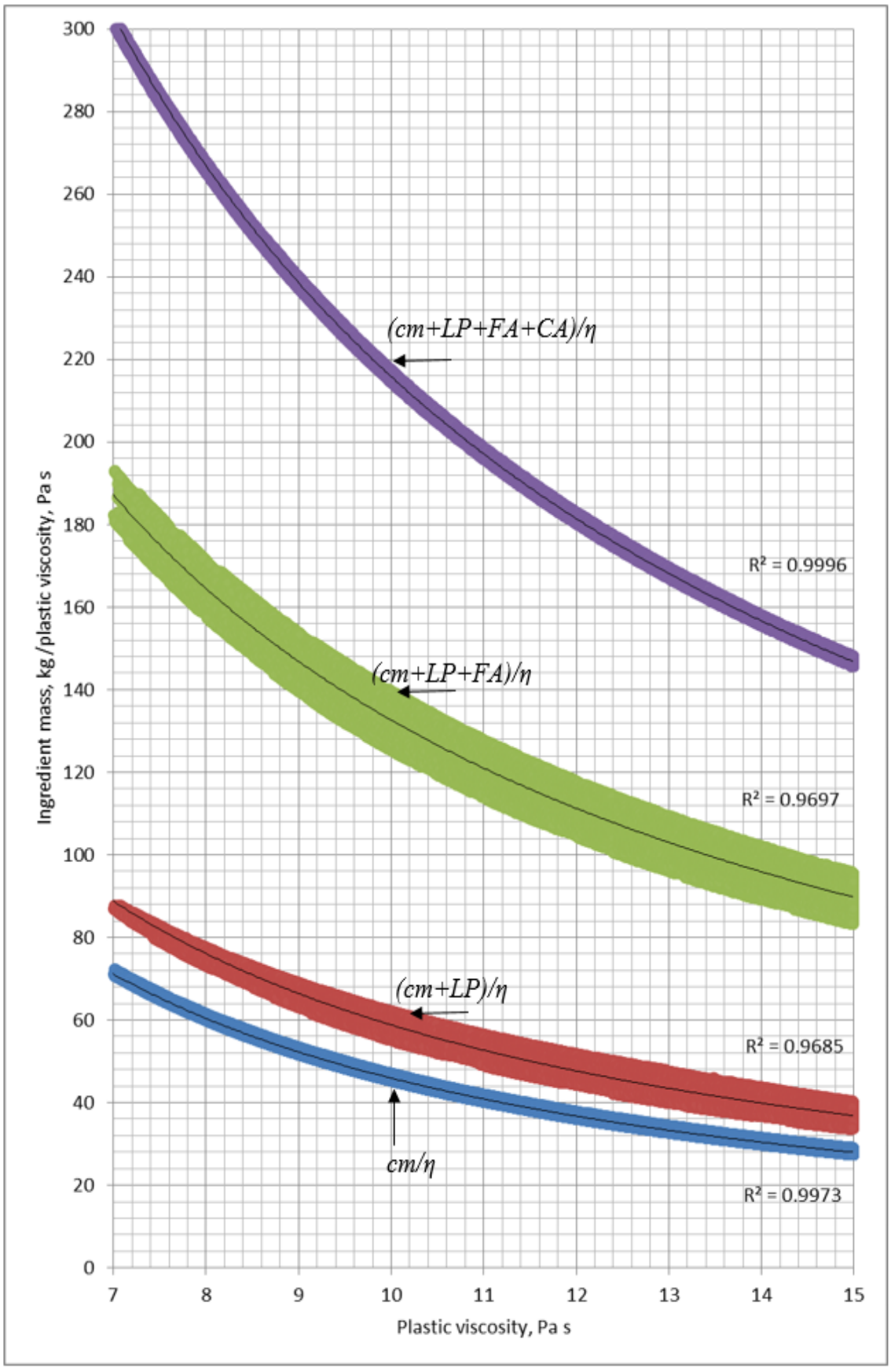

Figure 4. 11 Ingredient mass (kg) normalised by mix plastic viscosity vs. plastic viscosity for 70MPa mix

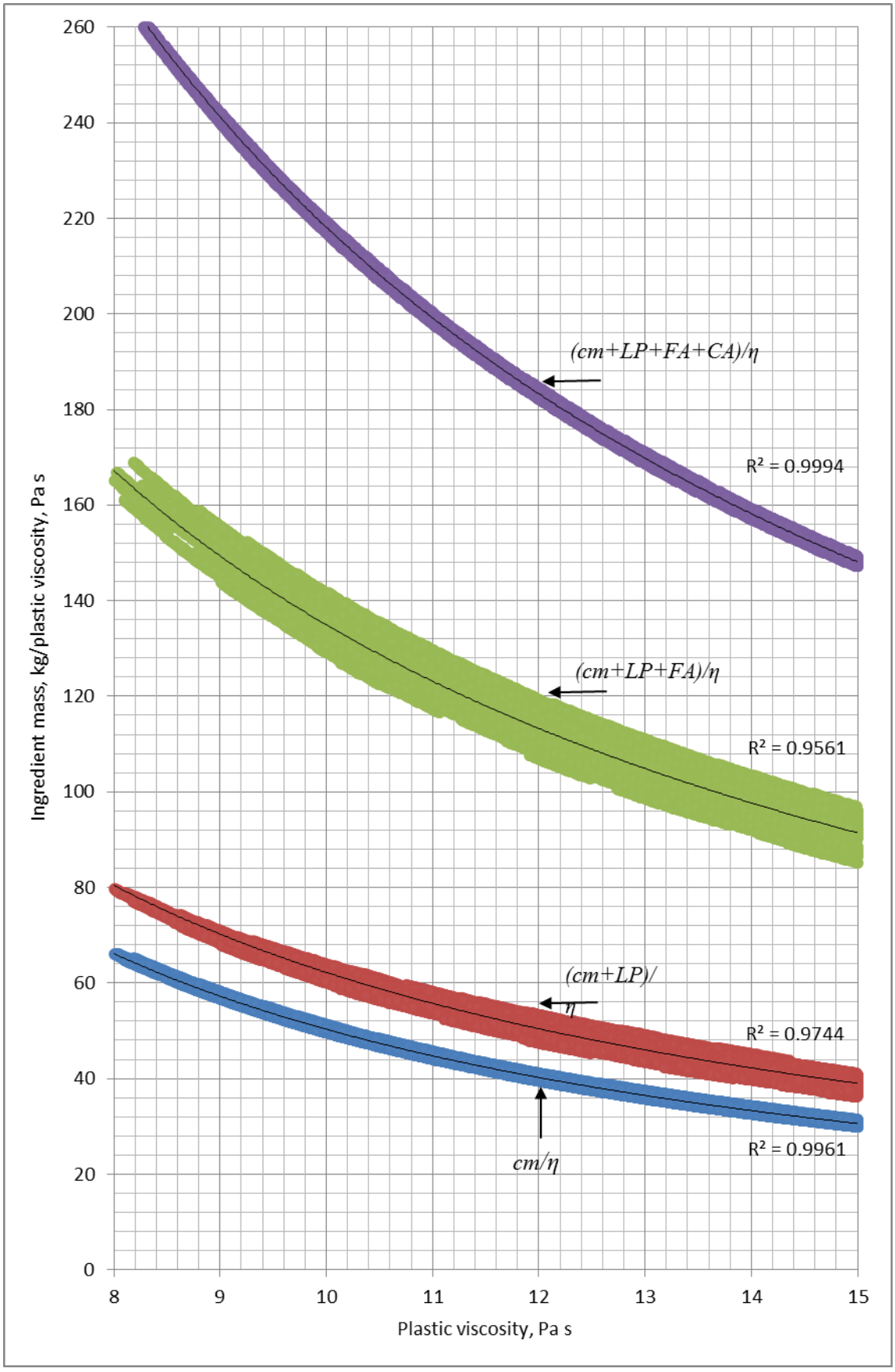

Figure 4. 12 Ingredient mass (kg) normalised by mix plastic viscosity vs. plastic viscosity for 80MPa mix

4.8 Examples of the use of design charts

In order to demonstrate how easy it is to use the design charts (Figures 4.7-4.12), let us assume we wish to design an SCC mix with a target cube compressive strength of 50MPa (Figure 4.13)

1. Suppose further that the desired target plastic viscosity of mix is 6Pa s;

2. For the desired target strength= 50MPa $\longrightarrow$ *w/cm* = 0.53 (Eq. 4.1);

3. Calculate the cementitious material content (*cm*);

For η_{mix} = 6Pa s $\longrightarrow$ $\frac{cm}{\eta}$ = 66 (bottom curve) $\longrightarrow$ *cm* = 6 × 66= 396kg/m^3;

c = 0.75 × 396 = 297 kg/m^3, ggbs = 0.25 × 396= 99kg/m^3 ;

As *w/cm* = 0.53 $\longrightarrow$ *w* = 0.53 × 396= 210*l*/m^3

4. Assume a trial super-plasticiser dosage (SP) as a per cent of mass of cementitious materials (say 0.60%) which equals to 2.4kg/m^3;

5. The plastic viscosity of the paste according to its *w/cm* and *SP/cm* ratios is equal to 0.23 (Table 4.3);

6. Calculate the solid phase ingredient contents (*LP, FA and CA*);

For η_{mix} = 6Pa s

$\frac{(cm+LP)}{\eta}$ = 92 (second curve from bottom);

(*cm*+*LP*) = 6 × 92 = 552 kg/m^3 $\longrightarrow$ *LP* = 552 – 396= 156kg/m^3

$\frac{(cm+LP+FA)}{\eta}$ = 210 (second curve from top)

(*cm* +*LP* +*FA*) = 6 × 210 = 1260kg/m^3 $\longrightarrow$ *FA* = 1260 – 396 –156= 708kg/m^3

$\frac{(cm+LP+FA+CA)}{\eta}$ = 345 (top curve)

(*cm*+*LP*+*FA*+*CA*) = 6 × 345 = 2070kg/m^3 $\longrightarrow$ *CA* = 2070 –396–156–708=810kg/m^3

7. Calculate the total volume of the mix;

$$\text{Total volume} = \frac{c}{\rho_c} + \frac{ggbs}{\rho_{ggbs}} + \frac{w}{\rho_W} + \frac{SP}{\rho_{SP}} + \frac{LP}{\rho_{LP}} + \frac{FA}{\rho_{FA}} + \frac{CA}{\rho_{CA}} + 0.02$$

$$\text{Total volume} = \frac{396\times0.75}{2950} + \frac{396\times0.25}{2400} + \frac{210}{1000} + \frac{2.4}{1070} + \frac{156}{2400} + \frac{708}{2650} + \frac{810}{2800} + 0.02 = 1\text{m}^3$$

8. Check the plastic viscosity using Eq. 4.6;

$$\eta_{mix} = \eta_{paste} \times \left(1 - \frac{\phi_{LP}}{\phi_m}\right)^{-1.9} \times \left(1 - \frac{\phi_{FA}}{\phi_m}\right)^{-1.9} \times \left(1 - \frac{\phi_{CA}}{\phi_m}\right)^{-1.9}$$

$$\eta_{mix} = 0.23 \times \left(1 - \frac{0.107}{0.524}\right)^{-1.9} \times \left(1 - \frac{0.421}{0.63}\right)^{-1.9} \times \left(1 - \frac{0.330}{0.74}\right)^{-1.9} = 6.3\text{Pa s}$$

$$\text{Viscosity diff.} = \frac{(\text{calculated } \eta_{mix} - \text{target } \eta_{mix})}{\text{target } \eta_{mix}} \times 100 = \frac{(6.3 - 6)}{6} \times 100 = +5.0\%$$

This is within the acceptable difference ± 5 %.

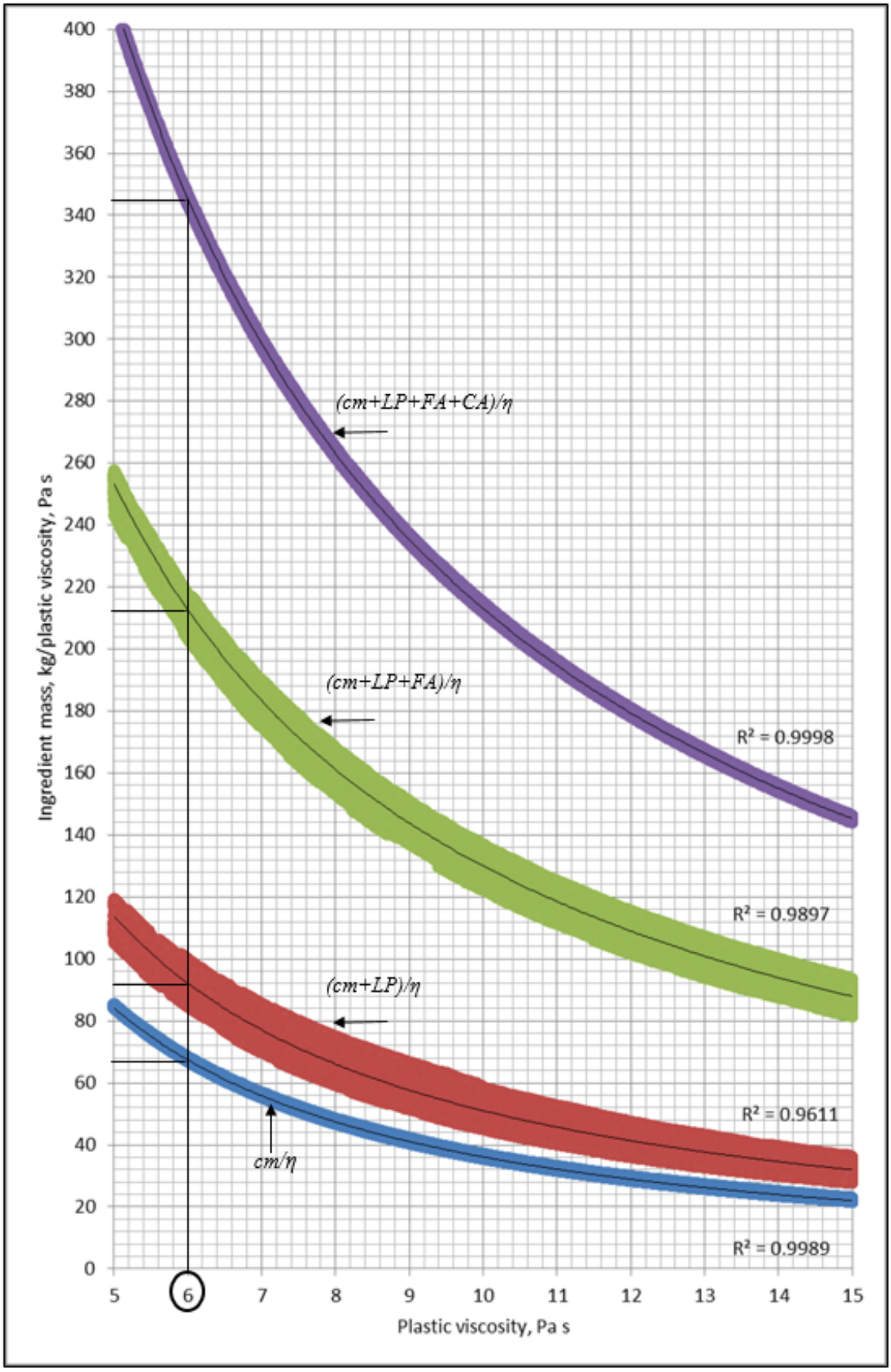

Figure 4. 13 Example for designing 50MPa mix with 6Pa s plastic viscosity

It is interesting to observe in this example that we chose the mix combinations corresponding to the best-fit lines in the curves. That is why the total mix volume worked out to be exactly 1.0 m^3 so that the plastic viscosity of the mix is within the acceptable deviation from the desired target value. This would not have been so had we chosen the mix combinations different from the best-fit lines within the scatter band. As a rule, the more the deviation from the best-fit lines, the more the total mix volume deviates from 1.0 m^3 and consequently the more the plastic viscosity of the resultant mix deviates from the target value. If the deviation is more than ± 5%, then as mentioned above the procedure would need to be repeated (see step 8 in the mix design procedure §4.5). Appendix B contains proportioning of ingredients for SCC mixes developed by using the proposed procedure.

In order to demonstrate this, we choose two examples with ingredient proportions away from the best-fit lines, and nearer the upper and lower limits of scatter. Let us design an SCC mix with a target cube compressive strength of 50MPa and choose the starting ingredient amounts at the upper limits of scatter in the design chart (Figure 4.14)

1. Suppose further that the desired target plastic viscosity of mix is 8Pa s;

2. For the desired target strength = 50MPa $\longrightarrow$ *w/cm*= 0.53 (Eq. 4.1);

3. Calculate the cementitious material content (*cm*);

For η_{mix} = 8Pa s $\longrightarrow$ $\frac{cm}{\eta}$ = 49 (bottom curve) $\longrightarrow$ *cm*= 8 × 49= 392kg/m^3;

c = 0.75 × 392 = 294kg/m^3, ggbs = 0.25 × 392 = 98kg/m^3 ;

As *w/cm* = 0.53$\longrightarrow$ *w* = 0.53 × 392 = 207.8*l*/m^3

4. Assume a trial super-plasticiser dosage (SP) as a per cent of mass of cementitious materials (say 0.60%) which equals to 2.35kg/m^3;

5. The plastic viscosity of the paste according to its *w/cm* and *SP/cm* ratios is equal to 0.23 (Table 4.3);

6. Calculate the solid phase ingredient contents (*LP, FA and CA*);

For η_{mix} = 8Pa s;

$\frac{(cm+LP)}{\eta}$ = 77 (second curve from bottom)

(*cm*+*LP*) = 8 × 77 = 616kg/m^3 $\longrightarrow$ *LP* = 616 – 392 = 224kg/m^3

$\frac{(cm+LP+FA)}{\eta}$ = 171 (second curve from top)

($cm + LP + FA$) = 8 × 171 = 1368kg/m^3 ⟶ FA = 1368 – 392 –224 = 752kg/m^3

$\frac{(cm+LP+FA+CA)}{\eta}$ = 269 (top curve)

($cm+LP+FA+CA$)= 8 × 296= 2152kg/m^3 ⟶ CA= 2152–392–224–752= 784kg/m^3

7. Calculate the total volume of the mix;

$$\text{Total volume} = \frac{c}{\rho_c} + \frac{ggbs}{\rho_{ggbs}} + \frac{w}{\rho_W} + \frac{SP}{\rho_{SP}} + \frac{LP}{\rho_{LP}} + \frac{FA}{\rho_{FA}} + \frac{CA}{\rho_{CA}} + 0.02$$

$$\text{Total volume} = \frac{392\times0.75}{2950} + \frac{392\times0.25}{2400} + \frac{208.7}{1000} + \frac{2.3}{1070} + \frac{224}{2400} + \frac{752}{2650} + \frac{784}{2800} + 0.02 = 1.028\text{m}^3$$

Owing to the total mix volume not being equal to 1 m^3, it must be scaled to 1.0, so the ingredient amounts will be:

cm = 392 / 1.028 = 381kg/m^3

w = 207.8 / 1.028 = 202kg/m^3

SP = 2.35 / 1.028 = 2.3kg/m^3

LP = 224 / 1.028 = 218kg/m^3

FA = 752 / 1.028 = 731.5kg/m^3

CA = 784 / 1.028 = 763kg/m^3

$$\text{Total volume} = \frac{381\times0.75}{2950} + \frac{381\times0.25}{2400} + \frac{202}{1000} + \frac{2.3}{1070} + \frac{218}{2400} + \frac{731.5}{2650} + \frac{763}{2800} + 0.02 =$$

$$\text{Total volume} = 1\text{m}^3$$

8. Check the plastic viscosity using Eq. 4.6;

$$\eta_{mix} = \eta_{paste} \times \left(1 - \frac{\phi_{LP}}{\phi_m}\right)^{-1.9} \times \left(1 - \frac{\phi_{FA}}{\phi_m}\right)^{-1.9} \times \left(1 - \frac{\phi_{CA}}{\phi_m}\right)^{-1.9}$$

$$\eta_{mix} = 0.23 \times \left(1 - \frac{0.201}{0.524}\right)^{-1.9} \times \left(1 - \frac{0.379}{0.63}\right)^{-1.9} \times \left(1 - \frac{0.272}{0.74}\right)^{-1.9} = 7.9\text{Pa s}$$

$$\text{Viscosity diff.} = \frac{(\text{calculated } \eta_{mix} - \text{target } \eta_{mix})}{\text{target } \eta_{mix}} \times 100 = \frac{(7.9-8)}{8} \times 100 = -1.3\%$$

This is within the acceptable difference ± 5%.

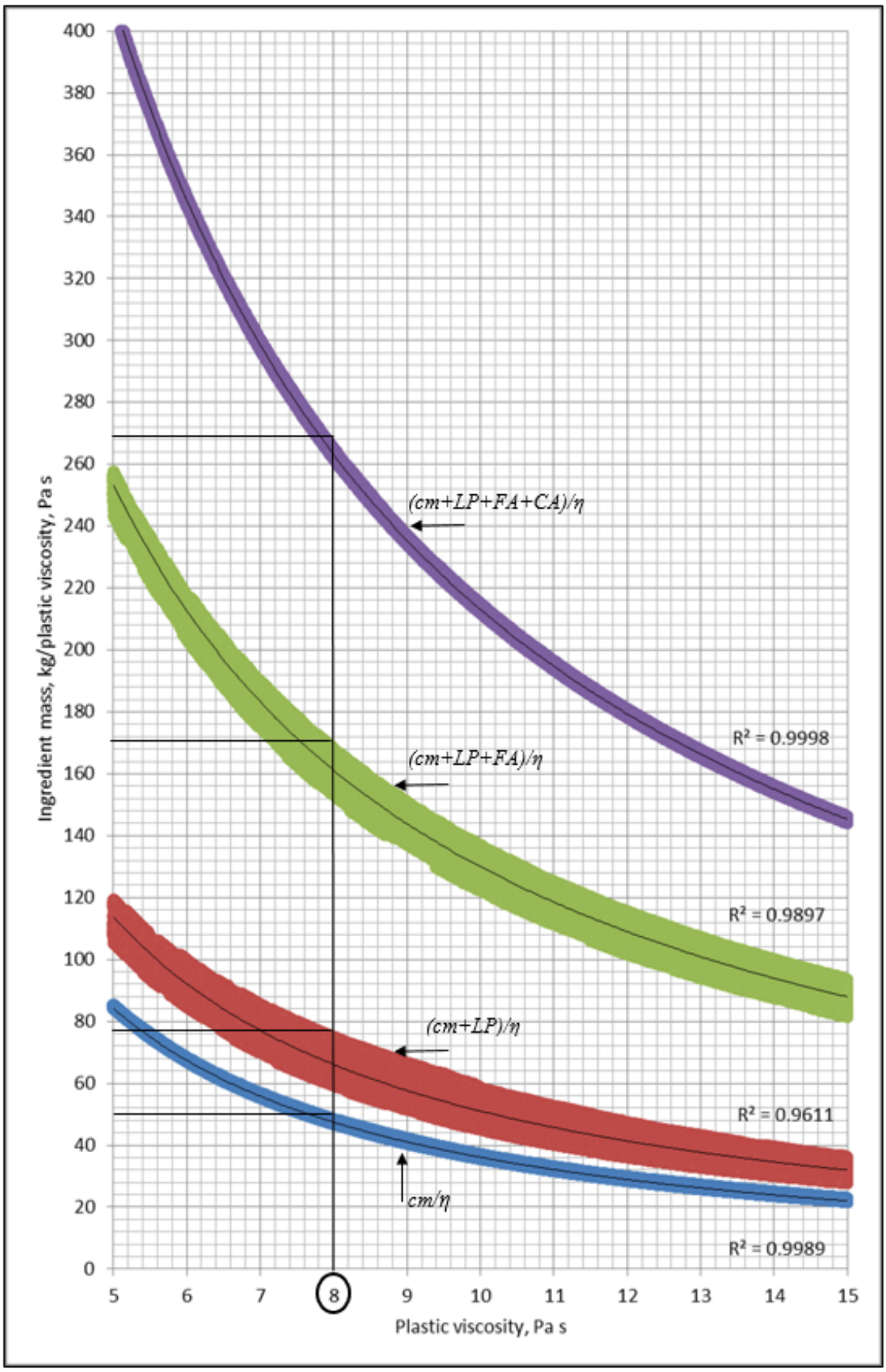

Figure 4. 14 Example for designing 50MPa mix with 8Pa s plastic viscosity

The next example deals with the design of an SCC mix with a target cube compressive strength of 50MPa. In this example, we choose the starting ingredient amounts at the lower limits of scatter in the design chart (Figure 4.15).

1. Suppose the desired target plastic viscosity of mix is 10Pa s;

2. For the desired target strength = 50MPa $\longrightarrow$ *w/cm*= 0.53 (Eq. 4.1);

3. Calculate the cementitious material content (*cm*);

For η_{mix} = 10Pa s $\longrightarrow$ $\frac{cm}{\eta}$ = 32 (bottom curve) $\longrightarrow$ *cm* =10 × 32= 320kg/m^3;

c = 0.75 × 320 = 240kg/m^3, ggbs = 0.25 × 320 = 80kg/m^3 ;

As *w/cm* = 0.53 $\longrightarrow$ *w* =0.53 × 320 = 170*l*/m^3

4. Assume a trial super-plasticiser dosage (SP) as a per cent of mass of cementitious materials (say 0.60%) which equals to 1.0kg/m^3;

5. The plastic viscosity of the paste according to its *w/cm* and *SP/cm* ratios is equal to 0.23 (Table 4.3);

6. Calculate the solid phase ingredient contents (*LP, FA and CA*);

For η_{mix} =10Pa s

$\frac{(cm+LP)}{\eta}$ = 44 (second curve from bottom)

(*cm*+*LP*) = 10 × 44 = 440kg/m^3 $\longrightarrow$ *LP* = 440 – 320 = 120kg/m^3

$\frac{(cm+LP+FA)}{\eta}$ = 119 (second curve from top)

(*cm*+*LP*+*FA*) = 10 × 119= 1190kg/m^3 $\longrightarrow$ *FA* = 1190 – 320 –120 = 750kg/m^3

$\frac{(cm+LP+FA+CA)}{\eta}$ = 208 (top curve)

(*cm*+*LP*+*FA*+*CA*) = 10× 208 = 2080kg/m^3 $\rightarrow$ *CA* = 2080–320–120–750=890kg/m^3

7. Calculate the total volume of the mix;

$$\text{Total volume} = \frac{320\times0.75}{2950} + \frac{320\times0.25}{2400} + \frac{170}{1000} + \frac{1.9}{1070} + \frac{120}{2400} + \frac{750}{2650} + \frac{890}{2800} + 0.02 =$$

Total volume = 0.957 m^3

Owing to the total mix volume not being equal to 1.0 m^3, it must be scaled to 1.0, so the ingredients amounts will be:

cm = 320 / 0.957 = 334kg/m^3

w = 170 / 0.957 = 178kg/m^3

SP = 1.9 / 0.957 = 2.0kg/m^3

LP = 120 / 0.957 = 125kg/m^3

FA=750 / 0.957 = 784kg/m^3

CA=890 / 0.957 = 930kg/m^3

Total volume $= \frac{334\times0.75}{2950} + \frac{334\times0.25}{2400} + \frac{178}{1000} + \frac{2.0}{1070} + \frac{125}{2400} + \frac{784}{2650} + \frac{930}{2800} + 0.02 = 1\text{m}^3$

8. Check the plastic viscosity using Eq. 4.6;

$\eta_{mix} = 0.23 \times \left(1 - \frac{0.140}{0.524}\right)^{-1.9} \times \left(1 - \frac{0.443}{0.63}\right)^{-1.9} \times \left(1 - \frac{0.332}{0.74}\right)^{-1.9} = 12.70\text{Pa s}$

Viscosity diff. $= \frac{(\text{calculated } \eta_{mix} - \text{target } \eta_{mix})}{\text{target } \eta_{mix}} \times 100 = \frac{(12.7-10)}{10} \times 100 = +27\%$

The difference exceeds the acceptable value(± 5%), so different ingredient masses need to be chosen from the design chart (Figure 4.15) beginning with the cementitious materials ($\frac{cm}{\eta}$).

For $\eta_{\text{mix}} = 10\text{Pa s}$,

$\frac{cm}{\eta}$ = 34 (bottom curve) $\longrightarrow$ *cm* = 10 × 34 = 340kg/m^3;

c = 0.75 × 340 = 255kg/m^3, ggbs = 0.25 × 340 = 85kg/m^3 ;

As *w/cm* = 0.53 $\longrightarrow$ *w* = 0.53 × 340 = 180.2*l*/m^3

$\frac{(cm+LP)}{\eta}$ = 44 (second curve from bottom) $\longrightarrow$ *LP* = 440 – 340 = 100kg/m^3

$\frac{(cm+LP+FA)}{\eta}$ = 119 (second curve from top) $\longrightarrow$ *FA* =1190– 340–100= 750kg/m^3

$\frac{(cm+LP+FA+CA)}{\eta}$ = 208 (top curve) $\longrightarrow$ *CA* = 2080 – 340 – 100 – 750 = 890kg/m^3

Total volume $= \frac{c}{\rho_c} + \frac{ggbs}{\rho_{ggbs}} + \frac{w}{\rho_W} + \frac{SP}{\rho_{SP}} + \frac{LP}{\rho_{LP}} + \frac{FA}{\rho_{FA}} + \frac{CA}{\rho_{CA}} + 0.02 = 0.966\text{m}^3$

The volume must be scaled to 1.0, so the ingredient amounts will be:

cm = 340 / 0.966 = 352kg/m^3

w = 180.2 / 0.966 = 186.5kg/m^3

SP = 2.0 / 0.966 = 2.1kg/m^3

LP= 100 / 0.966 = 103.5kg/m^3

FA = 750 / 0.966 = 776kg/m^3

CA = 890 / 0.966 = 921kg/m^3

$$\text{Total Volume} = \frac{c}{\rho_c} + \frac{ggbs}{\rho_{ggbs}} + \frac{w}{\rho_W} + \frac{SP}{\rho_{SP}} + \frac{LP}{\rho_{LP}} + \frac{FA}{\rho_{FA}} + \frac{CA}{\rho_{CA}} + 0.02 = 1 \text{ m}^3.$$

$\eta_{mix} =$ 10.53Pa s from Eq. 4.6.

$$\text{Viscosity diff.} = \frac{(\text{calculated } \eta_{mix} - \text{target } \eta_{mix})}{\text{target } \eta_{mix}} \times 100 = \frac{(10.53 - 10)}{10} \times 100 = + 5\%$$

This is within the acceptable difference, so the mix design is complete.

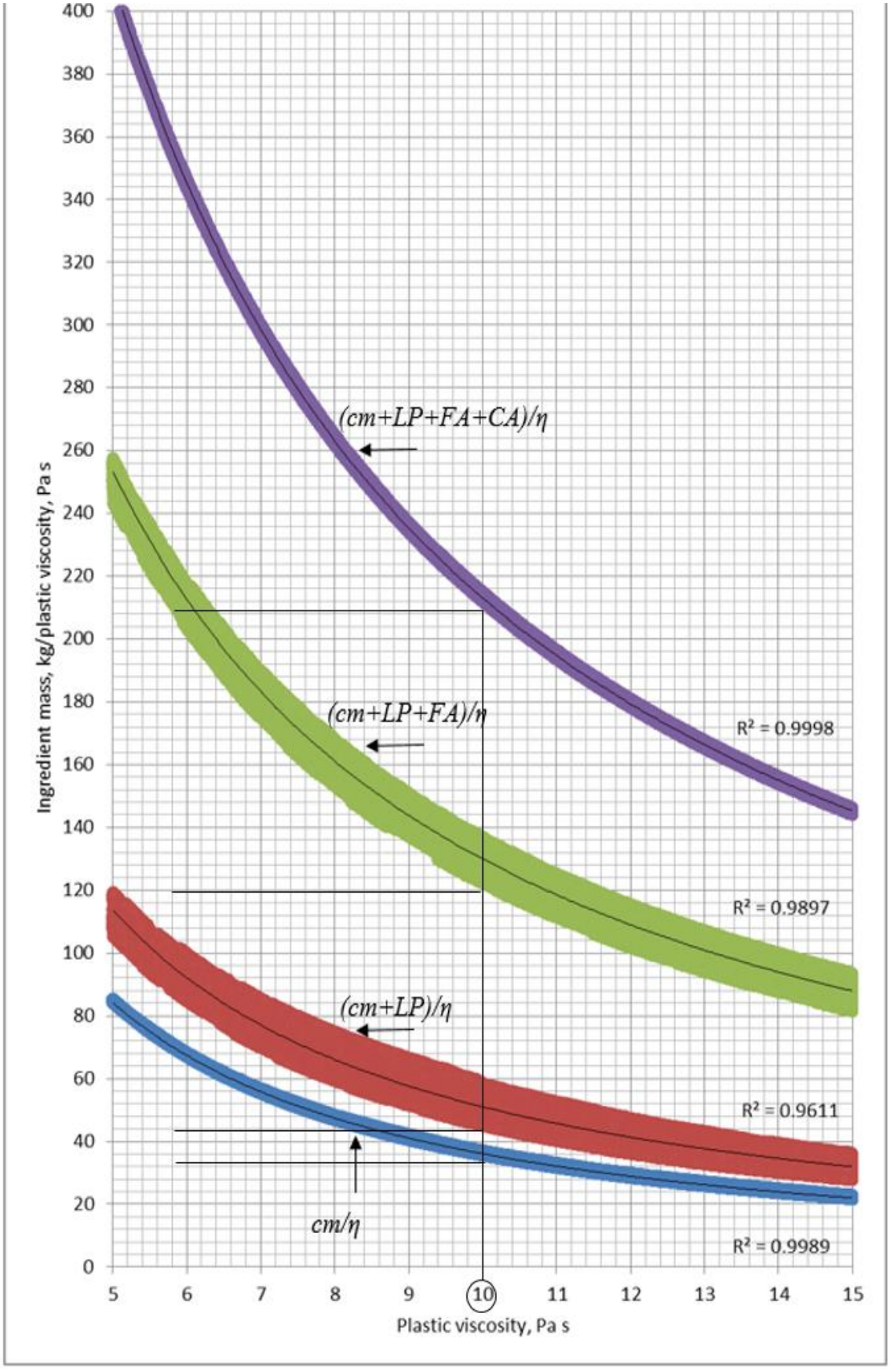

Figure 4. 15 Example for designing 50MPa mix with 10Pa s plastic viscosity

4.9 Examples for 60MPa

The next example deals with the design of an SCC mix with a target cube compressive strength of 60MPa. In this example, we choose the starting ingredient amounts at the lower limits of scatter in the design chart (Figure 4.16).

1. Suppose the desired target plastic viscosity of mix is 10Pa s;

2. For the desired target strength = 60MPa $\longrightarrow$ *w/cm* = 0.47 (Eq. 4.1);

3. Calculate the cementitious material content (*cm*);

For η_{mix} = 10Pa s;

$\frac{cm}{\eta}$ = 38 (bottom curve) $\longrightarrow$ *cm*= 38 ×10 = 380kg/m^3;

c = 0.75 × 380 = 285kg/m^3, ggbs = 0.25 × 380 = 95kg/m^3 ;

As *w/cm* = 0.47 $\longrightarrow$ *w* = 0.47 × 380 = 178.6 *l*/m^3

4. Assume a trial super-plasticiser dosage (SP) as a per cent of mass of cementitious materials (say 0.65%) which equals to 2.5 kg/m^3 ;

5. The plastic viscosity of the paste according to its *w/cm* and *SP/cm* ratios is equal to 0.29 (Table 4.3);

6. Calculate the solid phase ingredient contents (*LP, FA and CA*);

For η_{mix} = 10Pa s;

$\frac{(cm+LP)}{\eta}$ = 48 (second curve from bottom)

(*cm* + *LP*) = 48 × 10= 480kg/m^3 $\longrightarrow$ *LP* = 480 – 380= 100kg/m^3

$\frac{(cm+LP+FA)}{\eta}$ = 121 (second curve from top)

(*cm* + *LP* + *FA*) = 121×10 = 1210kg/m^3 $\longrightarrow$ *FA* = 1210 – 380 – 100=730kg/m^3

$\frac{(cm+LP+FA+CA\ )}{\eta}$ = 210 (top curve)

(*cm*+*LP*+*FA*+*CA*) = 210 × 10 = 2100kg/m^3 → *CA*=2100–380–100–730=890kg/m^3

7. Calculate the total volume of the mix;

Total volume = $\frac{285}{2950}+\frac{95}{2400}+\frac{178.6}{1000}+\frac{2.5}{1070}+\frac{100}{2400}+\frac{730}{2650}+\frac{890}{2800}+0.02=0.972\text{m}^3$

Owing to the total mix volume not being equal to 1.0 m^3, it must be scaled to 1.0, so the ingredients amounts will be:

cm = 380 / 0.972 = 391kg/m^3

w = 178.6 / 0.972 = 183.8kg/m^3

SP = 2.5 / 0.972= 2.60kg/m^3

LP = 100 / 0.972 = 103kg/m^3

FA = 730 / 0.972 = 751kg/m^3

CA = 890 / 0.972 = 917kg/m^3

$$\text{Total volume} = \frac{391\times0.75}{2950} + \frac{391\times0.25}{2400} + \frac{183.8}{1000} + \frac{2.6}{1070} + \frac{103}{2400} + \frac{751}{2650} + \frac{917}{2800} + 0.02 = 1.0\text{m}^3$$

8. Check the plastic viscosity using Eq. 4.6;

$$\eta_{mix} = 0.29 \times \left(1 - \frac{0.110}{0.524}\right)^{-1.9} \times \left(1 - \frac{0.421}{0.63}\right)^{-1.9} \times \left(1 - \frac{0.327}{0.74}\right)^{-1.9} = 11.3\text{Pa s}$$

$$\text{Viscosity diff.} = \frac{(\text{calculated } \eta_{mix} - \text{target } \eta_{mix})}{\text{target } \eta_{mix}} \times 100 = \frac{(11.3-10)}{10} \times 100 = +13\%$$

The difference exceeds the acceptable value (± 5%), so different ingredient masses need to be chosen from the design chart (Figure 4.16), beginning with the cementitious materials ($\frac{cm}{\eta}$).

For η_{mix} =10Pa s, choose

$\frac{cm}{\eta}$ = 39 (bottom curve) ⟶ *cm* = 39 × 10 = 390kg/m^3;

c = 0.75 × 390 = 292.5kg/m^3, ggbs = 0.25 × 390 = 97.5kg/m^3 ;

As *w/cm* = 0.47 ⟶ *w*= 0.47 × 390 = 183.3 *l*/m^3

$\frac{(cm+LP)}{\eta}$ = 48 (second curve from bottom) ⟶ *LP* = 480 – 390 = 90kg/m^3

$\frac{(cm+LP+FA)}{\eta}$ = 121 (second curve from top) ⟶ *FA* =1210–390– 90=730kg/m^3

$\frac{(cm+LP+FA+CA)}{\eta}$ = 210 (top curve) ⟶ *CA*= 2100 – 390 – 90 – 730= 890kg/m^3

$$\text{Total volume} = \frac{c}{\rho_c} + \frac{ggbs}{\rho_{ggbs}} + \frac{w}{\rho_W} + \frac{SP}{\rho_{SP}} + \frac{LP}{\rho_{LP}} + \frac{FA}{\rho_{FA}} + \frac{CA}{\rho_{CA}} + 0.02 = 0.976\text{m}^3$$

The volume must be scaled to 1.0, so the ingredient amounts will be:

cm = 390 / 0.976 = 400kg/m^3

w = 183.3 / 0.976 = 187.8kg/m^3

SP = 2.5 / 0.976 = 2.60kg/m^3

LP = 90 / 0.976 = 92kg/m^3

FA = 730 / 0.976 = 748kg/m^3

CA = 890 / 0.976 = 912kg/m^3

$$\text{Total Volume} = \frac{c}{\rho_c} + \frac{ggbs}{\rho_{ggbs}} + \frac{w}{\rho_W} + \frac{SP}{\rho_{SP}} + \frac{LP}{\rho_{LP}} + \frac{FA}{\rho_{FA}} + \frac{CA}{\rho_{CA}} + 0.02 = 1\text{m}^3$$

η_{mix}=10.37 Pa s from Eq. 4.6.

$$\text{Viscosity diff.} = \frac{(\text{calculated } \eta_{mix} - \text{target } \eta_{mix})}{\text{target } \eta_{mix}} \times 100 = \frac{(10.37-10)}{10} \times 100 = +3.7\%$$

This is within the acceptable difference, so the mix design is complete.

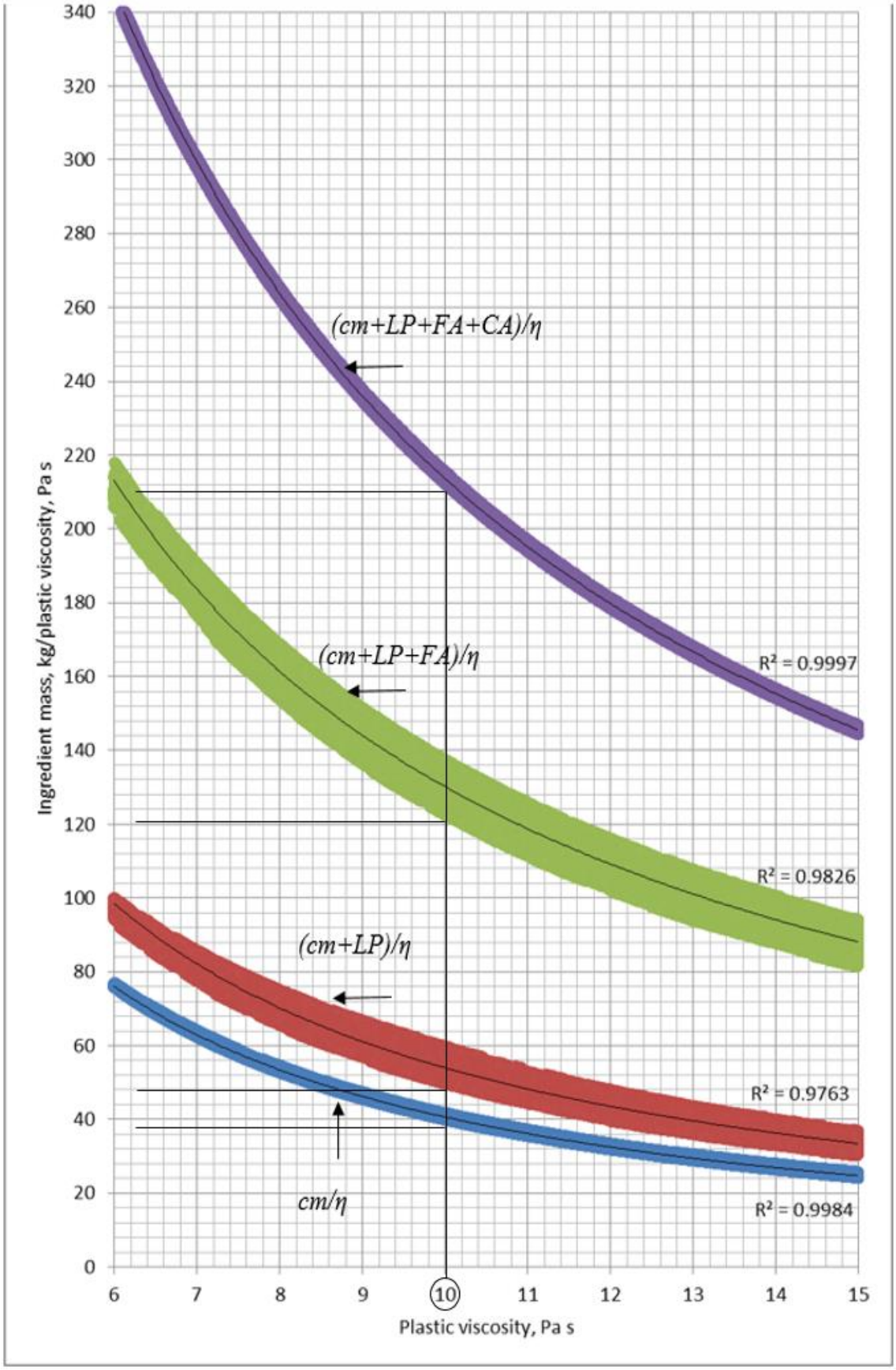

Figure 4. 16 Example for designing 60MPa mix with 10Pa s plastic viscosity

4.10 Concluding remarks

The methods for proportioning self-compacting concrete (SCC) mixes have not kept pace with their production techniques. A method for proportioning normal and high strength SCC mixes on the rheological characteristics represented by plastic viscosity has been proposed by Karihaloo and Ghanbari (2012) and been extended by Deeb and Karihaloo (2013). It exploits the expression for the plastic viscosity of an SCC mix developed by Ghanbari and Karihaloo (2009) using micromechanical principles. Although such method is rigorous and based on sound physical principles, it produces a bewildering array of mixes that reach the target plastic viscosity but does not give any practical guidelines on how to choose the most appropriate mix. Moreover, the method was developed on the basis of reference mixes of a range of known cube compressive strength, but the latter was not explicitly imposed as a design criterion.

All the above shortcomings have been overcome herein. Practical guidelines in the form of design charts have been provided for choosing the mix proportions that achieve the target plastic viscosity in the range 3 to 15Pa s and the target cube compressive strength in the range 30 to 80MPa. Several examples on the use of the design charts have been given. The developed mix proportioning has the advantage of being simple and efficient as evidenced by the examples. The procedure and design charts can also be used when the mix ingredients have different densities (apart from type II cement) because the plastic viscosity depends only on the volume fractions (Eq. 4.6). In order to design a mix whose target compressive strength is different from those of design charts in Figures 4.7-4.12, for example, a mix with target compressive strength 55MPa, the values of ingredient masses can be interpolated from charts for mixes with target compressive strengths 50 and 60MPa (Figure 4.9 and Figure 4.10).

Experimental validation of the mix design procedure will be provided in the next Chapter, on a series of SCC mixes with different volumes of paste to solid ratio in both fresh and hardened states.

Chapter 5

Proportioning of SCC mixes:

Experimental validation

5.1 Introduction

The mix design method for SCC based on the desired target plastic viscosity and compressive strength of the mix was described in Chapter 4. Design charts were provided as a guide for mix proportioning. The target plastic viscosity of these mixes varied between 3 to 15Pa s and the characteristic cube strength between 30 and 80MPa at 28 days age.

In this Chapter, an experimental validation of this mix design procedure is provided on a series of SCC mixes in both the fresh and hardened states. In order to verify and evaluate this proposed SCC mix design, three sets of SCC mixes have been prepared using the design charts jointly with other two PhD students (Abo Dhaheer, 2016; Al-Rubaye, 2016). These mixes are designated with A, B, and C for low, medium and high p/s ratios, respectively. (Note that mixes designated A and C were contributed by the other two PhD students mentioned above). All these mixes were extensively tested in the fresh state using the slump flow, J-ring, L-box and V-funnel apparatus (BS EN 206-9, 2010; EFNARC, 2005). These tests proved conclusively the validity of the mix proportioning method in the sense that all the mixes satisfied the self-compacting criteria and achieved the desired target plastic viscosity and compressive strength. The contents of this Chapter have been published as a journal paper in 'Sustainable Cement-Based Materials' (see publications list in Chapter 1).

5.2 Materials

The materials used in this study for preparing the SSC mix and the test specimens were as follows.

5.2.1 Cement

The cement used was ordinary Portland cement (CEM II/B-V 32.5R) supplied locally and manufactured to comply with the requirements of BS EN 197-1, 2011 with a specific gravity of 2.95. The cement was stored in the laboratory under airtight conditions to minimise its deterioration with time. Cement is made up of many compounds, which hydrate to form hardened cement paste. The main compounds of

the cement are tricalcium silicate (C_3S), dicalcium silicate (C_2S), tricalcium aluminate (C_3A), and tetracalcium aluminoferrite (C_4AF).

5.2.2 Ground granulated blast furnace slag (ggbs)

Ground granulated blast furnace slag is obtained by quenching molten iron slag (a by-product of iron and steel making) from a blast furnace in water or steam, to produce a granular product that is then dried and ground into a fine powder. The chemical composition of a slag varies considerably depending on the composition of the raw materials in the iron production process. This material exhibits pozzolanic properties. The main components of ggbs are CaO (30-50%), SiO_2 (28-38%), Al_2O_3 (8-24%), and MgO (1-18%). In general, increasing the CaO content in the slag results in an increase in compressive strength. Ground granulated blast-furnace slag is employed to make durable concrete structures in combination with ordinary Portland cement and/or other pozzolanic materials. Locally available ggbs has a specific gravity of 2.40.

5.2.3 Super-plasticisers

Super-plasticisers, also known as high range water reducers, are chemical admixtures used where well-dispersed particle suspension is required. These polymers are used as dispersants to avoid particle segregation (coarse and fine aggregates) and to improve the flow characteristics of suspensions such as in concrete applications. Their addition to concrete or mortar allows the reduction of the water to cement ratio and enables the production of self-compacting concrete and high-performance concrete. Throughout the experimental studies reported here on SSC concretes, the polycarboxylate ether-based super-plasticiser (PCE) type with a specific gravity of 1.07 was used. It is a synthetic brown liquid, and it is instantly dispersible in water. Polycarboxylate or GLENIUM ACE 499 complies with EN 934-2 with a relatively low dosage (up to 0.8% by cementitious material weight) it allows a water reduction up to 40%, due to its chemical structure, which enables good particle dispersion.

5.2.4 Filler

Limestone powder (*LP*) as a filler with maximum particle size of 125μm was used (specific gravity 2.40). A part of the river sand was replaced by an equivalent volume of the coarser fraction of limestone filler in size range of 125μm-2mm.

5.2.5 Fine aggregate

River sand having a specific gravity of 2.65 supplied locally and confirmed to BS 882 (1983) was used throughout the whole experimental work. The material was thoroughly dried prior to mixing. The sieve analysis results were performed in the laboratory with a maximum size 2mm.

5.2.6 Coarse aggregate

Crushed limestone coarse aggregate with a maximum size of 20mm and a specific gravity of 2.80 was used. It was obtained from a local quarry, and it conformed to BS 882 (1983).

5.3 Mix proportions

The verification of the proposed SCC mix design method using the design charts was carried out by testing many mixes of differing cube compressive strength. Six different mixes of strength 30, 40, 50, 60, 70, and 80MPa and different target plastic viscosity were prepared and subjected to the slump flow, J–ring, L–box and V–funnel tests in the fresh state to ensure that they met the flow and passing ability criteria without segregation. Standard cubes (100mm) were then cast, cured in water and tested for compressive strength at 7, 28 and 90 days of age. The amounts and details of the ingredients used in the test mixes are given in Tables 5.1-5.2. These were chosen using the design charts and the procedure described in the previous Chapter.

Table 5. 1 Mix proportions of test SCC mixes, kg/m^3

Mix designation	*cm* [a]		*w*	*SP* [b]	*w/cm*	*SP/cm*	*LP* [c]	*FA* [d]		*CA* [e]
	cement	ggbs						*FA***	*FA* ***	
30B	240	80	201.6	1.6	0.63	0.50	156	234	530	840
40B	262.5	87.5	199.5	[1.7]1.5	0.57	0.49	147	221	532	840
50B(50B)	281.2	93.8	198.8	[2.1]1.8	0.53	0.56	139	209(0)	530(760)	840
60B	315	105	197.5	2.4	0.47	0.57	125	188	528	840
70B	345	115	184	2.8	0.40	0.61	123	185	531	840
80B	367.5	122.5	171.5	3.0	0.35	0.61	125	188	529	840

a: Cementitious materials.

b: SP figures in square brackets refer to increase in SP needed for satisfying passing ability.

c: Limestone powder ≤125μm.

*d: Fine aggregate ≤2*mm *(Note: a part of the fine aggregate is the coarser fraction of the limestone powder, FA***125μm-2*mm*, whereas FA *** refers to natural river sand ≤2mm).*

e: Coarse aggregate ≤20mm.

Table 5. 2 Further details of test SCC mixes

Mix designation	Target plastic viscosity Pa s	Actual plastic viscosity Pa s	Paste volume fraction	Solid volume fraction	Paste/solid (by vol.)
30B	5.0	4.85	0.40	0.60	0.67
40B	7.0	7.11	0.41	0.59	0.69
50B(50B)	8.0(8.0)	8.13(8.13)	0.41	0.59	0.69
60B	9.0	8.58	0.42	0.58	0.72
70B	10.0	9.80	0.42	0.58	0.72
80B	11.0	11.02	0.42	0.58	0.72

As mentioned above, a part of the river sand was replaced by an equivalent volume of the coarser fraction of limestone filler in size range 125μm-2mm. However, tests were also done on three mixes of strength 50MPa (shown in parenthesis in Tables 5.1-5.2) in which no replacement of the river sand fine aggregate was made in order to check whether this replacement made any difference to the flow characteristics of the SCC mix in the fresh state or its compressive strength in the hardened state.

5.4 Experimental program flowchart

The flowchart of the experimental program is shown in Figure 5.1.

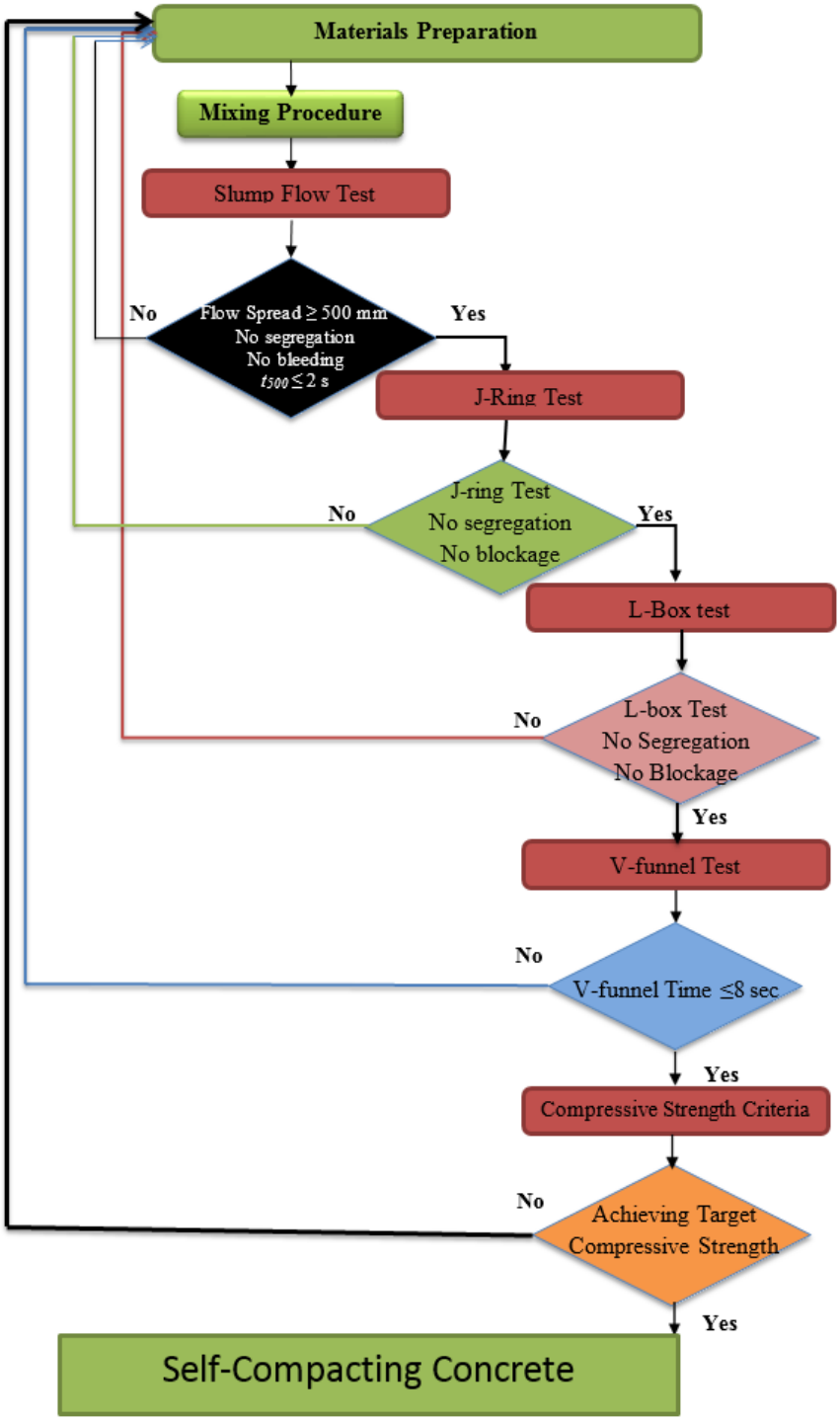

Figure 5. 1 Experimental program flowchart

5.5 Mix preparation

The mixes were prepared in a small planetary mixer by mixing the coarsest constituent (coarse aggregate up to 20mm) and the finest one (ggbs), followed by the next coarsest (fine aggregate) and next finest constituent (limestone powder), and so on. Before each addition, the dry constituents were mixed for 2mins. To fluidise the dry mix, two-thirds of the super-plasticiser (*SP*) was added to the water. One-half of this water-*SP* mixture was added to the dry constituents and was mixed for 2mins. One-half of the remaining water-*SP* mixture then was added and was mixed for two minutes. This process was continued until all water-*SP* mixture was added. The remaining one-third of the *SP* was added and was mixed for 2mins just before transferring the SCC mix into the slump cone. The horizontal spread up to 500mm was timed. If any segregation or bleeding was visible, the *SP* dosage was judiciously altered. This trial process was continued until the mix met the flow-ability criterion (BS EN 206-9, 2010) and was homogeneous with no visible segregation or bleeding. In this manner, all self-compacting mixes of different strength concrete mixes were developed. The binder refers to cement and ggbs.

5.6 Tests on fresh SCC

In the fresh state, the tests including slump flow, J-ring flow (blocking ring), L-box and V-funnel time were carried out in sequence. The average time spent on completing each test was up to 15mins by four people.

5.6.1 Flow-ability

The slump flow and the V-funnel tests were conducted to determine the t_{500} and $t_{v-funnel}$ times of the fresh SCC mixes. The time taken by the fresh SCC mix to reach a 500mm diameter spread in the slump flow (t_{500}) was determined from time sequencing a video recording of the test with an accuracy of a thousand of a second. While the time taken by the fresh SCC mix to flow out of the funnel (daylight appearing when viewed from above, Figure 5.2) was recorded as discharge time ($t_{v\text{-}funnel}$). The results are summarised in Table 5.3. Within the chosen flow spread range of 650-750mm, the t_{500} and $t_{v\text{-}funnel}$ varied between 0.88-2.06 s and 2.45-6.10s respectively.

Table 5. 3 Flow-ability test results, t_{500} and $t_{v\text{-}funnel}$ of SCC mixes

Mix designation	Slump flow test		V-funnel test
	Spread	t_{500}	$t_{v-funnel}$
	mm	s	s
30B	665	0.88	2.45
40B	675	1.13	3.10
50B(50B)	680(700)	1.23(1.21)	3.60(3.74)
60B	650	1.32	4.05
70B	750	1.45	4.95
80B	750	2.06	6.10

Figure 5. 2 Recording V-funnel time (daylight appearing when viewed from above)

Figures 5.3-5.6 show the horizontal spread of different SCC mixes. All tested self-compacting mixes showed no signs of segregation or bleeding on thorough visual inspection.

Figure 5. 3 Horizontal spread of SCC Mix 30MPa

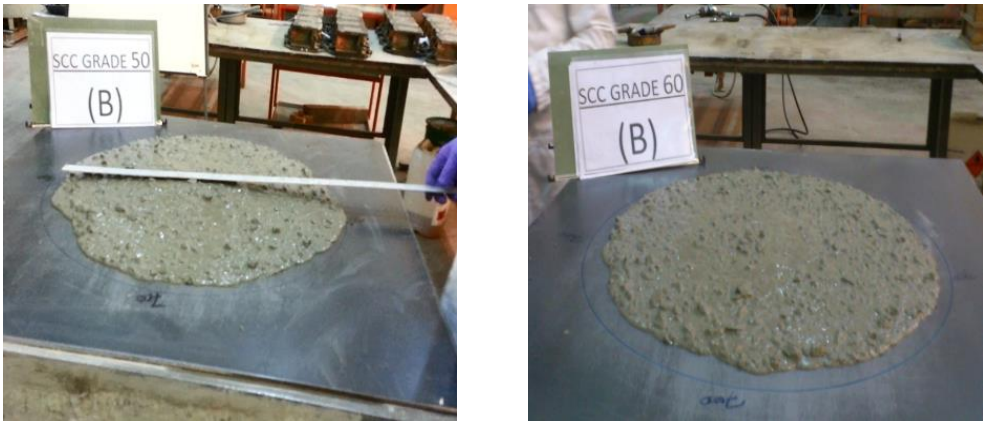

Figure 5. 4 Measurements of the spread

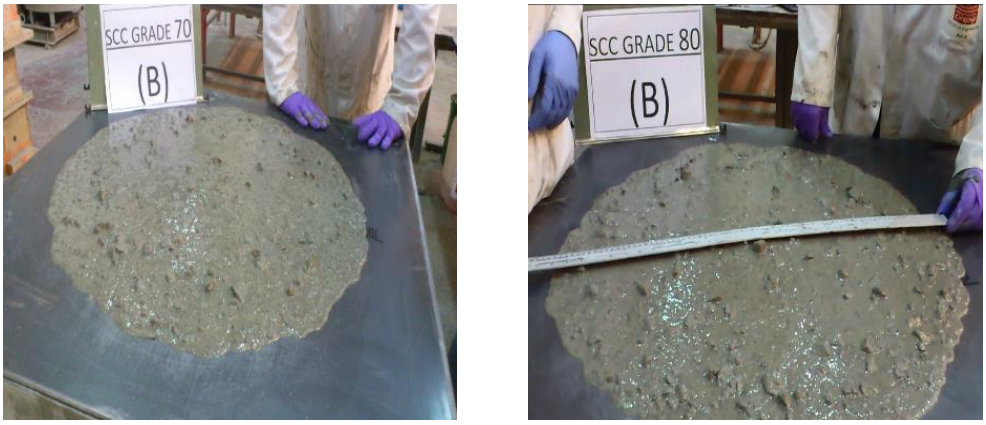

Figure 5. 5 Check the segregation visually (left) Check the spread diameters(right)

Figure 5. 6 Horizontal spread of SCC mix (Natural fine aggregate replacements by coarser limestone filler)

A comparison of the flow tests on 50MPa mixes in which a part of the river sand fine aggregate was replaced by the coarser fraction of limestone filler with the same grade mixes but without the replacement is shown in parenthesis in Tables 5.1-5.3. These tables indicate that the flow characteristics of the mixes are not significantly affected by this substitution. This is consistent with the small differences in the particle size distributions of the coarser fraction of limestone filler, and river sand is similar (Figure 5.7). Moreover, as the volume fractions (not the masses) of the fine aggregate (with or without replacement) in the mixes are the same (see Tables 5.1-5.2), their plastic viscosity will be the same (see Eq. 4.6 in the previous Chapter).

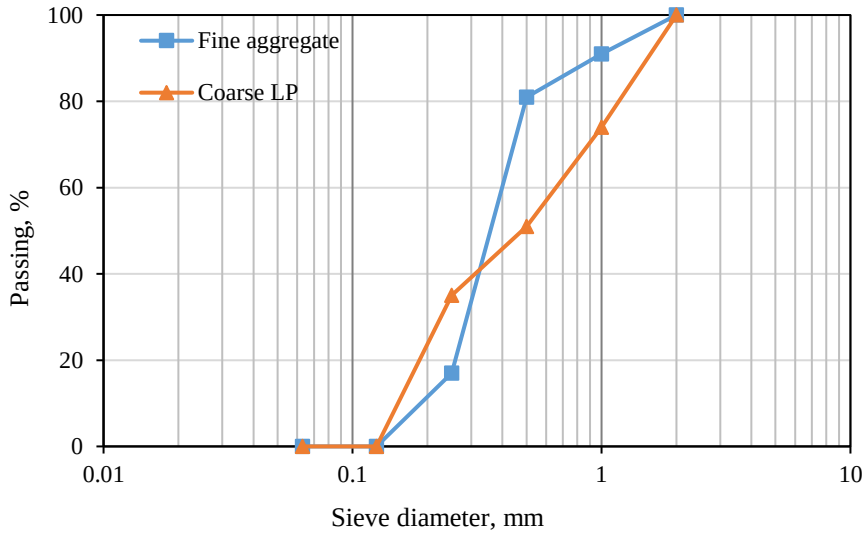

Figure 5. 7 Particle size distribution curves for coarser fraction of limestone filler and natural fine aggregate

Figure 5.8 shows a plot of the slump flow time of all SCC mixes and the corresponding water to powder (i.e. cement + ggbs + limestone powder ≤125μm) ratio (*w/p*). It can be seen that a larger t_{500} requires a higher powder or lower water content. The *w/p* ratio has a considerable influence on both the fresh and hardened properties of SCC, with often its impact on the fresh properties limiting the selection of its value (Domone, 2006). It has been reported that a decrease in the water content and an increase in the amount of fine particles can increase cohesion and viscosity of the mix (Felekoğlu et al., 2007), resulting in a proper distribution of the solid particles throughout the casting of SCC. However, mixes with low water content require relatively high dosages of super-plasticiser, especially at low cementitious materials contents, to achieve the accepted requirements of SCC deformability (Khayat et al., 1999a).

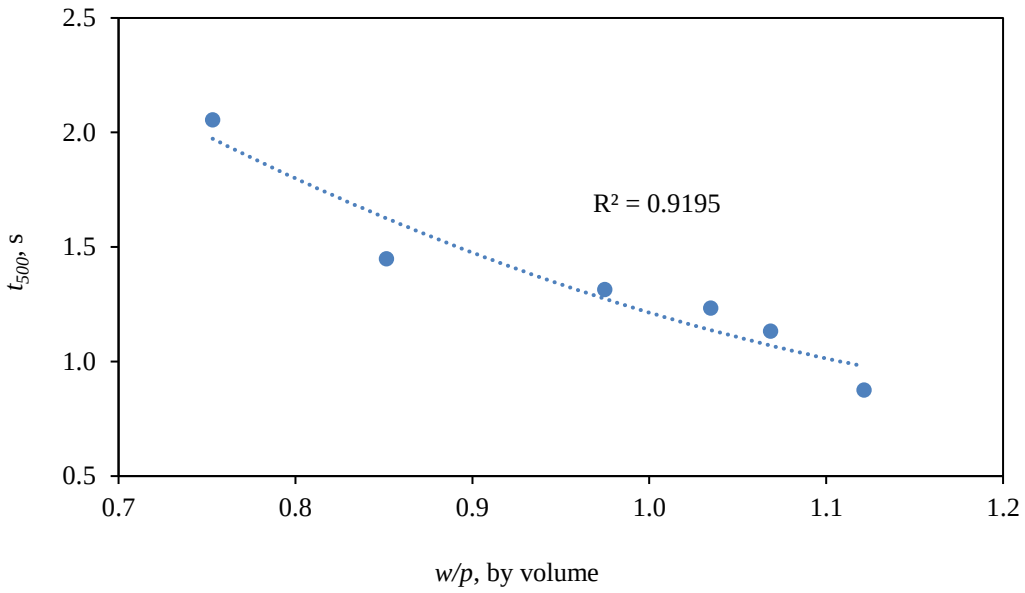

Figure 5. 8 Relationship between flow time (t_{500}) and water to powder ratio

The time needed to reach 500mm diameter spread is related to the plastic viscosity of the mix. This is clearly seen in Figure 5.9 for a given target flow spread. It should also be mentioned that the yield stress is well correlated with the slump flow spread (Koehler and Fowler, 2007; Wallevick, 2003; Tanigawa and Mori, 1989). That is why the target flow spread of our mixes have been determined within the range of 700±50mm. It is implied that these mixes have nearly the same yield stress and thus makes the plastic viscosity as the controlling parameter, which we have correlated with

t_{500} in Figure 5.10. The following statement from Koehler and Fowler (2007) supports this implicit assumption ‘‘the plastic viscosity is often the main factor distinguishing the workability of one mix from another. Changes in plastic viscosity can directly reflect changes in materials or mixture proportions, making the t_{500} measurement particularly valuable for quality control’’. Of course, a different choice of target flow spread, say from the EFNARC guidelines (2005) will necessarily require different t_{500}.

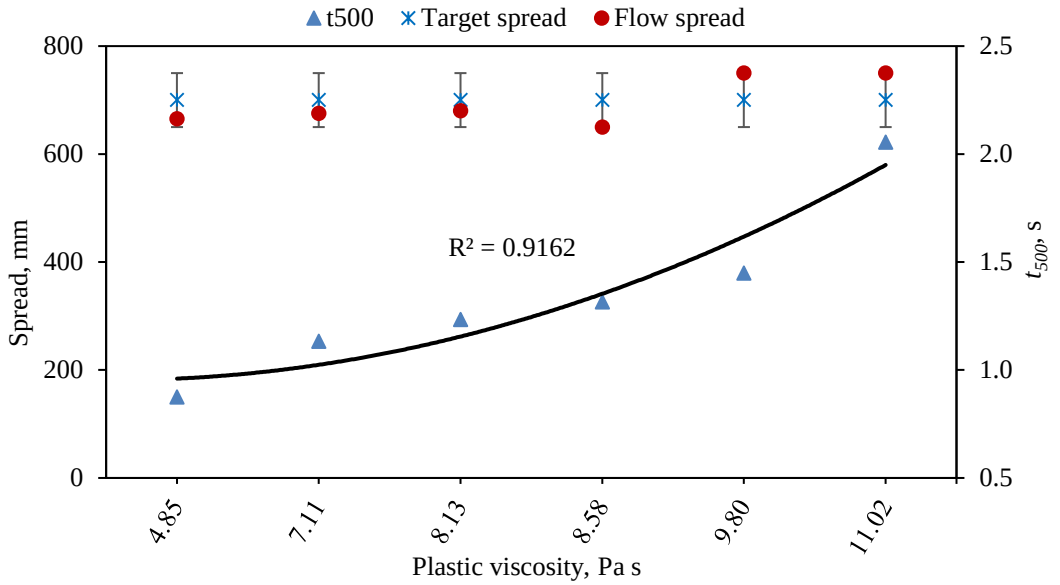

Figure 5. 9 Relationship between plastic viscosity and t_{500} for target flow spread 700 ± 50mm

The plastic viscosity has also been plotted against $t_{v-funnel}$ and flow spread as well in Figure 5.10. It can be seen that the $t_{v-funnel}$ of mixes having the flow spread in the range of 700±50mm increases with an increase in the mix plastic viscosity, despite an increase in the *SP* dosage. In other words, the flow time is dominated by the plastic viscosity rather than the super-plasticiser dosage. This has also been observed by Nepomuceno et al. (2012) and Takada and Tangtermsirikul (2000).

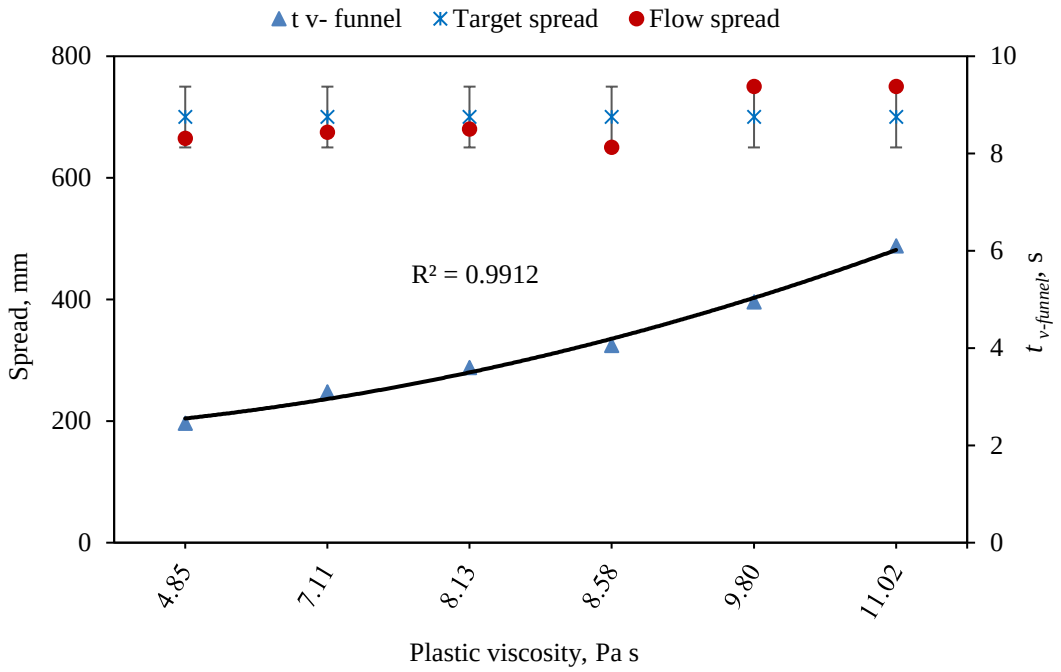

Figure 5. 10 Relationship between plastic viscosity and $t_{v-funnel}$ time with a target flow spread (700±50mm)

5.6.2 Passing and filling ability

All the above test mixes that satisfied the flow-ability criterion and showed no signs of segregation were subjected to the passing and filling ability test using the J-ring and L-box to ensure that they were able to pass through the narrow gaps that exist between reinforcing bars in real reinforced concrete structural elements. For this purpose, a 300mm diameter J-ring apparatus with ten steel rods (each of diameter 16 mm and 100mm height) was used, as recommended by EFNARC (2005).

The results are presented in Table 5.4. There were a few mixes (especially those with a low flow spread, i.e. low dosage of *SP*) that had passed the flow-ability test but did not meet the passing ability criterion. In such instances, the *SP* dosage had to be increased (shown in square brackets in Table 5.1). The results indicated that (after the increase in *SP*) all mixes met the passing ability criterion and showed no blockage or signs of segregation (Figures 5.11-5.13). Again, the influence of the replacement of some river sand fine aggregate by the coarser fraction of limestone filler on the flow characteristics was minimal, as can be judged by comparing the entries for 50MPa mixes within and without the parenthesis in Table 5.4.

Table 5. 4 Passing ability test results, J-ring and L-box

Mix designation	J-ring flow test		L-box test		
	Spread, mm	t_{500j}, s	t_{200}, s	t_{400}, s	H_2/H_1
30B	635	1.04	0.57	1.11	0.84
40B	670	1.20	0.63	1.23	0.91
50B(50B)	650(665)	1.43(1.38)	0.73(0.69)	1.37(1.41)	0.93(0.90)
60B	645	1.43	0.81	1.72	0.84
70B	720	2.09	1.15	2.49	0.95
80B	730	2.70	1.62	3.20	0.90

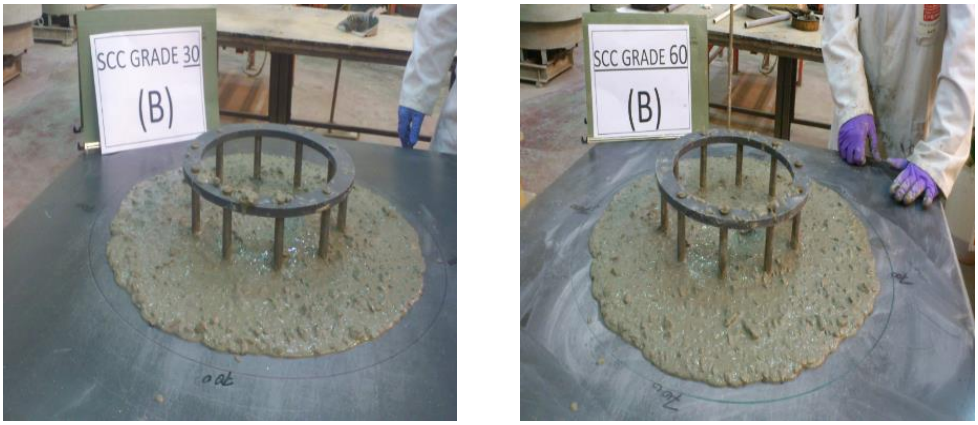

Figure 5. 11 Flowing and passing ability of SCC mix (30B-left, 60B-right)

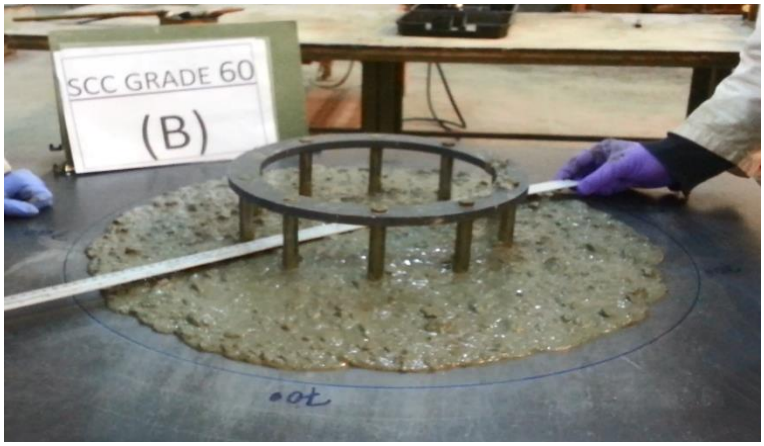

Figure 5. 12 Spread measurement of SCC mix

Figure 5. 13 Top-view of the passing ability (J-ring test)

Figure 5.14 shows that t_{500j} time correlates well with the plastic viscosity for all the mixes.

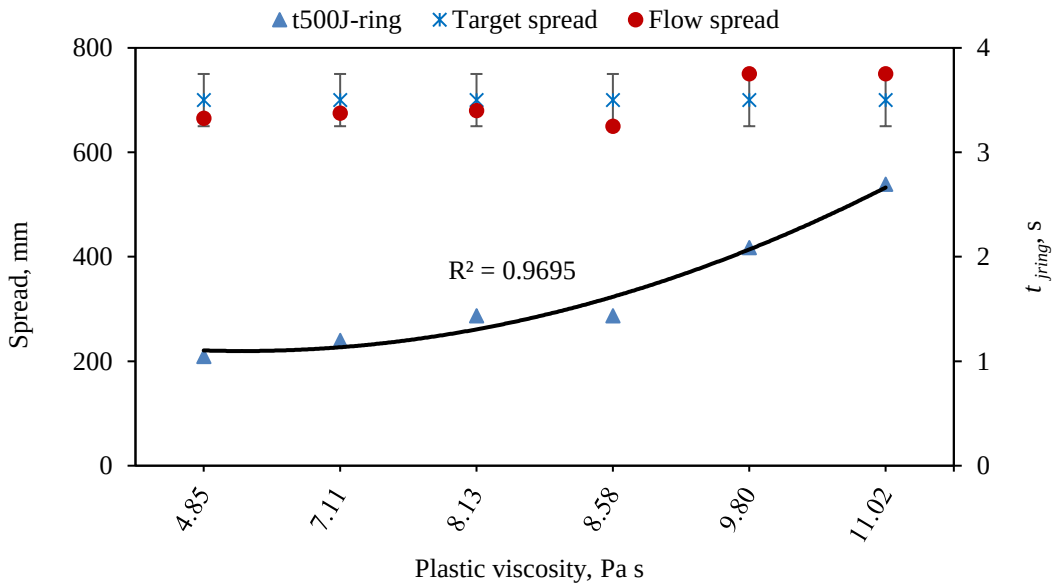

Figure 5. 14 t_{500J} time versus plastic viscosity

The relationship between the parameters t_{500} of J-ring and slump flow of SCC was also taken into consideration in this study. The best-fit curve of t_{500} against the plastic viscosity is plotted graphically alongside with the t_{500J} as indicated in Figure 5.15. It was found that the difference between these times is more pronounced in the higher plastic viscosities (9-12Pa s) than the lower ones. A possible explanation for this

increase is that the mixes become sticky (i.e. high viscosity) taking more time to pass through the obstacles of the J-ring.

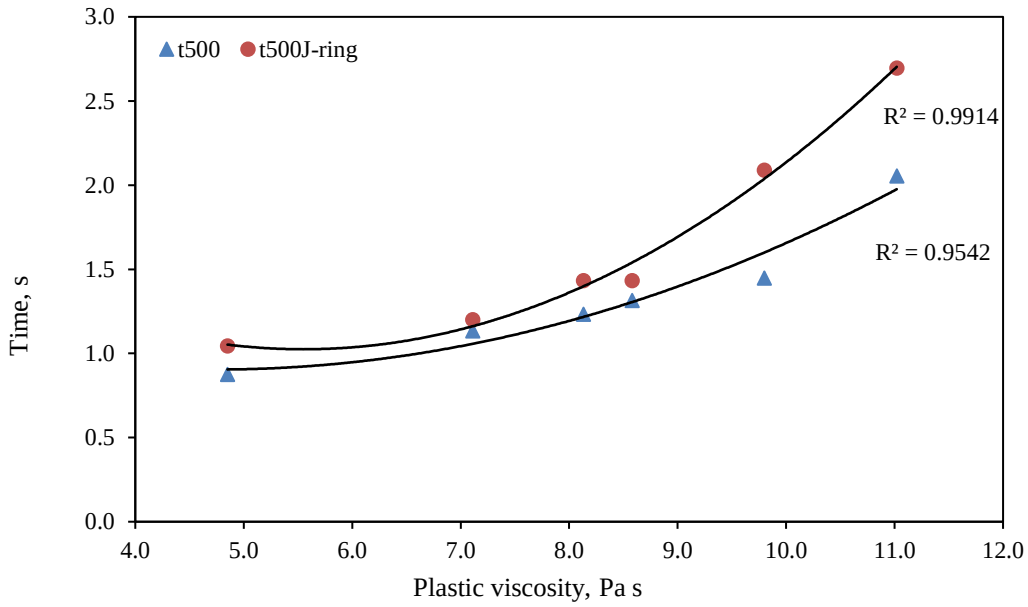

Figure 5. 15 Plastic viscosity versus t_{500} and t_{500J}

According to the ASTM C1621/C1621M (2008), the J-ring test can be used in combination with the slump flow test to assess the passing ability of SCC. If the difference between spread diameters (D_{flow}-$D_{J\text{-}ring}$) of the two tests is less than 25mm, then there is no visible blockage. If it is between 25 and 50mm, then there is minimal to noticeable blockage. Table 5.5 shows the differences from which it is clear that for all mixes there is minimal or no blockage.

Table 5. 5 Difference between flow and J-ring spread diameter

Mix designation	D_{flow} mm	$D_{J\text{-}ring}$ mm	D_{flow}-$D_{J\text{-}ring}$ mm
30B	665	635	30
40B	675	670	5
50B(50B)	680(700)	650(665)	30(35)
60B	650	645	5
70B	750	720	30
80B	750	730	20

In order to test the ability of an SCC mix to fill the formwork containing reinforcement under its own weight, the L-box apparatus with two adjustable steel rods (each of diameter 12mm) was used (BS EN 206-9 2010; EFNARC, 2005).

The times for the mix to reach 200mm (t_{200}) and 400mm (t_{400}) from the vertical leg, as well as the blockage ratio (H2/H1), were recorded. All mixes that had passed the J-ring test also passed the L-box test without any alteration in *SP* or mix ingredients (Figures 5.16-5.17).

Figure 5. 16 Passing and filling of SCC Mix 30MPa (left) and 50MPa (right)

Figure 5. 17 Measurements of the blocking ratio (BR)

Figure 5.18 shows that t_{200} and t_{400} times correlate well with the plastic viscosity for all the mixes. The results also revealed that no large aggregate particles had segregated or been blocked by the rods. In addition, it can be seen (Table 5.4) that the mixes exhibited a blockage ratio (BR) of more than 0.80, which reflects good filling ability. Therefore, from the flow and passing ability perspectives, all the test SCC mixes satisfied the required criteria for viscosity class 1 to qualify them as SCC in accordance with BS EN 206-9 (2010).

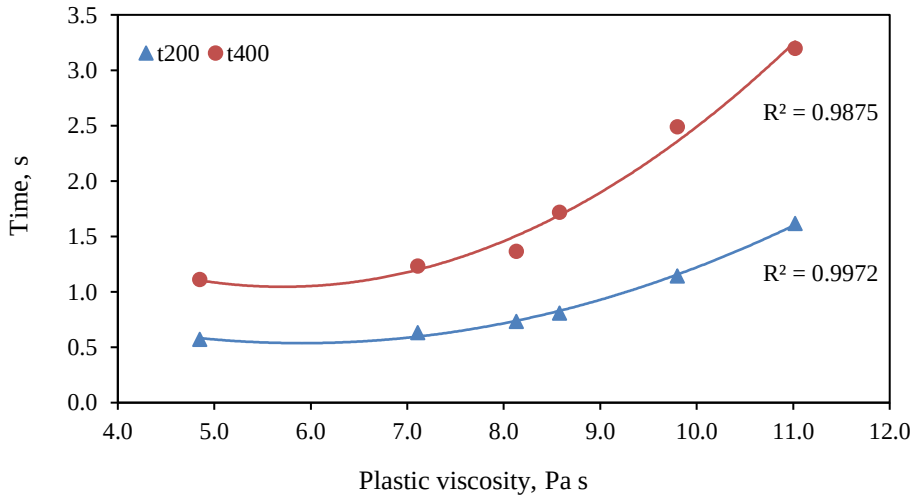

Figure 5.18 t_{200} and t_{400} times in L-box vs plastic viscosity

5.7 Testing of hardened SCC

The accuracy of the proposed design method has been validated through compressive strength tests performed on 100mm cube specimens (three per mix and age), cured in water at ambient temperature. The test was carried out at 7, 28 and 90 days of age. The results are presented in Table 5.6 and Figure 5.19. The results confirmed the popular trends against the *w/cm* ratio and upheld the reliability of the proposed mix design approach. The effect of the replacement of a part of the river sand fine aggregate by the coarser fraction of limestone powder is minimal also in the hardened state, as can be judged by the entries in the parenthesis in Table 5.6.

Table 5. 6 Cube compressive strength test results for SCC mixes

Mix designation	Compressive strength, MPa		
	7 days	28 days	90 days
30B	21.6	35.3	44.3
40B	31.2	43.8	52.9
50B(50B)	35.0	54.5(52.3)	61.1
60B	44.7	60.8	73.1
70B	48.9	77.9	91.6
80B	60.0	83.0	94.8

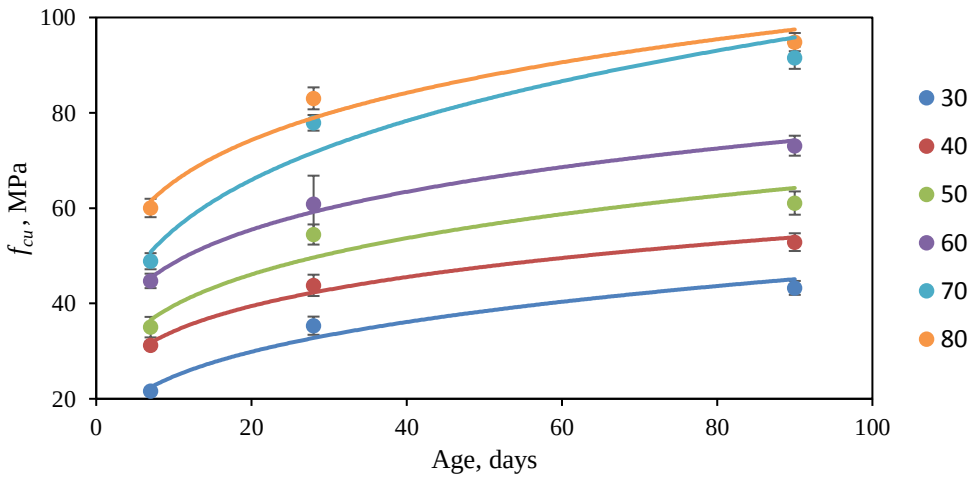

Figure 5. 19 Gain of compressive strength with age

5.8 Concluding remarks

Several mixes proportioned with the method proposed in the previous Chapter were prepared in the laboratory and found to meet the necessary self-compacting criteria and the target compressive strength. The method is simple and shows it is full validity on a series of mixes differing by the paste to solids volumetric ratios. It may be necessary to increase the *SP* content in order to meet the passing and filling ability tests, but the content will still be in the range 0.4-0.8% of the mass of cementitious materials. It is worth emphasising that the plastic viscosity of the paste remain practically unaltered in this range; the *SP* content mostly affects the yield stress of the paste.

The coarser fraction of limestone filler (125μm-2mm) can be used to replace an equivalent volume of river sand fine aggregate. Tests have shown that this replacement makes practically no difference to the properties of SCC in fresh and hardened tests. Such a replacement is environmentally friendly and economical, thus enhancing the sustainability of the SCC mixes. The proposed mix proportioning method reduces considerably the extent of laboratory work, the testing time and the materials used. The next Chapter will examine the role of the composition variations of SCC on its fracture behaviour.

The target strength is almost always exceeded because of the higher p/s ratio. The increase in the compressive strength of 70B and 80B mixes at 28 and 90 days is because they contain a higher amount of ggbs.

Chapter 6

Influence of mix composition and strength on the fracture properties of SCC

6.1 Introduction

It is generally known that plain and reinforced concrete structures contain inherent flaws, such as water-filled pores, air voids, micro-cracks due to shrinkage and low tensile strength, etc. even prior to load application. These defects, and especially the small cracks (micro-cracks), grow stably under external loading; coalesce with existing or newly formed micro-cracks until the large fracture is formed, which cause the collapse of the structure. These structures are designed without regard to either the propagation of large cracking zones through them or an energy failure criterion. Fracture mechanics provides an energy based failure theory that could be used in designing cement-based structures against the consequences of crack initiation and propagation (Karihaloo, 1995). The growth of any crack requires the consumption of a certain energy that represents the surface energy of the material. Hence, the propagation of cracks under loading can have a significant effect on the behaviour of the concrete structure. Therefore, an energy failure criterion is needed for the design of concrete structures.

6.2 Fracture behaviour parameters

Specific fracture energy and the tension-softening diagram of a concrete mix are the most important parameters describing its fracture behaviour. They form a basis for the evaluation of the load carrying capacity of cracked concrete structures (Karihaloo, 1995; Bažant and Planas, 1997).

6.2.1 Specific fracture energy

According to RILEM recommendations (1985), the specific fracture energy (or toughness) can be obtained by the work-of-fracture method requiring tests on notched three-point bend specimens of different sizes and notch to depth ratios. It is, however, widely recognised (Abdalla and Karihaloo, 2003; Bažant, 1996; Bažant and Kazemi, 1991; Carpinteri and Chiaia, 1996; Hu and Wittmann, 1992; Mindess, 1984; Nallathambi et al., 1985) that the specific fracture energy of concrete obtained using the RILEM method is dependent on the size of the test specimen and the notch to depth ratio. To eliminate this size dependency, Guinea and co-workers (Guinea et al., 1992;

Planas et al., 1992; Guinea et al., 1994) and Hu and Wittmann (2000) proposed methods to correct the measured size-dependent specific fracture energy (G_f) in order to obtain a size-independent value (G_F). The methodology proposed by Guinea and co-workers involves adding the non-measured work-of-fracture due to the curtailment of the tail of the load-central deflection (P-δ) curve recorded in the three-point bend test. On the other hand, the methodology of Hu and Wittmann (2000) is based on the observation that the local specific energy along the initially un-cracked specimen ligament varies during the crack propagation. The variation is becoming more pronounced as the crack approaches the stress-free back face of the specimen, the so-called free boundary effect.

Abdalla and Karihaloo (2003) and Karihaloo et al. (2003) simplified the free boundary effect formalism of Hu and Wittmann (2000). They proposed and validated extensively a simplified method by which the size-independent fracture energy can be determined by testing only geometrically identical specimens of the same size, half of which contain a shallow starter notch (notch to depth ratio = 0.1), while the other half contain a deep notch (notch to depth ratio = 0.6). Their method significantly reduces the number of specimens to be tested and eliminates the need for using the least squares method to solve an overdetermined system of simultaneous equations, as required in the Hu and Wittmann (2000) method.

6.2.2 Tension softening diagram (TSD)

Besides the size-independent fracture energy (G_F), the analysis of cracked concrete structures using the non-linear fictitious crack model (Hillerborg et al., 1976) requires the tension softening diagram ($\sigma(w)$) of the concrete mix relating the residual stress transfer capability (σ) to the opening displacement (w) of the fictitious crack faces. As the determination of the tension softening diagram using the direct tension test is not a simple task (Karihaloo, 1995), it is often approximated by a bilinear relationship whose parameters are determined in an inverse manner by matching the experimental load-displacement curve of a notched three-point bend beam. For this, an analytical model based on the concept of a non-linear hinge was proposed by Ulfkjaer et al. (1995) and Olesen (2001). In this model, the flexural response of a notched beam is obtained by allowing the fictitious crack to develop from the pre-existing notch in the

central region of the beam where the bending moment is the largest. The width of this region, proportional to the beam depth, fixes the width of the non-linear hinge. Outside of this region, the material is assumed to behave in a linear elastic manner. Abdalla and Karihaloo (2004), and Murthy et al. (2013b) showed how the non-linear hinge model could be adapted to construct the bilinear tension softening diagram of a concrete mix corresponding to its size-independent specific fracture energy.

6.3 Fracture behaviour of SCC

The fracture behaviour of concrete is significantly influenced by the properties of the interfacial transition zone (ITZ) (Akçaoğlu et al., 2004), which in turn are governed by the mix ingredients in normally vibrated concrete (NVC) and self-compacting concrete (SCC) as well. In comparison with NVC, SCC requires relatively high amounts of fine particles and paste, but low coarse aggregate content (Okamura and Ouchi, 2003; Okamura et al., 2000; Edamatsu and Nishida, 1998; Su et al., 2001). Although SCC has passed from the research phase into a real application, the differences in its composition from NVC raise concerns about its fracture behaviour (Beygi et al., 2014a; Domone, 2006). The concern is primarily because a lower coarse aggregate content in an SCC mix relative to an NVC mix of the same grade is likely to reduce its energy absorption capacity and thus its ductility. This needs to be addressed. Previous work (Beygi et al., 2014b; Beygi et al., 2014c; Nikbin et al., 2014; Beygi et al., 2013b; Cifuentes and Karihaloo, 2013; Rozière et al., 2007) on this topic was based on the size-dependent specific fracture energy, apart from the work of Cifuentes and Karihaloo (2013) who used the model of Hu and Wittmann (2000) and its simplified version proposed by Karihaloo et al. (2003). It is the aim of this Chapter to investigate in detail the role of several composition parameters of SCC mixes in their fracture behaviour. In particular, the influence of coarse aggregate volume, paste to solids (p/s) ratios, and water to binder (*w/cm*) ratios on the size-independent fracture energy (G_F) will be studied. First, the size-dependent fracture energy (G_f) has been determined using the RILEM work-of-fracture test on three point bend specimens of a single size, half of which contained a shallow starter notch (notch to depth ratio = 0.1), while the other half contained a deep notch (notch to depth ratio = 0.6). Then, the specific size-independent fracture energy (G_F) was calculated using the simplified

boundary effect approach (SBE) suggested by Abdalla and Karihaloo (2003) and validated by Karihaloo et al. (2003) in which the variation in the fracture energy along the unbroken specimen ligament is approximated by a bilinear diagram. The corresponding bilinear approximation of the tension softening diagram will then be obtained using the procedure based on the non-linear hinge model proposed by Abdalla and Karihaloo (2004), and Murthy et al. (2013a). In view of the many variables involved, the author joined forces with two other PhD students (Abo Dhaheer, 2016; Al-Rubaye, 2016) to perform a detailed investigation covering all variables in the limited time available. The content of this Chapter has been published in 'Construction and Building Materials' as a journal paper (see publications list in Chapter 1).

6.4 Theoretical background

The specific fracture energy (G_f), as defined by RILEM technical committee, is the average energy given by dividing the total work-of-fracture by the projected fracture area (i.e. cross-section of initially un-cracked ligament) based on the load-displacement *P*-δ curve. Hence, for a specimen of depth *W*, thickness *B* and initial notch depth *a* (as schematically shown in Figure 6.1) the specific fracture energy (G_f) can be expressed as:

$$G_f = \frac{1}{(W-a)B}\int P d\delta \qquad (6.1)$$

The specimen weight can be neglected for the small specimens used in this study.

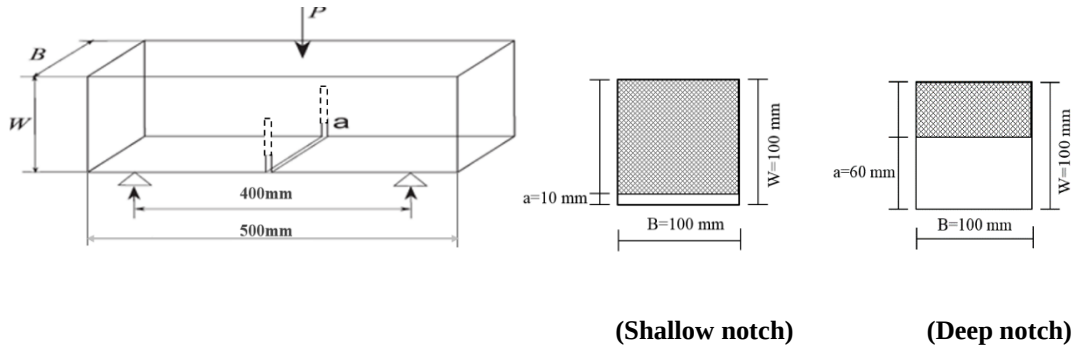

Figure 6. 1 Schematic representation of the three-point bending test

The specific fracture energy (G_f) can also be determined using a local energy (g_f) concept described by Duan et al. (Duan et al., 2003; Duan et al., 2007) as follows (see Figure 6.2):

$$G_f\left(\frac{a}{W}\right) = \frac{1}{W-a}\int_0^{W-a} g_f(x)dx \qquad (6.\ 2)$$

Hu and Wittman (2000) proposed a bilinear approximation for the local fracture energy variation (g_f) along the crack path (Figure 6.2) with the intersection of the two asymptotes defining a transition ligament size (a_l). The latter, unlike the asymptotic value of specific fracture energy (G_F), varies with the material properties and specimen geometry.

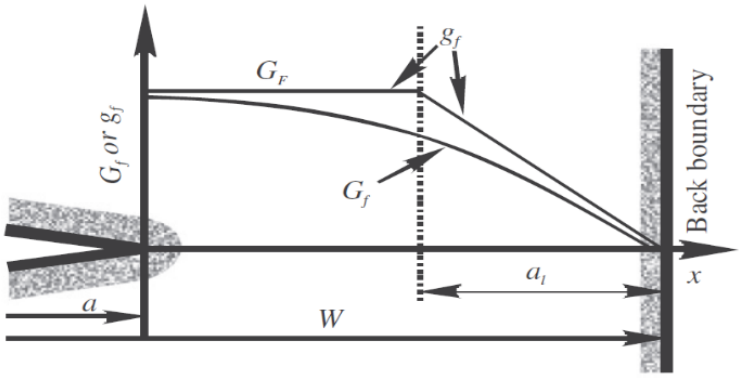

Figure 6. 2 Bilinear local fracture energy G_f(a/ W) variation along the un-notched ligament of a notched specimen (After Duan et al., 2003)

A relation between the measured size-dependent fracture energy (G_f), the transition length (a_l) and the size-independent fracture energy (G_F) can be obtained by substituting the bilinear approximation for the local fracture energy variation (Figure 6.2) into Eq. 6.2:

$$G_f\left(\frac{a}{W}\right) = \begin{cases} G_F\left[1 - \frac{\frac{a_l}{W}}{2\left(1-\frac{a}{W}\right)}\right] & 1 - \frac{a}{W} > \frac{a_l}{W} \\ G_F\left[\frac{\left(1-\frac{a}{W}\right)}{2\frac{a_l}{W}}\right] & 1 - \frac{a}{W} \leq \frac{a_l}{W} \end{cases} \qquad (6.\ 3)$$

The values of G_F and a_l of a concrete mix are obtained once the mean size-dependent specific fracture energy (G_f) of the mix has been measured on specimens of identical

sizes, half of which have a shallow starter notch ($a/W = 0.1$), while the other half have a deep starter notch ($a/W = 0.6$) by the RILEM work-of-fracture method using Eq. 6.1. Hu and Duan (2004) showed that although the measured values of G_f depend on W and a/W, the above procedure indeed leads to a G_F value that is essentially independent of the specimen size and relative notch depth.

In recent work, a trilinear approximation of the local fracture energy along the unbroken ligament was proposed by Muralidhara et al. (2010; 2011), and Karihaloo et al. (2013). As has been evidenced by acoustic emission data, the trilinear approximation is closer to how the local fracture energy varies as the crack grows from a notched specimen (Muralidhara et al., 2010). The local fracture energy (G_f) first rises from the fictitious boundary (notch tip), then remains nearly constant G_F before reducing again as the crack approaches both the stress-free back face boundary (Figure 6.3).

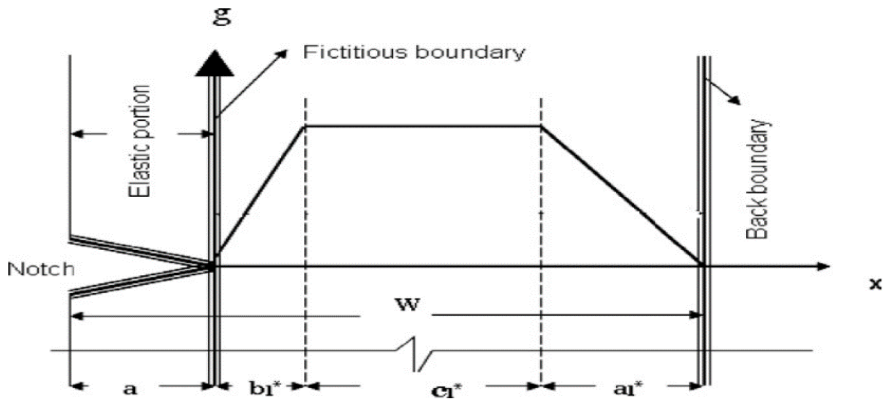

Figure 6. 3 Trilinear approximation of local fracture energy (g_f) variation over the un-notched ligament length (After Muralidhara et al., 2011)

The G_f and G_F relationship for the trilinear approximation is given in Eq. 6.4:

$$G_f\left(\frac{a}{W}\right) = \begin{cases} G_F\left[\dfrac{\frac{b_l^*}{W}}{2(1-\frac{a}{W})}\right] & 1-\dfrac{a}{W} \leq \dfrac{b_l^*}{W} \\ G_F\left[1-\dfrac{(\frac{a_l^*}{W}+\frac{b_l^*}{W})}{2(1-\frac{a}{W})}\right] & 1-\dfrac{a}{W} \geq \dfrac{a_l^*}{W} \end{cases} \quad (6.4)$$

To obtain the values of G_F, a_l^* and b_l^* of a concrete mix, the G_f of specimens of identical sizes and a range (more than three) of the notch to depth ratios is first determined by the RILEM method. Then, Eq. 6.4 is applied to the mean values of G_f different notch to depth ratios. This gives an over-determined system of equations which is solved by a least squares method to obtain the best estimation of G_F, a_l^* and b_l^*. It should be noted that the trilinear method proposed by Karihaloo et al. (2013) cannot be applied in the present study because the specimens have been tested with two notch to depth ratios only, as required by the bilinear model of Karihaloo et al. (2003). It is however known (Murthy et al., 2013b) that the bilinear and trilinear approximations give nearly the same values of the size-independent specific fracture energy (G_F).

6.5 Experimental program

6.5.1 Materials

These were described in Section 5.2.1 in the previous Chapter.

6.5.2 Mix design

A series of SCC mixes were designed according to the mix design method described in Chapter 4 having 28-day nominal cube compressive strengths of 30, 60 and 80MPa with *w/cm* ratios of 0.63, 0.47 and 0.35 respectively. The SCC mixes contained different volume fractions of coarse aggregate and pastes to solids ratios. They are designated B. They have been combined with mixes of low p/s, designated A, that were studied by Abo Dhaheer (2016) and with mixes of high p/s, designated C, that were studied by Al-Rubaye (2016) in order to get a complete picture of the role of low, medium and high p/s ratios. The compositions of all mixes are given in Table 6.1. In order to ensure that all mixes met the flow and passing ability criteria without segregation (SCC requirements), slump flow, J-ring, L-box and V-funnel tests were conducted (Table 6.2) according to EFNARC (2005).

Table 6. 1 Mix proportions of test SCC mixes, kg/m^3

Mix designation	*cm* [a]		*w*	*SP* [b]	*w/cm*	*SP/cm*	*LP* [c]	*FA* [d]		*CA* [e]	*p/s*
	cement	ggbs						*FA***	*FA****		*by vol.*
30A*	240	80	201.6	1.1	0.63	0.44	109	164	579	924	0.61
30B*	240	80	201.6	1.6	0.63	0.50	156	234	530	840	0.67
30C*	240	80	201.6	2.3	0.63	0.72	194	291	504	756	0.72
60A	315	105	197.5	2.0	0.47	0.48	94	141	536	924	0.69
60B	315	105	197.5	2.4	0.47	0.57	125	188	528	840	0.72
60C	315	105	197.5	2.8	0.47	0.67	172	258	477	756	0.79
80A	367.5	122.5	171.5	2.8	0.35	0.57	94	141	536	924	0.69
80B	367.5	122.5	171.5	3.0	0.35	0.61	125	188	529	840	0.72
80C	367.5	122.5	171.5	3.5	0.35	0.80	172	258	478	756	0.79

**A, B and C refer to the decrease in coarse aggregate (or the increase in paste volume for the same strength grade.*

a: cementitious material, i.e. binder.

b: super-plasticiser.

c: limestone powder≤125μm.

d: fine aggregate≤2mm (Note: a part of the fine aggregate is the coarser fraction of the limestone powder,

*FA**125μm-2mm, whereas FA *** refers to natural river sand≤2mm).*

e: coarse aggregate ≤20mm.

Table 6. 2 Flow and passing ability test results of SCC mixes

Mix designation	Slump flow		V-funnel	J-ring flow		L–box		
	Spread mm	t_{500} s	$t_{v-funnel}$ s	*Spread* mm	t_{500J} s	t_{200} s	t_{400} s	H_2/H_1
30A	685	0.50	2.30	665	0.60	0.47	1.08	0.91
30B	665	0.88	2.45	635	1.04	0.57	1.11	0.84
30C	655	0.81	2.76	650	0.74	0.53	1.10	0.92
60A	665	1.18	3.23	640	1.48	0.77	1.48	0.89
60B	650	1.32	4.05	645	1.43	0.81	1.72	0.84
60C	655	1.40	4.40	630	1.60	0.81	1.65	0.87
80A	730	1.92	5.67	705	2.43	1.45	3.10	0.93
80B	750	2.06	6.10	730	2.70	1.62	3.20	0.90
80C	670	2.09	7.44	655	2.80	1.45	3.07	0.91

6.5.3 Specimen preparation and test procedure

From each of the nine mixes (Table 6.1) 12 beam specimens (Figure 6.4), three cubes (100mm), and three cylinders (100×200mm) were cast. The specimens were de-moulded after one day and cured in water at ambient temperature for 28 days. The cube compressive strength was measured according to BS EN 12390-3 (2009). Six of the beams were notched to a depth of 10mm (notch to depth ratio $a/W = 0.1$) with a thin (2mm) diamond saw while the remaining six were notched to a depth of 60mm

(a/W = 0.6). The modulus of elasticity (E), and the split cylinder strength (f_{st}) were measured on cylinders according to BS EN 12390-6 and BS 1881-121 (2009;1983) respectively.

Figure 6. 4 Beam specimen used for TPB test

As schematically shown in Figure 6.1, the tests for the determination of the fracture energy were performed according to the RILEM work-of-fracture method (1985). The crack mouth opening displacement (CMOD) was used as the feedback control signal, and the load-point deflection was measured simultaneously by means of a linearly variable displacement transducer (LVDT). The tests were performed in a stiff Dartec closed-loop universal testing machine with a maximum load capacity of 250kN (see Figure 6.4).

During the test an X-Y plotter, as shown in Figure 6.5, recorded the load- displacement curves, and the data were also stored on a computer disk. The rate of loading was controlled by a crack mouth opening displacement (CMOD) control, and the beams were loaded at a very small CMOD rate (0.0002mm/s) so that a stable crack growth could be achieved.

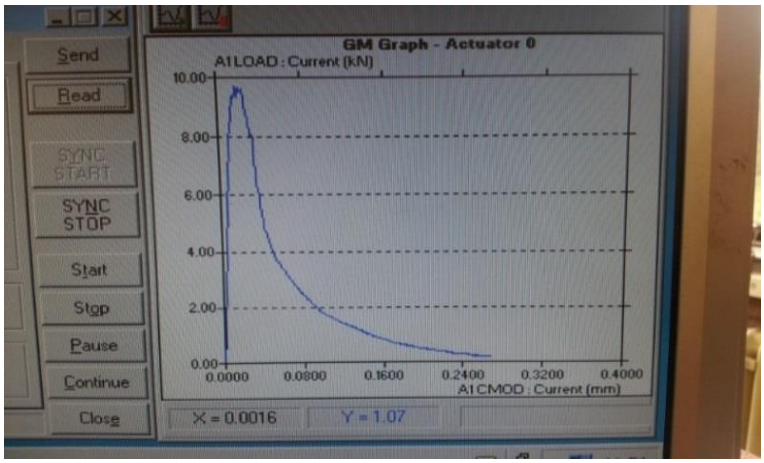

Figure 6. 5 X-Y plotters for the load-deflection curve

6.6 Results and discussion

Typical recorded load-deflection diagrams of three of the nine mixes are shown in Figure 6.6 (Appendixes C and D contain the load-deflection and load-CMOD curves of all specimens tested). The area under the load-deflection diagram was calculated from which the $G_f(a, W)$ was determined using Eq. 6.1. Table 6.3 shows the results of the measured fracture energy, $G_f(a, W)$, with an indication of the mean value, standard deviation and the coefficient of variation (COV %).

Table 6. 3 Measured fracture energy, G_f (a, W) for different SCC mixes from three-point bending test (TPB)

Mix designation	W mm	a/W	Mean [St. dev.] G_f (a, W), N/m	COV %
30A	100	0.1	96.20 [8.90]	9.20
		0.6	53.50 [5.00]	9.30
30B	100	0.1	85.90 [7.70]	9.00
		0.6	53.00 [4.00]	7.60
30C	100	0.1	73.40 [7.30]	10.0
		0.6	52.30 [4.30]	8.20
60A	100	0.1	108.6 [11.6]	10.7
		0.6	65.80 [1.70]	2.60
60B	100	0.1	91.90 [5.70]	6.20
		0.6	56.50 [5.00]	8.85
60C	100	0.1	83.90 [9.60]	11.4
		0.6	51.90 [3.20]	6.10
80A	100	0.1	105.5 [5.50]	5.30
		0.6	58.50 [5.70]	9.80
80B	100	0.1	100.1 [9.90]	9.90
		0.6	57.00 [4.90]	8.60
80C	100	0.1	97.60 [11.0]	11.3
		0.6	7.70 [2.50]	4.30

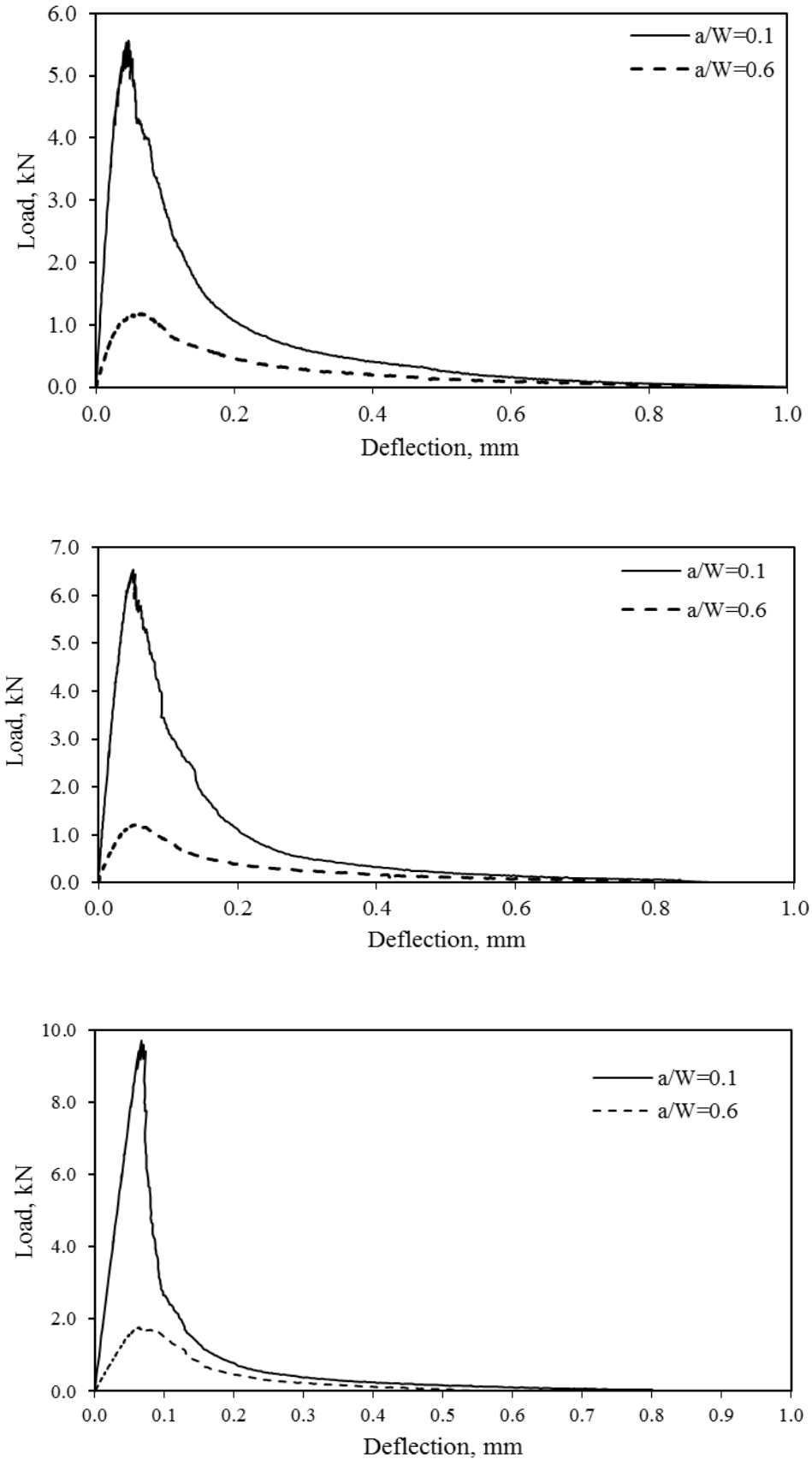

Figure 6. 6 Typical load-deflection diagrams of two notched beams from SCC mixes (30B (top), 60B (middle), and 80B (bottom))

The specific size-independent fracture energy (G_F) and the transition ligament length (a_l) of all mixes are determined from G_f (0.1) and G_f (0.6) of Table 6.3 using the first of the two equalities in Eq. 6.3. In many mixes, however, it transpired that the transition ligament length (a_l) so calculated violated the corresponding inequality for $a/W = 0.6$. In these cases, the first of the two equalities was used only for $a/W = 0.1$, while the second equality was used for the deeper notch $a/W = 0.6$ (A Matlab code has been provided in Appendix E that was used to find G_F and a_l). The resulting values of G_F and a_l are reported in Table 6.4 together with the cube compressive strength, split cylinder strength and modulus of elasticity, measured according to the relevant British standards.

Table 6. 4 Results of f_{cu}, f_{st}, E, G_F and a_l of test SCC mixes

Mix designation	f_{cu}, 28 days MPa	f_{st}, 28 days MPa	E, 28 days GPa	G_F GPa	a_l mm
30A	35.4	2.95	33.6	132.8	49.7
30B	37.0	3.04	32.7	112.3	42.4
30C	37.8	3.30	32.0	90.4	33.8
60A	60.5	3.40	36.7	143.2	43.6
60B	62.9	3.52	36.6	120.3	42.6
60C	65.2	3.65	34.5	109.7	42.3
80A	79.8	4.60	42.3	146.9	50.7
80B	81.6	5.00	40.8	136.5	47.9
80C	83.2	5.35	41.0	130.2	45.2

Within the range of coarse aggregate volume fraction (27-33%) investigated in this study, G_F increases with the increase of coarse aggregate fraction as is evident from Table 6.4 and Figure 6.7. This is due to the increase in the energy dissipation mechanisms (micro-cracking, crack branching, aggregate interlock) in much the same manner as in NVC (Karihaloo, 1995; Akcay et al., 2012; Prokopski and Langier, 2000). This observation is in agreement with previous research on SCC (Beygi et al., 2014c; Nikbin et al., 2014b). Moreover, it can be seen from Figure 6.7 that the increase in G_F with the coarse aggregate volume fraction is less pronounced in the high strength mix (grade 80) than in mix grades 30 and 60. This may be attributed to the fact that the ITZ (Beygi et al., 2014b) in grade 80 mixes is much denser and, therefore, more susceptible to cracking because it contains a higher proportion of cementitious materials as can be seen in Table 6.1.

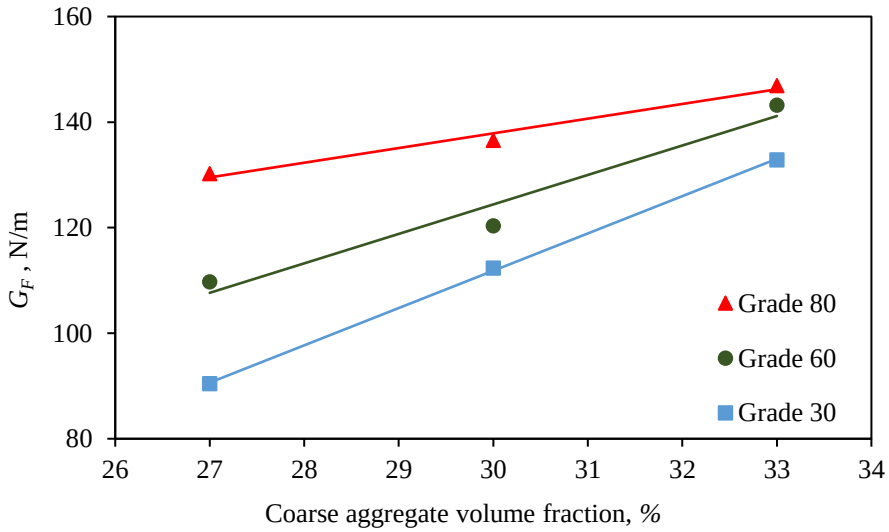

Figure 6. 7 Variation of G_F of SCC mixes of different grades with coarse aggregate volume fraction

An increase in the paste to solids (p/s) ratio in all mix grades, as expected, leads to a slight increase in the cube compressive strength (f_{cu}), but a noticeable decrease in G_F as shown in Figure 6.8.

Figure 6. 8 Variation of the G_F and f_{cu} with different p/s ratios

As expected, G_F decreases with increasing *w/cm* ratio in much the same manner as in NVC (Prokopski and Langier, 2000; Nallathambi et al., 1984) as shown in Figure 6.9. This result is consistent with the recent study on normal strength self-compacting concrete conducted by Beygi et al. (2013a) who found that fracture energy decreases by 38% as *w/cm* ratio is increased from 0.4 to 0.7. G_F of high strength self-compacting concrete (f_{cu} ~100MPa), on the other hand, has been reported by Cifuentes and Karihaloo (2013) to be just 90N/m for *w/cm* = 0.23. This is a consequence of the densification of ITZ as a result of using a relatively high volume fraction of micro-silica.

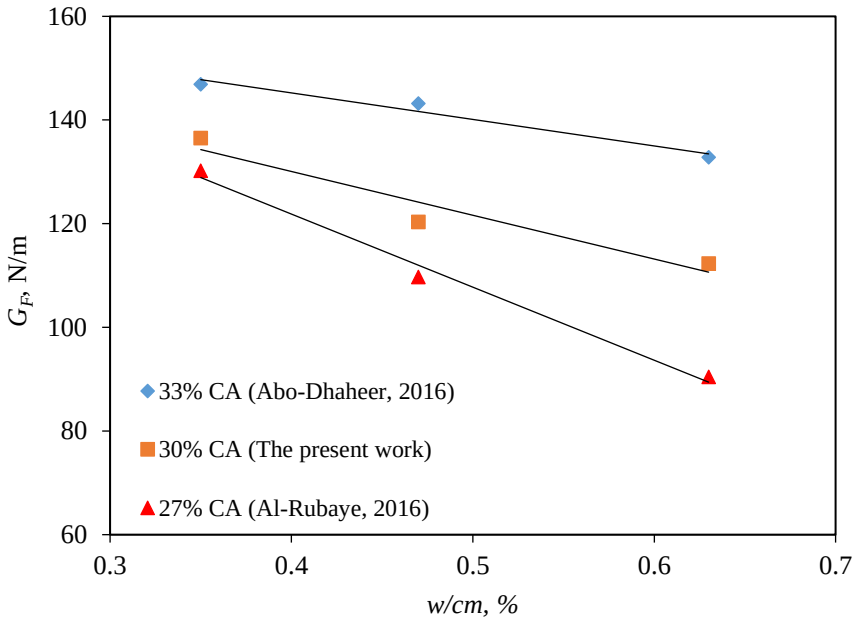

Figure 6. 9 Variation in G_F with *w/cm* ratio for different coarse aggregate (CA) volume fractions

6.7 Bilinear tension softening diagram

To complete the determination of the fracture properties of the SCC mixes, we now outline briefly an inverse procedure based on the non-linear hinge concept for identifying the parameters of the bilinear tension softening diagrams of the mixes corresponding to their size-independent values of the specific fracture energy (G_F). More details of the procedure may be found in (Abdalla and Karihaloo, 2004; Murthy et al., 2013b). It should be mentioned that the popularity of the bilinear approximation of the tension-softening diagram (Figure 6.10) stems from the fact that it captures the two major mechanisms responsible for the observed tension softening in a concrete mix, namely micro-cracking and frictional aggregate interlock. The initial linear branch of the bilinear diagram, which is steep, is a consequence of the micro-cracking, whereas the second linear branch, which is shallow, is a result of the frictional aggregate interlock.

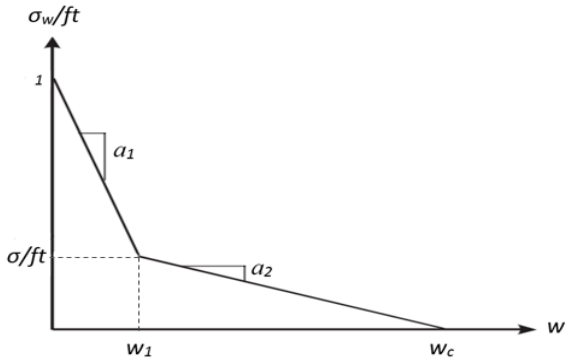

Figure 6. 10 Bilinear softening diagram

6.8 Hinge model

In the non-linear hinge model of a pre-notched beam, a part of the beam on either side of the notch is isolated as a short beam segment subjected to a bending moment and a normal force. The growth of the real crack and associated fictitious crack representing the fracture process zone is viewed as a local change in the overall stress and strain fields in this isolated beam segment. The constitutive relationship inside the hinge segment depends on the position of the fictitious crack along the depth of the beam. The axial load and bending moment are related to the hinge rotation in four phases depending on the crack propagation.

$$\sigma = \begin{cases} E\varepsilon & pre-cracked\ state \\ \sigma(w) = g(w)ft & cracked\ state \end{cases} \quad (6.\ 5)$$

where E is the modulus of elasticity; ε is the elastic strain; w is the width of opening crack; f_t is the uniaxial tensile strength; and $g(w)$ is a function representing the shape of the normalized stress-crack opening relationship, such that $g(0)$ =1. For the assumed bilinear shape (Figure 6.10), we have:

$$\sigma = b_i - a_i w = \begin{cases} b_1 - a_1 w & 0 \le w \le w_1 \\ b_2 - a_2 w & w_1 \le w \le w_c \end{cases} \quad (6.\ 6)$$

$$w_1 = \frac{1-b_2}{a_1-a_2} \qquad w_c = \frac{b_2}{a_2}$$

where $b_1 \equiv 1$; and the limits w_1 and w_c are given by the intersection of the two line segments, and the intersection of the second line segment with the abscissa, respectively (see Figure 6.10).

As the crack propagates from the bottom of the hinge, the stress distribution changes through three distinct phases (Figure 6.11). The crack-opening profile is divided into different intervals corresponding to various values of *i*. Besides y_0, these intervals are determined by the parameters y^*, y_1, and y_2

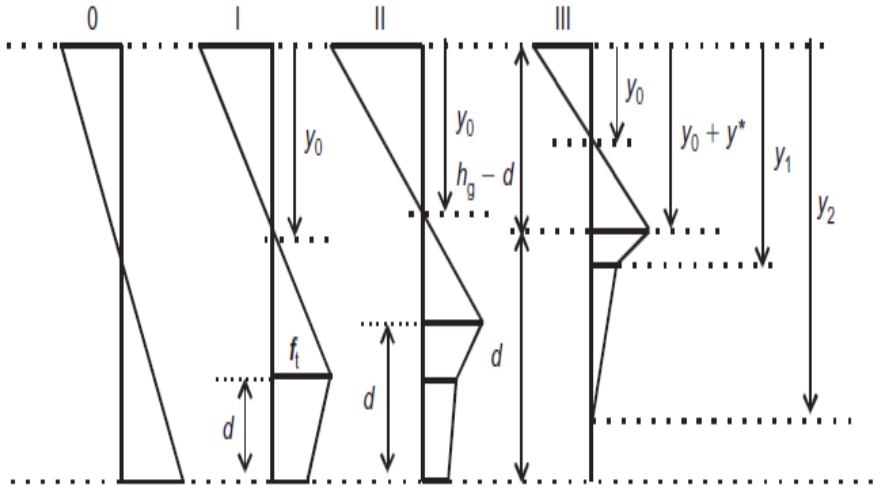

Figure 6. 11 Four phases of stress distribution inelastic layer of hinge (Phase 0=state of stresses prior to cracking; phases I–III=states of stresses during crack propagation) (After Olesen, 2001)

Analysis of the hinge element allows for the determination of the axial load (*N*) and bending moment (*M*) for any given hinge rotation (2φ) (see Figure 6.12). The problem now is solved in four stages, one for each phase of crack propagation. Phase 0 represents the elastic state when no fictitious crack has formed ahead of the pre-existing notch. Phases I, II and III represent different stages of crack propagation. In phase I, the fictitious crack of length (*d*) ahead of the notch is such that the maximum crack opening is less than w_1 corresponding to the knee in the bilinear diagram. In phase II, a part of the fictitious crack of length longer than (*d*) has a crack opening in excess of w_1, but in the remaining part, it is less than w_1. In phase III, a part of the fictitious crack has opened more than w_c and thus become traction-free, while the opening of the remaining part is still less than w_c or even w_1.

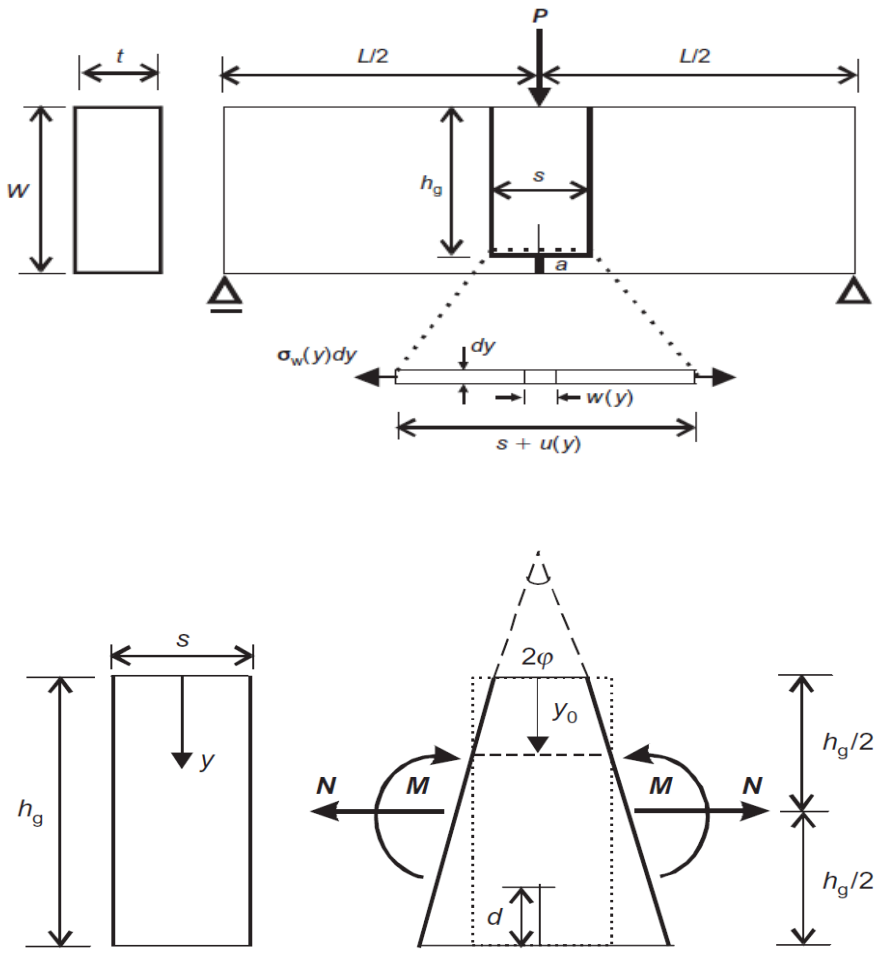

Figure 6. 12 Geometry, loading and deformation of cracked incremental horizontal strip of the hinge (After Olesen, 2001)

when the complete stress distribution is established for the non-linear hinge, a relation between the normal force (N) the normal moment (M) and the hinge rotation (φ) may be obtained in each phases of the crack propagation. The following normalized parameters are introduced:

$$\mu = \frac{6}{f_t h_g^2 t} M; \qquad \rho = \frac{1}{f_t h_g t} N; \qquad \theta = \frac{h_g E}{s f_t} \varphi; \qquad \alpha_h = \frac{d}{h_g}; \qquad (6.\ 7)$$

where t is the width of the hinge in the direction normal to the paper and d is the depth of the fictitious crack. Given these normalizations, the pre-pack elastic behaviour of the hinge is described by $\alpha_h = 0$ and $\mu = \theta$, where $0 \leq \theta < 1 - \rho$; at the onset of cracking $\theta = 1 - \rho$. For TPB specimens $\rho = 0$.

6.9 Application of hinge model to TPB

The crack mouth opening displacement (CMOD) in TPB specimens consists of three contributions. These are the opening due to the crack emanating from the starter crack (δ_{COD}) the opening due to the elastic deformation (δ_e) and the opening due to the geometric consideration because the line of application of the load is shifted relative to the mouth of the starter crack (δ_g)

$$CMOD = \delta_{COD} + \delta_e + \delta_g \tag{6. 8}$$

The δ_{COD} is the crack opening at the bottom of the hinge, i.e., at $y = h_g$ and could be determined from the following equation:

$$\delta_{COD} = \frac{sf_t(1-b_i+2\alpha_h\,\theta)}{E(1-\beta_i)} \tag{6. 9}$$

where β_i is defined as

$$\beta_i = \frac{sf_t a_i}{E} \tag{6. 10}$$

$$(b_i,\beta_i)=\begin{cases}(1,\beta_1) & \theta_{0-I} < \theta \le \theta_{I-II}\\ (b_2,\beta_2) & \theta_{I-II} < \theta \le \theta_{II-III}\\ (0,0) & \theta_{II-III} < \theta\end{cases} \tag{6. 11}$$

δ_e can be found from handbooks e.g. Tada et al.(1985) and is given by

$$\delta_e = \frac{4\sigma a}{E}\left(0.76 - 2.28\alpha + 2.87\alpha^2 - 2.04\alpha^3 + \frac{0.66}{(1-\alpha)^2}\right) \tag{6. 12}$$

where $\sigma = \frac{6M}{W^2 t}$, $M = \frac{PL}{4}$ and a is the initial crack length such that $\alpha = \frac{a}{W}$.

The contribution from δ_g has been found to be negligible for the specimen geometries tested.

The load on the beam is related to the normalised moment through the following relation

$$P(\theta) = \frac{2\,f_t h_g^2 t}{3L}\mu(\theta) \tag{6. 13}$$

where L is the total length of the beam. For each value of θ, the normalized moment ($\mu(\theta)$) and the crack length (α_h) are calculated (Eq. 6.7), followed by the theoretical CMOD and load P (Eqs. 6.8 and 6.13). Next, the sum of squares of the errors between the theoretical and experimental values of the load is minimized with respect to the three unknown parameters of the bilinear TSD:

$$\min._{(a_1,a_2,b_2)} \frac{1}{n}\sum_0^n (P_{theoritical} - P_{experimental})^2 \quad (6.\ 14)$$

where n is the total number of the observations representing the selected entries of θ that is, the selected values of P on the experimentally recorded load-CMOD diagram.

The above analytical expressions relating the hinge rotation to the bending moment and crack length in each phase and in turn to the applied central load on the beam and crack mouth opening displacement (CMOD) are given in Abdalla and Karihaloo (2004). The expressions for CMOD and central load are used to minimise the sum of squares of the errors between the experimental and theoretical values of the load with respect to the three unknown parameters of the bilinear tension-softening diagram. For this purpose, a Matlab code has been constructed and provided in Appendix F. The accuracy of this minimization procedure depends on the total number of observations from the recorded load-CMOD diagram used in this procedure and the allowable error (<3%). Typical results of this minimization procedure are shown in Figure 6.13 for some SCC mixes and pre-existing notch depths

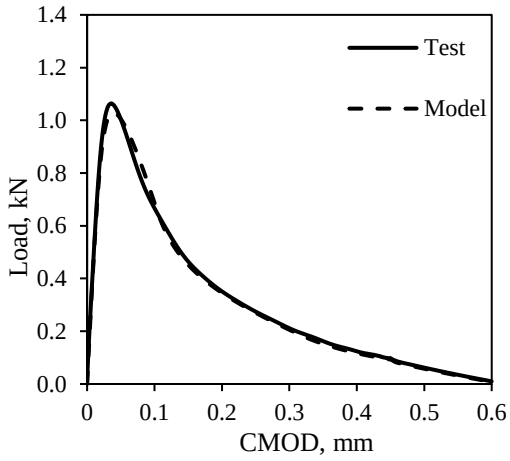

(a) 30B: *a/ W* = 0.6

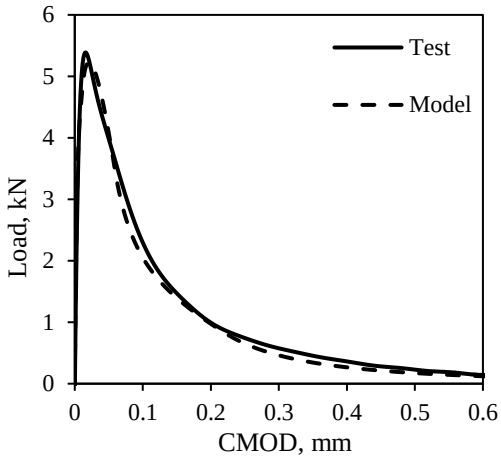

(b) 30B: *a/ W* = 0.1

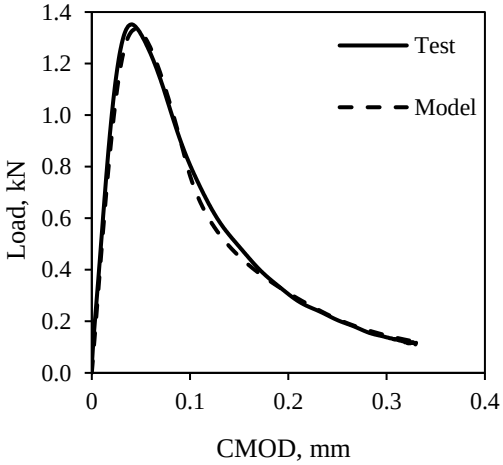

(c) 60B: *a/ W* = 0.6

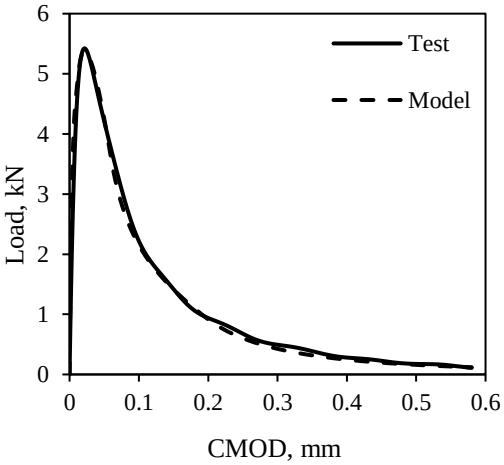

(d) 60B: *a/ W* = 0.1

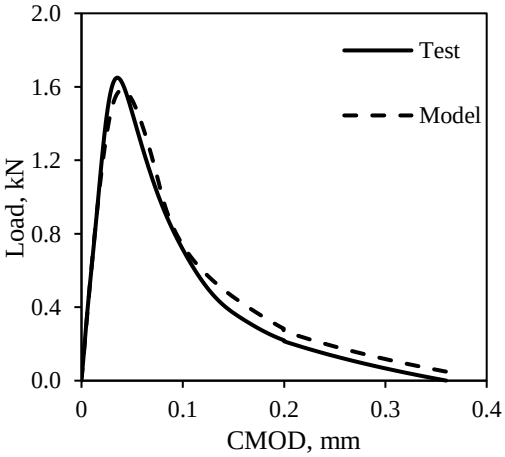

(e) 80B: *a/ W* = 0.6

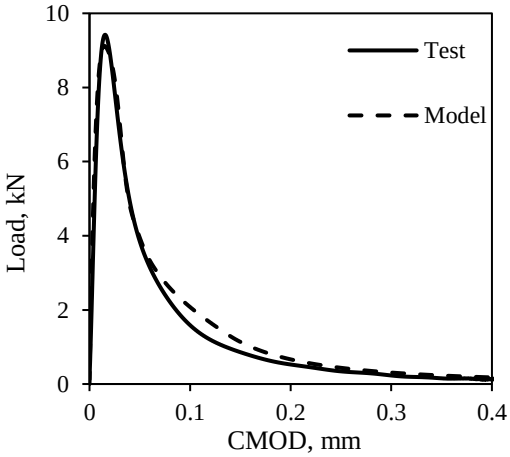

(f) 80B: *a/ W* = 0.1

Figure 6. 13 Load-CMOD curves generated by the hinge model and average experimental load-CMOD curves

As the load-CMOD diagrams are recorded on tests on beams with a notch to depth ratio of 0.1 or 0.6, the three unknown parameters of the bilinear tension softening diagram obtained from the above minimization procedure correspond not to the G_F of the SCC mix, but to its size-dependent G_f (0.1) and G_f (0.6). These pairs of three parameters need therefore to be appropriately scaled to reflect the size-independent G_F of the mix. The scaling procedure is described in Abdalla and Karihaloo (2004).

The size-dependent fracture energy (i.e. the area under the bilinear TSD) is given by

$$G_f^*(\alpha, W) = \frac{1}{2} f_t^* (w_1^* + \frac{\sigma_1^*}{f_t^*} w_c^*) \quad (6.15)$$

where the superscript * denotes the average parameters of the bilinear diagram obtained from the hinge model.

The size-independent fracture energy (i.e. the area under the bilinear TSD corresponding to G_F) can be similarly written as

$$G_F = \frac{1}{2} f_t (w_1 + \frac{\sigma_1}{f_t} w_c) \quad (6.16)$$

where w_1 and w_c and σ_1, which are to be determined, are the bilinear diagram parameters corresponding to true fracture energy (G_F), and f_t is the direct tensile strength of the mix obtained from an independent test, say a split cylinder test, f_{st}. It is assumed that f_t=0.65f_{st} (Neville, 1995).

The hinge model parameters corresponding to G_F (a, W) are now scaled to the true fracture energy, G_F that is;

$$\frac{1}{2} f_t (w_1 + \frac{\sigma_1}{f_t} w_c) = \frac{1}{2} f_t^* (w_1^* + \frac{\sigma_1^*}{f_t^*} w_c^*) \frac{G_F}{G_f^*(\alpha,\ W)} \quad (6.17)$$

The coordinate of the knee of the bilinear diagram predicted by the hinge model are related as follows (Figure 6.14)

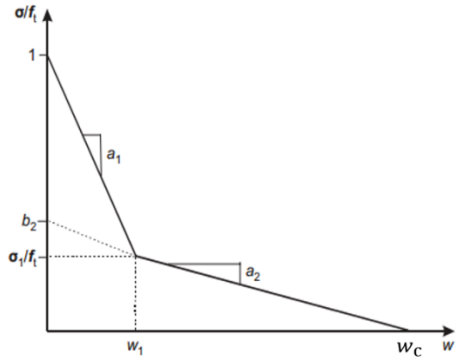

Figure 6. 14 Bilinear tension-softening details

$$\frac{\sigma_1^*}{f_t^*} = 1 - a_1^* w_1^* \tag{6. 18}$$

A term-by-term comparison of the two sides of Eq. 6.17 gives;

$$w_1 = w_1^* \frac{G_F}{G_f^*} \frac{f_t^*}{f_t} \tag{6. 19}$$

$$\frac{\sigma_1}{f_t} = \frac{G_F}{G_f^*} \frac{\sigma_1^*}{f_t^*} \frac{w_c^*}{w_c} \frac{f_t^*}{f_t} \tag{6. 20}$$

From Figure 6.14, we obtain an additional equation for the slope a_2 of the true bilinear diagram;

$$\frac{\sigma_1}{f_t} = (w_c - w_1) a_2 \tag{6. 21}$$

Equating Eqs. 6.20 and 6.21 gives a quadratic equation for calculating the crack opening (w_c);

$$w_c^2 - w_1 w_c = \frac{1}{a_2} \frac{G_F}{G_f^*} \frac{\sigma_1^*}{f_t} w_c^* \tag{6. 22}$$

Once w_1 has been determined from Eq. 6.19. Note that slope a_2 is chosen to coincide with a_2^* of TPB specimen, which is it assumed that the slope of the tail part of the bilinear diagram is not sensitive to α and W. This is a reasonable assumption in view of the fact that a_2 is a result of the aggregate interlock, which is primarily governed by the maximum size and texture of the coarse aggregate used in the concrete mix.

6.10 Bilinear TSD parameters corresponding to G_F

The bilinear tension softening diagrams of all nine SCC mixes corresponding to their size-independent specific fracture energy (G_F) are tabulated in Table 6.5 and shown in Figure 6.15. The three parameters describing the shape of the bilinear diagram, together with the direct tensile strength (f_{ct}) and the elastic modulus (E) of all SCC mixes are given in Table 6.5. The slope of the initial part of the bilinear softening curve increases with the increasing the p/s ratio, but the influence of p/s decreases as the f_{cu} of the mix increases.

Table 6. 5 Parameters of the bilinear softening diagram corresponding to the size-independent specific fracture energy (G_F)

Mix designation	a_1 mm	a_2 mm	w_1 mm	w_c mm	$\frac{\sigma}{f_t}$	G_F N/m	E GPa	l_{ch} mm
30A	10.07	1.12	0.078	0.272	0.218	132.8	33.6	1377
30B	13.21	1.05	0.060	0.254	0.203	112.3	32.7	976
30C	18.76	1.20	0.043	0.198	0.186	90.4	32.0	519
60A	10.97	1.14	0.073	0.251	0.203	143.2	36.7	1057
60B	13.17	1.25	0.062	0.213	0.189	120.3	36.6	771
60C	15.38	1.28	0.053	0.198	0.185	109.7	34.5	497
80A	16.19	1.18	0.048	0.238	0.225	146.9	42.3	647
80B	18.51	1.39	0.043	0.194	0.211	136.5	40.8	380
80C	19.75	1.38	0.041	0.177	0.188	130.2	41.0	289

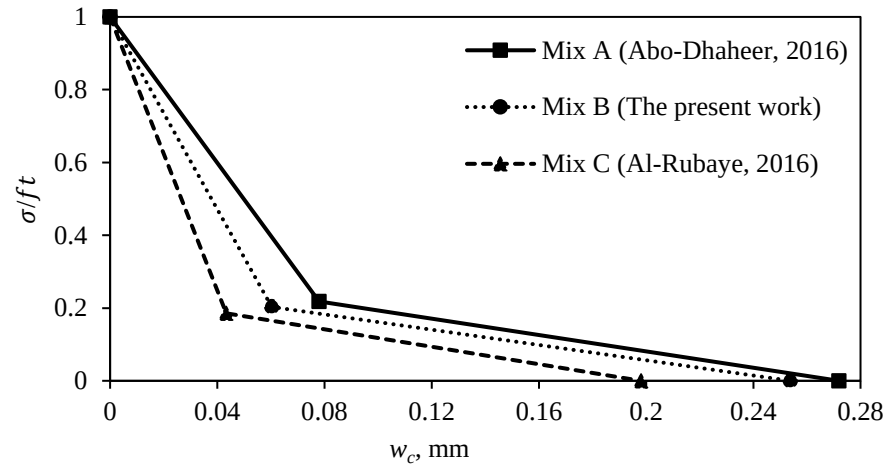

(a) Grade 30

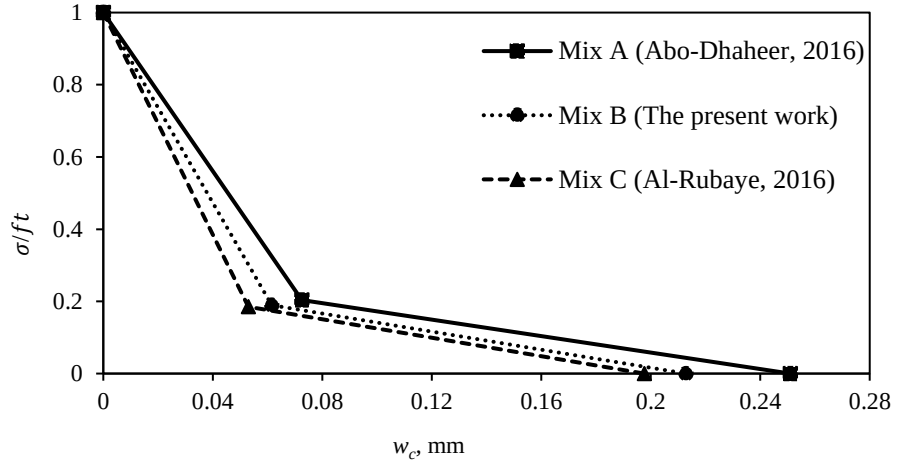

(b) Grade 60

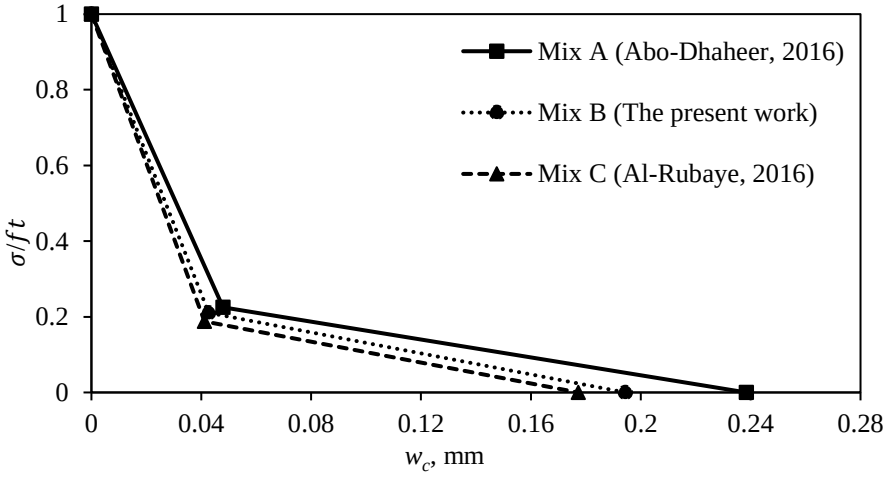

(c) Grade 80

Figure 6. 15 The normalised bilinear stress-crack opening relationship for different SCC grades corresponding to their size-independent fracture energy (G_F)

6.11 Direct and indirect tensile strength relationship

It is well documented that the direct tensile strength (f_{ct}) is approximately two-thirds of the indirect tensile strength (f_{st}). Although the literature is rich in reporting on SCC, the effect of p/s ratio and mix grade on tensile strength is still not fully addressed. The relationship between the direct tensile strength (determined by the inverse analysis using the non-linear hinge model) and indirect tensile (i.e. splitting) strengths (f_{ct}/f_{st}) of SCC mixes of different p/s ratio, and mix grade is summarised in Table 6.6 and Figure 6.16. It is found that f_{ct}/f_{st} is dominated by the p/s in the mix and the mix grade: it increases with both an increase in p/s and mix grade. This might provide a better understanding of the contribution of p/s and strength on the tensile strength of SCC and a useful guide for determining the f_{ct} from the f_{st} in SCC mixes. Note that the f_{ct}/f_{st} ratio is slightly different from the conventional 0.65 (Neville 1995). It depends on the p/s ratio and strength grade (Table 6.6).

Table 6. 6 Relation between f_{ct} and f_{st} of test SCC mixes

Mix designation	f_{ct} MPa	f_{st} MPa	$\frac{f_{ct}}{f_{st}}$	Mean $\frac{f_{ct}}{f_{st}}$
30A	1.80	2.95	0.61	
30B	1.94	3.04	0.64	0.66
30C	2.36	3.30	0.72	
60A	2.23	3.40	0.66	
60B	2.39	3.52	0.68	0.69
60C	2.76	3.65	0.76	
80A	3.10	4.60	0.67	
80B	3.83	5.00	0.77	0.75
80C	4.30	5.35	0.80	

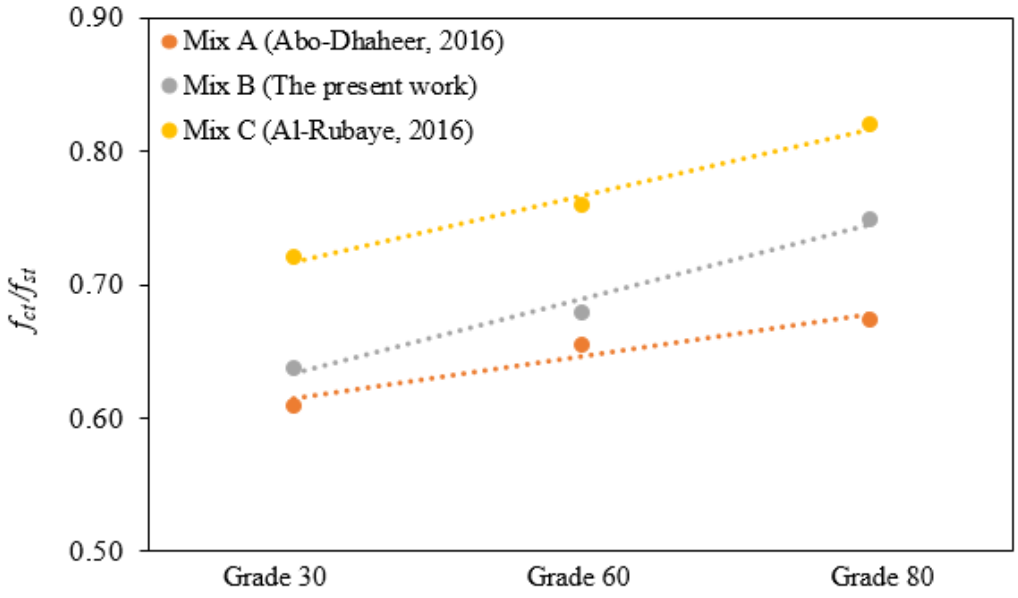

Figure 6. 16 Direct (f_{ct}) and indirect (f_{st}) tensile strengths of different SCC mixes

6.12 Characteristics length (l_{ch})

The characteristic length (l_{ch}) is also given in Table 6.5 of each mix calculated using the relation:

$$l_{ch}=\frac{E\ G_F}{{f_{ct}}^2} \qquad (6.\ 23)$$

The characteristic length represents the ductility of a mix; the larger the characteristic length, the more ductile the mix. l_{ch} is dominated by the coarse aggregate volume fraction, and it decreases with increasing strength grade (Figure 6.17).

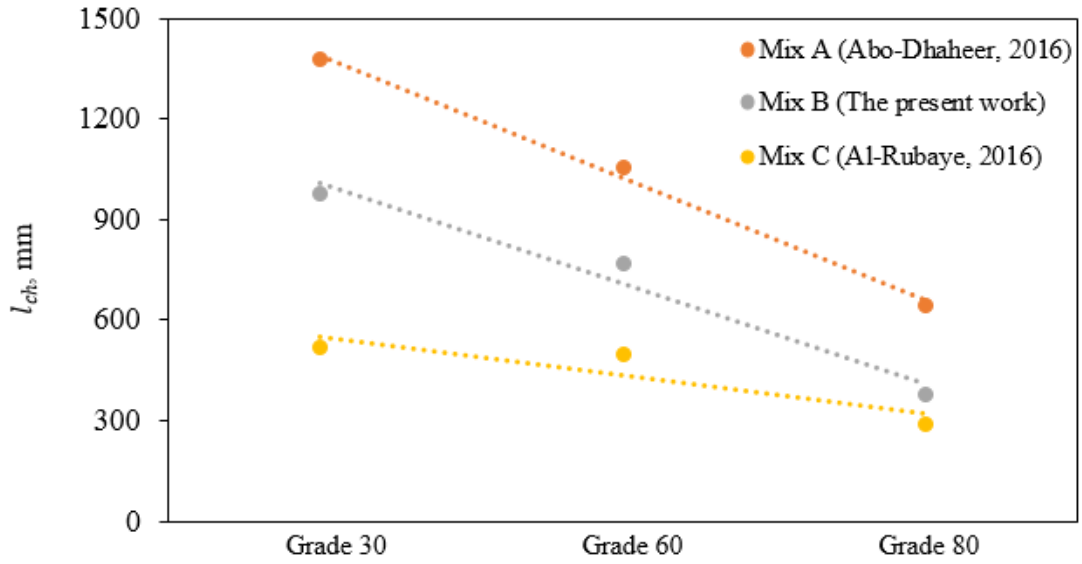

Figure 6. 17 Characteristic lengths (l_{ch}) of different test SCC mixes

6.13 Concluding remarks

This Chapter presented the results of a comprehensive experimental study on the fracture behaviour of SCC mixes varying by the volume of coarse aggregate, paste to solids (p/s) ratio and water to cementitious materials (*w/cm*) ratio. The non-linear hinge model has also been employed to obtain the bilinear approximation of the tension-softening diagram corresponding to G_F.

The results confirm the dependency of the RILEM fracture energy on the notch depth. The increase in the coarse aggregate volume fraction led to increasing of specific fracture energy (G_F), irrespective of the SCC mix grade. However, the increase is less pronounced in higher strength mix (grade 80) than in grades 30 and 60 of SCC.

Within the same nominal strength grade, an increase in the paste to solids (p/s) ratio results in a marginal increase in the strength itself, but a noticeable decrease in G_F. It was also found that an increase in the *w/cm* ratio reduces G_F. The decrease becomes more pronounced with decreasing coarse aggregate volume fraction.

The critical crack opening (w_c) is dominated by the coarse aggregate volume in the mix and the mix grade. The larger the coarse aggregate volume (or, the smaller the paste to solids (p/s) ratio) the larger is the critical crack opening (w_c). However, the

higher the mix grade, the lower is the critical crack opening (w_c). It was also found that the characteristic length (l_{ch}) dominates by the coarse aggregate volume fraction, and it decreases with increasing strength grade.

The next Chapter will examine the simulation of the flow of SCC in the V-funnel using SPH strategy.

Chapter 7

Simulation of the flow of SCC mixes in the V-funnel by SPH

7.1 Introduction

In concrete construction, insufficient filling of formwork, de-airing, and segregation of conventional vibrated mix components give rise to serious durability problems. The impact of such problems has increased sharply as complex formwork and/or dense reinforcements are being used. Self-compacting concrete (SCC), which flows and consolidates under the action of gravity without external vibration maintaining homogeneity has been developed to overcome these problems (Okamura and Ouchi, 2003). It ensures proper filling of formwork and produces a high-quality finish in heavily reinforced structural members and inaccessible areas even in the most complex formwork.

Various tests are performed to evaluate the fresh properties of SCC, including its filling ability, passing ability, and resistance to segregation (EFNARC, 2005). These tests are labour-intensive, time-consuming and therefore expensive. Moreover, observations made from tests under one set of conditions are not always unconditionally applicable to other circumstances in which dissimilar materials and mix proportions than the test mixes may be used. Thus, new tests are required in such circumstances. Repeated experimental tests can be avoided by performing a cost-effective computational simulation to save cost, time, effort and materials (Liu and Liu, 2003). It can also provide a thorough understanding of the SCC flow behaviour, particularly in complex formworks, which is essential to achieving high quality finish. Indeed, modelling has brought insight into the significance of the rheology as a tool for the optimisation of mix composition and the processing techniques to fulfil the levels of engineering properties required for the intended civil applications (Roussel et al., 2007).

The flow-ability, passing/filling ability and stability can be considered as the distinguishing requirements of fresh SCC. These requirements are not common to conventional vibrated concrete and, therefore, are handled through special tests. One of these tests is the V-funnel test, which is designed to reveal the filling ability and segregation resistance of an SCC mix; shorter discharge time ($t_{v\text{-}funnel}$) indicates greater filling ability (BS EN 12350-9, 2010). The V-shape restricts the flow, and prolonged discharge times may provide an indication of blocking.

In this Chapter, the flow of SCC through a V-funnel is simulated from the moment the gate is opened until the time when the light is first seen in the bottom opening through observation from the top. The choice of the right simulation strategy is an important issue, and several approaches have been tried to simulate the flow (Wu and Shu, 2010; Švec et al., 2012; Baaijens, 2001). Of these approaches, the smooth particle hydrodynamics (SPH) is particularly suitable because it permits the treatment of SCC as a homogeneous viscous fluid yet allows particles of different sizes to be tracked during the flow. This approach can also assist in proportioning SCC mixes, thus improving on the traditional trial and error SCC mix design (Deeb et al., 2012; Karihaloo and Ghanbari, 2012; Deeb and Karihaloo, 2013). It has already been successfully used to simulate the flow and to monitor the movement of large aggregates and/or short steel fibres of SCC in the slump cone flow, L-box and J-ring tests (Deeb et al., 2014; Deeb et al., 2014a; Deeb et al. 2014b; Kulasegaram et al., 2011; Abo Dhaheer et al., 2016). The SPH approach also provides a useful tool for an accurate estimation of the yield stress (τ_y) of SCC mixes in an inverse manner from the flow spread (Badry et al., 2016). This is particularly relevant to the characterisation of an SCC mix because the measurement of τ_y and that of the plastic viscosity (η) by rheometers is inconsistent and fraught with inaccuracies. For one and the same SCC mix different rheometers are known to give vastly different values of τ_y and η (Banfill, 2006; Wallevik and Wallevik, 2011). The published results are therefore highly unreliable.

The aim of this Chapter is to extend the SPH approach to simulating the flow of SCC through the V-funnel. The capabilities of the SPH methodology will be validated on several SCC mixes differing by their cube compressive strength and plastic viscosity. The simulated discharge times will be compared with those recorded in the laboratory on the same mixes. As the SPH allows the distribution of large coarse aggregates embedded in the homogeneous mixes to be tracked, it is possible to check whether or not they are homogeneously distributed during the flow and after the flow has stopped. For this, the distribution of large coarse aggregates in the mix will be examined along three zones of the V-funnel at different times during the flow and along three portions of the collecting container at the outlet of the funnel after the flow has stopped. Along all these cut regions, the distribution should be nearly the same if the large aggregates are indeed uniformly distributed.

The successful simulation of the flow of SCC through a V-funnel has the added advantage that the same methodology can be used to simulate the flow from a feed hopper into a mould which is the common method for the casting of SCC structural elements in a precast factory. There is a further advantage in simulating the flow in a V-funnel. As mentioned above, a well-proportioned SCC mix must provide a sufficient level of viscosity and prevent segregation of coarser aggregates in the pouring process. The coarser aggregates must remain homogeneously distributed in both the vertical and horizontal directions to ensure uniform filling of deep sections, such as walls and columns. In fact, the ASTM C1610/C1610M (2011) standard procedure for assessing the segregation resistance of an SCC mix requires that the masses (i.e. concentration) of coarse aggregates in two selected washed concrete portions of equal volume of a cylindrical container retained on a 4.75 mm (No. 4) sieve be the same. The procedure can be used on the SCC mix collected in a cylindrical container after it has been discharged fully from the V-funnel. Thus the V-funnel test is useful not only for assessing the flowability of an SCC mix, but also its segregation resistance.

The contents of this Chapter have been submitted to the 'Cement and Concrete Research' (see publications list in Chapter 1).

7.2 Test SCC mixes used for simulation

For the purposes of comparison with SPH simulations, a range of SCC mixes were designed (for mix proportions see Table 5.1) according to the rational mix design procedure described in (Abo Dhaheer et al., 2016b), and tested to satisfy the self-compactibility criteria i.e. the filling ability, passing ability, and resistance to segregation (i.e. stability) using the slump cone, V-funnel, J-ring, and L-box tests according to the requirements of BS EN12350-9 (2010; Abo Dhaheer et al., 2016a) (see Tables 5.3 and 5.4). It should be stressed that the simulation technique is generic and not restricted to the six test mixes.

7.3 SPH Modelling of SCC flow

Since SCC flow through the V-funnel test is a gravitational flow with large deformations, the three-dimensional smooth particle hydrodynamic (SPH) mesh-less

numerical approach is preferred to solve the governing equations of SCC flow (Liu and Liu, 2003). The essential equations solved in the SPH are the incompressible mass and momentum conservation equations, together with the constitutive relation of the viscous fluid. The fluid continuum is discretized into a limited number of particles (N), which possess all the individual material properties; this feature is the principal strength of the SPH approach. The field variables and their gradients are approximately considered and interpolated from values at a discrete set of particles in a domain of influence (Figure 7.1) (Kulasegaram et al., 2011; Deeb et al., 2014a; Deeb et al., 2014b). The partial differential equations of motion of continuum fluid dynamics are transformed into integral equations over the particles by using an interpolation function. This interpolation is conducted by ‘‘kernel estimate’’ of the field variable at any particle. All randomly generated particles, which represent the paste and the large aggregates, form a homogeneous mass with the same properties as the continuum except their assigned volumes.

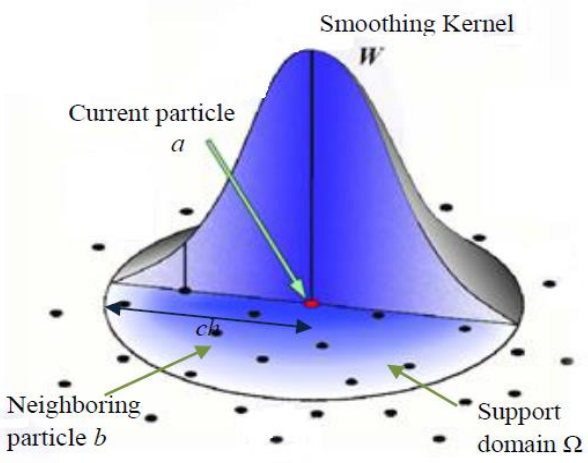

Figure 7. 1 Particle approximations using neighbouring particles within the support domain of the smoothing kernel *W* for particle *a* (Deeb, 2013)

7.4 Governing equations

Given its shear rate-dependent response, SCC can be considered as a non-Newtonian incompressible fluid and its rheology described by a Bingham-type model, which contains two material properties: yield stress (τ_y) and plastic viscosity (η). From a computational perspective, it is expedient to approximate the bi-linear Bingham

constitutive model with a kink at zero shear rate $\dot{\gamma}$= 0 by a continuous function (Eq. 7.1) (see, e.g. (Kulasegaram et al., 2011)). (Figure 7.2):

$$\boldsymbol{\tau} = \eta\dot{\gamma} + \tau_y\left(1 - e^{-m\dot{\gamma}}\right) \tag{7. 1}$$

in which m is a very large number, m = 10^5. This smooth function is practically indistinguishable from the original bilinear relation.

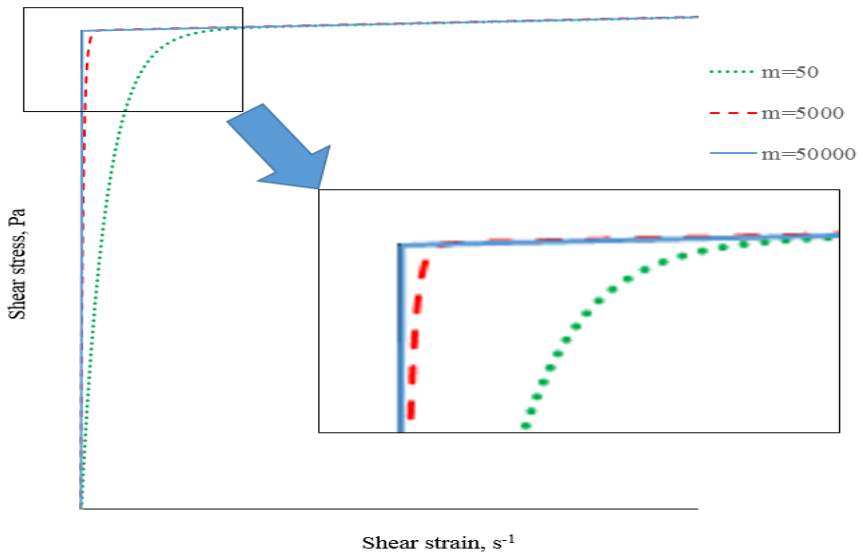

Figure 7. 2 A bi-linear Bingham fluid constitutive model replaced by the continuous function

The constitutive model is coupled with the isothermal Lagrangian mass and momentum conservation equations (Eqs. 7.2 and 7.3 respectively). A projection method based on the simple predictor-corrector time stepping scheme is used to track the Lagrangian non-Newtonian flow (Chorin, 1968; Cummins and Rudman, 1999), and the incompressibility condition is met exactly through a pressure Poisson equation. The time step is chosen based on the relevant stability conditions. In the present problem, the time step is primarily controlled by the effective plastic viscosity and the chosen (cubic spline) kernel function.

$$\frac{1}{\rho}\frac{D\rho}{Dt} + \nabla.\mathbf{v} = 0 \tag{7. 2}$$

$$\frac{D\mathbf{v}}{Dt} = -\frac{1}{\rho}\nabla P + \frac{1}{\rho}\nabla.\boldsymbol{\tau} + \mathrm{g} \tag{7. 3}$$

where $\rho, t, \mathbf{v}, P, \boldsymbol{\tau}$ and g represent the fluid particle density, time, particle velocity, pressure, shear stress tensor and gravitational acceleration, respectively. The first term in Eq. 7.2 vanishes since the density is constant due to the incompressible flow assumption.

7.5 Numerical implementation

As mentioned above, the predictor-corrector time stepping scheme has been used to track the Lagrangian non-Newtonian flow (Koshizuka et al., 1998; Chorin, 1968; Cummins and Rudman, 1999). The prediction step is an explicit integration in time without enforcing incompressibility. Only the viscous and gravity terms (second and third terms respectively) in Eq. 7.3 are initially considered to obtain an intermediate temporal velocity of particles ($\mathbf{v}_{n+1}^{*}$);

$$\mathbf{v}_{n+1}^{*} = \mathbf{v}_n + \left(\frac{1}{\rho}\nabla.\boldsymbol{\tau} + g\right)\Delta t \qquad (7.4)$$

Then, the correction step is performed by considering the pressure term (first term) in Eq. 7.3;

$$\frac{\mathbf{v}_{n+1} - \mathbf{v}_{n+1}^{*}}{\Delta t} = \mathbf{v}_n + \left(\frac{1}{\rho}\nabla P_{n+1}\right) \qquad (7.5)$$

where $\mathbf{v}_{n+1}$ is the corrected particle velocity at the time step n + 1.

The intermediate velocity $\mathbf{v}_{n+1}^{*}$ is usually not divergence-free, but this condition is imposed on the corrected velocity $\mathbf{v}_{n+1}$ by enforcing the incompressibility condition from Eq. 7.2;

$$\nabla.\mathbf{v}_{n+1} = 0 \qquad (7.6)$$

Hence, by writing the divergence of Eq. 7.5, the intermediate velocity can be projected on the divergence-free space, using Eq. 7.6 to give;

$$\nabla.\left(\frac{1}{\rho}\nabla P_{n+1}\right) = \frac{\nabla.\mathbf{v}_{n+1}^{*}}{\Delta t} \qquad (7.7)$$

As the density of particles remains constant in the present simulations, Eq. 7.7 can be rewritten as;

$$\nabla^2 P_{n+1} = \frac{\rho}{\Delta t} \nabla . \mathbf{v}^*_{n+1} \quad (7.\ 8)$$

where ∇^2 is the Laplace operator.

Once the pressure is obtained from Poisson's equation (Eq. 7.8), the particle velocity and position are updated by the computed pressure gradient (see Eq. 7.5);

$$\mathbf{v}_{n+1} = \mathbf{v}^*_{n+1} - \left(\frac{1}{\rho} \nabla P_{n+1}\right) \Delta t \quad (7.\ 9)$$

Finally, the particle position is corrected using the corrected velocity:

$$x_{n+1} = x_n + \mathbf{v}_{n+1} \Delta t \quad (7.\ 10)$$

7.6 Time step

The time step (Δt) is chosen based on the relevant stability conditions for the given problem. In the case of Bingham-type SCC fluid flow, the time step is primarily controlled by the effective plastic viscosity. Therefore, the time step size is generally decided by (Cummins and Rudman, 1999):

$$\Delta t = min\left(\frac{\alpha_1 r_0}{\mathrm{v}_{max}}, \frac{\alpha_2 r_0^2 \rho}{\mu}\right) \quad (7.\ 11)$$

where r_0 is the initial particle spacing, v_{max} is the maximum particle velocity, α_1 and α_2 are coefficients usually in order the of 0.1. These coefficients depend on the choice of SPH kernel functions and the nature of the engineering application.

7.7 Initial configuration and boundary conditions

To solve the mass and momentum conservation equations (Eqs.7.2 and 7.3), it is necessary to impose appropriate initial boundary conditions. Three sorts of boundary conditions have been taken into consideration in modelling the flow in the V-funnel: zero pressure condition on the free surface (*P=0*), Dirichlet boundary condition on the normal component of the particle velocity at the V-funnel walls ($\boldsymbol{v}_n$=0), and Neumann conditions on the pressure gradient ($\partial P/\partial n = 0$) (zero pressure gradient is used only

for solving the second-order Poisson equation to find the pressure), as illustrated in Figure 7.3, where the dimensions of the V-funnel apparatus are also given (BS EN 12350-9, 2010). The boundary conditions are the same along all the V-funnel and rectangular outlet sidewalls. Four arrays of rigid dummy particles are placed outside the walls of the V-funnel to implement the wall boundary conditions with space r_0 between the arrays, where r_0 is the initial particle spacing. For clarity of presentation, the dummy particles are shown in two dimensions in Figure 7.3.

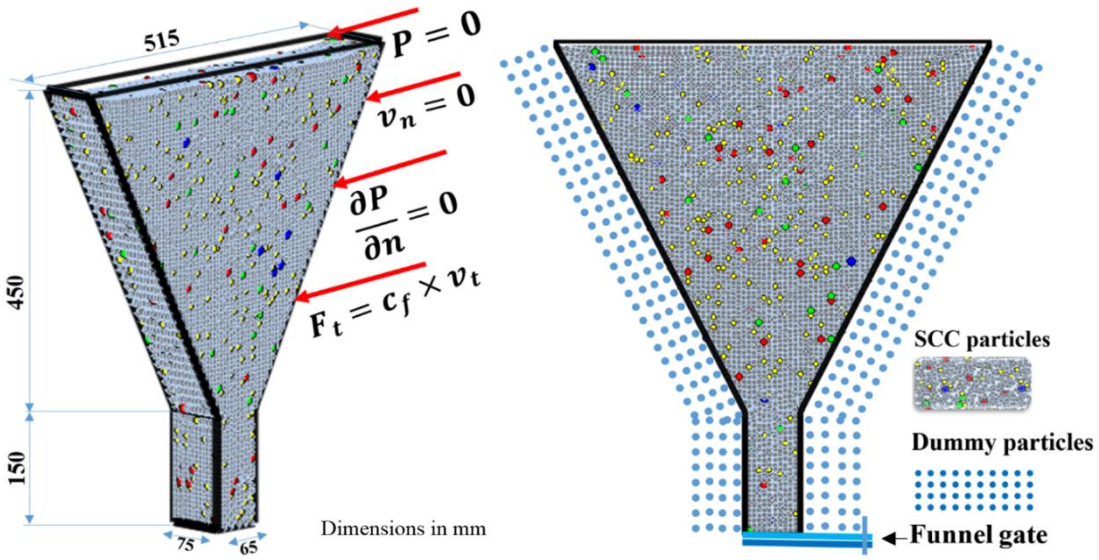

Figure 7. 3 Boundary conditions and geometry of the V-funnel apparatus

In order to calculate the frictional force on the sides of the V-funnel resisting the free gravitational flow, the kinematic coefficient of friction (c_f) between the V-funnel walls and the SCC mix acting on the tangential component of the particle velocity has to be known. This is the only free parameter in the simulations. It has been established by matching the experimental and simulated discharge times of one test mix. The coefficient so obtained is then used for all the remaining five SCC mixes. After several trials on Mix30B, an appropriate coefficient of friction for the numerical simulations was chosen to be 0.55 N s/m for all SCC mixes. The coefficient so obtained is then held unchanged for all other SCC mixes.

7.8 Treatment of aggregates

An essential requirement of an SCC mix is that heavier aggregate particles do not segregate from the paste but remain homogeneously distributed during the flow. The number of particles used to represent the volume of the V-funnel contents sets a lower limit on the volume element that can be distinguished from the homogeneous mass, i.e. the resolution of the modelling technique. In the numerical implementation, a total of 53,846 particles has been used to represent the volume of the SCC mix in the funnel ($\approx 10.5 \times 106$ mm^3) giving a resolution of 195.35 mm^3, if all particles have the same density as the homogeneous viscous continuum. The resolution will be somewhat different if the particles have various densities. Thus, in all mixes, the volume of large aggregates that can be distinguished from the homogeneous mass must exceed this minimum value. That is why only the aggregates of size approximately 8 mm can be distinguished in the homogeneous mass. To track the positions and velocity vectors of coarse aggregates of different representative sizes, the particles are represented by distinct colours and generated randomly as shown in Figure 7.4. It should be emphasised however that the homogeneous mass characterised by its yield stress (τ_y) and plastic viscosity (η) is formed by all particles, including the large aggregates, and the viscous mortar.

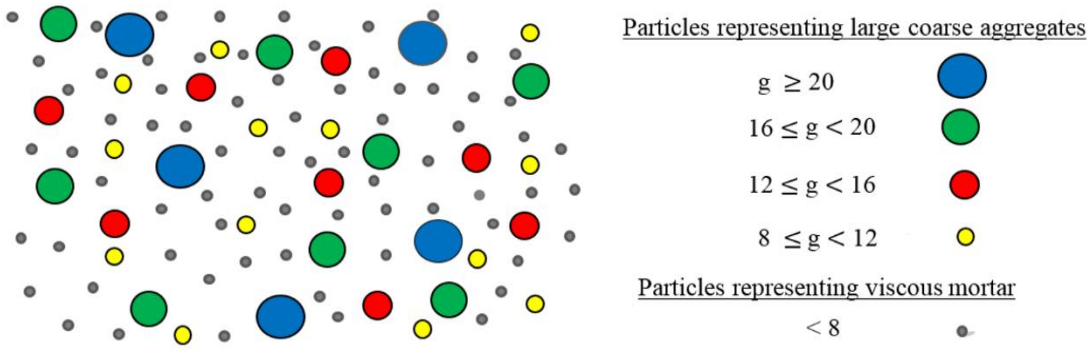

Figure 7. 4 Schematic sketch of particle size (g) representation when modelling large aggregate distribution (After Deeb, 2013)

The following steps were also taken during the numerical simulations:

- All particles representing the SCC mix were randomly generated;
- Particles representing the mortar and the large aggregates form a homogeneous mass and have the same continuum properties except for their assigned volumes;

- The masses of the SPH particles representing the various aggregate particles in the SCC mix were determined based on their respective volume fractions in SCC mix;
- Particles representing the large aggregates according to their assigned volumes were tagged and colour coded (as shown above in Figure 7.4) throughout the simulation process to monitor their positions and velocity vectors.

7.9 Calculation of the assigned volumes

In order to calculate the assigned volume of each size range of particles (i.e. g≥20, 16≤g<20, 12≤g<16, 8≤g<12 and particles<8mm), it is necessary to know the volume fractions of these ranges. A sieve analysis, which determines the grading curve of aggregate particle sizes within a given test sample can provide these volume fractions (Table 7.1).

Table 7. 1 Volume fractions percentage of various size ranges of coarse aggregates

g≥20	16≤g<20	12≤g<16	8≤g<12	g<8
1.42	8.02	4.62	8.80	77.14

For the modelling purpose, each aggregate size range was replaced by a single aggregate size that best represented the range. The representative aggregate diameter in each size range is given in Table 7.2. The assigned volume (V_a) for each particle size that appears in the discrete form of SPH equations is equal to the ratio of its actual mass to the density of the continuum.

The following steps are a calculation example of the assigned volume of the discrete particles in the SPH.

1. Determine the density of mortar

Firstly, the volume fraction of mortar (i.e. cement + ggbs+ water + LP + FA +SP+CA particles <8mm) can be calculated as:

$$\text{Volume fraction of mortar} = \text{total volume} - \text{volume fraction of CA} \geq 8\text{mm}$$

$$\text{Volume fraction of mortar} = 1.0 - 0.0142 - 0.0802 - 0.0462 - 0.088 = 0.7714$$

By using the rule of mixtures, the density of mortar can be determined.

$$\text{Mix density} = \sum \text{coarse aggregate volume fraction} \times \text{coarse aggregate density} + \text{mortar volume fraction} \times \text{mortar density}$$

$$2365.5 = (0.0142 + 0.0802 + 0.0462 + 0.0880) \times 2800 + 0.7714 \times \text{mortar density}$$

$$\text{mortar density} = 2236.7 \text{kg/m}^3$$

2. Determine the number of particles of each range size

$$\text{Np} = \frac{\text{the volume fraction of each size} \times \text{funnel volume}}{\text{average volume of representative size particle}}$$

$$\text{Np } (g \geq 20) = \frac{0.0142 \times 10518750}{4190.5} = 36$$

$$\text{Np } (16 \leq g < 20) = \frac{0.0802 \times 10518750}{3054.9} = 276$$

$$\text{Np } (12 \leq g < 16) = \frac{0.0462 \times 10518750}{1437.3} = 338$$

$$\text{Np } (8 \leq g < 12) = \frac{0.088 \times 10518750}{523.8} = 1769$$

$$\text{Np (mortar} < 8) = 53846 - (36 + 276 + 338 + 1769) = 51427$$

3. Determine the assigned volume of each particle size range

$$\text{Assigned volume (Va)} = \frac{\text{average volume of one representative size particle} \times \text{density}}{\text{density of continuum}}$$

$$\text{Va } (g \geq 20) = \frac{4190.5 \times 2800}{2365.5} = 4960.2$$

$$\text{Va } (16 \leq g < 20) = \frac{3054.9 \times 2800}{2365.5} = 3616.0$$

$$\text{Va } (12 \leq g < 16) = \frac{1437.3 \times 2800}{2365.5} = 1701.3$$

$$\text{Va}\ (8 \leq g < 12) \quad = \frac{523.8 \times 2800}{2365.5} = 620.0$$

For mortar $(\text{particles} < 8)$

$$\text{Average volume of one representative size particle} = \frac{\text{volume of mortar in the funnel}}{\text{Np}(< 8)}$$

$$\text{Volume of mortar in the funnel} = \text{mortar volume fraction} \times \text{ funnel volume}$$

$$\text{Volume of mortar in the funnel} = 0.7714 \times 10518750 = 8113112\text{mm}^3$$

$$\text{Average volume of one representative size particle} = \frac{\text{Volume of mortar in the funnel}}{\text{Np}\ (< 8)}$$

$$\text{Average volume of one representative size particle} = \frac{8113112}{51427} = 157.76\text{mm}^3$$

$$\text{Va}\ (< 8)\ = \frac{157.76 \times 2236.7}{2365.5} = 149.2$$

Table 7. 2 Volume fractions of particles of SCC mix in the 3D simulation of V-funnel

		Particle size range mm	Rep. particle diameter mm	Density kg/m^3	Volume fraction %	3D V-funnel test	
						Number of particles N_p	Assigned volume per particle mm^3
Particles	≥8mm	g≥20	20	2800	1.42	36	4960.2
		16≤g<20	18		8.02	276	3616.0
		12≤ g<16	14		4.62	338	1701.3
		8≤g<12	10		8.80	1769	620.0
	<8mm	mortar<8	8	2236.7	77.14	51427	149.2
	Total	-	-	2365.5	100	53846	-

7.10 Numerical results

In the three-dimensional numerical simulation of the flow through the V-funnel, each SCC mix has been represented by a limited number of particles (53,846) to investigate its flow characteristics and compare with the corresponding experimental results. This number of particles has been chosen to provide adequate accuracy in a reasonable time. The simulation also reveals the distribution of the large components in SCC mixes (coarse aggregate size (g) ≥8 mm) so that it can be ascertained whether these heavier aggregates remain homogeneously distributed in the viscous mix during the flow. As mentioned above, the measurement of τ_y and that of η by rheometers is inconsistent and fraught with inaccuracies. For one and the same SCC mix different rheometers are known to give vastly different values of τ_y and η (Banfill et al., 2000; Wallevik and Wallevik, 2011). Thus, the published data cannot be regarded as reliable. For this reason, the plastic viscosity of all test SCC mixes was estimated following the procedure described in (Ghanbari and Karihaloo, 2009), based on the plastic viscosity of the paste (i.e. cement, ground granulated blast furnace slag (ggbs), water, super-plasticiser, and entrapped air). This procedure is based on the rheology of concentrated suspensions (de Kruif et al., 1985; Krieger and Dougherty, 1959), and it can predict accurately in a stepwise way the plastic viscosity of the heterogeneous SCC mixes beginning with the plastic viscosity of the homogeneous paste which can be accurately measured with a viscometer. The yield stress, on the other hand, was estimated in an inverse manner from the measured time (t_{500}) to reach 500 mm spread of the SCC mixes in a flow cone test using SPH (Badry et al., 2016). The plastic viscosities and yield stresses, as well as the densities of all test SCC mixes, are given in Table 7.3.

Table 7. 3 Rheological properties and density of the test SCC mixes

	SCC mix designation by compressive strength (MPa)					
	30B	40B	50B	60B	70B	80B
Plastic viscosity, Pa s	4.85	7.11	8.13	8.58	9.80	11.02
Yield stress, Pa	175	175	178	180	180	190
Density, kg/m^3	2307.1	2313.2	2315.1	2319.9	2344.8	2365.5

The flow patterns of two representative test mixes obtained from the numerical simulation at various time steps are shown in Figures. 7.5 and 7.6. The experimental

discharge times of all six mixes agree well with the simulated ones from SPH as reported in Table 7.4. The slight difference between the experimental and simulated discharge time ($t_{v\text{-}funnel}$) may be due to two possible reasons. Firstly, the assumption that the SCC particles are spherical in shape and secondly, the slight time delay in opening the bottom gate

Table 7. 4 Experimental and simulation results by SPH of V-funnel discharge times

		SCC mix designation					
		30B	40B	50B	60B	70B	80B
Discharge time ($t_{v\text{-}funnel}$), s	Experimental result	2.45	3.10	3.60	4.05	4.95	6.10
	Simulation result	2.35	2.95	3.40	3.80	4.55	5.60

The delay is the greater, the higher the pressure on the gate, i.e. the higher the density of the mix. Thus, the difference is the least in the 30B mix because it is the lightest (density 2307.1 kg/m^3) and it is the largest in the 80B mix because it is the heaviest (density 2365.5 kg/m^3). (see Table 7.5).

Table 7. 5 Force acting on the V-funnel gate for SCC mixes

Mix designation	Density, kg/m^3	Funnel volume, m^3	Force acting on the gate, N
30B	2307.1	10.51875×10^{-3}	238067
40B	2313.2		238697
50B	2315.1		238893
60B	2319.9		239388
70B	2344.8		241957
80B	2365.5		244093

It is worth stressing that the only free variable that has been altered in the simulation to get this excellent fit was the kinematic coefficient of friction between the SCC mix and the V-funnel sidewalls. The value that gave this agreement with the experimental result was equal to 0.55 N s/m. This value was held constant for all the remaining five mixes. It can be observed from the simulated flow illustrated in Figures 7.5 and 7.6 that the larger aggregates do indeed appear to remain homogeneously distributed in the mix at various times during the flow and do not settle downwards. However, this needs detailed investigation, as will be described later. The flow patterns of the remaining simulated SCC mixes are presented in Appendix G.

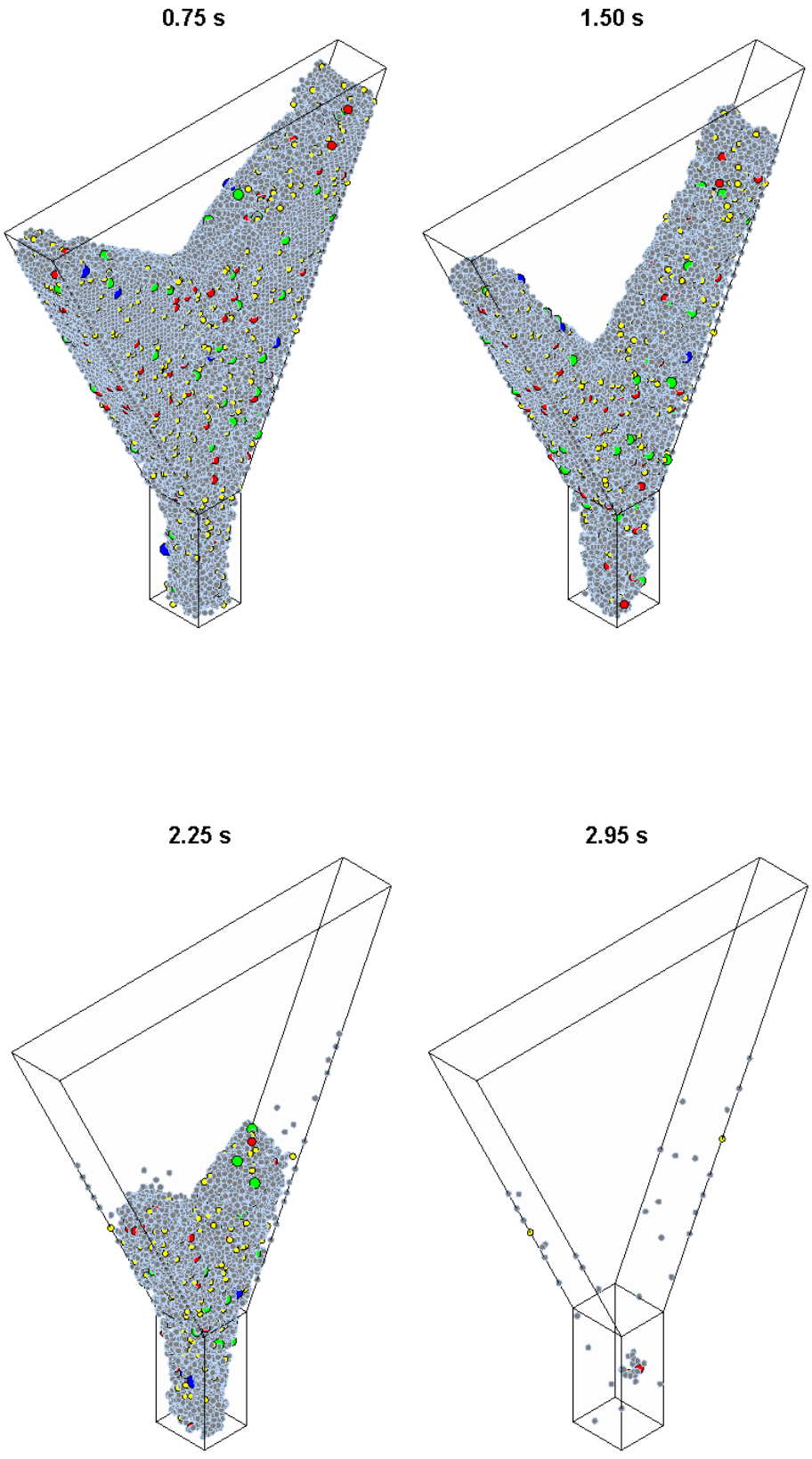

Figure 7. 5 Simulated flow patterns of 40B mix at different time steps

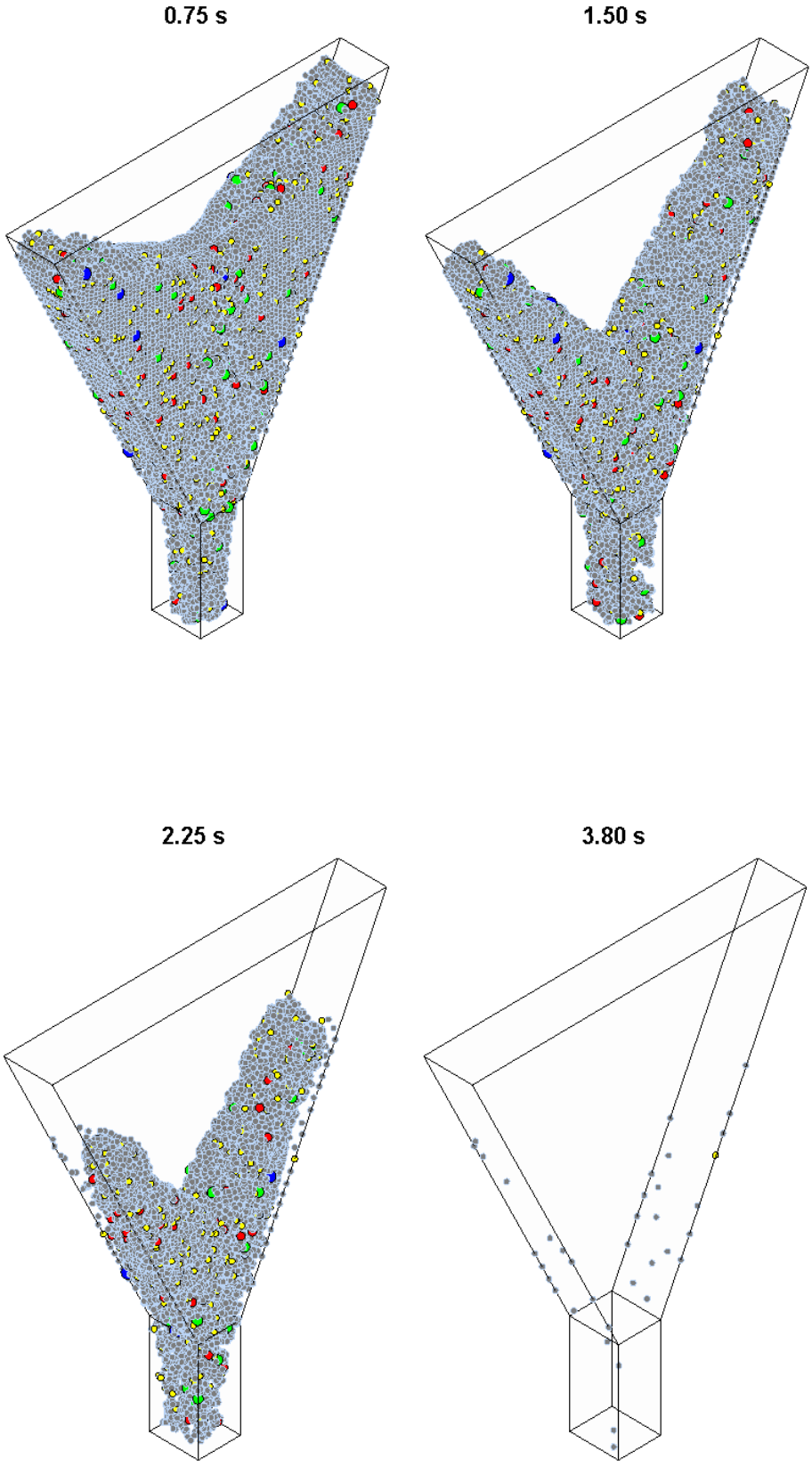

Figure 7. 6 Simulated flow patterns of 60B mix at different time steps

The three-dimensional plots in Figures 7.5 and 7.6 give an exaggerated and somewhat misleading impression that the particles have separated far away from the walls of the rectangular outlet. To get an accurate picture, the front and side views of the flow of the two mixes of Figures. 7.5 and 7.6 are shown in Figures. 7.7 and 7.8 at the beginning of flow and at a later time. It is clear that the particles do indeed lose contact with the sides of the rectangular outlet. This is because the flow now is essentially gravitational with the velocity vectors of the particles near the sides being primarily vertical so that the Dirichlet boundary condition on the normal component of the particle velocity ($\boldsymbol{v}_n$=0, Figure 7.3) is identically satisfied. This is confirmed by the velocity vector field of particles shown in Figure 7.9. For clarity of presentation, the magnified field is shown in two dimensions.

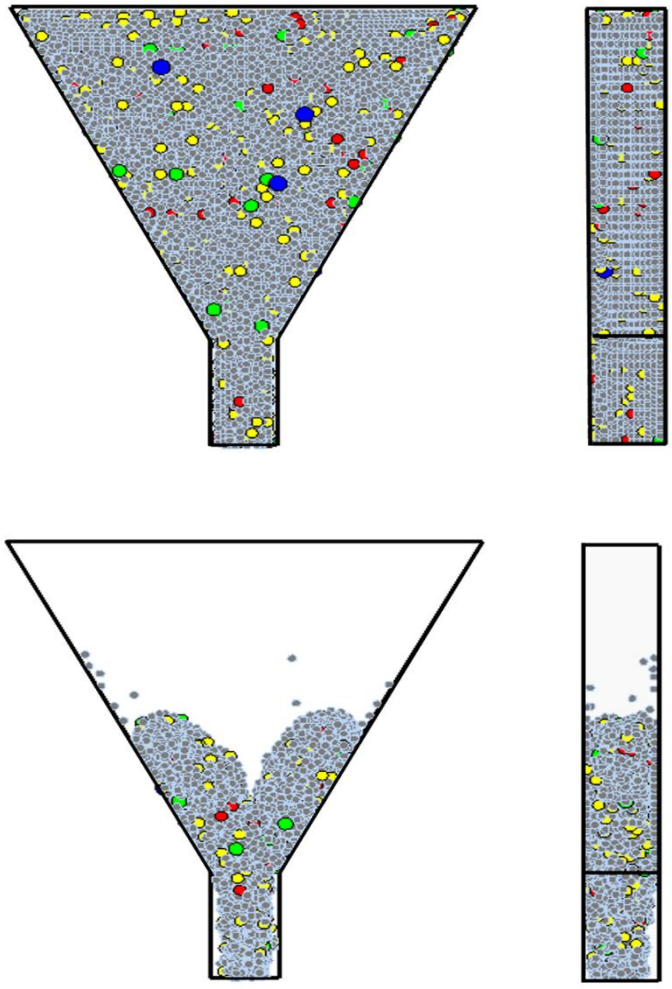

Figure 7. 7 Front and side views of the flow pattern of 40B mix at two time steps (top: 0.01 s, bottom: 2.25 s)

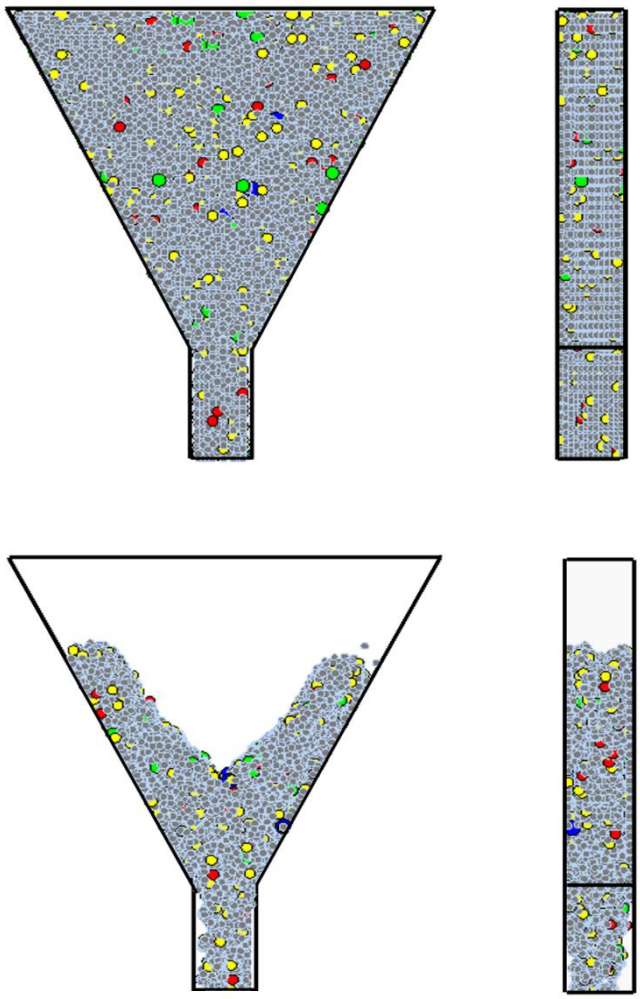

Figure 7. 8 Front and side views of the flow pattern of 60B mix at two time steps (top: 0.01 s, bottom: 2.25 s)

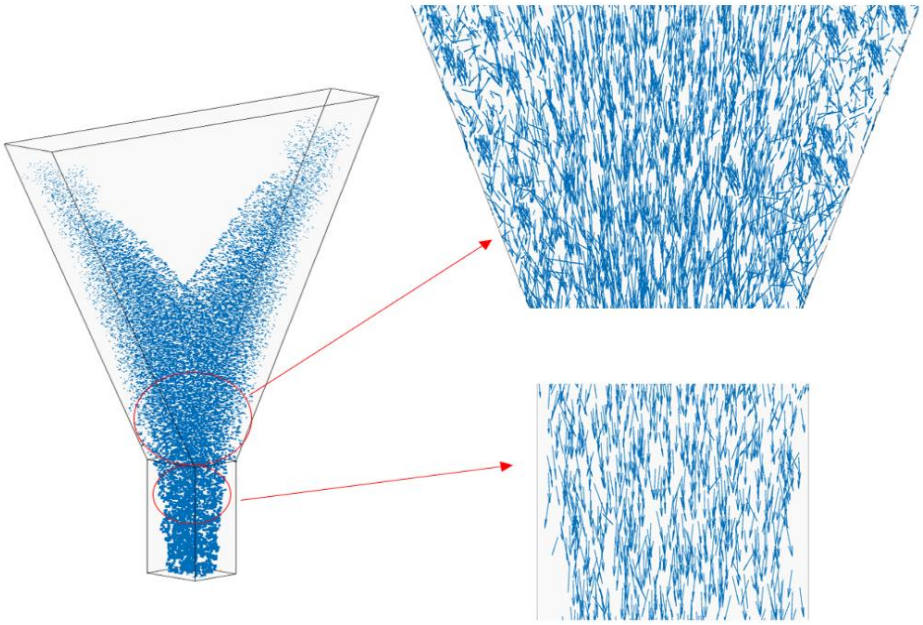

Figure 7. 9 Snapshot of the velocity vector field of a typical mix during the flow. The magnified 2D projection of the velocity vectors clearly shows that the dominant component of the particle velocities in the rectangular outlet is vertical

7.11 Large coarse aggregate distribution

The three-dimensional SPH simulation is very useful in revealing whether heavier aggregates (aggregates ≥ 8 mm) remain homogeneously distributed in the viscous SCC mix during the flow and when it has fully discharged to the container below. For the former, the distribution of large coarse aggregates in SCC mixes will be examined by two different approaches: (i) the volume of material in the funnel and the outlet rectangular portion is divided into equal halves vertically and the distribution of large coarse aggregates examined in each half, (ii) and the volume of material in the funnel and the outlet rectangular portion is divided into three zones, not necessarily of equal volume, and the distribution of large coarse aggregates examined in each zone. The first approach examines the homogeneity of the mix, whereas the second approach reveals if the heavier aggregates have settled. The distribution of large coarse aggregates in the cylindrical container used to collect the SCC mix after it has been fully discharged from the V-funnel will be examined by dividing the container into three equal volumes. The results are discussed below.

7.11.1 Distribution in vertical halves

The large coarser aggregate distribution along left and right halves of the V-funnel, as shown in Figure 7.10 was investigated on the 40B SCC mix by performing a statistical analysis on the large coarse aggregates exposed in these halves at various time steps using the Weibull cumulative distribution function (CDF).

It can be noticed from Figure 7.11 that the distributions of the large coarse aggregates of various size ranges are almost identical along the left and right halves, thus attesting to their homogeneous distribution in the mix during the flow. In addition, there is no sign of any grouping (i.e. blockage) of coarser aggregates in the narrow outlet opening.

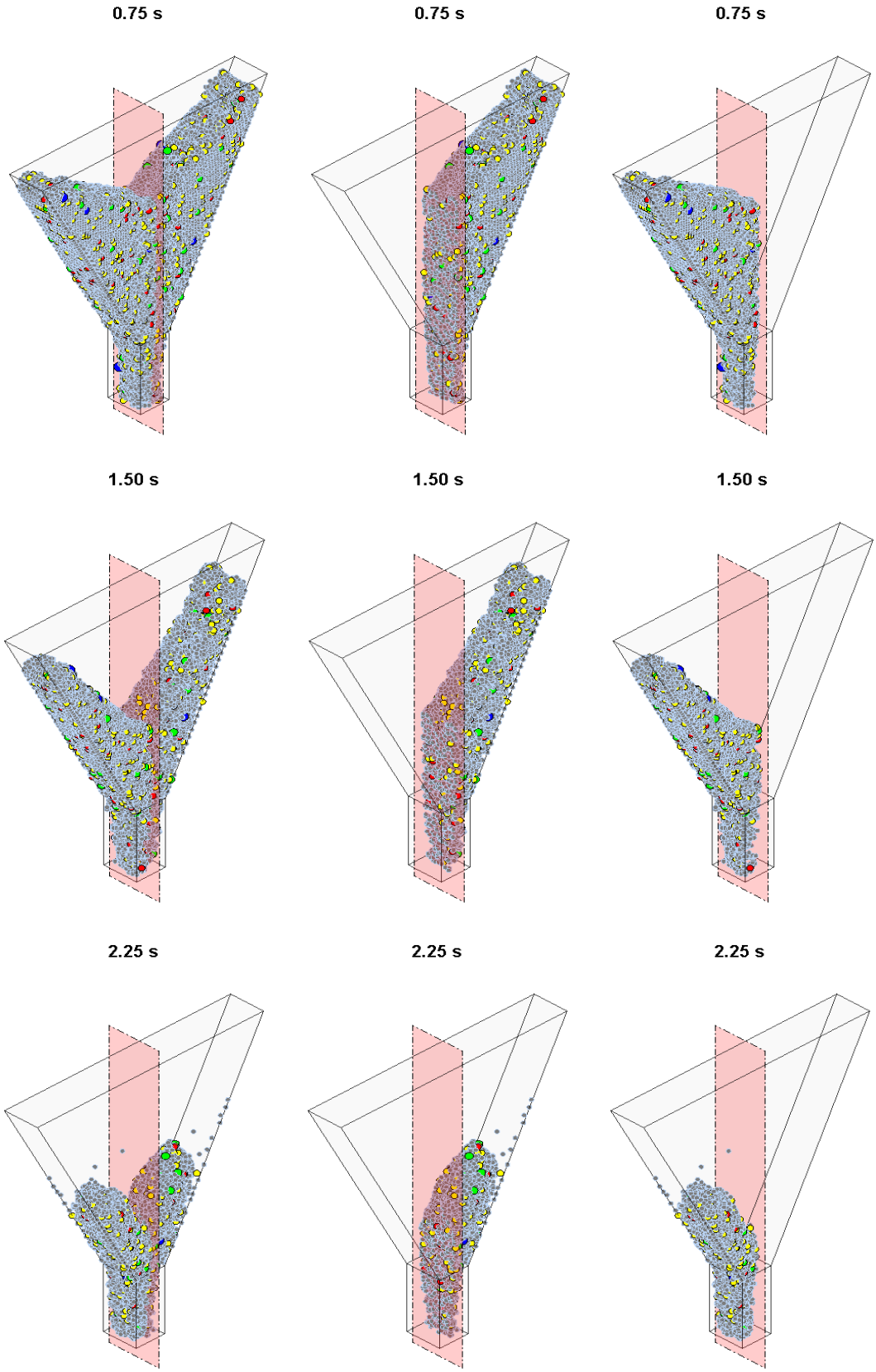

Figure 7. 10 The left and right halves of the V-funnel for 40B Mix at various time steps (top: 0.75 s, middle: 1.50 s and bottom: 2.25 s)

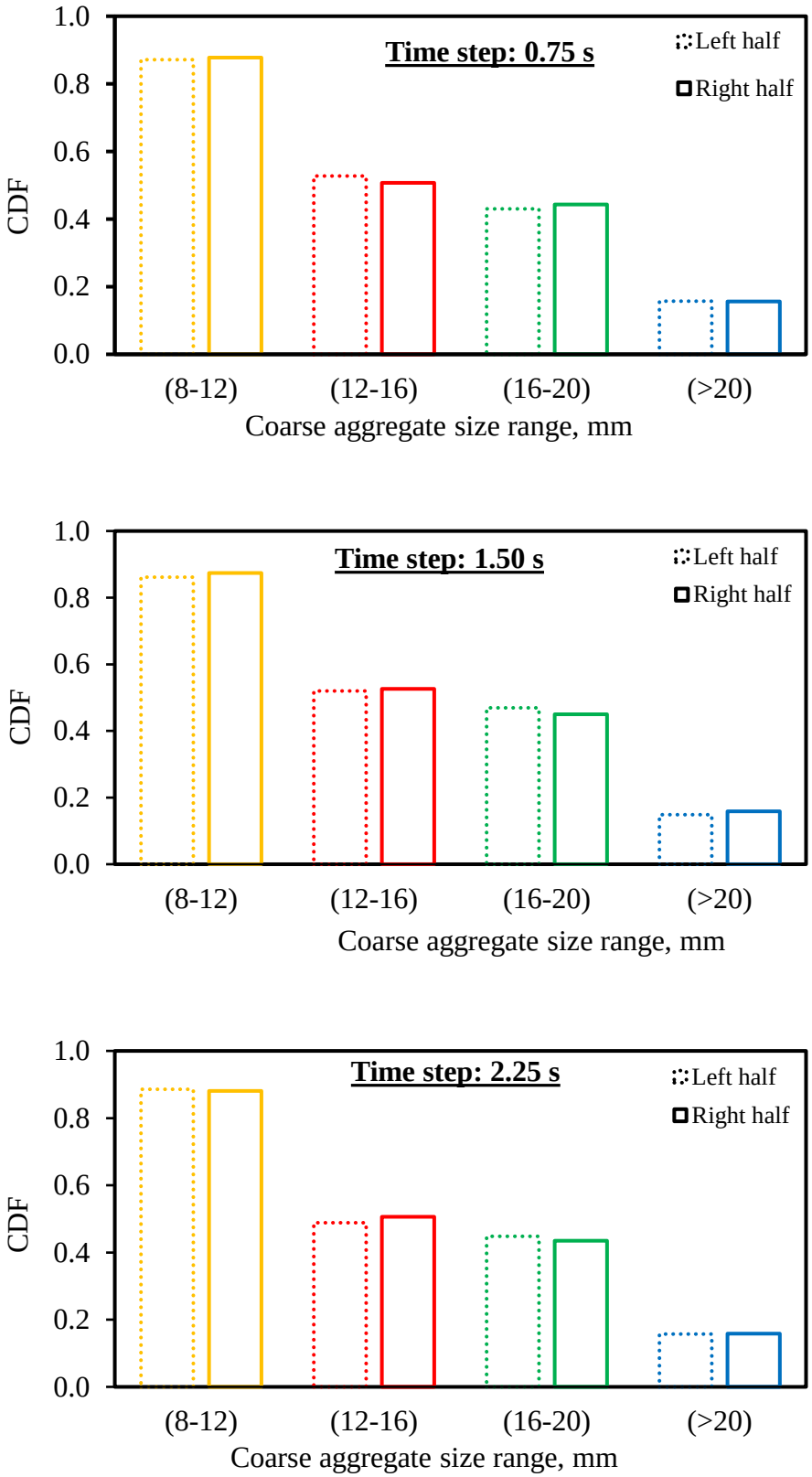

Figure 7. 11 Distribution of large coarse aggregates along the left and right halves of the V-funnel for Mix 40B at various time steps during the flow

7.11.2 Distribution in three horizontal zones

In this approach, the distribution of large coarse aggregates of the 60B SCC mix was examined by dividing the V-funnel into three zones horizontally : top, middle and bottom zones (as shown in Figure 7.12), and counting the number of large coarse aggregate particles of each size range in the volume of material within each zone. It can be seen from the Weibull cumulative distribution function in Figure 7.13 that the larger aggregates are indeed distributed almost identically in all three zones with no bias.

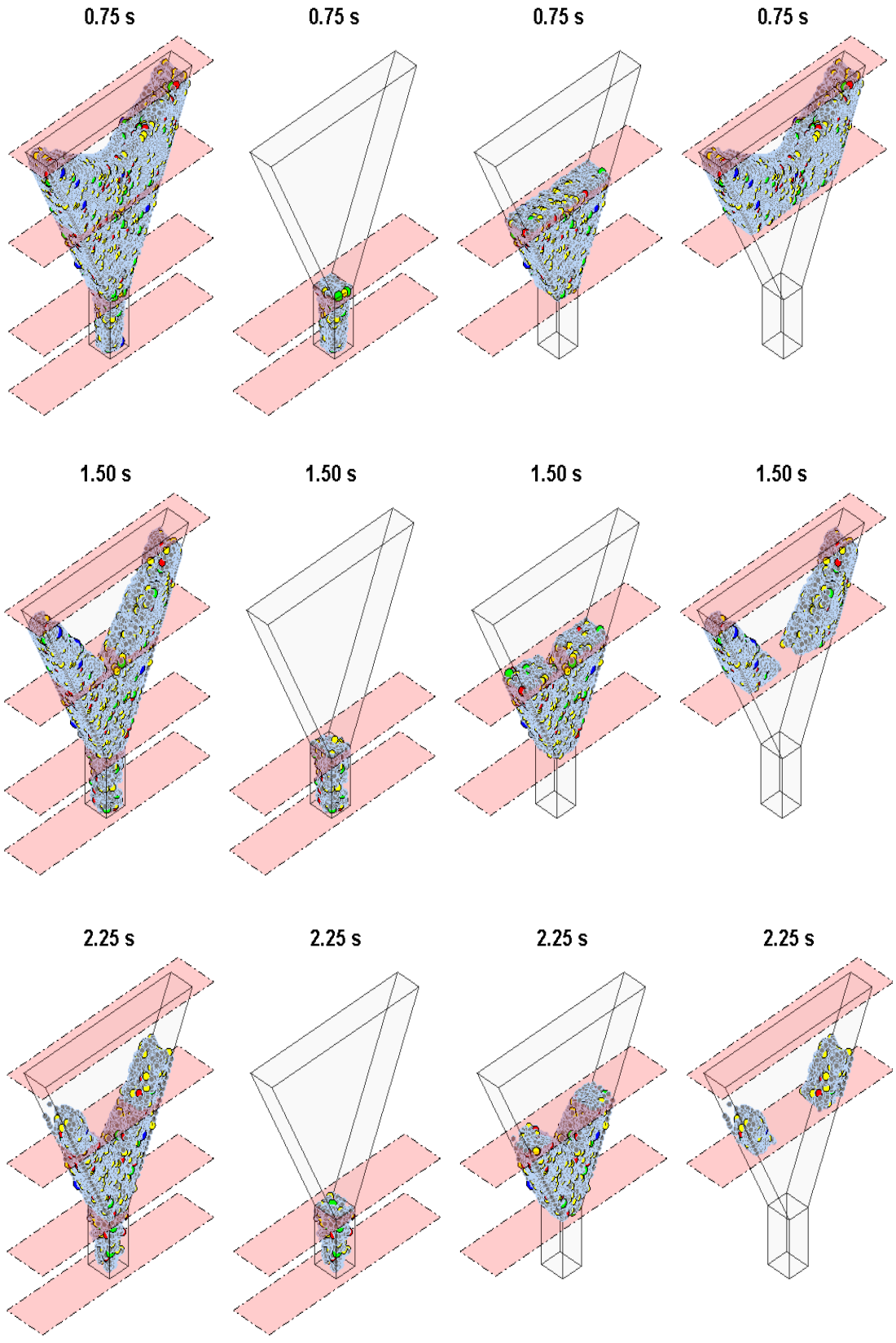

Figure 7. 12 The three zones of the V-funnel for 60B Mix at various time steps

(from left; first: the funnel; second: bottom zone; third: middle zone, and fourth: top zone)

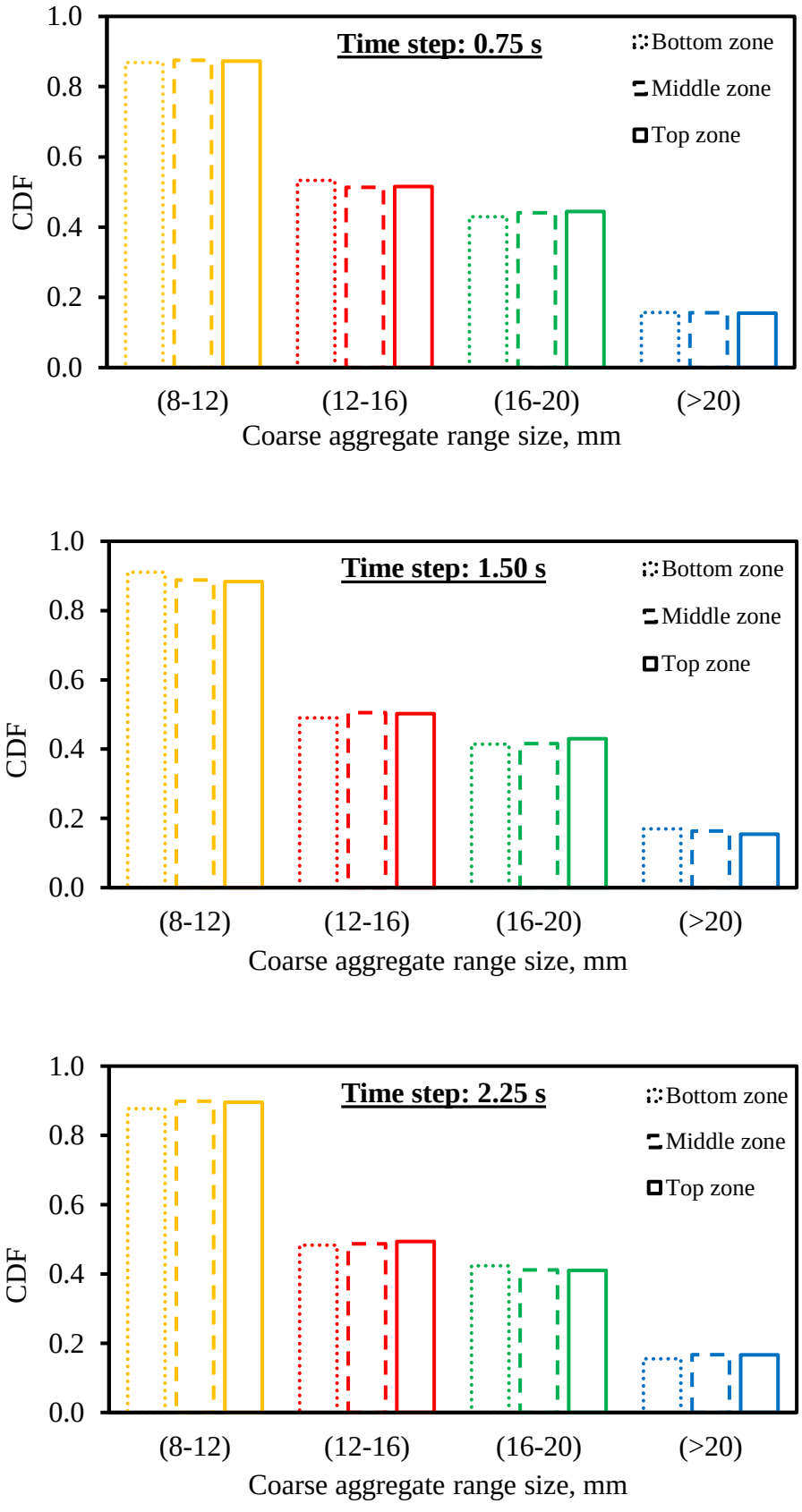

Figure 7. 13 Large coarse aggregate distributions in three zones of the V-funnel for 60B Mix at various time steps

7.11.3 Large coarse aggregate distribution in the collection container

The procedure proposed in ASTM C1610/C1610M (2011) to assess the segregation resistance of an SCC mix has been applied here to investigate the distribution of large coarse aggregates than their concentration on 40B SCC mix after it has fully discharged into a cylindrical container from the V-funnel. The distribution has been examined in three equal portions (top, middle and bottom) of the cylindrical container beneath the V-funnel (Figure 7.14). The distribution of the large coarse aggregates in each of three portions should be nearly identical to claim that there is no segregation in the mix. Equality of total concentration (i.e. mass) of large coarse aggregates in the three portions is no guarantee that the concentration in one or more portions is not dominated by one or more large aggregate size ranges.

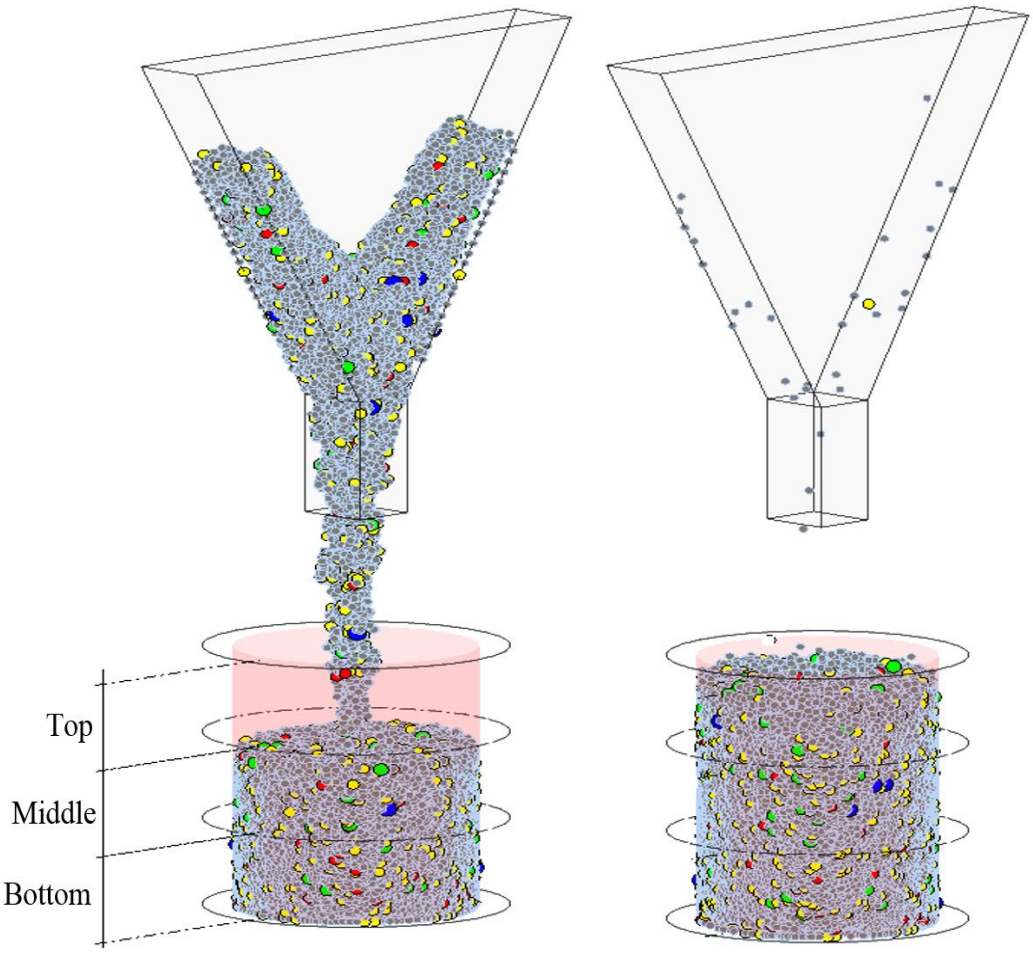

Figure 7. 14 Division of the cylindrical container into three equal portions to evaluate the distribution of large coarser aggregates in the 40B SCC (left: during discharge from V-funnel; right: after full discharge)

The Weibull cumulative distribution function (CDF) of the different large aggregate size ranges in the three equal portions of the cylindrical collection container (Figure 7.15) shows that the large aggregates do stay remarkably homogeneously distributed in the test mix without any settlement of the heavier aggregates.

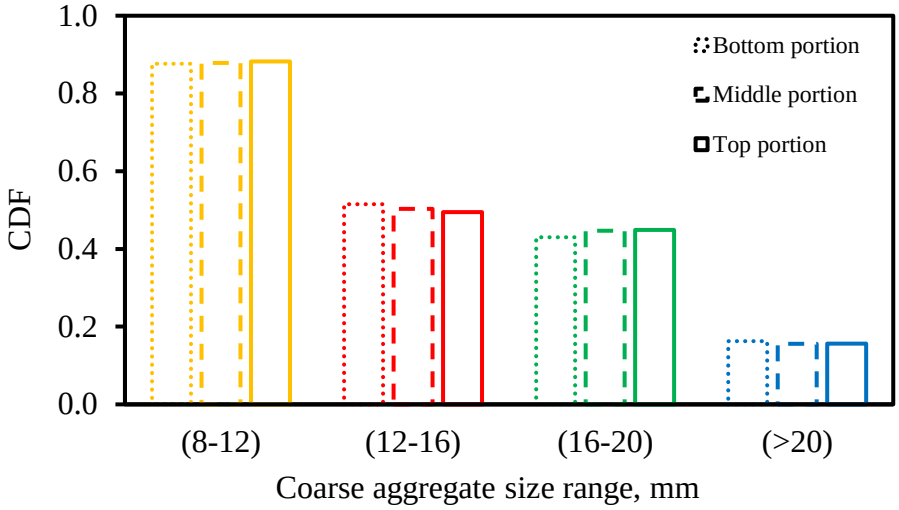

Figure 7. 15 Large coarse aggregate distributions in three portions of the cylindrical collector of the discharge from the V-funnel of 60B Mix

7.12 Remarks on simulation strategies

The flow through V-funnel has been modelled above in the real three-dimensional configuration. This takes time and effort. That is why approximate two-dimensional simulations have been reported in the past. It is unlikely that such approximate simulations will produce realistic discharge times. Moreover, two-dimensional simulations can be rather misleading because the coarse aggregate particles will appear in a single plane irrespective of their distribution. The real three-dimensional simulation shows the actual distribution of different sizes of coarse aggregate and their locations, as shown above. To compare the approximate two-dimensional simulations with the real three-dimensional ones, the two SCC mixes developed in (Zerbino et al., 2009) and simulated by Lagrangian smooth particle hydrodynamics (SPH) in the two-dimensional approximation of V-funnel in (Lashkarbolouk et al., 2013), have been simulated three-dimensionally. These mixes designated Mix-12 and Mix-20 in Table 7.6 contained coarse aggregates of maximum size 12mm and 20mm, respectively. The plastic viscosity and the yield stress have been predicted (Table 7.6) following the

same procedure as for the test SCC mixes reported above (Ghanbari and Karihaloo, 2009; Badry et al., 2016).

Table 7. 6 Rheological properties, densities and the discharge times results from 2D and 3D simulations in comparison with the experimental test of SCC mixes in the V-funnel

		Mix-12	Mix-20
Plastic viscosity, Pa s		12.68	12.95
Yield stress, Pa		175	175
Density, kg/m^3		2296	2319
Discharge time ($t_{v\text{-}funnel}$), s	Experimental (Zerbino et al., 2009)	5.50	5.80
	2D simulation (Lashkarbolouk et al., 2013)	2.95	2.50
	3D simulation [present work]	5.05	5.30

It is evident from Table 7.6 that the discharge times predicted by the 2D simulation deviate markedly from the experimental values, whereas the three-dimensional simulation values are in good agreement with the experimental results. This can be attributed to two main reasons. Firstly, the reduced frictional resistance on the side walls. Secondly, the assumption that the SCC is a single phase material. SCC is a heterogeneous composite consisting of a solid phase (aggregates) immersed in a liquid phase (mortar).

7.13 Remarks on incompressibility treatment

In the aforementioned numerical results, the incompressibility of SCC has been imposed following the incompressible SPH (ISPH) approach. It is a semi-implicit approach requiring the solution of a matrix equation at each time. The pressure Poisson equation (Eq. 7.8) is solved following the pressure-correction technique, where the velocity field is projected onto the divergence-free space (Cummins and Rudman, 1999). This was found to be a very time-consuming approach. Alternatively, the weakly compressible SPH (WSPH) approach could also be implemented to simulate the fluid flow in which the pressure is related to particle density using a stiff equation of state (Monaghan and Kos, 1999). It is an explicit time-stepping procedure with simple updating of velocities, positions and densities at each time step. However, it

requires a comparatively smaller time step in order to keep the density fluctuation down to 1% (Lee et al., 2008).

In this study, WSPH was implemented on one selected SCC mix (Mix50B) to check whether it can reduce the simulation time in comparison with the ISPH approach used above. Both numerical simulations were simultaneously conducted using a STONE PC-1210 workstation (3.60 GHz, Intel(R) Core(TM) i7-4790 CPU). It was found that WSPH does not reduce the simulation time in comparison with ISPH. The CPU times for 2 seconds of flow of the 53,846 particles were 79 and 100 hours in ISPH and WSPH respectively. This is most likely due to the smaller time step required by WSPH to reduce the occurrence of numerical instability as compared with ISPH.

7.14 Concluding remarks

A Lagrangian SPH method has been employed to model the flow of SCC mixes using a suitable Bingham model that has been coupled with the Lagrangian momentum and continuity equations. The mix characteristics of the SCC mix have been fully incorporated implicitly through the rheological properties (i.e. plastic viscosity and yield stress). The former has been calculated using the micromechanical model described in (Ghanbari and Karihaloo, 2009), while the latter determined in an inverse manner from the modelling of the cone flow by SPH (Badry et al., 2016). All the self-compacting mixes developed in Chapter 5 have been simulated in the V-funnel test. The simulation of SCC mixes followed the distribution of aggregates of different sizes (8mm and 20mm) throughout the gravitational flow. A comparison between the simulation and the experimental results is very encouraging. The developed numerical methodology is able to capture the flow behaviour of SCC mixes of varying compressive strengths through a V-funnel and to provide insight into the distribution of large aggregates during the flow and after the flow has stopped from which it is possible to assess the segregation resistance of an SCC mix.

In contrast, the two-dimensional approximation of the V-funnel is neither able to give any indication of the real distribution of large aggregates during the flow nor is it able to predict the discharge times because it underestimates the frictional resistance to free gravity flow from the V-funnel sidewalls.

Regarding the treatment of incompressibility in the numerical solution used in SPH, it is found that there is no reduction in the simulation time to be gained by approximating ISPH by a WSPH for the computational platform used in this study. In fact, the actual simulation time is longer.

The next Chapter will provide a brief and succinct summary of the major conclusions and recommendations for future work.

Chapter 8

Conclusions and recommendations for future research

8.1 Conclusions

Detailed findings of each aspect of the investigation have been drawn and reported at the end of each Chapter. This Chapter, therefore, will provide a brief and succinct summary of the major conclusions.

8.1.1 Experimental investigation

- Over the last two decades, the extensive investigations on SCC have led to confidence in its applicability in various application areas. Nevertheless, a lack of rules or specifications to be followed in its mix proportioning is still absent. This is intimately linked with its special flow properties. A new successful rational method for mix proportioning for SCC has been developed with a target plastic viscosity within a range of 3-15Pa s and a target compressive strength within a range of 30 to 80MPa, in addition to compliance with the fresh property requirements of SCC. Chapter 4 provided a clear and straightforward procedure to obtain specific quantities of SCC ingredients and minimise the need for a trial mix. This is in contrast to what has previously been proposed for SCC mix proportioning that gave only general ranges and guidelines on quantities of ingredients based significantly on trial mixes to correct any deviations in the fresh or hardened properties. At the core of the proposed rational method was the micromechanical procedure expression for the prediction of the plastic viscosity of a suspension like an SCC. Design charts have been built to be used as a guide for mix proportioning. These design charts can also be used regardless of any potential changes in the ingredient densities as the micromechanical expression depends on the volume fractions of the ingredients rather than their masses.
- The proposed mix design procedure has been validated experimentally on a series of SCC mixes in the fresh and hardened states (Chapter 5). The series of mixes, which contained different volumetric ratios of paste to solid phases, were prepared using the aforementioned design charts. All these mixes were extensively tested in the hardened state using compressive strength test and in the fresh state using the slump cone, J-ring, L-box, and V- funnel apparatus. These tests proved conclusively the validity of the mix proportioning method

in the sense that all the mixes satisfied the self-compacting criteria and achieved the desired target plastic viscosity and compressive strength. Thus, this method will reduce the extent of laboratory work considerably by eliminating the need for trial mixes to correct any deviations in the fresh or hardened properties. Furthermore, the experimental validation includes an equivalent volume replacement of the river sand fine aggregate by the coarser fraction of available limestone filler (i.e. 125μm-2mm). The results showed that the flow characteristics are not significantly affected by such environmentally friendly and economical replacement, which enhances the sustainability of the SCC mixes.

- An experimental study on the fracturing phenomena of SCC specimens under three-point bend was conducted (Chapter 6). The specimens were made from various SCC mixes differing by the coarse aggregate volume, paste to solids ratio and water to binder (*w/cm*) ratio. The experimental results revealed that there exists significant notch to depth dependency in RILEM fracture energy of SCC in which the latter decreases with an increase of the former for the same sized specimens. Also, it was found that the increase in the coarse aggregate volume fraction in a range varying from 27% to 33% led to an increase in the specific fracture energy (G_F), irrespective of the SCC mix grade. However, the increase was less pronounced in higher strength mix (grade 80) than in grades 30 and 60 of SCC. Moreover, it was found that an increase in the paste to solids (p/s) ratio resulted in a noticeable decrease in G_F, but a marginal increase in the strength itself within the same nominal strength grade. The results also showed that a more ductile SCC could be achieved with lower *w/cm*. The ductility becomes more pronounced with an increasing coarse aggregate volume fraction.
- The effect of the above composition parameters on the stress-crack opening (σ-w) relation was also evaluated. It has been revealed that the coarse aggregate volume in the mix and the mix grade dominated the critical crack opening (w_c). The critical crack opening (w_c) was more, the larger the coarse aggregate volume (or, the smaller the paste to solids ratio) in the mix. However, the higher the mix grade, the lower the critical crack opening (w_c). The characteristic

length (l_{ch}) increases with increasing coarse aggregate volume fraction, and it decreases with increasing strength grade.

8.1.2 Modelling investigation

- To reveal the flow of SCC through a narrow opening represented by the V-funnel test, an incompressible mesh-less smooth particle hydrodynamics (SPH) methodology has been implemented in the 3D configuration. The Lagrangian momentum and continuity equations have been coupled with a suitable Bingham-type constitutive model for this purpose. The mix characteristics of the SCC mix have been fully incorporated implicitly through the rheological properties (i.e. plastic viscosity and yield stress). The former has been calculated using the micromechanical model, while the latter determined in an inverse manner from the modelling of the slump cone flow by SPH. The simulation of SCC mixes followed the distribution of aggregates of different sizes (8mm and 20mm) throughout the gravitational flow. The capability of the SPH methodology has been confirmed by comparison between the experimental and modelling results of a series of SCC mixes prepared in the laboratory (Chapter 7). The results of the comparison were found to be encouraging and in very good agreement for all six simulated mixes. The developed numerical methodology was able to capture the flow behaviour of SCC mixes of varying compressive strengths through a V-funnel and to provide insight into the distribution of large aggregates during the flow. Thus, the simulation can be used to assess, discharge times, particle paths and detect possible dead zones.
- It was found that in contrast to the three-dimensional simulation, the two-dimensional approximation of the V-funnel is neither able to give any indication of the real distribution of large aggregates during the flow nor is it able to predict the discharge times. This is due to the fact that the two-dimensional approximation underestimates the frictional resistance to free gravity flow from the V-funnel sidewalls.
- The results of flow simulation indicate that SPH simulation approach is a powerful modelling tool for simulating the behaviour of fresh SCC such that

other flow related parametric studies could be performed very easily, thus saving time, effort and materials.

- The modelling approach may also bring further understanding into the effect of the yield stress and plastic viscosity on the form filling characteristics. This may help to broaden the use of rheology for characterization of the flow properties of SCC and bring it from research and development into the field of practical applications.

8.2 Recommendations for future research

Based on the work carried out for this research and the conclusions made in the previous section, the following potential future investigation areas are recommended:

- One of the most important factors that determine the reliability of the mix design approach is the right value of the estimated plastic viscosity of the mix. Therefore, it will be very useful to measure accurately the plastic viscosity of the paste using the viscometer rather than estimating its value from published data.
- The method could be enriched further if new design charts for proportioning SCC mixes are developed by going far beyond the investigated range of the plastic viscosity to include low viscosity SCC mixes (<3Pa s) or high viscosity SCC (>15Pa s). The use of high dosages of super-plasticisers can help in achieving the former, while the employment of a significant amount of fine materials and/or using viscosity modifying agents (VMAs) can be effective in producing the latter.
- It would be advisable to extend the mix design approach by employing various types and amounts of the cementitious replacement materials such as silica fume, fly ash and rice husk. The different types and quantities of replacement have no doubt an effect on the paste viscosity, which will, in turn, affect the mix viscosity.
- It will be quite useful if the proposed design procedure could be extended to be able to design SCC mixes with different ratios of fibres.

- There is no doubt that the presence of fibres will have an influence on the fracture behaviour of SCC, as it will inhibit the propagation of cracks through the brittle cementitious matrix. Thus, further analysis needs to be done to investigate the role of composition parameters (CA volume p/s, and *w/cm*) of SCC mixes alongside various ratios of fibre.
- The use of the existing numerical tools for casting prediction is very time-consuming, which prevents the numerical simulations being widely utilised in the concrete industry. Thus, it will be quite useful to investigate ways to reduce the taken time without sacrificing the accuracy.
- There is a need to simulate practical size formworks of various shapes in the presence of reinforcement to explore the full potential of SPH approach.

- It will be worthwhile to study the influence of rheological parameters of SCC mix such as plastic viscosity and yield stress in addition to the mix density on the flow behaviour and pattern. Such investigation will be highly beneficial for different applications of SCC.

References

Aarre, T. and Domone, P. 2004. *Summary report on workpackage 2: Development of mix designs and material selection*. Dansk Beton Teknik and University College London.

Abdalla, H.M. and Karihaloo, B.L. 2003. Determination of size-independent specific fracture energy of concrete from three-point bend and wedge splitting tests. *Magazine of Concrete Research* 55(2), pp. 133–141.

Abdalla, H.M. and Karihaloo, B.L. 2004. A method for constructing the bilinear tension softening diagram of concrete corresponding to its true fracture energy. *Magazine of Concrete Research* 56(10), pp. 597–604.

Abo Dhaheer, M.S. 2016. *Design and properties of self-compacting concrete mixes and its simulation in the J-ring*. PhD thesis, School of Engineering, Cardiff University, UK.

Abo Dhaheer, M.S., Al-Rubaye, M.M., Alyhya, W.S., Karihaloo, B.L. and Kulasegaram, S. 2016a. Proportioning of self-compacting concrete mixes based on target plastic viscosity and compressive strength: Experimental validation. *Journal of Sustainable Cement-Based Materials* 5(4), pp. 217–232.

Abo Dhaheer, M.S., Al-Rubaye, M.M., Alyhya, W.S., Karihaloo, B.L. and Kulasegaram, S. 2016b. Proportioning of self-compacting concrete mixes based on target plastic viscosity and compressive strength: Mix design procedure. *Journal of Sustainable Cement-Based Materials* 5(4), pp. 199–216.

Abo Dhaheer, M.S., Kulasegaram, S. and Karihaloo, B.L. 2016. Simulation of self-compacting concrete flow in the J-ring test using smoothed particle hydrodynamics (SPH). *Cement and Concrete Research* 89, pp. 27–34.

ACI Committee 211 1991. Standard practice for selecting proportions for normal, heavyweight, and mass concrete. (Reapproved 2002), pp. 1–38.

ACM Centre. 2005. *Measurement of properties of fresh self-compacting concrete-Final Report*. University of Paisley, UK.

Akcay, B., Agar-Ozbek, A.S., Bayramov, F., Atahan, H.N., Sengul, C. and Tasdemir, M.A. 2012. Interpretation of aggregate volume fraction effects on fracture behavior of concrete. *Construction and Building Materials* 28(1), pp. 437–443.

Al-Rubaye, M.M. 2016. *Self-compacting concrete: Design, properties and simulation of the flow characteristics in the L-box*. PhD thesis, School of Engineering, Cardiff University, UK.

American Concrete Institute-ACI 237R. 2007. *Self-Consolidating Concrete*. USA.

Amini, Y., Emdad, H. and Farid, M. 2011. A new model to solve fluid-hypo-elastic solid interaction using the smoothed particle hydrodynamics (SPH) method. *European Journal of Mechanics, B/Fluids* 30(2), pp. 184–194.

ASTM C1610/C1610M 2011. *Standard test method for static segregation of self-consolidating concrete using column technique*.

ASTM C1621/C1621M 2008. *Standard test method for passing ability of self-consolidating concrete by J-ring*.

Atiş, C.D. 2003. High-volume fly ash concrete with high strength and low drying shrinkage. *Journal of Materials in Civil Engineering* 15(2), pp. 153–156.

Baaijens, F.P.T. 2001. A fictitious domain/mortar element method for fluid–structure interaction. *International Journal For Numerical Methods In Fluids* 35(May 1999), pp. 743–761.

Badry, F.F. 2015. *Experimental and numerical studies in self-compacting concrete*. PhD thesis, School of Engineering, Cardiff Unversity, UK.

Badry, F.F., Kulasegaram, S. and Karihaloo, B.L. 2016. Estimation of the yield stress and distribution of large aggregates from slump flow test of self-compacting concrete mixes using smooth particle hydrodynamics simulation. *Journal of Sustainable Cement-Based Materials* 5(3), pp. 117–134.

Banfill, P., Beaupr, D., Chapdelaine, F., de Larrard, F., Domone, P., Nachbaur, L., et al. 2000. *Comparison of concrete rheometers: International tests at LCPC*. Ferraris, C. F. and Brower, L. E. ed. National Institute of Standards and Technology, Nantes, France.

Banfill, P.F. 2006. Rheology of fresh cement and concrete. *Rheology Reviews*, pp. 61–130.

BASF 2014. *MasterGlenium ACE 499: High range water reducing admixture for concrete*.

Bayraktar, S., Güdükbay, U. and Özgüç, B. 2009. GPU-based neighbor-search algorithm for particle simulations. *Journal of Graphics, GPU, and Game Tools* 14(1), pp. 31–42.

Bažant, Z.P. 1996. Analysis of work-of-fracture method for measuring fracture energy of concrete. *Journal of Engineering Mechanics* 122, pp. 138–144.

Bažant, Z.P. and Kazemi, M.T. 1991. Size-dependence of concrete fracture energy determined by RILEM work-of-fracture method. *International Journal of Fracture* 51(2), pp. 121–138.

Bažant, Z.P. and Planas, J. 1997. *Fracture and size effect in concrete and other quasi-brittle materials.* UK: CRC Press.

Benz, W. and Asphaug, E. 1994. Impact simulations with fracture: I. method and tests. *Icarus* 107(1), pp. 98–116.

Beygi, M., Kazemi, M.T., Amiri, J. V., Nikbin, I.M., Rabbanifar, S. and Rahmani, E. 2014. Evaluation of the effect of maximum aggregate size on fracture behavior of self-compacting concrete. *Construction and Building Materials* 55, pp. 202–211.

Beygi, M., Kazemi, M.T., Nikbin, I.M. and Amiri, V.J. 2013. The effect of water to cement ratio on fracture parameters and brittleness of self-compacting concrete. *Materials and Design* 50, pp. 267–276.

Beygi, M., Kazemi, M.T., Nikbin, I.M. and Amiri, V.J. 2014. The effect of aging on the fracture characteristics and ductility of self-compacting concrete. *Materials and Design* 55, pp. 937–948.

Beygi, M., Kazemi, M.T., Nikbin, I.M., Amiri, V.J., Rabbanifar, S. and Rahmani, E. 2014. The influence of coarse aggregate size and volume on the fracture behavior and brittleness of self-compacting concrete. *Cement and Concrete Research* 66, pp. 75–90.

Beygi, M.H., Berenjian, J., Omran, O.L., Nik, A.S. and Nikbin, I.M. 2013. An experimental survey on combined effects of fibers and nanosilica on the mechanical, rheological, and durability properties of self-compacting concrete. *Materials and Design* 50, pp. 1019–1029.

Bignozzi, M.C. and Sandrolini, F. 2006. Tyre rubber waste recycling in self-

compacting concrete. *Cement and Concrete Research* 36(4), pp. 735–739.

Billberg, P., Petersson, Ö., Westerholm, M., Wüstholz, T. and Reinhardt, H. 2004. Summary report on work package 3.2: Test methods for passing ability. *Cement and Concrete Research Institute , CBI Universität Stuttgart , IWB*.

Bonen, D. and Shah, S.P. 2005. Fresh and hardened properties of self-consolidating concrete. *Concrete construction* 104(7), pp. 14–26.

Bonet, J. and Kulasegaram, S. 2000. Correction and stabilization of smooth particle hydrodynamics methods with applications in metal forming simulations. *International Journal for Numerical Methods in Engineering* 47, pp. 1189–1214.

Bonet, J. and Peraire, J. 1991. An alternating digital tree (ADT) algorithm for 3D geometric searching and intersection problems. *International Journal for Numerical Methods in Engineering* 31(1), pp. 1–17.

Bosiljkov, V.B. 2003. SCC mixes with poorly graded aggregate and high volume of limestone filler. *Cement and Concrete Research* 33(9), pp. 1279–1286.

Boukendakdji, O., Kadri, E. and Kenai, S. 2012. Effects of granulated blast furnace slag and super-plasticizer type on the fresh properties and compressive strength of self-compacting concrete. *Cement and Concrete Composites* 34(4), pp. 583–590.

Bouziani, T. 2013. Assessment of fresh properties and compressive strength of self-compacting concrete made with different sand types by mixture design modelling approach. *Construction and Building Materials* 49, pp. 308–314.

Bouzoubaa, N. and Lachemi, M. 2001. Self-compacting concrete incorporating high-volumes of class F fly ash : Preliminary results. *Cement and Concrete Research* 31, pp. 413–420.

BS 1881-121 1983. Method for determination of static modulus of elasticity in compression.

BS 8500-1 2006. Concrete-complementary: Method of specifying and guidnace for the specifier.

BS EN 12350-8 2010. Testing fresh concrete: Self-compacting concrete-slump flow test.

BS EN 12350-9 2010. Testing fresh concrete: Self-compacting concrete-V-funnel test.

BS EN 12390-3 2009. Testing hardened concrete: Compressive strength of test specimens.

BS EN 12390-6 2009. Testing hardened concrete: Tensile splitting strength of test specimens.

BS EN 197-1 2011. Cement: Composition, specifications and conformity criteria for common cements.

BS EN 206-9 2010. Additional rules for self-compacting concrete (SCC).

Bui, H.H., Fukagawa, R., Sako, K. and Ohno, S. 2008. Lagrangian meshfree particles method (SPH) for large deformation and failure flows of geomaterial using elastic-plastic soil constitutive model. *International Journal for Numerical and Analytical Methods in Geomechanics* 32, pp. 189–213.

Bui, V.K., Akkaya, Y. and Shah, S.P. 2002. Rheological model for self-consolidating concrete. *ACI Materials Journal* 99(6), pp. 549–559.

Bui, V.K. and Montgomery, D. 1999. Drying shrinkage of self-compacted concrete containing mild limestone. In: Å. Skarendahl and Ö. Petersson ed. *1st International RILEM Symposium on Self-Compacting Concrete*. RILEM Publications SARL, Stockholm, Sweden, pp. 227–238.

Burke, D.R., Moslemi-Tabrizi, S. and Smy, T.J. 2010. Simulation of inhomogeneous models using the finite cloud method. *Materialwissenschaft und Werkstofftechnik* 41(5), pp. 336–340.

Carlsward, J., Emborg, M., Utsi, S. and Oberg, P. 2003. Effect of constituents on the workability and rheology of self-compacting concrete. In: O. Wallevik and I. Nielsson ed. *3rd International RILEM Symposium on Self-Compacting Concrete*. RILEM Publications SARL, Reykjavik, Iceland, pp. 143–153.

Carpinteri, A. and Brighenti, R. 2010. Fracture behaviour of plain and fiber-reinforced concrete with different water content under mixed mode loading. *Materials and Design* 31(4), pp. 2032–2042.

Carpinteri, A. and Chiaia, B. 1996. Size effects on concrete fracture energy: Dimensional transition from order to disorder. *Materials and Structures* 29(5), pp. 259–266.

Chan, Y.W., Chen, Y.S. and Liu, Y.S. 2003. Development of bond strength of reinforcement steel in self-consolidating concrete. *ACI Structural Journal* 100(4), pp. 490–498.

Chaniotis, a. K., Poulikakos, D. and Koumoutsakos, P. 2002. Remeshed smoothed particle hydrodynamics for the simulation of viscous and heat conducting flows. *Journal of Computational Physics* 182(1), pp. 67–90.

Chen, J.K., Beraun, J.E. and Jih, C.J. 1999. Improvement for tensile instability in smoothed particle hydrodynamics. *Computational Mechanics* 23(4), pp. 279–287.

Chidiac, S.E. and Mahmoodzadeh, F. 2009. Plastic viscosity of fresh concrete-A critical review of predictions methods. *Cement and Concrete Composites* 31(8), pp. 535–544.

Chorin, A.J. 1968. Numerical solution of the Navier-Stokes equations. *Mathematics of Computation* 22(104), pp. 745–762.

Cifuentes, H. and Karihaloo, B.L. 2013. Determination of size-independent specific fracture energy of normal and high strength self-compacting concrete from wedge splitting tests. *Construction and Building Materials* 48(2), pp. 548–553.

Cleary, P., Ha, J., Alguine, V. and Nguyen, T. 2002. Flow modelling in casting processes. *Applied Mathematical Modelling* 26(2), pp. 171–190.

Colagrossi, A. and Landrini, M. 2003. Numerical simulation of interfacial flows by smoothed particle hydrodynamics. *Journal of Computational Physics* 191(2), pp. 448–475.

Collepardi, M. 1998. Admixtures used to enhance placing characteristics of concrete. *Cement and Concrete Composites* 20, pp. 103–112.

Collepardi, M., Collepardi, S. and Troli, R. 2007. Properties of SCC and flowing concrete. In: Kraus, R. N. Naik, T. R. Pouya, P. ed. *Proceeding International Conference: Sustainable Construction Materials and Technologies*. Coventry, UK: Special papers proceedings, UW Milwaukee CBU, pp. 25–31.

Corinaldesi, V. and Moriconi, G. 2004. Durable fiber reinforced self-compacting concrete. *Cement and Concrete Research* 34(2), pp. 249–254.

Cummins, S.J. and Rudman, M. 1999. An SPH projection method. *Journal of*

Computational Physics 152(2), pp. 584–607.

Daczko, J.A. 2012. *Self-consolidating concrete: Applying what we know*. USA: Spon Press.

Dalrymple, R.A. and Rogers, B.D. 2006. Numerical modeling of water waves with the SPH method. *Coastal Engineering* 53, pp. 141–147.

Deeb, R. 2013. *Flow of self-compacting concrete*. PhD thesis, School of Engineering, Cardiff University, UK.

Deeb, R., Ghanbari, A. and Karihaloo, B.L. 2012. Development of self-compacting high and ultra high performance concretes with and without steel fibres. *Cement and concrete composites* 34(2), pp. 185–190.

Deeb, R. and Karihaloo, B.L. 2013. Mix proportioning of self-compacting normal and high-strength concretes. *Magazine of Concrete Research* 65(9), pp. 546–556.

Deeb, R., Karihaloo, B.L. and Kulasegaram, S. 2014. Reorientation of short steel fibres during the flow of self-compacting concrete mix and determination of the fibre orientation factor. *Cement and Concrete Research* 56, pp. 112–120.

Deeb, R., Kulasegaram, S. and Karihaloo, B.L. 2014a. 3D modelling of the flow of self-compacting concrete with or without steel fibres. Part I: Slump flow test. *Computational Particle Mechanics* 1, pp. 373–389.

Deeb, R., Kulasegaram, S. and Karihaloo, B.L. 2014b. 3D modelling of the flow of self-compacting concrete with or without steel fibres. Part II: L-box test and the assessment of fibre reorientation during the flow. *Computational Particle Mechanics* 1, pp. 391–408.

Dehn, F., Holschemacher, K. and Weiße, D. 2000. Self-compacting concrete (SCC): Time development of the material properties and the bond behaviour. *LACER* 5, pp. 115–124.

Desnerck, P., Boel, V., Craeye, B. and Itterbeeck, P.V. 2014. Mechanical properties of self-compacting concrete. In: K. H. Khayat and G. De Schutter ed. *Self-Compacting Concrete - State-of-the-Art Report of RILEM*. RILEM Publications SARL, pp. 15–72.

Desnerck, P., Itterbeeck, P. V., Boel, V., Craeye, B. and De Schutter, G. 2011. Survey on the mechanical properties of self-compacting concrete : 20 years of research. In:

36th Conference on Our World in Concrete and Structures. Singapore: CI-Premier PTE LTD, pp. 4–11.

Dilts, G.A. 1998. Moving-least-squares hydrodynamics - I. Consistency and stability. *International Journal for Numerical Methods in Engineering* 44(8), pp. 1115–1155.

Dinakar, P., Babu, K.G. and Santhanam, M. 2008. Durability properties of high volume fly ash self-compacting concretes. *Cement and Concrete Composites* 30(10), pp. 880–886.

Dinakar, P., Reddy, M.K. and Sharma, M. 2013. Behaviour of self-compacting concrete using Portland pozzolana cement with different levels of fly ash. *Materials and Design* 46, pp. 609–616.

Dinakar, P., Sethy, K.P. and Sahoo, U.C. 2013. Design of self-compacting concrete with ground granulated blast furnace slag. *Materials and Design* 43, pp. 161–169.

Domone, P.L. 2000. Mix design. In: Å. Skarendahl and Ö Petersson ed. *Self-Compacting Concrete - State-of-the-Art Report of RILEM TC 174-SCC*. RILEM Publications SARL, France, pp. 49–65.

Domone, P.L. 2003. Fresh concrete: Advanced concrete technology. In: Newman, J. and Choo, B. eds. UK: Elsevier Ltd.

Domone, P.L. 2006. Self-compacting concrete: An analysis of 11 years of case studies. *Cement and Concrete Composites* 28(2), pp. 197–208.

Domone, P.L. 2007. A review of the hardened mechanical properties of self-compacting concrete. *Cement and Concrete Composites* 29(1), pp. 1–12.

Domone, P.L. 2010. *Proportioning of self-compacting concrete – the UCL method*. Department of Civil , Environmental and Geomatic Engineering, University College of London, UK.

Domone, P.L. and Illston, J. 2010. *Construction materials: Their nature and behaviour*. New York, USA: Spon Press.

Dransfield, J. 2003. Admixtures for concrete, mortar, and grout. In: Newman, J. and Choo, B. S. ed. *In Advanced Concrete Technology*. USA: Elsevier Ltd.

Duan, K., Hu, X. and Wittmann, F.H. 2003. Boundary effect on concrete fracture and non-constant fracture energy distribution. *Engineering Fracture Mechanics* 70(16),

pp. 2257–2268.

Duan, K., Hu, X. and Wittmann, F.H. 2007. Size effect on specific fracture energy of concrete. *Engineering Fracture Mechanics* 74, pp. 87–96.

Dufour, F. and Pijaudier-Cabot, G. 2005. Numerical modelling of concrete flow: Homogenous approach. *International Journal for Numerical and Analytical Methods in Geomechanics* 29(4), pp. 395–416.

Dyka, C.T., Randles, P.W. and Ingel, R.P. 1997. Stress points for tension instability in SPH. *International Journal for Numerical Methods in Engineering* 40(13), pp. 2325–2341.

Edamatsu, Y., Nishida, N. and Ouchi, M. 1998. A rational mix design method for self-compacting concrete interaction between coarse aggregate and mortar particles. In: Å. Skarendahl and Ö. Pettersson ed. *1st International RILEM Symposium on Self-Compacting Concrete*. RILEM Publications SARL, Stockholm, Sweden, pp. 309–320.

EFNARC 2005. *The European guidelines for self-compacting concrete; specification, production and use*.

Elinwa, A.U., Ejeh, S.P. and Mamuda, A.M. 2008. Assessing of the fresh concrete properties of self-compacting concrete containing sawdust ash. *Construction and Building Materials* 22(6), pp. 1178–1182.

Emborg, M. 2000. *Self-compacting concrete: Mixing and transport: Final report of task 8.1*. Brite EuRam Proposal.

Felekoğlu, B. 2008. A comparative study on the performance of sands rich and poor in fines in self-compacting concrete. *Construction and Building Materials* 22(4), pp. 646–654.

Felekoğlu, B. and Sarikahya, H. 2008. Effect of chemical structure of polycarboxylate-based superplasticizers on workability retention of self-compacting concrete. *Construction and Building Materials* 22(9), pp. 1972–1980.

Felekoğlu, B., Türkel, S. and Baradan, B. 2007. Effect of water/cement ratio on the fresh and hardened properties of self-compacting concrete. *Building and Environment* 42(4), pp. 1795–1802.

Ferrara, L., Park, Y.D. and Shah, S.P. 2007. A method for mix design of fiber-

reinforced self-compacting concrete. *Cement and Concrete Research* 37(6), pp. 957–971.

Ferraris, C.F. 1999. Measurement of the rheological properties of high performance concrete: State of the art report. *Journal of Research of the National Institute of Standards and Technology* 104(5), pp. 461–478.

Ferraris, C.F. and Martys, N.S. 2012. Concrete rheometers. In: Roussel, N. ed. *Understanding the Rheology of Concrete*. Woodhead Publishing Limited, pp. 63–82.

Feys, D., Heirman, G., Schutter, G. De, Verhoeven, R., Vandewalle, L. and Gemert, D. Van 2007. Comparison of two concrete rheometers for shear thickening behaviour of SCC. In: G. De Schutter and V. Boel ed. *5th International RILEM Symposium on Self-Compacting Concrete*. RILEM Publications SARL, Ghent, Belgium, pp. 365–370.

Figueiras, H., Nunes, S., Coutinho, J.S. and Andrade, C. 2014. Linking fresh and durability properties of paste to SCC mortar. *Cement and Concrete Composites* 45, pp. 209–226.

Frandsen, J. and Schultz, K. 1997. *Investigation of poker vibration: Concrete execution*. Danish Road Directorate, Ministry of Transport.

Gao, J. and Fourie, A. 2015. Spread is better: An investigation of the mini-slump test. *Minerals Engineering* 71, pp. 120–132.

Garboczi, E.J. 2002. Three-dimensional mathematical analysis of particle shape using X-ray tomography and spherical harmonics: Application to aggregates used in concrete. *Cement and Concrete Research* 32(10), pp. 1621–1638.

Ghanbari, A. and Karihaloo, B.L. 2009. Prediction of the plastic viscosity of self-compacting steel fibre reinforced concrete. *Cement and Concrete Research* 39(12), pp. 1209–1216.

Gibbs, J.C. and Zhu, W. 1999. Strength of hardened self-compacting concrete. In: Å. Skarendahl and Ö. Petersson ed. *1st International RILEM Symposium on Self-Compacting Concrete*. RILEM Publications SARL, Stockholm, Sweden, pp. 199–209.

Gingold, R.A. and Monaghan, J.J. 1977. Smoothed particle hydrodynamics: theory and application to non-spherical stars. *Monthly Notices of the Royal Astronomical*

Society 181(3), pp. 375–389.

Gram, A. 2009. Numerical modelling of self-compacting concrete flow. MSc thesis, Royal Institute of Technology, Department of Civil and Architectural Engineering, Division of Structural Design and Bridges, Stockholm, Sweden.

Gram, A. and Silfwerbrand, J. 2011. Numerical simulation of fresh SCC flow: applications. *Materials and Structures* 44(4), pp. 805–813.

Gram, H. and Piiparinen, P. 1999. Properties of SCC especially early age and long term shrinkage and salt frost resistance. In: Å. Skarendahl and Ö. Petersson ed. *1st International RILEM Symposium on Self-Compacting Concrete*. RILEM Publications SARL, Stockholm, Sweden, pp. 211–225.

Grezeszczyk, S. and Lipowski, G. 1997. Effect of content and particalsize distribution of high-calcium fly ash on the rheological properties of cement pastes. *Cement and Concrete Research* 27(6), pp. 907–916.

Guinea, G.V., Planas, J. and Elices, M. 1992. Measurement of the fracture energy using three-point bend tests: Part 1-Influence of experimental procedures. *Materials and Structures* 25(4), pp. 212–218.

Guinea, G.V., Planas, J. and Elices, M. 1994. A general bilinear fit for the softening curve of concrete. *Materials and Structures* 27(2), pp. 99–105.

Heirman, G., Hendrickx, R., Vandewalle, L., Van Gemert, D., Feys, D., De Schutter, G., et al. 2009. Integration approach of the Couette inverse problem of powder type self-compacting concrete in a wide-gap concentric cylinder rheometer: Part II. Influence of mineral additions and chemical admixtures on the shear thickening flow behaviour. *Cement and Concrete Research* 39(3), pp. 171–181.

Heymann, L. and Aksel, N. 2007. Transition pathways between solid and liquid state in suspensions. *Physical Review* 75, pp. 1–9.

Hillerborg, A., Modeer, M. and Petersson, P.E. 1976. Analysis of crack formation and crack growth in concrete by means of fracture mechanics and finite elements. *Cement and Concrete Research* 6, pp. 773–782.

Ho, D.W.S., Sheinn, A.M.M., Ng, C.C. and Tam, C.T. 2002. The use of quarry dust for SCC applications. *Cement and Concrete Research* 32(4), pp. 505–511.

Hoffmann, C. and Leemann, A. 2005. Properties of self-compacting and conventional concrete-differences and similarities. *Magazine of Concrete Research* 57(6), pp. 315–319.

Holschmacher, K. and Klug, Y. 2002. A database for the evaluation of hardened properties of SCC . *LACER*, pp. 123–134.

Holton, I. 2003. *A review of the potential use of secondary and recycled aggregates in self-compacting concrete: Final report*. DTI Project Report, Building Research Establishment Ltd.

Hu, X. and Duan, K. 2004. Influence of fracture process zone height on fracture energy of concrete. *Cement and Concrete Research* 34(8), pp. 1321–1330.

Hu, X. and Wittmann, F. 1992. Fracture energy and fracture process zone. *Materials and Structures* 25(6), pp. 319–326.

Hu, X. and Wittmann, F. 2000. Size effect on toughness induced by crack close to free surface. *Engineering Fracture Mechanics* 65, pp. 209–221.

Jin, J. 2002. *Properties of mortar for self-compacting concrete*. PhD thesis, Department of Civil and Environmental Engineering University College London, UK.

Kadri, E.H. and Duval, R. 2002. Effect of ultra fine particles on heat of hydration of cement mortars. *ACI Materials Journal* 99(2), pp. 138–142.

Kanadasan, J. and Razak, H.A. 2014. Mix design for self-compacting palm oil clinker concrete based on particle packing. *Materials and Design* 56, pp. 9–19.

Karihaloo, B.L. 1995. *Fracture Mechanics and Structural Concrete*. UK: Addison Wesley Longman.

Karihaloo, B.L., Abdalla, H.M. and Imjai, T. 2003. A simple method for determining the true specific fracture energy of concrete. *Magazine of Concrete Research* 55(5), pp. 471–481.

Karihaloo, B.L. and Ghanbari, A. 2012. Mix proportioning of self-compacting high and ultra high performance concretes with and without steel fibres. *Magazine of Concrete Research* 64(12), pp. 1089–1100.

Karihaloo, B.L., Murthy, R.A., Iyer, N.R., Karihaloo, B.L., Iyer, N.R., Raghu, P.B.K., et al. 2013. Determination of size- independent specific fracture energy of concrete

mixes by the tri-linear model. *Cement and Concrete Research* 49, pp. 82–88.

Kasemchaisiri, R. and Tangtermsirikul, S. 2008. Deformability prediction model for self-compacting concrete. *Magazine of Concrete Research* 60(2), pp. 93–108.

Kelecy, F.J. and Pletcher, R.H. 1997. The development of a free surface capturing approach for multidimensional free surface flows in closed containers. *Journal of Computational Physics* 138(2), pp. 939–980.

Khaloo, A., Raisi, E.M., Hosseini, P. and Tahsiri, H. 2014. Mechanical performance of self-compacting concrete reinforced with steel fibers. *Construction and Building Materials* 51, pp. 179–186.

Khayat, K., Hu, C. and Monty, H. 1999. Stability of self-consolidating concrete, advantages, and potential applications. In: Å. Skarendahl, Ö. Petersson ed. *1st International RILEM Symposium on Self-Compacting Concrete*. RILEM Publications SARL, Stockholm, Sweden, pp. 143–152.

Khayat, K.H. 1998. Use of viscosity modifying admixture to reduce top-bar effect of anchored bars cast with fluid concrete. *ACI Materials Journal* 95(2), pp. 158–167.

Khayat, K.H. 1999. Workability, testing, and performance of self-consolidating concrete. *ACI Materials Journal* 96(3), pp. 346–353.

Khayat, K.H. 2000. Optimization and performance of air-entrained, self-consolidating concrete. *ACI Structural Journal* 97(5), pp. 526–535.

Khayat, K.H., Ghezal, A. and Hadriche, M.S. 1999. Factorial design model for proportioning self-consolidating concrete. *Materials and Structures* 32(9), pp. 679–686.

Kheder, G.F. and Al Jadiri, R.S. 2010. New method for proportioning self-consolidating concrete based on compressive strength requirements. *ACI Materials Journal* 107(5), pp. 490–497.

Kim, B.G., Jiang, S., Jolicoeur, C. and Aïtcin, P.C. 2000. Adsorption behavior of PNS superplasticizer and its relation to fluidity of cement paste. *Cement and Concrete Research* 30(6), pp. 887–893.

Kim, J.H., Noemi, N. and Shah, S.P. 2012. Effect of powder materials on the rheology and formwork pressure of self-consolidating concrete. *Cement and Concrete*

Composites 34(6), pp. 746–753.

Koehler, E.P. and Fowler, D.W. 2007. *Aggregates in self-consolidating concrete*. International Center for Aggregate Research(ICAR), University of Texas, Austin.

Koshizuka, S., Nobe, A. and Oka, Y. 1998. Numerical analysis of breaking waves using the moving particle semi-implicit method. *International Journal for Numerical Methods in Fluids* 26(7), pp. 751–769.

Kosmatka, S.H., Kerkhoff, B. and Panarese, W.C. 2003. *Design and control of concrete mixtures*. 14th ed. Skokie, Illinois, USA: Portland Cement Association (PCA).

Krieger, I.M. and Dougherty, T.J. 1959. A mechanism for Non-Newtonian flow in suspensions of rigid spheres. *Transactions of The Society of Rheology* 3, pp. 137–152.

de Kruif, C.G., Van Iersel, E.M.F., Vrij, A. and Russel W. B. 1985. Hard sphere colloidal dispersions: Viscosity as a function of shear rate and volume fraction. *The Journal of Chemical Physics* 83(9), pp. 4717–4725.

Kulasegaram, S. and Karihaloo, B.L. 2013. Fibre-reinforced, self-compacting concrete flow modelled by smooth particle hydrodynamics. *Proceedings of the Institution of Civil Engineers - Engineering and Computational Mechanics* 166(1), pp. 22–31.

Kulasegaram, S., Karihaloo, B.L. and Ghanbari, A. 2011. Modelling the flow of self-compacting concrete. *International Journal for Numerical and Analytical Methods in Geomechanics* 35(6), pp. 713–723.

Kuroda, M., Watanabe, T. and Terashi, N. 2000. Increase of bond strength at interfacial transition zone by the use of fly ash. *Cement and Concrete Research* 30(2), pp. 253–258.

Kuzmin, D. 2006. Introduction to computational fluid dynamics. *Institute of Applied Mathematics, Lecture in the University of Dortmund, Germany*.

Lashkarbolouk, H., Halabian, A.M. and Chamani, M.R. 2014. Simulation of concrete flow in V-funnel test and the proper range of viscosity and yield stress for SCC. *Materials and Structures* 47(10), pp. 1729–1743.

Lee, E.S., Moulinec, C., Xu, R., Violeau, D., Laurence, D. and Stansby, P. 2008. Comparisons of weakly compressible and truly incompressible algorithms for the SPH

mesh free particle method. *Journal of Computational Physics* 227(18), pp. 8417–8436.

Li, L.G. and Kwan, A.K.H. 2013. Concrete mix design based on water film thickness and paste film thickness. *Cement and Concrete Composites* 39, pp. 33–42.

Li, L.G. and Kwan, a. K.H. 2011. Mortar design based on water film thickness. *Construction and Building Materials* 25(5), pp. 2381–2390.

Libersky, L.D., Petschek, A.G., Carney, T.C., Hipp, J.R. and Allahdadi, F.A. 1993. High strain lagrangian hydrodynamics: A three-dimensional SPH code for dynamic material response. *Journal of Computational Physics* 109(1), pp. 67–75.

Lilliu, G. and van Mier, J.G.M. 2003. 3D lattice type fracture model for concrete. *Engineering Fracture Mechanics* 70(7), pp. 927–941.

Liu, G.R. and Liu, M.B. 2003. *Smoothed particle hydrodynamics - A meshfree particle method*. Singapore: World Scientific Publishing Co. Pte. Ltd.

Liu, M. 2009. *Wider application of additions in self-compacting concrete*. Phd thesis, Department of Civil, Environmental and Geomatic Engineering University College London, London, UK.

Lucy, L.B. 1977. A numerical approach to the testing of the fission hypothesis. *The Astronomical Journal* 82(12), pp. 1013–1024.

Macosko, C.W. 1994. *Rheology: Principles, measurements and applications*. USA: Wiley-VCH.

Martys, N.S. 2005. Study of a dissipative particle dynamics based approach for modeling suspensions. *Journal of Rheology* 49(2), pp. 401–424.

Mechtcherine, V., Gram, A., Krenzer, K., Schwabe, J.-H., Shyshko, S. and Roussel, N. 2014. Simulation of fresh concrete flow using Discrete Element Method (DEM): theory and applications. *Materials and Structures* 47(4), pp. 615–630.

Mehta, P.K. 2002. Greening of the concrete industry for sustainable development. *Concrete International*, pp. 23–28.

Memon, F.A., Nuruddin, M.F. and Shafiq, N. 2013. Effect of silica fume on the fresh and hardened properties of fly ash-based self-compacting geopolymer concrete. *International Journal of Minerals, Metallurgy and Materials* 20(2), pp. 205–213.

Mindess, S. 1984. The effect of specimen size on the fracture energy of concrete.

Cement and Concrete Research 14(3), pp. 431–436.

Mindess, S., Young, J.F. and Darwin, D. 2003. *Concrete*. 2nd ed. USA: Pearson Education Ltd.

Monaghan, J. 2000. SPH without a tensile instability. *Journal of Computational Physics* 159(2), pp. 290–311.

Monaghan, J. and Kos, A. 1999. Soiltary waves on a cretan beach. *ASCE Journal of Waterway, Port, Coastal, and Ocean Engineering* 125(3), pp. 145–154.

Monaghan, J.J. 1992. Smoothed particle hydrodynamics. *Annual Review of Astronomy and Astrophysics* 30, pp. 543–574.

Monaghan, J.J. 1994. Simulating free surface flows with SPH. *Journal of Computational Physics* 110(2), pp. 399–406.

Monaghan, J.J. 1996. Gravity currents and solitary waves. *Physica D* 98, pp. 523–533.

Monaghan, J.J. 2005. *Smoothed particle hydrodynamics*. Institute of physics publishing: Reports on progress in physics.

Monaghan, J.J. and Kocharyan, A. 1995. SPH simulation of mulpi-phase flow. *Computer Physics Communications* 87, pp. 225–235.

Morris, J.P., Fox, P.J. and Zhu, Y. 1997. Modeling low reynolds number incompressible flows using SPH. *Journal of Computational Physics* 136, pp. 214–226.

Most, T. and Bucher, C. 2003. Application of the 'Fictitious Crack Model' to meshless crack growth simulations. In: Gurlebeck, k., Hempel, L. and Konke, C. ed. *Proceedings 16th International Conference on the Applications of Computer Science and Mathematics in Architecture and Civil Engineering*. Bauhaus-University Weimar, Germany, pp. 1–11.

Muralidhara, S., Prasad, B.K.R., Eskandari, H. and Karihaloo, B.L. 2010. Fracture process zone size and true fracture energy of concrete using acoustic emission. *Construction and Building Materials* 24(4), pp. 479–486.

Muralidhara, S., Prasad, B.K.R., Karihaloo, B.L. and Singh, R.K. 2011. Size-independent fracture energy in plain concrete beams using tri-linear model. *Construction and Building Materials* 25(7), pp. 3051–3058.

Murthy, A.R., Karihaloo, B.L., Iyer, N.R. and Prasad, B.K.R. 2013. Determination of

size-independent specific fracture energy of concrete mixes by two methods. *Cement and Concrete Research* 50, pp. 19–25.

Murthy, A.R., Karihaloo, B.L., Iyer, N.R. and Prasad, R.B.K. 2013. Bilinear tension softening diagrams of concrete mixes corresponding to their size-independent specific fracture energy. *Construction and Building Materials* 47, pp. 1160–1166.

Nallathambi, P., Karihaloo, B.L. and Heaton, B.S. 1984. Effect of specimen and crack sizes, water/cement ratio and coarse aggregate texture upon fracture toughness of concrete. *Magazine of Concrete Research* 36(129), pp. 227–236.

Nallathambi, P., Karihaloo, B.L. and Heaton, B.S. 1985. Various size effects in fracture of concrete. *Cement and Concrete Research* 15(1), pp. 117–126.

Nanthagopalan, P. and Santhanam, M. 2009. Experimental investigations on the influence of paste composition and content on the properties of self-compacting concrete. *Construction and Building Materials* 23(11), pp. 3443–3449.

Nehdi, M. and Rahman, M.A. 2004. Estimating rheological properties of cement pastes using various rheological models for different test geometry, gap and surface friction. *Cement and Concrete Research* 34(11), pp. 1993–2007.

Nepomuceno, M.C., Oliveira, L.A. and Lopes, S.M. 2012. Methodology for mix design of the mortar phase of self-compacting concrete using different mineral additions in binary blends of powders. *Construction and Building Materials* 26(1), pp. 317–326.

Neville, A.M. 1995. *Properties of concrete*. 4th ed. UK: Longman Scientific Group Ltd.

Neville, A.M. and Brooks, J.J. 2010. *Concrete Technology*. 2nd ed. UK: Pearson Education Ltd.

Nikbin, I.M., Beygi, M.H.A., Kazemi, M.T., Amiri, J. V., Rabbanifar, S., Rahmani, E., et al. 2014. A comprehensive investigation into the effect of water to cement ratio and powder content on mechanical properties of self-compacting concrete. *Construction and Building Materials* 57, pp. 69–80.

Nikbin, I.M., Beygi, M.H.A., Kazemi, M.T., Amiri, J. V., Rahmani, E., Rabbanifar, S., et al. 2014a. A comprehensive investigation into the effect of aging and coarse

aggregate size and volume on mechanical properties of self-compacting concrete. *Construction and Building Materials* 59, pp. 199–210.

Nikbin, I.M., Beygi, M.H.A., Kazemi, M.T., Amiri, J. V., Rahmani, E., Rabbanifar, S., et al. 2014b. Effect of coarse aggregate volume on fracture behavior of self-compacting concrete. *Construction and Building Materials* 52, pp. 137–145.

Noguchi, T., Oh, S.G. and Tomosawa, F. 1999. Rheological approach to passing ability between reinforcing bars of self-compacting concrete. In: Å. Skarendahl and Ö. Petersson ed. *1st International RILEM Symposium on Self-Compacting Concrete*. RILEM Publications SARL, Stockholm, Sweden, pp. 59–70.

Nuruddin, M.F., Chang, K.Y. and Azmee, N.M. 2014. Workability and compressive strength of ductile self-compacting concrete (DSCC) with various cement replacement materials. *Construction and Building Materials* 55, pp. 153–157.

Okamura, H. and Ouchi, M. 1998. Self-compacting high performance concrete. *Progress in Structural Engineering and Materials* 1(4), pp. 378–383.

Okamura, H. and Ouchi, M. 2003. Self-compacting concrete. *Journal of Advanced Concrete Technology* 1(1), pp. 5–15.

Okamura, H., Ozawa, K. and Ouchi, M. 2000. Self-compacting concrete. *Structural Concrete* 1(1), pp. 3–17.

Okumara, H. and Ouchi, M. 1999. Self-compacting concrete development, present use and future. In: Å. Skarendahl and Ö. Petersson ed. *1st International RILEM Symposium on Self-Compacting Concrete*. RILEM Publications SARL, Stockholm, Sweden, pp. 3–14.

Olesen, J.F. 2001. Fictitious crack propagation in fiber-reinforced concrete beams. *Journal of Engineering Mechanics* 127, pp. 272–280.

Ouchi, M. 2001. Self-compacting concrete: Development, applications and key technologies. In: *Proceedings of the 26th Conference on Our World in Concrete and Structures, Singapore*. CI-Premier PTE Ltd., pp. 89–97.

Ouchi, M. 2003. Self-compacting concrete. *Journal of Advanced Concrete Technology* (3), pp. 26–40.

Ouchi, M., Hibino, M., Ozawa, K. and Okamura, H. 1998. A rational mix design

method for mortar in self-compacting concrete. In: *Proceedings of the Sixth East Asia-Pacific Conference on Structural Engineering and Construction*. Taiwan, pp. 1307–1312.

Ozbay, E., Oztas, A., Baykasoglu, A. and Ozbebek, H. 2009. Investigating mix proportions of high strength self-compacting concrete by using Taguchi method. *Construction and Building Materials* 23(2), pp. 694–702.

Pade, C., Larsen, F., Luping, T., Karlsson, M., Carlström, S., Johansen, K., et al. 2005. *Self-compacting concrete: Test methods for SCC*. Danish Technological Institute, Denmark.

Panesar, D.K. and Shindman, B. 2011. Elastic properties of self-consolidating concrete. *Construction and Building Materials* 25(8), pp. 3334–3344.

Papanastasiou, T.C. 1987. Flows of materials with yield. *Journal of Rheology* 31(5), pp. 385–404.

Parra, C., Valcuende, M. and Gómez, F. 2011. Splitting tensile strength and modulus of elasticity of self-compacting concrete. *Construction and Building Materials* 25(1), pp. 201–207.

Patzák, B. and Bittnar, Z. 2009. Modeling of fresh concrete flow. *Computers and Structures* 87, pp. 962–969.

Péra, J., Husson, S. and Guilhot, B. 1999. Influence of finely ground limestone on cement hydration. *Cement and Concrete Composites* 21(2), pp. 99–105.

Persson, B. 1997. Moisture in concrete subjected to different kinds of curing. *Materials and Structures* 30(9), pp. 533–544.

Persson, B. 2000. Consequence of cement constituents, mix composition and curing conditions for self-desiccation in concrete. *Materials and Structures* 33, pp. 352–362.

Persson, B. 2001. A comparison between mechanical properties of self-compacting concrete and the corresponding properties of normal concrete. *Cement and Concrete Research* 31(2), pp. 193–198.

Petersson, Ö. and Billberg, P. 1999. Investigation on blocking of self-compacting concrete with different maximum aggregate size and use of viscosity agent instead filler. In: Å. Skarendahl and Ö. Petersson ed. *1st International RILEM Symposium on*

Self-Compacting Concrete. RILEM Publications SARL, Stockholm, Sweden, pp. 333–344.

Petit, J.Y., Wirquin, E., Vanhove, Y. and Khayat, K. 2007. Yield stress and viscosity equations for mortars and self-consolidating concrete. *Cement and Concrete Research* 37(5), pp. 655–670.

Pettitt, A.R. 2014. *Constructing a map of the Galaxy from numerical simulations and synthetic observations*. PhD thesis, University of Exeter, UK.

Ping, X. and Beaudoin, J.J. 1992. Modification of transition zone microstructure-silica fume coating of aggregate surfaces. *Cement and Concrete Research* 22(4), pp. 597–604.

Planas, J., Elices, M. and Guinea, G.V. 1992. Measurement of the fracture energy using three-point bend tests: Part 2-Influence of bulk energy dissipation. *Materials and Structures* 25(5), pp. 305–312.

Poppe, A.M. and De Schutter, G. 2005. Cement hydration in the presence of high filler contents. *Cement and Concrete Research* 35(12), pp. 2290–2299.

Price, D.J. 2012. Smoothed particle hydrodynamics and magnetohydrodynamics. *Journal of Computational Physics* 231(3), pp. 759–794.

Prokopski, G. and Langier, B. 2000. Effect of water/cement ratio and silica fume addition on the fracture toughness and morphology of fractured surfaces of gravel concretes. *Cement and Concrete Research* 30(9), pp. 1427–1433.

Rabehi, M., Mezghiche, B. and Guettala, S. 2013. Correlation between initial absorption of the cover concrete, the compressive strength and carbonation depth. *Construction and Building Materials* 45, pp. 123–129.

Ramezanianpour, A.A. 2014. *Cement replacement materials: Properties, durability, sustainability*. Concrete Technology Center, Department of Civil Engineering, Amirkabir University of Technology, Tehran, I. ed. Springer Geochemistry/Mineralogy Ltd.

RILEM State-of-the-Art Reports 2014. *Simulation of fresh concrete flow*. Roussel, N. and Gram, A. ed. Netherlands: Springer Ltd.

RILEM State-of-the-Art Reports TC174 2000. *Self-compacting concrete*. Petersson,

Å. S. and Ö. ed. France: RILEM Publications SARL.

RILEM TCS50 1985. Determination of the fracture energy of mortar and concrete by means of three-point bend tests on notched beams. *Materials and Structures* 18(106), pp. 285–290.

Rosswog, S. 2009. Astrophysical smooth particle hydrodynamics. *New Astronomy Reviews* 53, pp. 78–104.

Rosswog, S. 2015. Boosting the accuracy of SPH techniques: Newtonian and special-relativistic tests. *Monthly Notices of the Royal Astronomical Society* 448(4), pp. 3628–3664.

Roussel, N. 2006. A Theoretical frame to study stability of fresh concrete. *Materials and Structures* 39(1), pp. 81–91.

Roussel, N. 2006. Correlation between yield stress and slump: Comparison between numerical simulations and concrete rheometers results. *Materials and Structures* 39(4), pp. 501–509.

Roussel, N. 2007. Rheology of fresh concrete: from measurements to predictions of casting processes. *Materials and Structures* 40(10), pp. 1001–1012.

Roussel, N. and Coussot, P. 2005. 'Fifty-cent rheometer' for yield stress measurements: From slump to spreading flow. *Journal of Rheology* 49(3), pp. 705–718.

Roussel, N., Geiker, M.R., Dufour, F., Thrane, L.N. and Szabo, P. 2007. Computational modeling of concrete flow: General overview. *Cement and Concrete Research* 37(9), pp. 1298–1307.

Roussel, N., Lemaitre, A., Flatt, R.J. and Coussot, P. 2010. Steady state flow of cement suspensions: A micromechanical state of the art. *Cement and Concrete Research* 40(1), pp. 77–84.

Roussel, N., Nguyen, T.L.H., Yazoghli, O. and Coussot, P. 2009. Passing ability of fresh concrete: A probabilistic approach. *Cement and Concrete Research* 39(3), pp. 227–232.

Rozière, E., Granger, S., Turcry, P. and Loukili, A. 2007. Influence of paste volume on shrinkage cracking and fracture properties of self-compacting concrete. *Cement and*

Concrete Composites 29(8), pp. 626–636.

Saak, A.W., Jennings, H.M. and Shah, S.P. 2001. New methodology for designing self-compacting concrete. *ACI Materials Journal* 98(6), pp. 429–439.

Sebaibi, N., Benzerzour, M., Sebaibi, Y. and Abriak, N.E. 2013. Composition of self-compacting concrete (SCC) using the compressible packing model, the Chinese method and the European standard. *Construction and Building Materials* 43, pp. 382–388.

Sedran, T. and Larrard, F. 1999. Optimization of self-compacting concrete thanks to packing model. In: Å. Skarendahl and Ö. Petersson ed. *1st International RILEM Symposium on Self-Compacting Concrete*. RILEM Publications SARL, Stockholm, Sweden, pp. 321–332.

Shao, S. and Lo, E.Y.M. 2003. Incompressible SPH method for simulating Newtonian and non-Newtonian flows with a free surface. *Advances in Water Resources* 26(7), pp. 787–800.

Shi, C., Wu, Z., Lv, K. and Wu, L. 2015. A review on mixture design methods for self-compacting concrete. *Construction and Building Materials* 84, pp. 387–398.

Solenthaler, B. and Pajarola, R. 2009. Predictive-corrective incompressible SPH. *ACM Transactions on Graphics* 28(3), pp. 1–6.

Sonebi, M., Bartos, P., Zhu, W., Gibbs, J. and Tamimi, A. 2000. *Final Report:Properties of hardened concrete*. Advanced Concrete Masonry Centre, University of Paisley, Scotland, UK.

Sonebi, M. and Bartos, P.J.M. 2002. Filling ability and plastic settlement of self-compacting concrete. *Materials and Structures* 35, pp. 462–469.

Sonebi, M., Svermova, L. and Bartos, P.J. 2004. Factorial design of cement slurries containing limestone powder for self-consolidating slurry-infiltrated fiber concrete. *ACI Materials Journal* 101(2), pp. 136–145.

Springel, V. 2010. Galilean-invariant cosmological hydrodynamical simulations on a moving mesh. *Monthly Notices of the Royal Astronomical Society* 401(2), pp. 791–851.

Struble, L. and Sun, G.K. 1995. Viscosity of portland cement paste as a function of

concentration. *Advanced Cement Based Materials* 2(2), pp. 62–69.

Su, N., Hsu, K.-C. and Chai, H.-W. 2001. A simple mix design method for self-compacting concrete. *Cement and Concrete Research* 31, pp. 1799–1807.

Su, N. and Miao, B. 2003. A new method for the mix design of medium strength flowing concrete with low cement content. *Cement and Concrete Composites* 25(2), pp. 215–222.

Suksawang, N., Nassif, H.H. and Najm, H.S. 2006. Evaluation of mechanical properties for self-consolidating, normal, and high performance concrete. *Transportation Research Record*, pp. 36–45.

Sun, Z., Voigt, T. and Shah, S.P. 2006. Rheometric and ultrasonic investigations of viscoelastic properties of fresh Portland cement pastes. *Cement and Concrete Research* 36(2), pp. 278–287.

Švec, O., Skoček, J., Stang, H., Geiker, M.R. and Roussel, N. 2012. Free surface flow of a suspension of rigid particles in a non-Newtonian fluid: A lattice Boltzmann approach. *Journal of Non-Newtonian Fluid Mechanics* 179–180, pp. 32–42.

Tada, H., Paris, P.C. and Irwin, G.R. 1985. *The stress analysis of cracks handbook*. 3rd ed. ASME Press.

Takada K. and Tangtermsirikul S. 2000. Self-compacting concrete: Testing of fresh concrete IV. In: Å. Skarendahl and Ö Petersson ed. *RILEM State-of-the-Art Report TC174*. RILEM Publications SARL, France, pp. 25–39.

Takeda, H., Miyama, S.M. and Sekiya, M. 1994. Numerical simulation of viscous flow by smoothed particle hydrodynamics. *Progress of Theoretical Physics* 92(5), pp. 939–960.

Tanigawa, Y. and Mori, H. 1989. Analytical study on deformation of fresh concrete. *Journal of Engineering Mechanics* 115(3), pp. 493–508.

Tattersall, G.H. 2003. *Workability and Quality Control of Concrete*. UK: E and FN Spon Ltd.

Tejchman, J. and Bobinski, J. 2012. *Continuous and discontinuous modelling of fracture in concrete using FEM: Springer series in Geomechanics and Geoengineering*. Wu, W. and Borja, R. I. ed. Springer Science and Business Media.

The Cement Sustainability Initiative 2009. *Concrete recycling: World Business Council for Sustainable Development*.

The Concrete Society (BRE) 2005. *Self-compacting concrete-A review*. Surrey, UK.

Thrane, L.N., Szabo, P., Geiker, M., Glavind, M. and Stang, H. 2004. Simulation of the test method ‘ L-box ’ for self-compacting concrete. *Annual Transactions of the Nordic Rheology Society* 12, pp. 47–54.

Topçu, I.B. and Uğurlu, A. 2003. Effect of the use of mineral filler on the properties of concrete. *Cement and Concrete Research* 33(7), pp. 1071–1075.

Tragardh, J. 1999. Microstructural features and related properties of self-compacting concrete. In: Å. Skarendahl and Ö. Petersson ed. *1st International RILEM Symposium on Self-Compacting Concrete*. RILEM Publications SARL, Stockholm, Sweden, pp. 175–186.

Tregger, N., Gregori, A., Ferrara, L. and Shah, S. 2012. Correlating dynamic segregation of self-consolidating concrete to the slump-flow test. *Construction and Building Materials* 28(1), pp. 499–505.

Uchikawa, H., Sawaki, D. and Hanehara, S. 1995. Influence of kind and added timing of organic admixture on the composition, structure and property of fresh cement paste. *Cement and Concrete Research* 25(2), pp. 353–364.

Ulfkjær, J.P., Krenk, S. and Brincker, R. 1995. Analytical model for fictitious crack propagation in concrete beams. *Journal of Engineering Mechanics* 121, pp. 7–15.

Uomoto, T. and Ozawa, K. 1999. Recommendation for self-compacting concrete. *JSCE*, pp. 1–19.

Vasilić, K. 2015. *A numerical model for self-compacting concrete flow through reinforced sections : A porous medium analogy*. PhD thesis, Faculty of Civil Engineering, The Technical University of Dresden, Berlin, Germany.

Vesenjak, M. and Ren, Z. 2007. Application aspects of the meshless SPH method. *Journal of the Serbian Society for Computational Mechanics* 1(1), pp. 74–86.

Viramgama, P.D., Vaniya, P.S.R. and Parikh, P.K.B. 2016. Effect of ceramic waste powder in self-compacting concrete properties : A critical review. *IOSR Journal of Mechanical and Civil Engineering* 13(1), pp. 8–13.

Vorobyev, A. 2012. *A Smoothed particle hydrodynamics method for the simulation of centralized sloshing experiments*. KIT Scientific Publishing.

Wallevick, J.E. 2003. *Rheology of particle suspension: fresh concrete, mortar and cement paste with various types of lignosulfates*. Department of Structural Engineeringh, The Norwegian University of Science and Technology (NTNU), Norway.

Wallevik, O.H. and Wallevik, J.E. 2011. Rheology as a tool in concrete science: The use of rheographs and workability boxes. *Cement and Concrete Research* 41(12), pp. 1279–1288.

Welton, W.C. 1998. Simulations of compressible turbulent flows. *Journal of Computational Physics* 139(2), pp. 410–443.

Wong, Y.L., Lam, L., Poon, C.S. and Zhou, F.P. 1999. Properties of fly ash-modified cement mortar-aggregate interfaces. *Cement and Concrete Research* 29(12), pp. 1905–1913.

Wu, J. and Shu, C. 2010. An improved immersed boundary-lattice Boltzmann method for simulating three-dimensional incompressible flows. *Journal of Computational Physics* 229(13), pp. 5022–5042.

Wu, Q. and An, X. 2014. Development of a mix design method for SCC based on the rheological characteristics of paste. *Construction and Building Materials* 53, pp. 642–651.

Xiong, S., Liu, W.K., Cao, J., Li, C.S., Rodrigues, J.M. and Martins, P.A. 2005. Simulation of bulk metal forming processes using the reproducing kernel particle method. *Computers and Structures* 83, pp. 574–587.

Yahia, A., Tanimura, M. and Shimoyama, Y. 2005. Rheological properties of highly flowable mortar containing limestone filler-effect of powder content and W/C ratio. *Cement and Concrete Research* 35(3), pp. 532–539.

Yamada, K., Takahashi, T., Hanehara, S. and Matsuhisa, M. 2000. Effects of the chemical structure on the properties of polycarboxylate-type superplasticizer. *Cement and Concrete Research* 30(2), pp. 197–207.

Yammamuro, H., Izumi, T. and Mizunuma, T. 1997. Study of non-adsorptive viscosity

agents applied to self-compacting concrete. *ACI Materials Journal* 173, pp. 427–444.

Yang, C.T. 2013. Application of reproducing kernel particle method and element-free Galerkin method on the simulation of the membrane of capacitive micromachined microphone in viscothermal air. *Computational Mechanics* 51(3), pp. 295–308.

Ye, G., Liu, X., De Schutter, G., Poppe, a. M. and Taerwe, L. 2007. Influence of limestone powder used as filler in SCC on hydration and microstructure of cement pastes. *Cement and Concrete Composites* 29(2), pp. 94–102.

Yen, T., Tang, C., Chang, C. and Chen, K. 1999. Flow behaviour of high strength high-performance concrete. *Cement and Concrete Composites* 21, pp. 413–424.

Zerbino, R., Barragán, B., Garcia, T., Agulló, L. and Gettu, R. 2009. Workability tests and rheological parameters in self-compacting concrete. *Materials and Structures* 42(7), pp. 947–960.

Zhu, W. and Gibbs, J.C. 2005. Use of different limestone and chalk powders in self-compacting concrete. *Cement and Concrete Research* 35, pp. 1457–1462.

Zhu, W., Sonebi, M. and Bartos, P.J.M. 2004. Bond and interfacial properties of reinforcement in self-compacting concrete. *Materials and Structures* 37(7), pp. 442–448.

Zhu, Y., Fox, P.J. and Morris, J.P. 1999. A pore-scale numerical model for flow through porous media. *International Journal for Numerical and Analytical Methods in Geomechanics* 23(9), pp. 881–904.

Appendix A

Mix design MATLAB Code

```
%%%%%%%%%%%%%%%%%%%%%%%%%%%%%%%%%%%%%%%%%%%%%%%%%%%%%%%%%%%%%%%%%%%%%%%%
%                    CARDIFF UNIVERSITY                                   %
%                   SCHOOL OF ENGINEERING                                 %
% A MATLAB Code for designing Self-Compacting Concrete mixes 2016
%   according to its target compressive strength and plastic viscosity
%%%%%%%%%%%%%%%%%%%%%%%%%%%%%%%%%%%%%%%%%%%%%%%%%%%%%%%%%%%%%%%%%%%%%%%%
***
%     List of variables
%    Name          Description
%    -----         ------------
%    WCM            Water to cementitious materials (binder) ratio
%    PV            Paste viscosity (values based on w/cm and sp dosage)
%    TMV            Target mix viscosity
%    Z, U and X     Random names are used to solve equations
%    t1, t2 and t3  Arbitrarily factors are chosen such that t1*t2*t3=1
%    H              Unity factor (H=t1*t2*t3)
%    CM             Cementitious materials
%    WTR            Water content (kg)
%    CEM            Cement content (kg)
%    GG             Cement replacement materials (kg) e.g. ggbs
%    SP             Super-plasticiser dosage (kg)
%    VPS            Volume of paste per cubic meter
%    FLP            Volume fraction of filler (materials<125µm)
%    FS             Volume fraction of fine aggregate
%    FG             Volume fraction of coarse aggregate
%    WLP            Mass of filler
%    WS             Mass of fine aggregate
%    WG             Mass of coarse aggregate
%    VLP            Volume of filler per cubic meter
%    VS             Volume of fine aggregate per cubic meter
%    VG             Volume of coarse aggregate per cubic meter
%    TV             Total volume of the mix (m3)
%    PSRATIO        Paste to solid ratio
%    FFLP           A factor larger than unity that predicts the
%                   increase in the plastic viscosity induced by
%                   addition of filler
%    FFS            A factor larger than unity that predicts the
%                   increase in the plastic viscosity induced by
%                   addition of fine aggregate
%    FFG            A factor larger than unity that predicts the
%                   increase in the plastic viscosity induced by
%                   addition of coarse aggregate
%    AMV            Actual mix plastic viscosity calculated by
%                   micromechanical procedure
%    ERR            Percentage difference between target (TMV) and
%                   actual mix viscosity (AMV)
%    PWDR           Powder content (Any materials<=125µm i.e.
%                   (cementitious materials and filler))
%    WTPR           Water to powder ratio
%    FIRSTLINE      Normalized cementitious materials content
%    SECONDLINE     Normalized cementitious materials and filler
%                   contents
%    THIRDLIN       Normalized cementitious materials, filler and fine
%                    aggregate contents
%    FOURTHLINE     Normalized cementitious materials, filler, fine
%                    aggregate and coarse aggregate contents

%%%%%%%%%%%%%%%%%%%%%%%%%%%%%%%%%%%%%%%%%%%%%%%%%%%%%%%%%%%%%%%%%%%%%%%%
%%%%%%%%%%%%%%%%%%%%%%%%%%%%%%%%%%%%%%%%%%%%%%%%%%%%%%%%%%%%%%%%%%%%%%%%
%%%%%%%%%%%%%%%%%%%%%%%%%%%%%%%%%%%%%%%%%%%%%%%%%%%%%%%%%%%%%%%%%%%%%%%%
clear
```

```
clc
% Input water to binder (cementitious materials) ratio from Eq. 3.1
WCM=0.63;
% Input the paste viscosity from Table 3.1
PV=0.11;
%*****************************************************************
s=0;
p=0;
for TMV=3.5:0.05:15
Z=0.524^ (-1.9)*0.63^ (-1.9)*0.74^ (-1.9);
U= (Z*TMV/PV) ^ (-1/1.9);
X=U^ (1/3);
t1=0.424/X ;
t2=0.53/X ;
t3=0.64/X ;
a=linspace (0, t1, 200) ;
b=linspace (0, t2, 200) ;
c=linspace (0, t3, 200) ;
for i= 1:200
for j= 1:200
for k= 1:200

H=a (i)*b (j)*c (k);
if (H<=1.0001 && H>=0.9999)
s=s+1;
% Input the cementitious materials contents limits
for CM=230:5:350
WTR(s) =CM*WCM;
CEM(s) =0.75*CM;
GG(s) =0.25*CM;
SP(s) =0.005*CM;
VPS(s) =CEM(s)/2950+GG(s)/2400+WTR(s)/1000+SP(s)/1070+0.02;

FLP(s) =0.524-a (i)*X;
FS(s) =0.63-b (j)*X;
FG(s) =0.74-c (k)*X;
WLP(s) =2400*FLP(s)*VPS(s)/ (1-FLP(s));
WS(s) =2650*FS(s)*(VPS(s) + (WLP(s)/2400))/ (1-FS(s));
WG(s) =2800*FG(s)*(VPS(s) + (WLP(s)/2400) + (WS(s)/2650))/ (1-FG(s));

VLP(s) =WLP(s)/2400;
VS(s) =WS(s)/2650;
VG(s) =WG(s)/2800;
TV(s) =VLP(s) +VS(s) +VG(s) +VPS(s)-0.02;

WCEMnew(s) =CEM(s)*0.98/TV(s);
WGGnew(s) =GG(s)*0.98/TV(s);
WWTRnew(s) =WTR(s)*0.98/TV(s);
WSPnew(s) =SP(s)*0.98/TV(s);
WLPnew(s) =WLP(s)*0.98/TV(s);
WSnew(s) =WS(s)*0.98/TV(s);
WGnew(s) =WG(s)*0.98/TV(s);

VCEMnew(s) =WCEMnew(s)/2950;
VGGnew(s) =WGGnew(s)/2400;
VWTRnew(s) =WWTRnew(s)/1000;
VSPnew(s) =WSPnew(s)/1070;
VLPnew(s) =WLPnew(s)/2400;
VSnew(s) =WSnew(s)/2650;
VGnew(s) =WGnew(s)/2800;
```

```
TVnew(s)  =VCEMnew(s)  +VGGnew(s)  +VWTRnew(s)  +VSPnew(s)  +VLPnew(s)
+VSnew(s) +VGnew(s) +0.02;

 WCMnew(s) =WCEMnew(s) +WGGnew(s);
 STAG(s) =VSnew(s)/ (VSnew(s) +VGnew(s))*100;
 GTAG(s) =VGnew(s)/ (VSnew(s) +VGnew(s))*100;
 VPSnew(s) =VCEMnew(s) +VGGnew(s) +VWTRnew(s) +VSPnew(s) +0.02;
 PSRATIO(s) = (VPSnew(s) +VLPnew(s))/ (VSnew(s) +VGnew(s));
 FLPnew(s) =VLPnew(s)/ (VLPnew(s) +VPSnew(s));
 FSnew(s) =VSnew(s)/ (VSnew(s) +VLPnew(s) +VPSnew(s));
 FGnew(s) =VGnew(s)/ (VGnew(s) +VSnew(s) +VLPnew(s) +VPSnew(s));
 FFLP(s) = (1-FLPnew(s)/0.524) ^ (-1.9);
 FFS(s) = (1-FSnew(s)/0.63) ^ (-1.9);
 FFG(s) = (1-FGnew(s)/0.74) ^ (-1.9);
 AMV(s) =PV*FFLP(s)*FFS(s)*FFG(s);
 ERR(s) = (AMV(s)-TMV)/TMV*100;
 PWDR=WCMnew(s) +WLPnew(s);
 WTPR(s) =VWTRnew(s)/ (VLPnew(s) +VCEMnew(s) +VGGnew(s))*100;

            A=TVnew(s);
            B=WLPnew(s);
            C=WSnew(s);
            D=WGnew(s);
            E=STAG(s);
            F=GTAG(s);
            G=PSRATIO(s);
            I=AMV(s);
            L=ERR(s);
            J=WTPR(s);
            K=WCMnew(s);
            R=WSPnew(s);
            WCMRnew(s) =WWTRnew(s)/WCMnew(s);
            EEE=WCMRnew(s);
            WWTR=WWTRnew(s);

 % Check the typical range of SCC mix compositions according to EFNARC
          if (PWDR>=380 && PWDR<=600)
          if (WWTR>=150 && WWTR<=210)
          if (D>=750 && D<=1000)
          if (J>=85 && J<=130)
          if (E>=48 && E<=55)
 % Check the percentage difference between (TMV) and (AMV)
          if (L>=-5 && L<=5)

                    p=p+1;
                    AA (p) =K/I;
                    BB (p) = (K+B)/I;
                    CC (p) = (K+B+C)/I;
                    DD (p) = (K+B+C+D)/I;
                    EE (p) =C/I;
                    FF (p) =D/I;
                    RR (p) =B/I;
                    TT (p) =(C+D)/I;
                    StoTOTAL (p) =E/I;
                    SANDplusLP (p) = (B+C)/I;
                    CMplusSAND (p) = (K+C)/I;

                    AAA=AA (p);
                    BBB=BB (p);
                    CCC=CC (p);
```

```
                    DDD=DD (p);

                    GGG=EE (p);
                    FFF=FF (p);
                    RRR=RR (p);
                    TTT=TT (p);
                    STST=StoTOTAL (p);
                    SLP=SANDplusLP (p);
                    CMSAND=CMplusSAND (p);

                    TotalVolume (p) =A;
                    Limestone (p) =B;
                    Sand (p) =C;
                    CoarseAGG (p) =D;
                    StoTAG (p) =E;
                    GtoTAG (p) =F;
                    PtoSRATIO (p) =G;
                    Viscosity (p) =I;
                    ERROR (p) =L;
                    SUPER (p) =R;
                    WATER (p) =WWTR;
                    CMmaterials (p) =K;
                    WtoPRatio (p) =J;
                    FIRSTLINE (p) =AAA;
                    SECONDLINE (p) =BBB;
                    THIRDLINE (p) =CCC;
                    FOURTHLINE (p) =DDD;

                    WATERtoCM (p) =EEE;
                    SANDtoVISCOSITY (p) =GGG;
                    GRAVELtoVISCOSITY (p) =FFF;
                    LIMEtoVISCOSITY (p) =RRR;
                    CAplusFA (p) =TTT;
                    StoTOTALAGG (p) =STST;
                    LPplusLSAND (p) =SLP;
                    CMandSAND (p) =CMSAND;

            end
            end
            end
            end
            end
            end
end
end
end
end
end
end


%*****************************************************************
% print the results in order to plot the graphs
GtoTAG = round (GtoTAG);
Limestone = round (Limestone);
Sand = round (Sand);
CoarseAGG = round (CoarseAGG);
StoTAG = round (StoTAG);
TotalVolume = round (TotalVolume*1000)/1000;
ERR = round (ERR);
```

```
PSRATIO = round (PSRATIO);

%*********************************************************************
% Desired parameters to be printed in the output sheet

myMatrix =
[CMmaterials;Limestone;Sand;CoarseAGG;WATER;SUPER;TotalVolume;WATERt
oCM;WtoPRatio;StoTAG;GtoTAG;PtoSRATIO;ERROR;Viscosity;FIRSTLINE;SECO
NDLINE;THIRDLINE;FOURTHLINE]';

HeaderNames='CMmaterials,Limestone,Sand,CoarseAGG,WATER,SUPER,TotalV
olume,WATERtoCM,WtoPRatio,StoTAG,GtoTAG,PtoSRATIO,ERROR,Viscosity,FI
RSTLINE,SECONDLINE,THIRDLINE,FOURTHLINE';
%*********************************************************************
% preferable output sheet name printed here (change the underline
text)

fileName ='choose output file name here.csv';
outid = fopen (fileName, 'w+');
fprintf (outid, '%s', HeaderNames);
fclose (outid);

dlmwrite(fileName,myMatrix,'roffset',1,'-append', 'precision', 4);
% you may need to increase precision to allow all digits to be saved
disp (strcat ('Generated report ''', fileName,''''))

%*********************************************************************
%*********************************************************************
%*********************************************************************
```

Appendix B

Mix proportioning of SCC mixes

Table B.1 Mix constituents (kg/m^3) for mixes grade 30

Cementatious Materials kg/m^3	Water kg/m^3	Superplasticizer kg/m^3	*w/cm*	Filler (Limestone powder) kg/m^3	Fine aggregate kg/m^3	Coarse aggregate kg/m^3	Total volume m^3	Paste volume m^3	Solid volume m^3	P/S %	Viscosity Pa s
346	218	1.73	0.63	195	758	754	1	0.445	0.555	0.8018	3.707
340.4	214.5	1.702	0.63	249	697	770	1	0.4619	0.5381	0.8585	3.938
334.9	211	1.675	0.63	191	739	810	1	0.432	0.568	0.7607	4.081
334.1	210.5	1.671	0.63	174	811	755	1	0.4243	0.5757	0.737	4.403
323.2	203.6	1.616	0.63	187	742	842	1	0.419	0.581	0.7212	4.662
322.6	203.2	1.613	0.63	202	764	804	1	0.4244	0.5756	0.7374	4.857
321.4	202.5	1.607	0.63	252	730	786	1	0.444	0.556	0.7986	5.026
321.2	202.4	1.606	0.63	270	727	768	1	0.4516	0.5484	0.8234	5.149
314.7	198.3	1.574	0.63	215	750	825	1	0.4223	0.5777	0.7311	5.317
312.8	197.1	1.564	0.63	245	743	803	1	0.4327	0.5673	0.7627	5.589
307.6	193.8	1.538	0.63	189	765	860	1	0.4042	0.5958	0.6783	5.766
309	194.7	1.545	0.63	218	795	790	1	0.4178	0.5822	0.7176	6.012
302	190.2	1.51	0.63	239	759	824	1	0.4195	0.5805	0.7227	6.452
300.8	189.5	1.504	0.63	265	753	803	1	0.429	0.571	0.7513	6.741
302.2	190.4	1.511	0.63	211	841	769	1	0.4081	0.5919	0.6896	6.91
296.3	186.6	1.481	0.63	259	767	807	1	0.4222	0.5778	0.7308	7.203
298.7	188.2	1.493	0.63	199	862	770	1	0.3997	0.6003	0.6657	7.406
290.8	183.2	1.454	0.63	207	804	845	1	0.3949	0.6051	0.6526	7.638
290.8	183.2	1.454	0.63	163	841	857	1	0.3767	0.6233	0.6043	7.885
288.2	181.6	1.441	0.63	149	827	895	1	0.3683	0.6317	0.583	7.989
288.6	181.8	1.443	0.63	214	838	807	1	0.3958	0.6042	0.6551	8.302
282.7	178.1	1.414	0.63	241	774	859	1	0.4011	0.5989	0.6696	8.518
289.8	182.6	1.449	0.63	171	898	790	1	0.3789	0.6211	0.6101	8.819
279.3	176	1.397	0.63	242	782	858	1	0.3983	0.6017	0.6619	9.055

Table B.2 Mix constituents (kg/m^3) for mixes grade 30

280.2	176.5	1.401	0.63	156	843	892	1	0.3635	0.6365	0.571	9.235
281.2	177.1	1.406	0.63	162	869	856	1	0.3666	0.6334	0.5787	9.523
279.3	175.9	1.396	0.63	186	860	841	1	0.375	0.625	0.6	9.694
278.5	175.4	1.392	0.63	162	872	859	1	0.3641	0.6359	0.5727	9.988
271.4	171	1.357	0.63	166	819	930	1	0.3589	0.6411	0.5597	10.15
275.3	173.5	1.377	0.63	158	870	874	1	0.3594	0.6406	0.5611	10.47
267.9	168.8	1.34	0.63	233	788	895	1	0.3833	0.6167	0.6215	10.68
273	172	1.365	0.63	159	873	877	1	0.3573	0.6427	0.556	10.93
278.9	175.7	1.394	0.63	155	929	807	1	0.3613	0.6387	0.5658	11.14
273.2	172.1	1.366	0.63	145	890	875	1	0.3515	0.6485	0.5421	11.33
270.1	170.2	1.35	0.63	190	880	841	1	0.3675	0.6325	0.5809	11.6
264	166.3	1.32	0.63	167	838	930	1	0.3517	0.6483	0.5424	11.81
265.8	167.5	1.329	0.63	172	863	893	1	0.3555	0.6445	0.5515	12.02
264.9	166.9	1.325	0.63	154	866	913	1	0.3474	0.6526	0.5323	12.31
263.6	166	1.318	0.63	172	866	896	1	0.3535	0.6465	0.5467	12.55
263.4	165.9	1.317	0.63	155	868	915	1	0.346	0.654	0.529	12.69
259.6	163.5	1.298	0.63	154	847	947	1	0.3422	0.6578	0.5201	12.98
262.9	165.6	1.315	0.63	218	887	821	1	0.372	0.628	0.5924	13.35
257.4	162.1	1.287	0.63	155	850	950	1	0.3401	0.6599	0.5155	13.56
259.3	163.3	1.296	0.63	204	874	861	1	0.3624	0.6376	0.5685	13.78
258.4	162.8	1.292	0.63	177	874	895	1	0.3506	0.6494	0.5398	13.93
260.6	164.2	1.303	0.63	179	901	859	1	0.3534	0.6466	0.5465	14.16
263.1	165.8	1.316	0.63	177	929	824	1	0.3551	0.6449	0.5505	14.42
256	161.3	1.28	0.63	145	867	948	1	0.3345	0.6655	0.5026	14.48
255.8	161.2	1.279	0.63	160	879	917	1	0.3409	0.6591	0.5173	14.8
259.4	163.5	1.297	0.63	176	922	843	1	0.3508	0.6492	0.5404	15.17

Table B.3 Mix constituents (kg/m^3) for mixes grade 40

Cementatious Materials kg/m^3	Water kg/m^3	Superplasticizer kg/m^3	*w/cm*	Filler (Limestone powder) kg/m^3	Fine aggregate kg/m^3	Coarse aggregate kg/m^3	Total volume m^3	Paste volume m^3	Solid volume m^3	P/S %	Viscosity Pa s
384.5	219.2	1.923	0.57	164	708	800	1	0.4472	0.5528	0.8089	4.849
384.6	219.2	1.923	0.57	136	764	774	1	0.4355	0.5645	0.7716	5.03
379.3	216.2	1.897	0.57	137	770	780	1	0.4311	0.5689	0.7577	5.321
381.6	217.5	1.908	0.57	117	812	753	1	0.4248	0.5752	0.7384	5.428
376	214.3	1.88	0.57	109	793	797	1	0.4162	0.5838	0.7129	5.599
368.3	209.9	1.841	0.57	149	746	819	1	0.4258	0.5742	0.7416	5.816
368.7	210.2	1.844	0.57	212	737	755	1	0.4526	0.5474	0.8267	6.007
360.4	205.4	1.802	0.57	164	742	828	1	0.4244	0.5756	0.7374	6.314
367.1	209.3	1.836	0.57	132	828	755	1	0.4176	0.5824	0.7171	6.418
363.6	207.3	1.818	0.57	123	828	775	1	0.4107	0.5893	0.697	6.647
358	204	1.79	0.57	111	812	822	1	0.4001	0.5999	0.667	6.904
354.2	201.9	1.771	0.57	238	726	774	1	0.4496	0.5504	0.8169	7.073
350.1	199.5	1.75	0.57	230	720	800	1	0.4426	0.5574	0.7941	7.287
349.3	199.1	1.746	0.57	199	773	783	1	0.4289	0.5711	0.7509	7.506
344.1	196.1	1.72	0.57	168	778	826	1	0.4112	0.5888	0.6985	7.827
346.9	197.7	1.734	0.57	241	761	753	1	0.4442	0.5558	0.7991	7.931
349.2	199	1.746	0.57	131	855	776	1	0.4003	0.5997	0.6675	8.082
343	195.5	1.715	0.57	107	829	847	1	0.3846	0.6154	0.6251	8.367
339.8	193.7	1.699	0.57	209	791	776	1	0.4242	0.5758	0.7368	8.574
336.3	191.7	1.681	0.57	127	805	867	1	0.3865	0.6135	0.6301	8.73
345.2	196.7	1.726	0.57	106	893	775	1	0.3863	0.6137	0.6296	9.013
330.9	188.6	1.655	0.57	108	797	911	1	0.3737	0.6263	0.5966	9.204
334.1	190.4	1.67	0.57	100	835	872	1	0.3734	0.6266	0.5959	9.401
333.5	190.1	1.667	0.57	155	846	799	1	0.3956	0.6044	0.6545	9.596

Table B.4 Mix constituents (kg/m^3) for mixes grade 40

328.3	187.1	1.641	0.57	153	816	846	1	0.3902	0.6098	0.6398	9.786
324.9	185.2	1.625	0.57	109	804	919	1	0.3684	0.6316	0.5834	10
325.2	185.4	1.626	0.57	154	819	849	1	0.3876	0.6124	0.6329	10.2
321.9	183.5	1.609	0.57	152	809	871	1	0.3837	0.6163	0.6225	10.47
326.6	186.2	1.633	0.57	182	855	776	1	0.4005	0.5995	0.668	10.66
329.4	187.8	1.647	0.57	107	886	821	1	0.3722	0.6278	0.5928	10.85
315.6	179.9	1.578	0.57	167	787	893	1	0.384	0.616	0.6233	11.04
318.2	181.4	1.591	0.57	166	827	845	1	0.3861	0.6139	0.629	11.3
325.6	185.6	1.628	0.57	108	891	826	1	0.3689	0.6311	0.5844	11.5
315.4	179.8	1.577	0.57	110	827	917	1	0.3604	0.6396	0.5634	11.72
319.4	182.1	1.597	0.57	123	869	849	1	0.3691	0.6309	0.585	11.91
309	176.1	1.545	0.57	155	798	912	1	0.3731	0.6269	0.5951	12.15
318.9	181.8	1.595	0.57	99	878	867	1	0.3589	0.6411	0.5598	12.36
306.7	174.8	1.534	0.57	156	801	915	1	0.3711	0.6289	0.5902	12.57
315.6	179.9	1.578	0.57	182	881	776	1	0.3904	0.6096	0.6406	12.76
311	177.3	1.555	0.57	135	856	869	1	0.3664	0.6336	0.5783	12.99
310.1	176.8	1.55	0.57	135	857	870	1	0.3656	0.6344	0.5764	13.18
309.6	176.5	1.548	0.57	118	858	891	1	0.358	0.642	0.5576	13.36
308.5	175.8	1.542	0.57	135	859	872	1	0.3643	0.6357	0.573	13.52
317.8	181.2	1.589	0.57	84	916	847	1	0.3517	0.6483	0.5426	13.78
304.2	173.4	1.521	0.57	134	850	895	1	0.3596	0.6404	0.5615	14.12
312.3	178	1.562	0.57	123	911	821	1	0.3627	0.6373	0.5692	14.23
300.4	171.2	1.502	0.57	141	835	913	1	0.359	0.641	0.56	14.47
301.9	172.1	1.509	0.57	177	854	847	1	0.3754	0.6246	0.601	14.67
298.7	170.3	1.494	0.57	141	837	915	1	0.3575	0.6425	0.5565	14.86
308.7	176	1.544	0.57	124	916	825	1	0.3596	0.6404	0.5616	15.12

Table B.5 Mix constituents (kg/m^3) for mixes grade 50

Cementatious Materials kg/m^3	Water kg/m^3	Superplasticizer kg/m^3	*w/cm*	Filler (Limestone powder) kg/m^3	Fine aggregate kg/m^3	Coarse aggregate kg/m^3	Total volume m^3	Paste volume m^3	Solid volume m^3	P/S %	Viscosity Pa s
414	219.4	2.07	0.53	139	710	796	1	0.4477	0.5523	0.8107	5.501
410.1	217.4	2.051	0.53	140	714	801	1	0.4446	0.5554	0.8005	5.709
408.1	216.3	2.04	0.53	123	740	798	1	0.4358	0.5642	0.7723	5.909
403.4	213.8	2.017	0.53	153	715	801	1	0.4441	0.5559	0.799	6.1
403.2	213.7	2.016	0.53	100	805	769	1	0.4216	0.5784	0.7289	6.581
402.3	213.2	2.012	0.53	100	806	770	1	0.4209	0.5791	0.7267	6.642
399.4	211.7	1.997	0.53	100	810	773	1	0.4185	0.5815	0.7196	6.85
391.7	207.6	1.959	0.53	201	719	770	1	0.4535	0.5465	0.8297	7.042
391.5	207.5	1.957	0.53	135	785	778	1	0.426	0.574	0.7422	7.228
388.2	205.7	1.941	0.53	202	723	774	1	0.4507	0.5493	0.8205	7.304
386.7	205	1.934	0.53	148	809	750	1	0.4269	0.5731	0.745	7.806
378.9	200.8	1.894	0.53	187	740	797	1	0.4363	0.5637	0.7739	8
375.5	199	1.878	0.53	106	765	873	1	0.3997	0.6003	0.6657	8.185
377.6	200.1	1.888	0.53	144	787	801	1	0.4171	0.5829	0.7156	8.305
372	197.2	1.86	0.53	107	769	877	1	0.3967	0.6033	0.6576	8.52
373.1	197.8	1.866	0.53	176	767	795	1	0.4264	0.5736	0.7435	8.632
368.9	195.5	1.845	0.53	107	772	881	1	0.3942	0.6058	0.6507	8.827
375.3	198.9	1.877	0.53	144	839	751	1	0.4152	0.5848	0.7099	9.065
368.6	195.4	1.843	0.53	154	799	799	1	0.4132	0.5868	0.7041	9.264
367.5	194.8	1.837	0.53	154	801	800	1	0.4123	0.5877	0.7015	9.385
366.5	194.3	1.833	0.53	105	808	851	1	0.3913	0.6087	0.6427	9.484
366.2	194.1	1.831	0.53	154	802	801	1	0.4113	0.5887	0.6985	9.529
367	194.5	1.835	0.53	111	829	822	1	0.3938	0.6062	0.6496	9.723

Table B.6 Mix constituents (kg/m^3) for mixes grade 50

362.7	192.2	1.814	0.53	106	812	856	1	0.3881	0.6119	0.6342	9.936
360.1	190.9	1.801	0.53	181	787	801	1	0.417	0.583	0.7152	10.11
360.3	190.9	1.801	0.53	216	777	770	1	0.4317	0.5683	0.7596	10.27
354.3	187.8	1.771	0.53	156	780	852	1	0.4013	0.5987	0.6704	10.53
354	187.6	1.77	0.53	101	797	899	1	0.3782	0.6218	0.6082	10.71
355.2	188.2	1.776	0.53	217	783	775	1	0.4278	0.5722	0.7475	10.91
351.2	186.1	1.756	0.53	101	800	903	1	0.3758	0.6242	0.6021	11.1
353	187.1	1.765	0.53	121	822	852	1	0.3857	0.6143	0.6278	11.22
348.4	184.7	1.742	0.53	102	803	906	1	0.3735	0.6265	0.5962	11.5
350	185.5	1.75	0.53	122	825	855	1	0.3833	0.6167	0.6214	11.66
352.8	187	1.764	0.53	153	865	770	1	0.3987	0.6013	0.663	11.99
346.5	183.6	1.732	0.53	117	821	873	1	0.3783	0.6217	0.6084	12.08
350.9	186	1.755	0.53	153	867	772	1	0.3971	0.6029	0.6588	12.3
352.1	186.6	1.761	0.53	113	885	797	1	0.3816	0.6184	0.6171	12.52
343.7	182.2	1.719	0.53	130	835	850	1	0.3813	0.6187	0.6164	12.71
350.1	185.6	1.751	0.53	113	887	799	1	0.38	0.62	0.6128	12.87
338.5	179.4	1.692	0.53	211	786	821	1	0.4101	0.5899	0.6953	13.09
335.5	177.8	1.678	0.53	139	797	900	1	0.3778	0.6222	0.6071	13.25
339.5	179.9	1.697	0.53	131	840	855	1	0.3778	0.6222	0.6072	13.47
340.9	180.7	1.705	0.53	185	854	773	1	0.4015	0.5985	0.6709	13.68
339.7	180.1	1.699	0.53	141	859	823	1	0.3822	0.6178	0.6187	13.84
331.7	175.8	1.659	0.53	140	801	905	1	0.3746	0.6254	0.5991	13.95
339.9	180.2	1.7	0.53	86	867	877	1	0.3596	0.6404	0.5614	14.3
329.4	174.6	1.647	0.53	141	804	907	1	0.3728	0.6272	0.5943	14.4
342.1	181.3	1.711	0.53	93	904	825	1	0.3641	0.6359	0.5727	14.87
333	176.5	1.665	0.53	109	855	880	1	0.3629	0.6371	0.5697	15.09
332.4	176.2	1.662	0.53	109	856	881	1	0.3625	0.6375	0.5685	15.22

Table B.7 Mix constituents (kg/m^3) for mixes grade 60

Cementatious Materials kg/m^3	Water kg/m^3	Superplasticizer kg/m^3	*w/cm*	Filler (Limestone powder) kg/m^3	Fine aggregate kg/m^3	Coarse aggregate kg/m^3	Total volume m^3	Paste volume m^3	Solid volume m^3	P/S %	Viscosity Pa s
453	212.9	2.265	0.47	124	727	775	1	0.4489	0.5511	0.8147	6.504
449.8	211.4	2.249	0.47	124	730	779	1	0.4465	0.5535	0.8066	6.691
447	210.1	2.235	0.47	135	727	775	1	0.4488	0.5512	0.8141	6.851
444.9	209.1	2.224	0.47	116	732	798	1	0.4387	0.5613	0.7817	6.94
442.4	207.9	2.212	0.47	109	723	821	1	0.4339	0.5661	0.7663	7.002
443.2	208.3	2.216	0.47	109	744	798	1	0.4345	0.5655	0.7682	7.099
439.4	206.5	2.197	0.47	109	726	824	1	0.4315	0.5685	0.759	7.199
436.7	205.2	2.183	0.47	110	729	827	1	0.4294	0.5706	0.7526	7.378
436.9	205.3	2.184	0.47	110	750	805	1	0.4296	0.5704	0.7531	7.524
430.8	202.5	2.154	0.47	146	724	804	1	0.4397	0.5603	0.7848	7.833
429.1	201.7	2.145	0.47	149	731	797	1	0.4395	0.5605	0.7841	8.005
426.7	200.5	2.133	0.47	149	733	800	1	0.4377	0.5623	0.7783	8.19
428.2	201.2	2.141	0.47	162	761	753	1	0.4442	0.5558	0.7993	8.364
423.3	198.9	2.116	0.47	150	736	804	1	0.4351	0.5649	0.7703	8.456
425	199.7	2.125	0.47	163	764	756	1	0.4418	0.5582	0.7915	8.626
417.8	196.4	2.089	0.47	158	723	821	1	0.434	0.566	0.7669	8.792
421.9	198.3	2.109	0.47	163	767	759	1	0.4395	0.5605	0.7842	8.889
415.5	195.3	2.077	0.47	159	725	823	1	0.4323	0.5677	0.7616	8.987
419	196.9	2.095	0.47	128	794	778	1	0.4226	0.5774	0.7318	9.234
412.1	193.7	2.06	0.47	149	747	819	1	0.4255	0.5745	0.7406	9.411
412.3	193.8	2.062	0.47	157	757	799	1	0.4289	0.5711	0.7509	9.531
414.5	194.8	2.073	0.47	132	803	775	1	0.4202	0.5798	0.7247	9.728
405.4	190.5	2.027	0.47	148	740	844	1	0.4194	0.5806	0.7222	9.91

Table B.8 Mix constituents (kg/m^3) for mixes grade 60

403.1	189.5	2.015	0.47	148	742	846	1	0.4176	0.5824	0.7171	10.14
402.4	189.1	2.012	0.47	148	743	847	1	0.4171	0.5829	0.7155	10.22
408.6	192.1	2.043	0.47	153	807	760	1	0.424	0.576	0.7362	10.39
399	187.5	1.995	0.47	154	744	848	1	0.4166	0.5834	0.714	10.58
404.4	190	2.022	0.47	148	805	777	1	0.4186	0.5814	0.7199	10.76
402.8	189.3	2.014	0.47	148	807	779	1	0.4174	0.5826	0.7164	10.95
402.6	189.2	2.013	0.47	99	823	820	1	0.3967	0.6033	0.6575	11.1
400.3	188.1	2.001	0.47	149	810	781	1	0.4155	0.5845	0.7108	11.25
395.5	185.9	1.977	0.47	177	771	800	1	0.4232	0.5768	0.7338	11.41
399	187.5	1.995	0.47	95	829	827	1	0.3919	0.6081	0.6445	11.61
390.7	183.6	1.953	0.47	102	782	888	1	0.3878	0.6122	0.6336	11.81
388.6	182.6	1.943	0.47	160	764	843	1	0.4104	0.5896	0.6962	11.98
398.2	187.1	1.991	0.47	116	856	776	1	0.3999	0.6001	0.6663	12.14
386	181.4	1.93	0.47	161	767	846	1	0.4085	0.5915	0.6906	12.32
395.7	186	1.978	0.47	116	858	779	1	0.3979	0.6021	0.6609	12.5
385.7	181.3	1.928	0.47	109	799	873	1	0.3867	0.6133	0.6305	12.7
381.4	179.2	1.907	0.47	162	771	851	1	0.4051	0.5949	0.6809	12.96
384.3	180.6	1.922	0.47	146	810	821	1	0.4011	0.5989	0.6698	13.14
386.4	181.6	1.932	0.47	141	833	798	1	0.4007	0.5993	0.6685	13.25
385	180.9	1.925	0.47	141	834	800	1	0.3996	0.6004	0.6656	13.46
378.5	177.9	1.892	0.47	115	794	888	1	0.3832	0.6168	0.6214	13.59
383.7	180.3	1.918	0.47	142	836	801	1	0.3986	0.6014	0.6628	13.67
384	180.5	1.92	0.47	158	841	775	1	0.4058	0.5942	0.6828	13.78
376.3	176.9	1.882	0.47	115	796	890	1	0.3816	0.6184	0.6171	13.94
375.4	176.4	1.877	0.47	199	772	820	1	0.4156	0.5844	0.7113	14.12
380	178.6	1.9	0.47	142	839	805	1	0.3959	0.6041	0.6552	14.27
373.7	175.6	1.869	0.47	116	799	893	1	0.3796	0.6204	0.6118	14.38

Table B.9 Mix constituents (kg/m^3) for mixes grade 70

Cementatious Materials kg/m^3	Water kg/m^3	Superplasticizer kg/m^3	*w/cm*	Filler (Limestone powder) kg/m^3	Fine aggregate kg/m^3	Coarse aggregate kg/m^3	Total volume m^3	Paste volume m^3	Solid volume m^3	P/S %	Viscosity Pa s
502.1	200.9	2.511	0.4	127	698	784	1	0.4563	0.5437	0.8391	7.071
497.6	199.1	2.488	0.4	151	691	774	1	0.4628	0.5372	0.8615	7.349
494	197.6	2.47	0.4	129	706	793	1	0.4506	0.5494	0.8201	7.536
490.6	196.2	2.453	0.4	130	719	785	1	0.4485	0.5515	0.8132	7.811
487.8	195.1	2.439	0.4	130	721	787	1	0.4465	0.5535	0.8067	7.99
484.5	193.8	2.423	0.4	131	724	791	1	0.4443	0.5557	0.7994	8.204
489.8	195.9	2.449	0.4	110	775	750	1	0.4395	0.5605	0.7842	8.229
483.5	193.4	2.417	0.4	108	759	784	1	0.4337	0.5663	0.766	8.471
484.6	193.8	2.423	0.4	129	765	750	1	0.4436	0.5564	0.7971	8.514
481.2	192.5	2.406	0.4	108	761	786	1	0.4322	0.5678	0.7611	8.632
480	192	2.4	0.4	161	736	753	1	0.4534	0.5466	0.8295	8.713
478.9	191.6	2.395	0.4	108	763	788	1	0.4305	0.5695	0.756	8.805
477.1	190.8	2.385	0.4	162	739	756	1	0.4514	0.5486	0.8229	8.928
475.2	190.1	2.376	0.4	109	767	792	1	0.4279	0.5721	0.7479	9.092
471	188.4	2.355	0.4	130	742	802	1	0.4334	0.5666	0.7651	9.221
471.1	188.4	2.355	0.4	140	765	766	1	0.4377	0.5623	0.7784	9.475
465.5	186.2	2.327	0.4	131	747	808	1	0.4296	0.5704	0.7532	9.671
466.8	186.7	2.334	0.4	140	770	770	1	0.4347	0.5653	0.7691	9.837
464.7	185.9	2.323	0.4	141	772	772	1	0.4333	0.5667	0.7645	10.02
462.5	185	2.313	0.4	141	774	774	1	0.4318	0.5682	0.7599	10.22
451.7	180.7	2.259	0.4	139	738	837	1	0.4226	0.5774	0.732	10.71
450.3	180.1	2.252	0.4	139	739	839	1	0.4216	0.5784	0.729	10.85
447.9	179.2	2.24	0.4	140	741	841	1	0.42	0.58	0.724	11.09

Table B.10 Mix constituents (kg/m^3) for mixes grade 70

444.5	177.8	2.222	0.4	140	744	845	1	0.4176	0.5824	0.7169	11.45
447.3	178.9	2.237	0.4	148	771	801	1	0.4228	0.5772	0.7326	11.55
442.8	177.1	2.214	0.4	140	746	846	1	0.4164	0.5836	0.7135	11.63
446.2	178.5	2.231	0.4	148	772	802	1	0.422	0.578	0.7302	11.68
449.7	179.9	2.249	0.4	124	809	784	1	0.4148	0.5852	0.7087	11.74
445.1	178	2.226	0.4	148	773	803	1	0.4213	0.5787	0.728	11.79
443.1	177.3	2.216	0.4	148	775	805	1	0.4199	0.5801	0.724	12.02
446	178.4	2.23	0.4	124	813	787	1	0.4121	0.5879	0.7011	12.18
440.6	176.2	2.203	0.4	149	778	807	1	0.4182	0.5818	0.7187	12.31
443.4	177.4	2.217	0.4	125	815	789	1	0.4103	0.5897	0.6959	12.49
438.9	175.5	2.194	0.4	145	791	801	1	0.4153	0.5847	0.7102	12.67
437.8	175.1	2.189	0.4	93	799	855	1	0.3929	0.6071	0.6471	12.83
439.9	175.9	2.199	0.4	127	823	786	1	0.4087	0.5913	0.6912	13
435.1	174	2.175	0.4	93	802	858	1	0.391	0.609	0.6419	13.18
435.5	174.2	2.178	0.4	145	812	786	1	0.4129	0.5871	0.7033	13.38
431	172.4	2.155	0.4	138	796	821	1	0.4065	0.5935	0.685	13.62
426.1	170.4	2.131	0.4	122	773	874	1	0.3961	0.6039	0.656	13.77
429	171.6	2.145	0.4	142	796	820	1	0.4068	0.5932	0.6857	13.86
424.2	169.7	2.121	0.4	126	773	874	1	0.3964	0.6036	0.6566	14.01
426.8	170.7	2.134	0.4	143	798	823	1	0.4052	0.5948	0.6813	14.18
437.7	175.1	2.189	0.4	98	879	766	1	0.3948	0.6052	0.6524	14.38
421.7	168.7	2.108	0.4	100	788	895	1	0.3833	0.6167	0.6215	14.59
426.6	170.6	2.133	0.4	118	826	821	1	0.3949	0.6051	0.6526	14.7
434.6	173.8	2.173	0.4	98	882	769	1	0.3926	0.6074	0.6463	14.88
424.9	170	2.124	0.4	115	830	825	1	0.3921	0.6079	0.645	15.02
416.6	166.7	2.083	0.4	127	780	881	1	0.391	0.609	0.6421	15.15
432.4	173	2.162	0.4	99	884	771	1	0.391	0.609	0.6421	15.24

Table B.11 Mix constituents (kg/m³) for mixes grade 80

Cementatious Materials kg/m³	Water kg/m³	Superplasticizer kg/m³	*w/cm*	Filler (Limestone powder) kg/m³	Fine aggregate kg/m³	Coarse aggregate kg/m³	Total volume m³	Paste volume m³	Solid volume m³	P/S %	Viscosity Pa s
528.9	185.1	2.644	0.35	108	693	829	1	0.4421	0.5579	0.7925	8.022
531	185.8	2.655	0.35	116	721	787	1	0.4471	0.5529	0.8087	8.134
532.4	186.4	2.662	0.35	114	750	756	1	0.447	0.553	0.8085	8.267
526.9	184.4	2.634	0.35	117	724	790	1	0.4444	0.5556	0.8	8.386
520	182	2.6	0.35	114	692	841	1	0.4384	0.5616	0.7806	8.523
522.8	183	2.614	0.35	104	733	804	1	0.4362	0.5638	0.7738	8.655
515.4	180.4	2.577	0.35	115	696	846	1	0.4354	0.5646	0.7711	8.822
517.9	181.3	2.589	0.35	105	738	808	1	0.433	0.567	0.7636	8.988
510.6	178.7	2.553	0.35	112	695	859	1	0.4308	0.5692	0.757	9.102
515.3	180.3	2.576	0.35	105	740	811	1	0.4313	0.5687	0.7583	9.171
507	177.5	2.535	0.35	113	698	863	1	0.4285	0.5715	0.7498	9.355
514.7	180.1	2.573	0.35	114	770	770	1	0.4343	0.5657	0.7679	9.522
505.4	176.9	2.527	0.35	116	720	839	1	0.4285	0.5715	0.7498	9.671
505.8	177	2.529	0.35	116	736	821	1	0.4288	0.5712	0.7508	9.795
508.9	178.1	2.544	0.35	107	772	787	1	0.4275	0.5725	0.7467	9.924
504.1	176.4	2.52	0.35	101	756	821	1	0.4213	0.5787	0.7281	10.08
503.6	176.2	2.518	0.35	108	777	792	1	0.424	0.576	0.736	10.37
499.7	174.9	2.498	0.35	101	760	825	1	0.4184	0.5816	0.7195	10.45
493	172.6	2.465	0.35	103	742	856	1	0.4144	0.5856	0.7077	10.76
500.7	175.3	2.504	0.35	115	798	767	1	0.4248	0.5752	0.7385	10.85
493.1	172.6	2.466	0.35	103	758	838	1	0.4145	0.5855	0.7079	10.95
498.1	174.3	2.491	0.35	115	800	770	1	0.4231	0.5769	0.7333	11.1
490	171.5	2.45	0.35	103	761	841	1	0.4124	0.5876	0.7019	11.25

Table B.12 Mix constituents (kg/m^3) for mixes grade 80

485.5	169.9	2.428	0.35	104	748	863	1	0.4094	0.5906	0.6933	11.46
492.1	172.2	2.461	0.35	112	800	785	1	0.4177	0.5823	0.7174	11.6
484.9	169.7	2.424	0.35	112	761	841	1	0.4123	0.5877	0.7015	11.72
488.5	171	2.442	0.35	102	802	802	1	0.4108	0.5892	0.6972	11.94
488.2	170.9	2.441	0.35	111	810	784	1	0.4145	0.5855	0.7079	12.09
476.7	166.8	2.383	0.35	95	747	892	1	0.3995	0.6005	0.6652	12.25
482.4	168.8	2.412	0.35	99	793	828	1	0.4051	0.5949	0.6809	12.38
472.9	165.5	2.365	0.35	95	750	896	1	0.397	0.603	0.6584	12.66
476.9	166.9	2.385	0.35	104	788	838	1	0.4035	0.5965	0.6764	12.84
471.7	165.1	2.358	0.35	103	764	875	1	0.3993	0.6007	0.6648	13.01
468	163.8	2.34	0.35	96	754	901	1	0.3937	0.6063	0.6494	13.22
463.4	162.2	2.317	0.35	101	732	927	1	0.3926	0.6074	0.6463	13.38
471.3	164.9	2.356	0.35	105	793	843	1	0.3997	0.6003	0.6659	13.52
466.3	163.2	2.332	0.35	104	769	880	1	0.3958	0.6042	0.655	13.66
460.6	161.2	2.303	0.35	96	742	928	1	0.3886	0.6114	0.6355	13.84
471.9	165.2	2.359	0.35	105	827	806	1	0.4001	0.5999	0.6669	14.07
457.6	160.1	2.288	0.35	97	744	931	1	0.3865	0.6135	0.6301	14.24
463.8	162.3	2.319	0.35	92	792	873	1	0.3892	0.6108	0.6372	14.37
476.2	166.7	2.381	0.35	95	868	766	1	0.3991	0.6009	0.6641	14.41
465.4	162.9	2.327	0.35	99	812	842	1	0.393	0.607	0.6474	14.55
462	161.7	2.31	0.35	92	794	875	1	0.388	0.612	0.6339	14.62
454.1	158.9	2.27	0.35	97	747	935	1	0.3842	0.6158	0.6239	14.71
460	161	2.3	0.35	93	795	877	1	0.3867	0.6133	0.6304	14.89
462	161.7	2.31	0.35	99	815	845	1	0.3907	0.6093	0.6411	15.04
461.3	161.5	2.307	0.35	105	817	837	1	0.3928	0.6072	0.6468	15.16
470.3	164.6	2.352	0.35	95	874	771	1	0.3951	0.6049	0.6533	15.28

Appendix C

Load-deflection diagrams

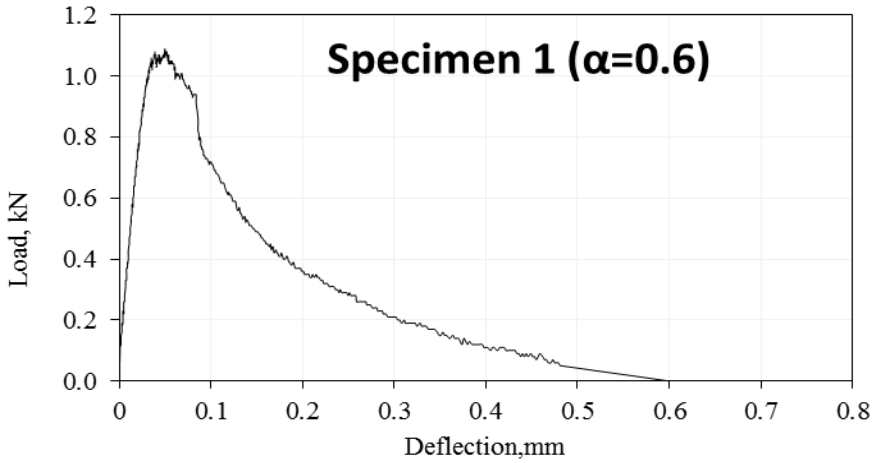

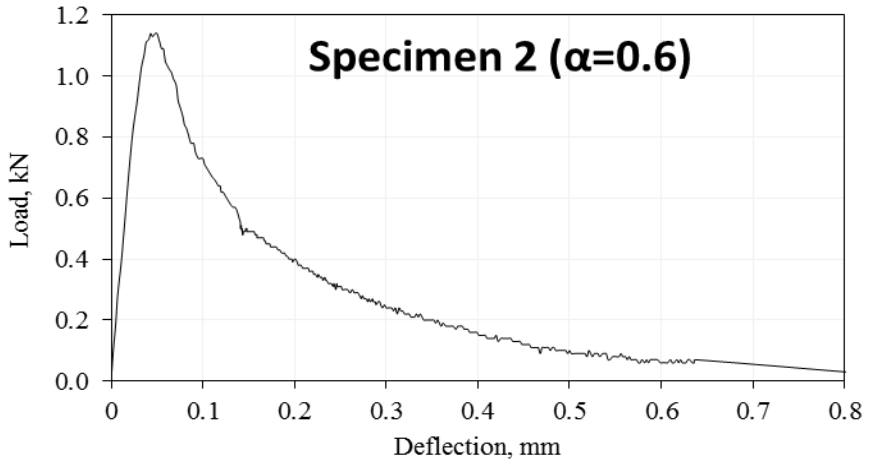

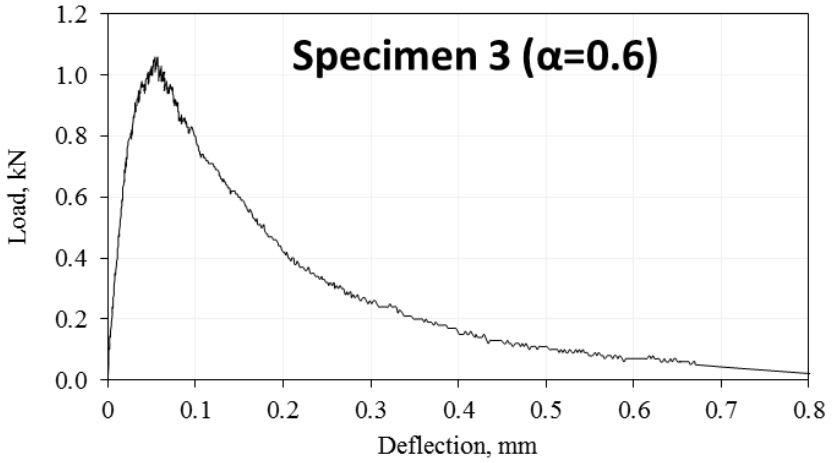

Appendix C. 1 The experimental load-deflection curves for 100mm specimen size

30B MPa (Deep notch)

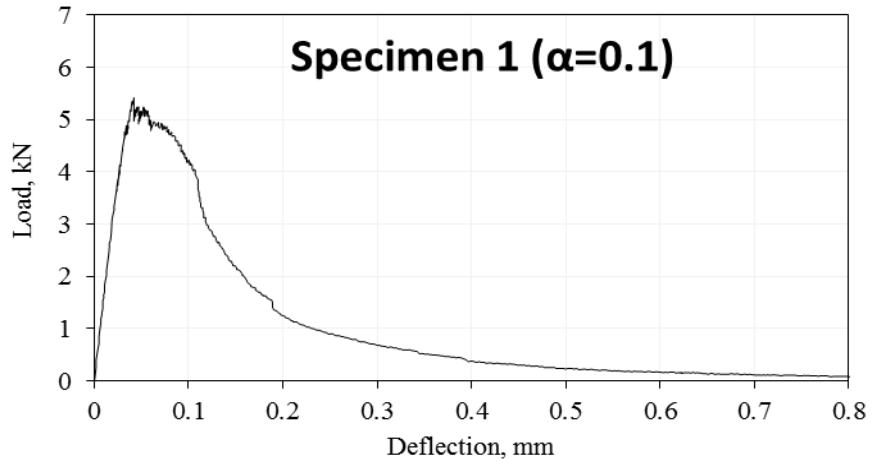

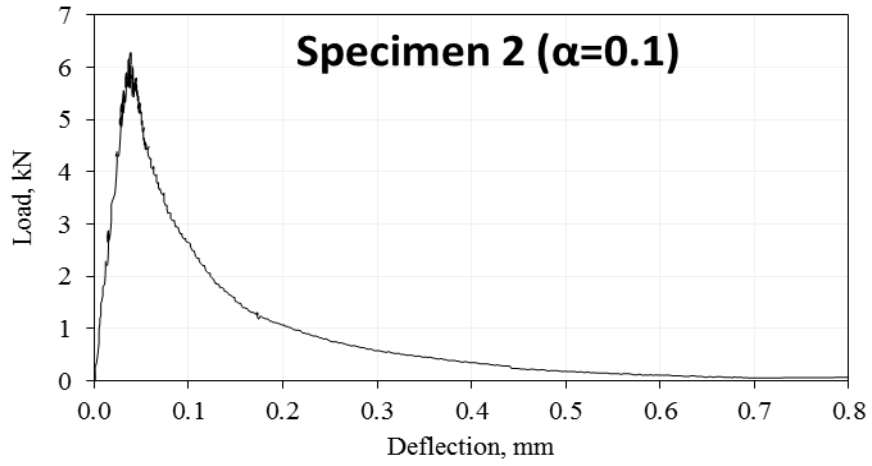

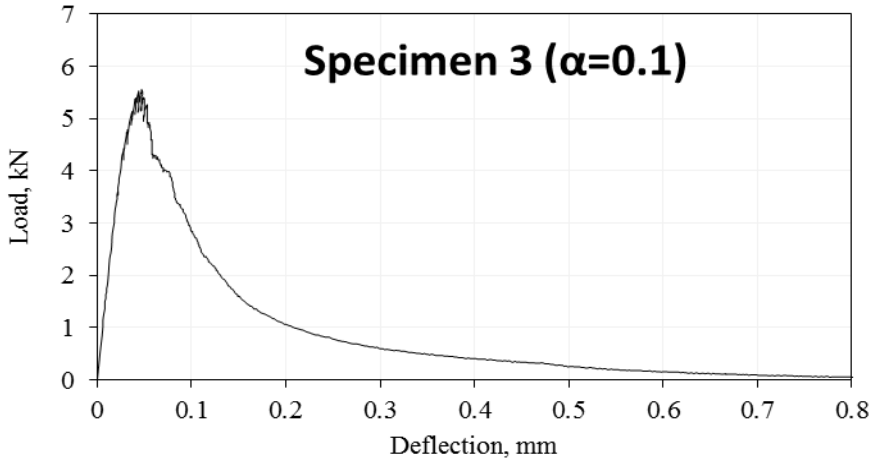

Appendix C. 2 The experimental load-deflection curves for 100mm specimen size

30B MPa (Shallow notch)

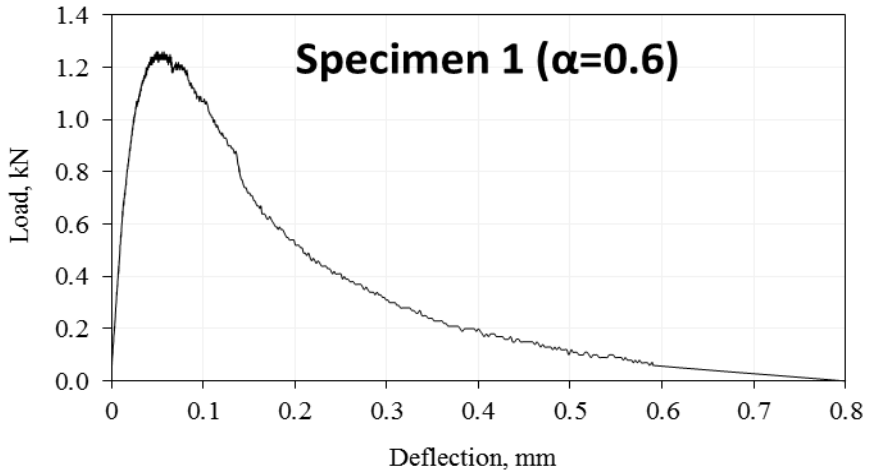

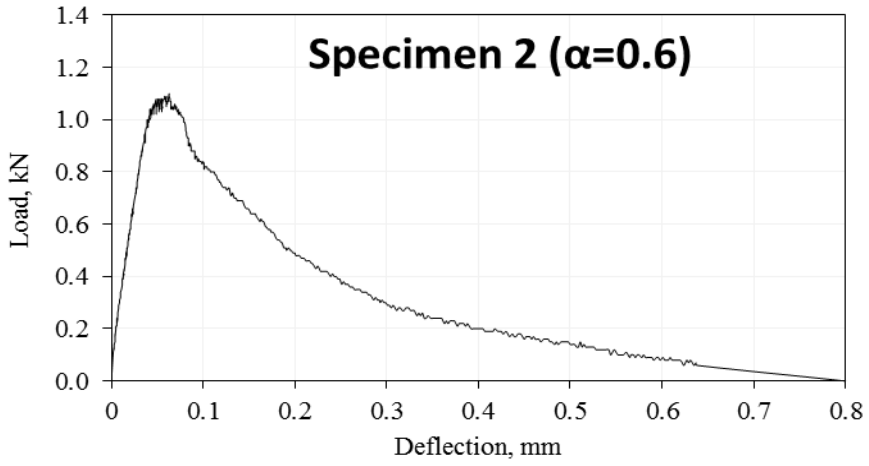

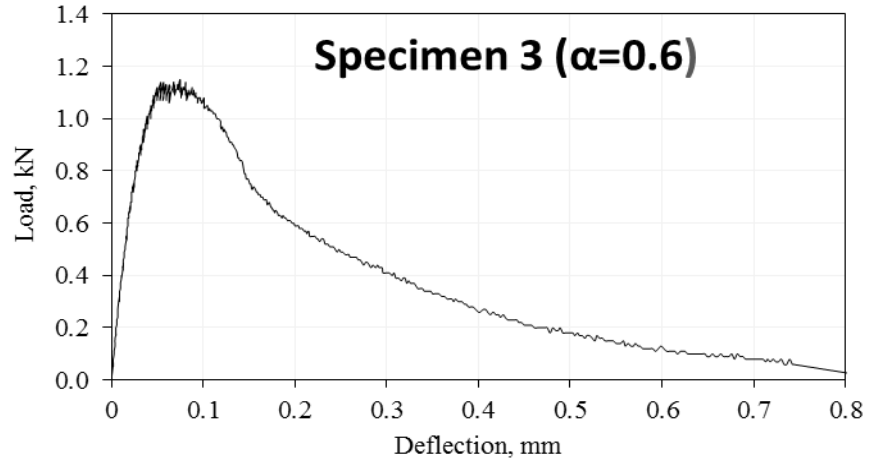

Appendix C. 3 The experimental load-deflection curves for 100mm specimen size 60B MPa (Deep notch)

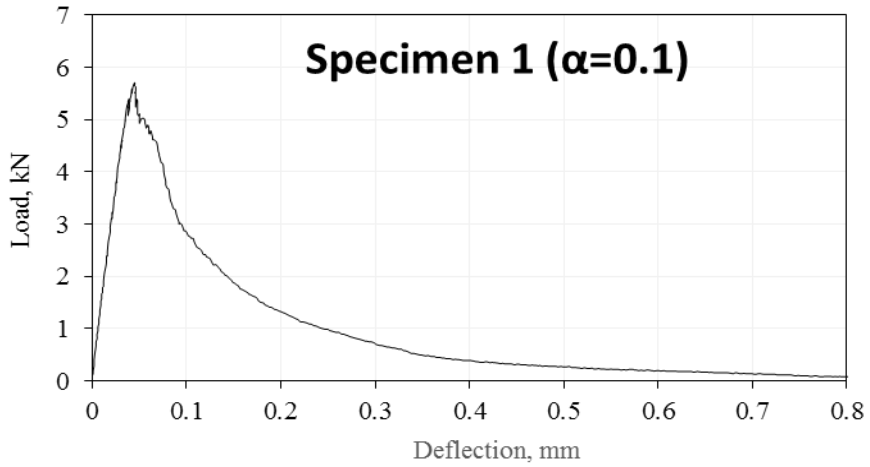

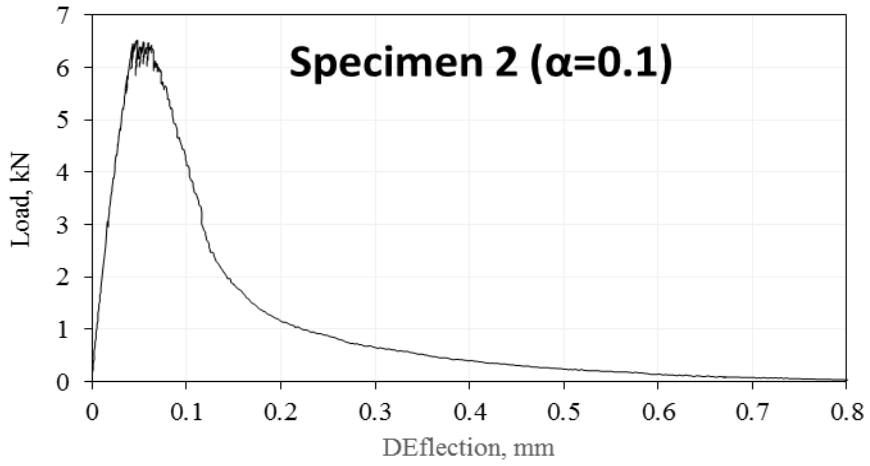

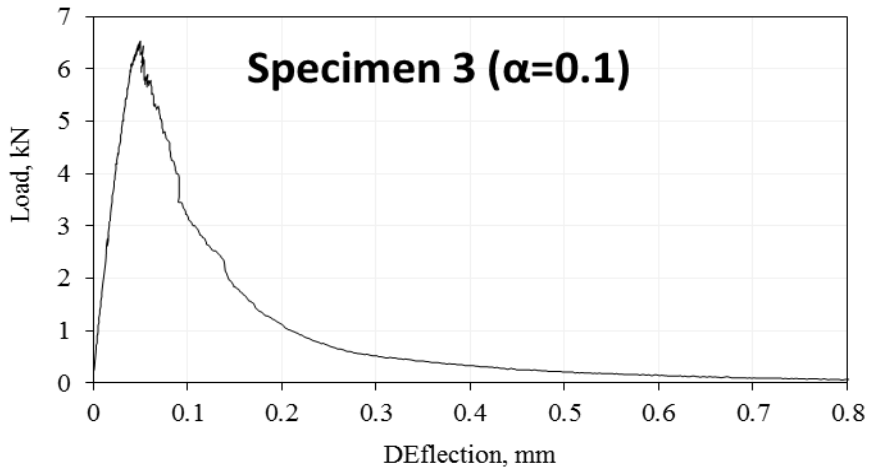

Appendix C. 4 The experimental load-deflection curves for 100mm specimen size

60B MPa (Shallow notch)

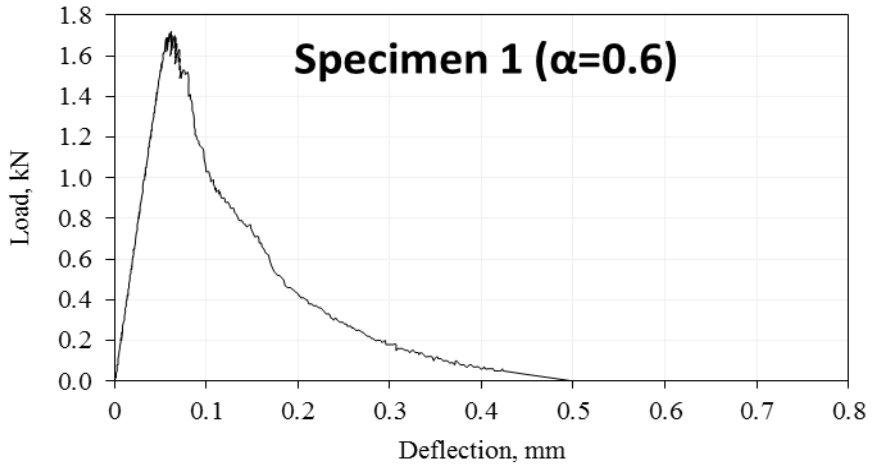

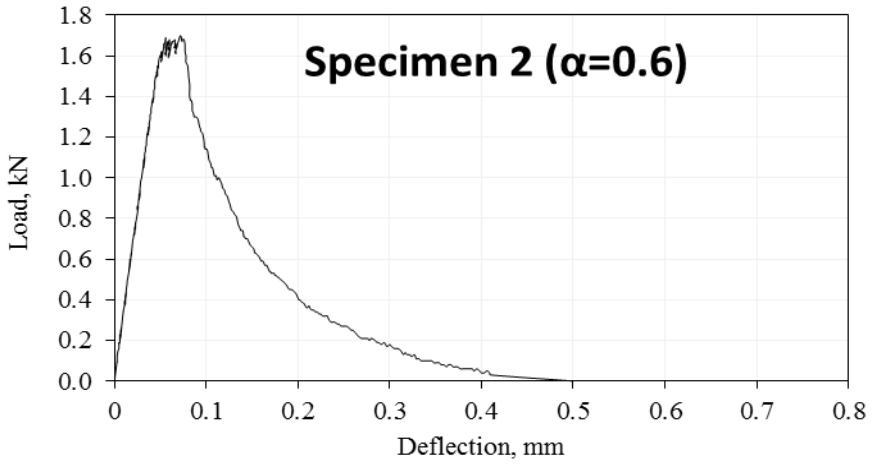

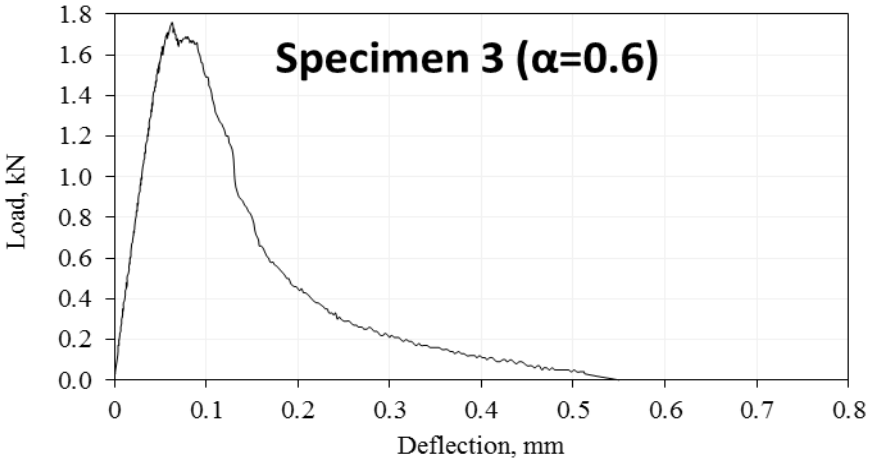

Appendix C. 5 The experimental load-deflection curves for 100mm specimen size 80B MPa (Deep notch)

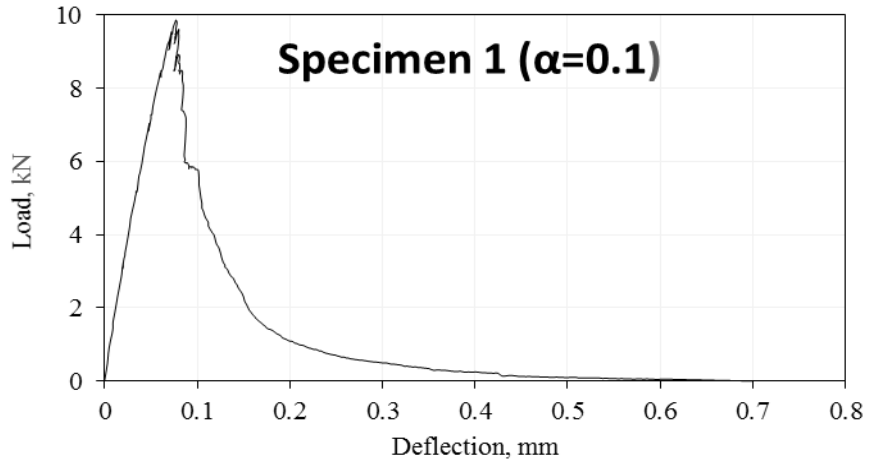

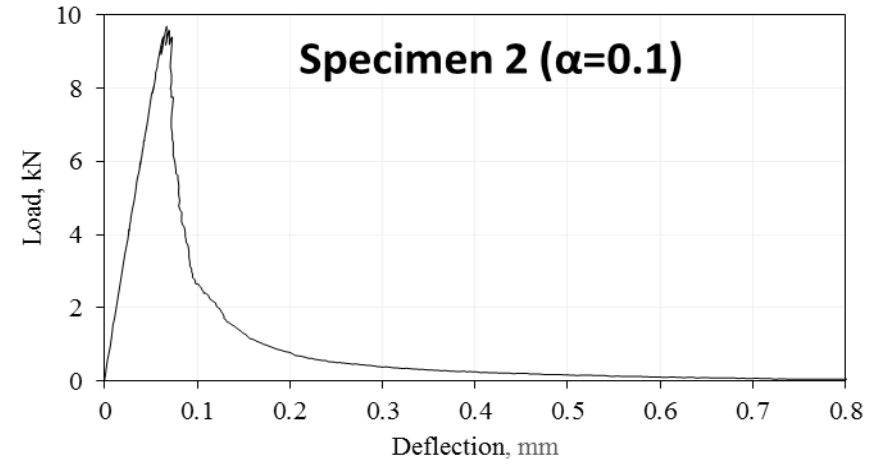

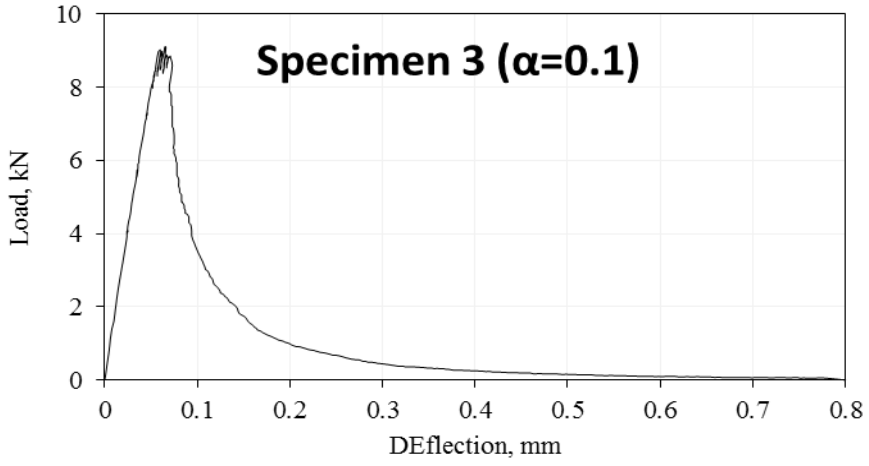

Appendix C. 6 The experimental load-deflection curves for 100mm specimen size

80B MPa (Shallow notch)

Appendix D

Load-CMOD curves used to determine TSD

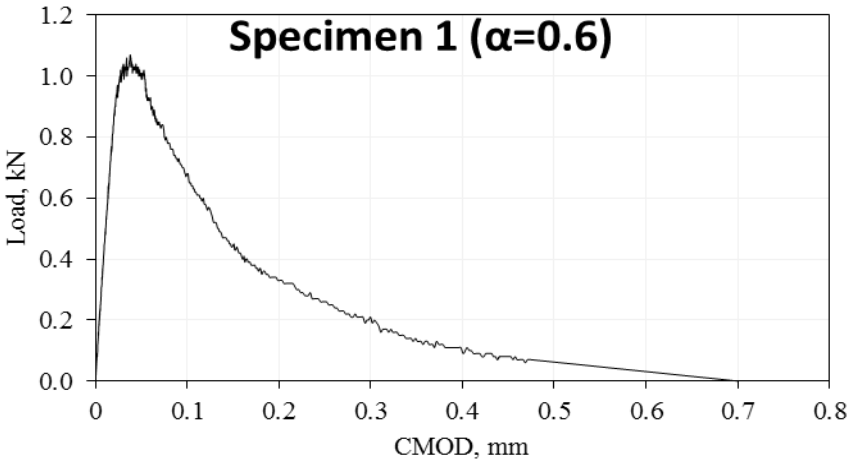

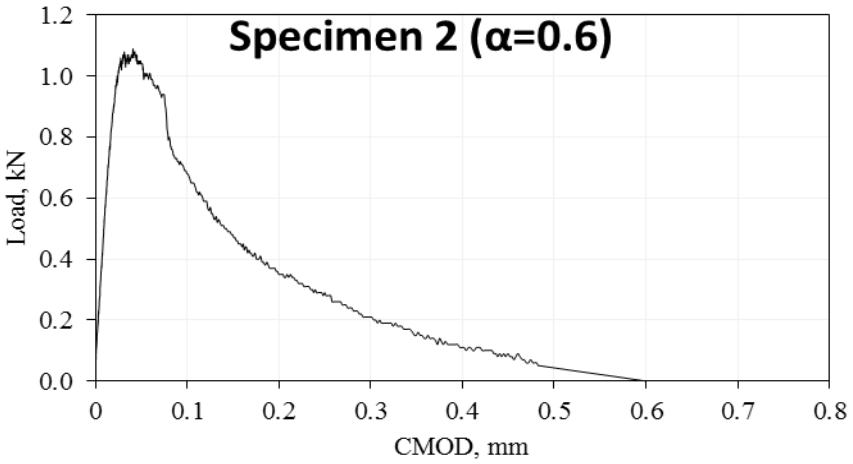

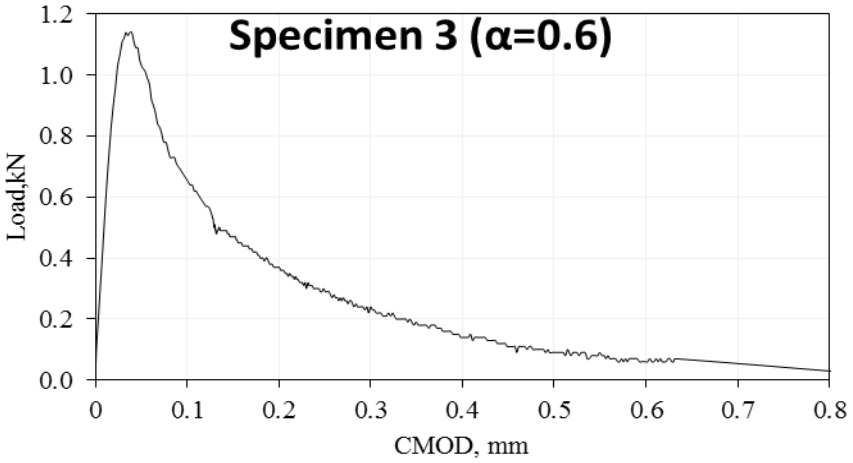

Appendix D. 1 The experimental load-CMOD curves for specimens' size 100mm for 30B MPa (Deep notch)

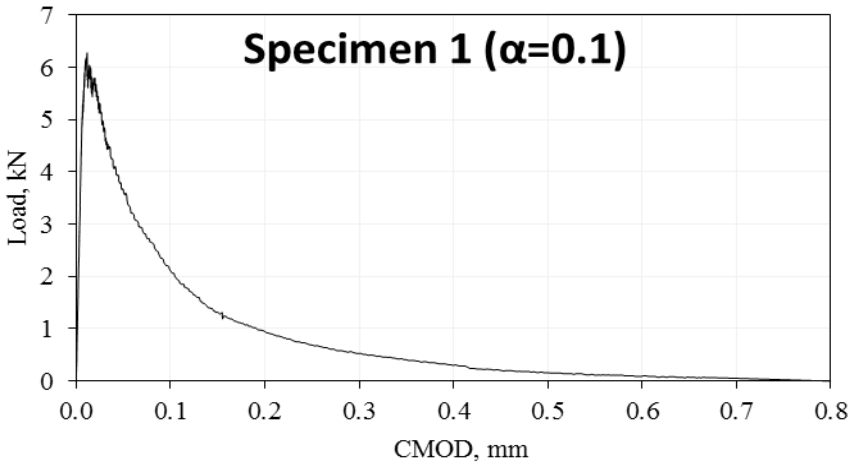

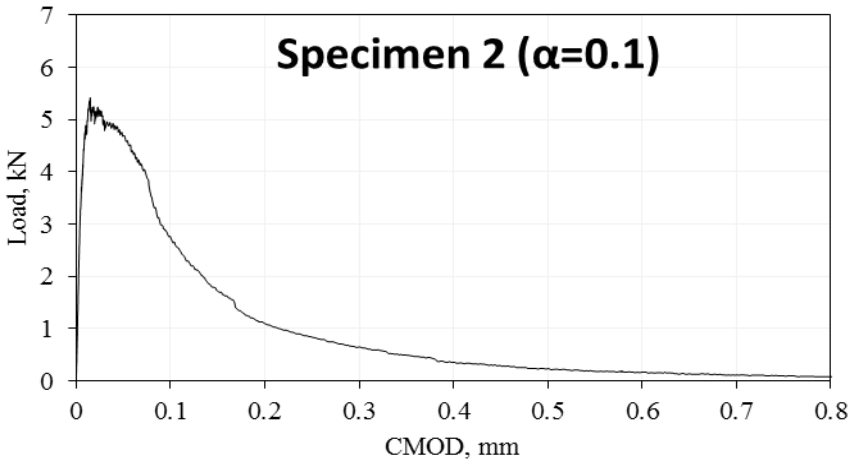

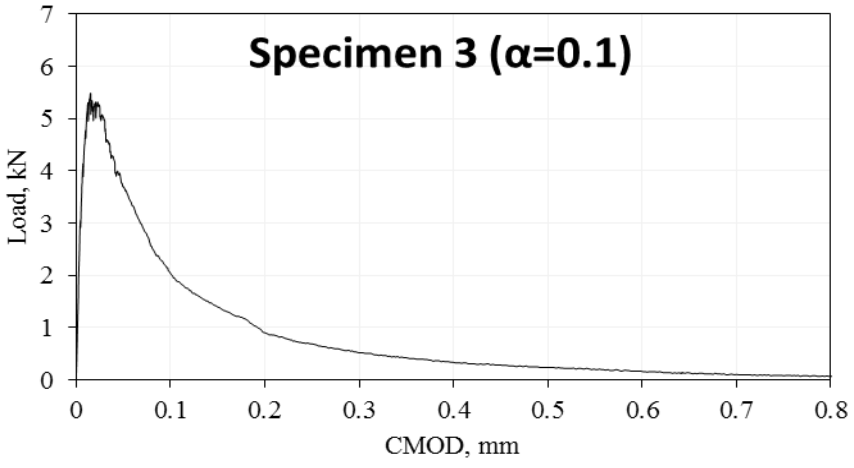

Appendix D. 2 The experimental load-CMOD curves for specimens' size 100mm for 30B MPa (Shallow notch)

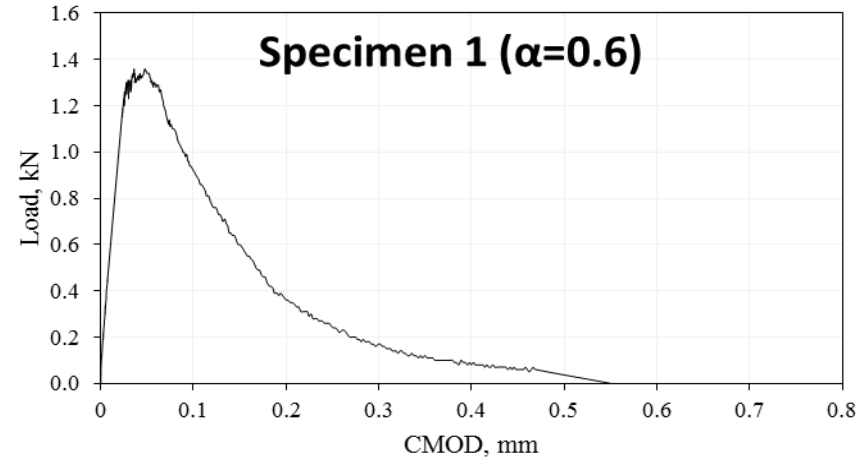

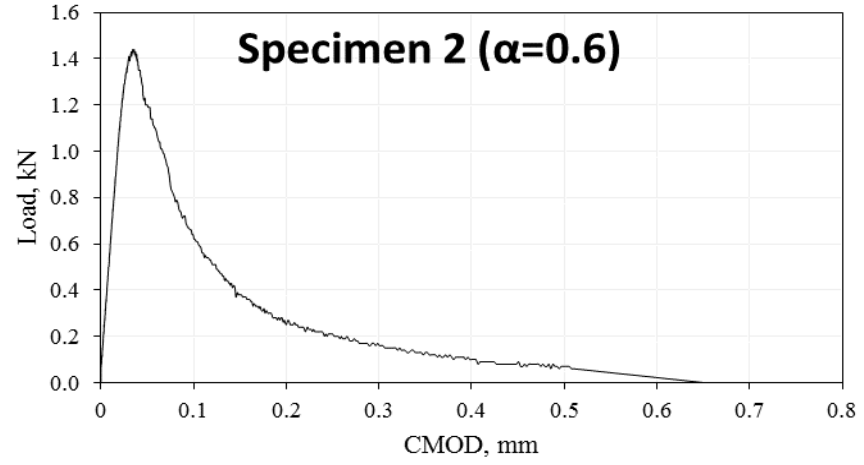

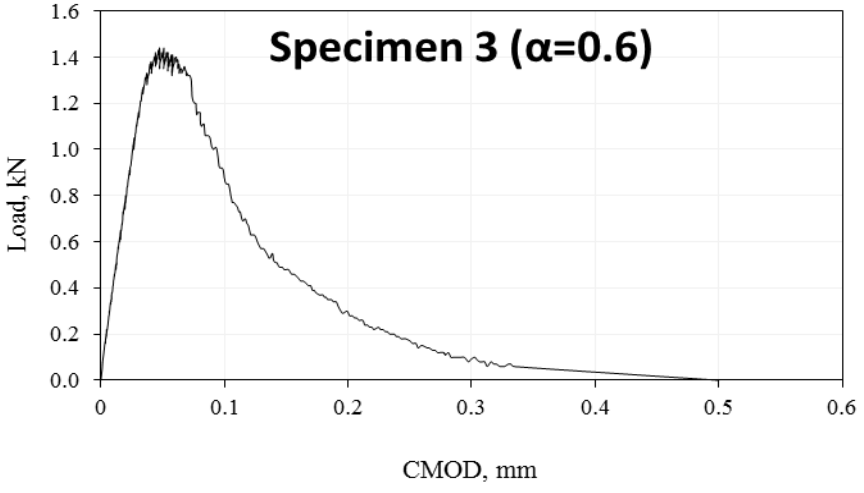

Appendix D. 3 The experimental load-CMOD curves for specimens' size 100mm for 60B MPa (Deep notch)

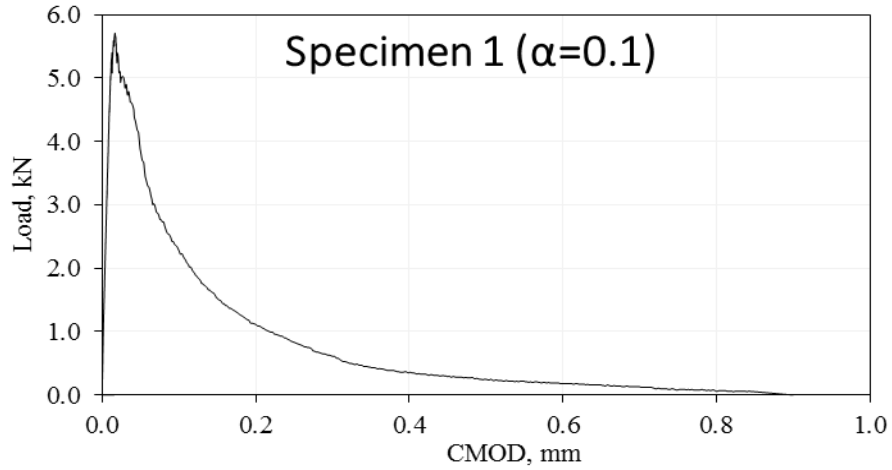

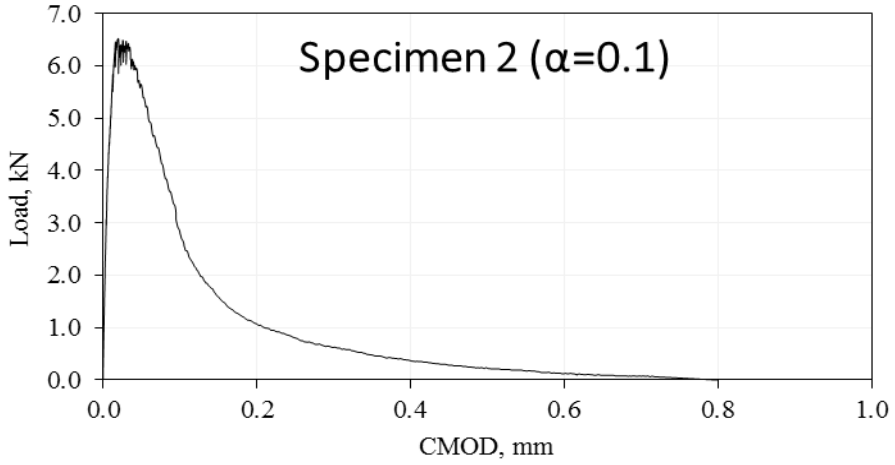

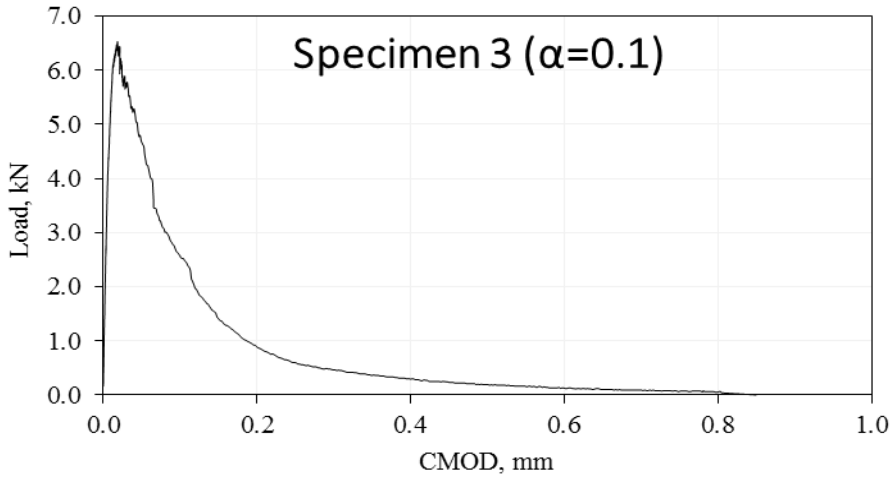

Appendix D. 4 The experimental load-CMOD curves for specimens' size 100mm for 60B MPa (Shallow notch)

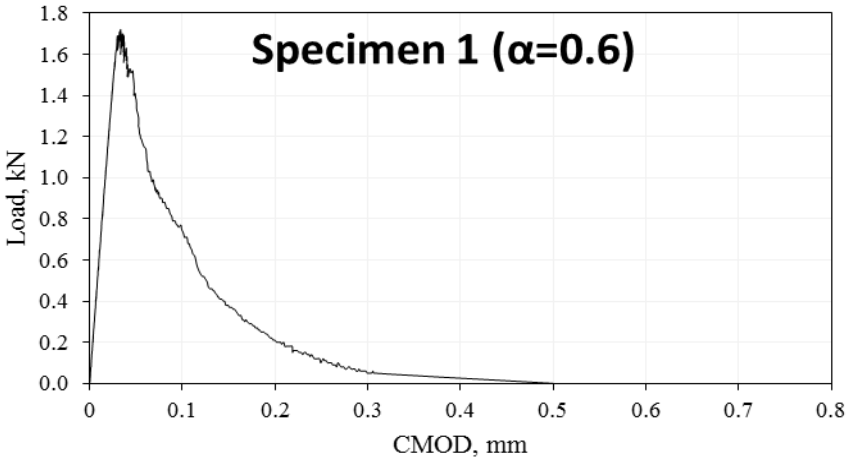

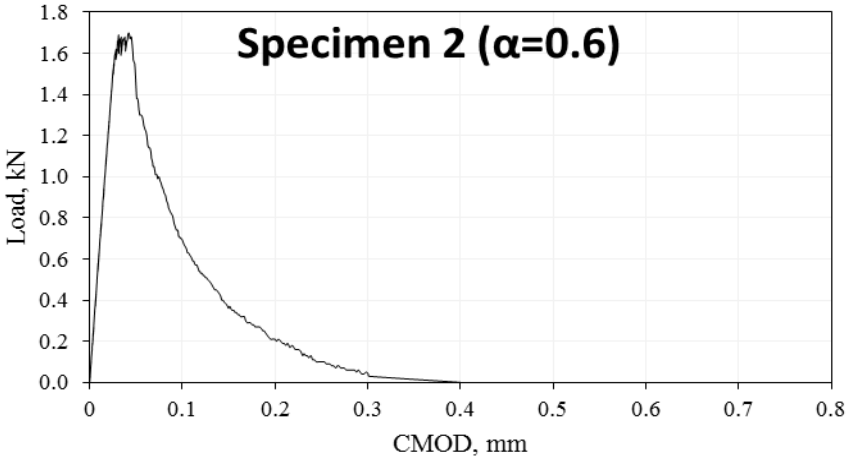

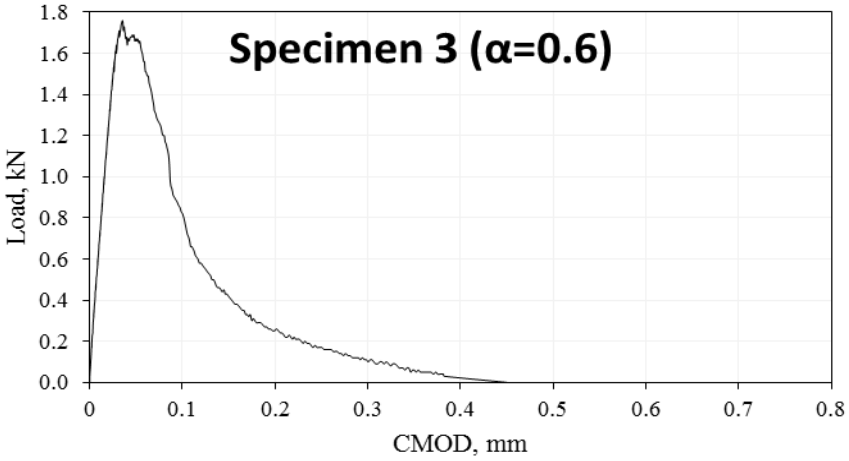

Appendix D. 5 The experimental load-CMOD curves for specimens' size 100mm for 80B MPa (Deep notch)

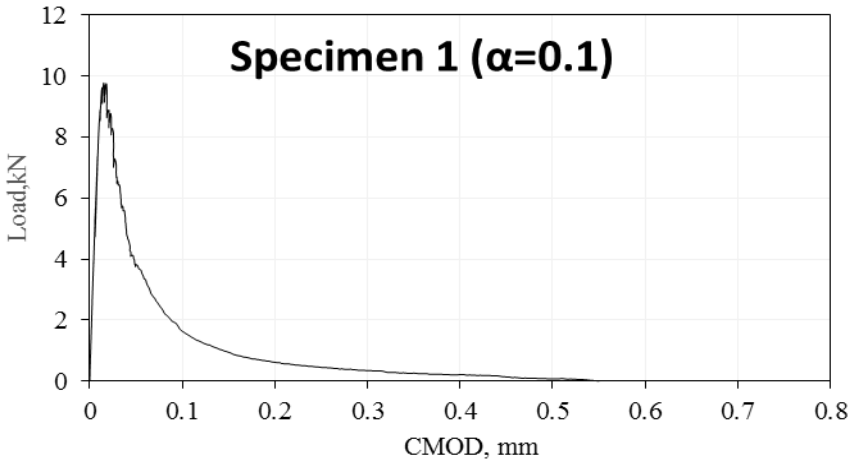

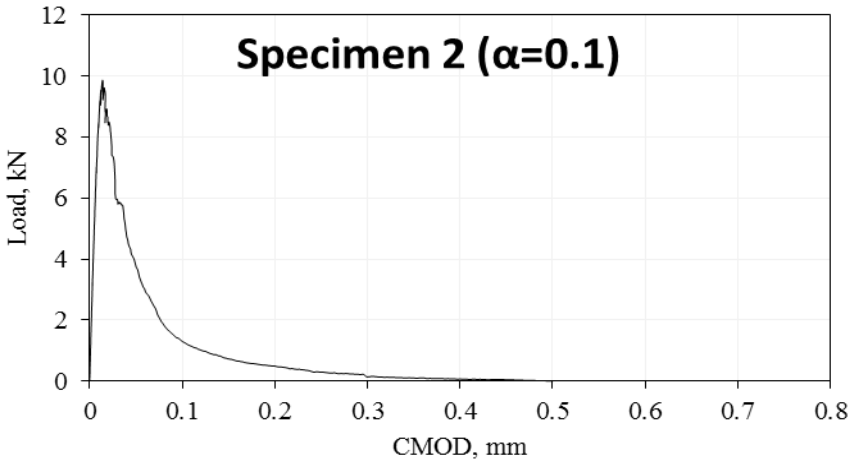

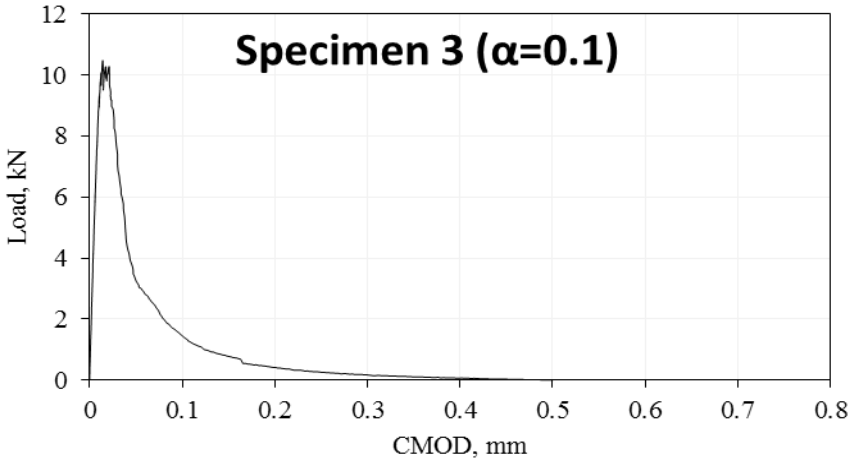

Appendix D. 6 The experimental load-CMOD curves for specimens' size 100mm for 80B MPa (Shallow notch)

Appendix E

Fracture energy MATLAB code

```
%*********************************************************************
%                    CARDIFF UNIVERSITY                              %
%                   SCHOOL OF ENGINEERING                            %
%                                                                    %
%  Size-independent specific fracture energy MATLAB Code 2014-2015
%
%               using the simplified boundary effect method (SBE)
%
%*********************************************************************
%     List of variables
%     Name            Description
%     -----           ------------
%     A01             Area of the shallow notch under load-deflection
%                     curve, kN/mm
%     A06             Area of the deep notch under load-deflection
%                     curve, kN/mm
%     WOF01          Work of fracture of the shallow beams according %
to RILEM FCM-50 (Size-dependent fracture energy, %                N/m)
%     WOF06           Work of fracture of the deep beams according to
%                     RILEM FCM-50 (Size-dependent fracture energy,
%                     N/m)
%     mean (WOF01)    the mean values of work of fracture of shallow
%                     notches
%     mean (WOF06)    the mean values of work of fracture of deep
%                     notches
%    std (WOF01)    the standard deviation values of work of fracture
%                     of shallow notches
%     std (WOF06)   the standard deviation values of work of fracture
%                     of deep notches
%     COV01           The coefficient of variation values of work of
%                     fracture of shallow notches
%     COV06           The coefficient of variation values of work of
%                     fracture of deep notches
%     q1              Shallow notch to depth ratio
%     q2              Deep notch to depth ratio
%     w               Depth of beam, m
%     B               width of beam, m
%     GF              Specific size-independent fracture energy, N/m
%     ALIGMENT        The transition ligament length, mm
%*********************************************************************
clear
clc
%*********************************************************************
% input beam dimension details
q1=0.1;
q2=0.6;
w=0.1;
B=0.1;
%*********************************************************************
% calculate notch depth, m
a1=q1*w;
a2=q2*w;
%*********************************************************************
% Input load-deflection curves areas for shallow and deep notches
beams
A01 = [0.80 0.85 0.86 0.82 0.79]; % Input the shallow values here
A06 = [0.20 0.21 0.25 0.19 0.23]; % Input the deep values here
% Determining the size dependent work of fracture based on RILEM FMC-
50
WOF01=A01/ (w-a1)/B;
WOF06= [A06/ (w-a2)/B];
```

```
mean (WOF01);
mean (WOF06);
std (WOF01);
std (WOF06);
COV01=std (WOF01)/mean (WOF01);
COV06=std (WOF06)/mean (WOF06);
c1=mean (WOF01);
c2=mean (WOF06);
% determining the size independent specific fracture energy %according
to the simplified boundary effect method

z1=w-a1;
z2=w-a2;
r=z1*c2;
x=(2*z1*z2*(c2-c1))/(c2*z2-c1*z1);
y=c1/(1-x/(2*z1));
m=1-q2;
f= 1-q1;
n= x/w;
if ( m > n && f > n )
GFF=y
Aligment=x
end
if (m <= n)
x1=(2*r+((2*r)^2-4*r*c1*z2)^0.5)/(2*c2);
x2=(2*r-((2*r)^2-4*r*c1*z2)^0.5)/(2*c2);
y1=c1/ (1-x1/(2*z1));
y2=c1/ (1-x2/(2*z1));

if ( x1 < w)
GFF=y1;
Aligment=x1;
end
if ( x2 < w)
GFF=y2;
Aligment=x2;
end
end
%*********************************************************************
GF=GFF
ALIGMENT=Aligment*1000
%*********************************************************************
cov01Percent=COV01*100;
cov06Percent=COV06*100;

COVAR01=cov01Percent;
COVAR06=cov06Percent;

COVGf01=COVAR01;
COVGf06=COVAR06;

meanGf01=mean (WOF01);
meanGf06=mean (WOF06);
%*********************************************************************
% Desired parameters to be printed in the output sheet
MyMatrix = [meanGf01; COVGf01; meanGf06; COVGf06; GF; ALIGMENT]';
HeaderNames='meanGf01, COVGf01, meanGf06, COVGf06, GF, ALIGMENT';
%*********************************************************************
% preferable output sheet name printed here
fileName = 'choose output file name here.csv';
```

```
outid = fopen(fileName, 'w+');
fprintf(outid, '%s', HeaderNames);
fclose(outid);

dlmwrite(fileName,myMatrix,'roffset',1,'-append', 'precision', 4); %
increased precision to allow all digits to be saved
disp(strcat('Generated report ''',fileName,''''))
%**********************************************************************
%**********************************************************************
```

Appendix F

MATLAB code for the bilinear tension-softening construction

```
%*****************************************************************
%                          CARDIFF UNIVERSITY
%                        SCHOOL OF ENGINEERING
% A MATLAB code for Determination of the static response of self-
% compacting concrete beams under three-point bending, using a
% bilinear tension-softening (stress-crack opening) relationship
% based on the fictitious crack model
%*****************************************************************
%     References
% 1. Hillerborg A. (1980). Analysis of fracture by means of the
%    fictitious crack model, particularly for fibre-reinforced
%    concrete, Int J Cement Composites, 2, 177-184.
% 2. Hillerborg A., Modeer M. and Petersson P. (1976). Analysis of
%    crack formation and crack growth in concrete by means of
%    fracture mechanics and finite elements, Cement Concrete
%    Research, 6, 773-782.
% 3. Olesen J.F. (2001). Fictitious crack propagation in fibre-
%    reinforced concrete beams, J Engineering Mechanics, 127, 272-80
%*****************************************************************
%     List of variables
%     Name              Description
%     -----             ------------
%     alp0              Initial notch depth to beam depth ratio
%     db                beam depth, mm
%     h                 Height of the hinge, mm
%     L                 Span length of the TPB, mm
%     t                 Thickness of the hinge, mm
%     S                 Width of the hinge, mm
%     a1, a2, b1 & b2    Parameters for the bilinear relation
%     a1 & a2           1/mm
%     b1 & b2           Dimensionless
%     E                 Young modulus, GPa
%     ft                Splitting tensile strength, GPa
%     GF                Specific size-independent fracture energy
%*****************************************************************
%*****************************************************************
% Part one for calculation the shallow notch parameters
%*****************************************************************
%*****************************************************************
clc
clear all
close all
polyfitOrder = 30;
% Enter the path of the experimental results Excel files of load-
% CMOD curves
v_matpath='C: \Users\Wajde1975\Desktop\ Fracture\80B';
% Enter the maximum displacement of the shallow and deep notches
MaxDisplacement01=0.42;
MaxDisplacement06=0.30;
% Enter the beam dimensions details
L=400;
t=100;
db=100;
```

```
a0shallow=10;
a0deep=60;
% Enter the rho value (use 0 for plain concrete or 0.045 for fibre
reinforced concrete)
rho=0;
% Enter the selected sheets numbers for shallow samples
SheetNo1 = [1 2 3 4 5];
% Enter the selected sheets numbers for deep samples
SheetNo6 = [7 8 9 10 11];
% Enter a proposed values of minimum and maximum theta
themin=0;
themax=200;
increment=themax/499;
incrementxq=MaxDisplacement01/499;
% xq is a constant increments in the x-direction of the average
experimental load-CMOD curves
xq = 0: incrementxq:MaxDisplacement01;
% Change the path to the file location
cd(v_matpath)
% Find the excel files in the folder
files = dir ('*.xlsx');
% [status, sheets] = xlsfinfo (filename)
filename = files(1).name;
[AA BB] = size(SheetNo1);
for n=1:BB
% Read Microsoft Excel spreadsheet file
clear subsetA
sheet = SheetNo1(1,n);
% Enter column range of the Excel sheets
xlRange = 'A:E';
subsetA = xlsread(filename,sheet,xlRange);
%*********************************************************************
% Fit curve or surface to data
%*********************************************************************
% Enter the column number of the x value (CMOD column in the excel
%sheet)
x = subsetA (:, 5);
% Enter the column number of the y value (load column in the excel
%sheet)
y = subsetA (:, 3);
hold on
plot(x,y);
p = polyfit(x,y, polyfitOrder);
f = polyval(p,x);
ff = polyval(p,xq);
% save all the results in one matrix (each column is a excel file)
Final_results(:,n)= ff(1,:);
hold on
end
% find the average of the final matrix
[m z] = size(Final_results);
for i = 1:m
    C(i,1) = mean(Final_results(i,1:z));
end
   plot(xq,C,':.');
   hold on
   plot(x,y,'o');
%*********************************************************************
%Except parameters that can be used later on
%*********************************************************************
```

```
clearvars -except xq C  polyfitOrder a0shallow a0deep db L t rho
SheetNo6 v_matpath MaxDisplacement06 themin increment themax
%*********************************************************************
a0=a0shallow;
alp0=a0/db;
h=(1-alp0)*db;
s=0.5*h;
%*********************************************************************
% Enter a1, a2, b2, ft, E limits values
%*********************************************************************
count = 1;
for a1=1:0.5:50
for a2=0.1:0.05:1.5
for b2=0.1:0.05:0.9
for ft=0.0018:0.0001:0.0048
for E=25:0.5:40
bet1=ft*a1*s/E;
bet2=ft*a2*s/E;
c =(1-b2)*(1-bet1)/(bet2-bet1);
rho=0;
the01=1-rho ;
the12=.5*(1-rho-c+((1-rho-c)^2+c^2/(bet1-1))^0.5);
the23=.5*(rho*(bet2-1)+b2/bet2+(rho^2*(bet2-1)^2+2*rho*(bet2-
1)*b2/bet2+(1-b2)^2/(bet1 -bet2)+b2^2/bet2)^.5);
k=0;
for the=themin :increment: themax
%*********************************************************************
% Alpha & Mu Calculation
%*********************************************************************
% For phase 0
if (0<=the & the<=the01)
alp = 0;
mu = the;
cod = 0;
% For phase I
elseif(the01<the & the<=the12)
bi= 1;
beti = bet1;
alp = 1-bet1-((1-bet1)*((1-rho)/the-bet1))^.5;
mu = 4*(1-3*alp+3*alp^2-alp^3/(1-bet1))*the+(6*alp-3)*(1-rho);
cod = s*ft/E*(1-bi+2*alp*the)/(1-beti);
% For phase II
elseif(the12<the & the<=the23)
bi = b2;
beti = bet2;
alp  =1-bet2-(1-b2)/(2*the)-((  1-bet2)*((  1-b2)^2/(4*the^2)/(bet1  -
bet2)-bet2+(b2-rho)/the))^.5;
mu  =  4*(1-3*alp+3*alp^2-alp^3/(1-bet2))*the+(6*alp-3)*(1-rho)-(((1-
b2)*(3*alp^2-(c/(2*the))^2))/(1-bet2));
cod = s*ft/E*(1-bi+2*alp*the)/(1-beti);
% For phase III
elseif(the23<the)
bi =0;
beti = 0;
alp     =     1     -1     /(2*the)*(1+((1-b2)^2/(bet1-bet2)+b2^2/bet2-
4*rho*the)^.5);
mu          =          4*(1-3*alp+3*alp^2-alp^3)*the+(6*alp-3)*(1-rho)-
3*alp^2+1/(4*the^2)*(1-b2/bet2)*(1-b2/bet2+c)*(1+bet1*c/(1-
bet1))+(c/(2*the))^2;
cod = s*ft/E*(1-bi+2*alp*the)/(1-beti);
end
```

```
k=k+1;
pp(k) = 2/3*ft*h^2*t/L*mu;
m = pp(k)*L/4;
sigm = 6*m/(t*db^2);
cod0  =  4*sigm*a0/E*(0.76-2.28*alp0+3.87*alp0^2-2.04*alp0^3+0.66/(1-
alp0)^2);
CMOD(k) = cod + cod0;
end
AA = [CMOD;pp]';
x = AA(:,1); % the x value
y = AA(:,2); % the y value

% select either spline fit or polyfit (choose one option as shown
here)
%*********************************************************************
% spline fit option
ff=interp1(x,y,xq,'spline');
%*********************************************************************
% poly fit option
% p = polyfit(x,y, polyfitOrder);
% f = polyval(p,x);
% ff = polyval(p,xq);
%*********************************************************************
%Check the maximum differences in theoretical and experimental %peak
%load
%*********************************************************************
H1=max(ff);
H2=max(C);
H3=(H2-H1)/H2*100;
if(-2<=H3 && H3<=2)
clear Error
[mm nn]= size(xq);
for ii = 1:nn
Error(ii,2) = (ff(1,ii)-C(ii,1))^2;
Error(ii,1) = xq(1,ii);
end
SumError (count,1) = sum (Error(:,2))/nn;
SumError (count,2) = a1;
SumError (count,3) = a2;
SumError (count,4) = b2;
SumError (count,5) = ft;
SumError (count,6) = E;
count = count +1;
end
end
end
end
end
end
EE=sortrows(SumError,[1 6]);
MinERR=EE(1,1);
a1=EE(1,2);
a2=EE(1,3);
b2=EE(1,4);
ft=EE(1,5);
E=EE(1,6);
w1=(1-b2)/(a1-a2);
w2=b2/a2;
sigmaft=a2*(w2-w1);
Gf01=0.5*ft*1000*(w1+sigmaft*w2);
D=[0 w1 w2];
```

```
EEE=[1 sigmaft 0];
KneeCoordinatesSHallow= [D; EEE]';
%*********************************************************************
%Except parameters that can be used later on
%*********************************************************************
clearvars -except sigmaft C xq alp0 E ft db h L t s rho a1 a2 b2
themin increment themax KneeCoordinatesSHallow w1 w2 Gf01 MinERR
SumError polyfitOrder a0 a0deep SheetNo6 v_matpath MaxDisplacement06
B1
%*********************************************************************
bet1=ft*a1*s/E;
bet2=ft*a2*s/E;
c =(1-b2)*(1-bet1)/(bet2-bet1);
rho=0;
the01=1-rho ;
the12=0.5*(1-rho-c+((1-rho-c)^2+c^2/(bet1-1))^0.5);
the23=0.5*(rho*(bet2-1)+b2/bet2+(rho^2*(bet2-1)^2+2*rho*(bet2-
1)*b2/bet2+(1-b2)^2/(bet1 -bet2)+b2^2/bet2)^.5);
k=0;
%*********************************************************************
% Alpha & MU Calculation
%*********************************************************************
% input theta values
for the=themin :increment:themax
% For phase 0
if (0<=the & the<=the01)
alp = 0;
mu = the;
cod = 0;
% For phase I
elseif(the01<the & the<=the12)
bi= 1;
beti = bet1;
alp = 1-bet1-((1-bet1)*((1-rho)/the-bet1))^.5;
mu = 4*(1-3*alp+3*alp^2-alp^3/(1-bet1))*the+(6*alp-3)*(1-rho);
cod = s*ft/E*(1-bi+2*alp*the)/(1-beti);
% For phase II
elseif(the12<the & the<=the23)
bi = b2;
beti = bet2;
alp =1-bet2-(1-b2)/(2*the)-(( 1-bet2)*(( 1-b2)^2/(4*the^2)/(bet1 -
bet2)-bet2+(b2-rho)/the))^.5;
mu = 4*(1-3*alp+3*alp^2-alp^3/(1-bet2))*the+(6*alp-3)*(1-rho)-(((1-
b2)*(3*alp^2-(c/(2*the))^2))/(1-bet2));
cod = s*ft/E*(1-bi+2*alp*the)/(1-beti);
% For phase III
elseif(the23<the)
bi =0;
beti = 0;
alp = 1 -1 /(2*the)*(1+((1-b2)^2/(bet1-bet2)+b2^2/bet2-
4*rho*the)^.5);
mu = 4*(1-3*alp+3*alp^2-alp^3)*the+(6*alp-3)*(1-rho)-
3*alp^2+1/(4*the^2)*(1-b2/bet2)*(1-b2/bet2+c)*(1+bet1*c/(1-
bet1))+(c/(2*the))^2;
cod = s*ft/E*(1-bi+2*alp*the)/(1-beti);
end
k=k+1;
pp(k) = 2/3*ft*h^2*t/L*mu;
m = pp(k)*L/4;
sigm = 6*m/(t*db^2);
```

```
cod0  =  4*sigm*a0/E*(0.76-2.28*alp0+3.87*alp0^2-2.04*alp0^3+0.66/(1-
alp0)^2);
CMOD(k) = cod + cod0;
end
AA = [CMOD;pp]';
x = AA(:,1); % the x value
y = AA(:,2); % the y value
% select either spline fit or polyfit (choose one option as shown
here)
%*********************************************************************
% spline fit option
ff=interp1(x,y,xq,'spline');
%*********************************************************************
% poly fit option
% p = polyfit(x,y,polyfitOrder);
% f = polyval(p,x);
% ff = polyval(p,xq);
%*********************************************************************
W1(:,1)=xq;
W2(:,1)=C;
W3(:,1)=ff;
ModelCurve = [xq;ff]';
TestCurve=[W1,W2];
ModelTestCurveShallow = [W1';W2';W3']';
HeaderNames1='xq,PTest,PModel';
% Preferable output sheet name printed here
fileName1 = 'ModelTest01.csv';
outid = fopen(fileName1, 'w+');
fprintf(outid, '%s', HeaderNames1);
fclose(outid);
dlmwrite(fileName1,ModelTestCurveShallow,'roffset',1,'-append',
'precision', 4);
disp(strcat('Generated report ''',fileName1,''''))
% Preferable output sheet name printed here
filename = 'Parameters.xlsx';
% Desired parameters to be printed in the output sheet
A                                                                    =
{'a1','a2','b2','w1','w2','Gf01','ft01','E','MinERR';a1,a2,b2,w1,w2,
Gf01,ft,E,MinERR};
B1=[a1,a2,b2,Gf01,ft,E,MinERR];
sheet = 1;
xlRange = 'A';
xlswrite(filename,A,sheet,xlRange)
filename = 'Parameters.xlsx';
A = {'Xknee','Yknee';0,1;w1,sigmaft;w2,0};
sheet = 1;
xlRange = 'J';
xlswrite(filename,A,sheet,xlRange)
%*********************************************************************
%*********************************************************************
% Part two for calculation the deep notch parameters
%*********************************************************************
clearvars -except polyfitOrder MaxDisplacement06 SheetNo6 a0deep db L
t s rho themin increment themax KneeCoordinatesSHallow v_matpath B1
%*********************************************************************
incrementxq = MaxDisplacement06/499;
xq = 0:incrementxq:MaxDisplacement06;
% change the path to the file location automatically
cd(v_matpath)
% find the excel files in the folder
files = dir('*.xlsx');
```

```
filename = files(1).name;
[AA BB] = size(SheetNo6);
for n=1:BB
% Read Microsoft Excel spreadsheet file
clear subsetA
sheet = SheetNo6(1,n);
xlRange = 'A:E';
subsetA = xlsread(filename,sheet,xlRange);
%*********************************************************************
% Fit curve or surface to data
%*********************************************************************
% Enter the column number of the x value (CMOD column in the excel
% sheet)
x = subsetA(:,5);
% Enter the column number of the y value (load column in the excel
% sheet)
y = subsetA(:,3);
hold on
plot(x,y);
p = polyfit(x,y,polyfitOrder);
f = polyval(p,x);
ff = polyval(p,xq);
% save all the results in one matrix (each column is a excel file)
Final_results(:,n)= ff(1,:);
hold on
end
% find the average of the final matrix
[m z] = size(Final_results);
for i = 1:m
C(i,1) = mean(Final_results(i,1:z));
end
plot(xq,C,':.');
clearvars -except xq C  polyfitOrder L t s rho db themin increment
themax KneeCoordinatesSHallow a0deep B1
%*********************************************************************
% Enter constant values
%*********************************************************************
a0=a0deep;
alp0=a0/db;
h=(1-alp0)*db;
% Enter a1, a2, b2, ft, E limits values
count = 1;
for a1=1:0.5:50
for a2=0.1:0.05:1.5
for b2=0.1:0.05:0.9
for ft=0.0018:0.0001:0.0048
for E=25:0.5:40
bet1=ft*a1*s/E;
bet2=ft*a2*s/E;
c =(1-b2)*(1-bet1)/(bet2-bet1);
rho=0;
the01=1-rho ;
the12=.5*(1-rho-c+((1-rho-c)^2+c^2/(bet1-1))^0.5);
the23=.5*(rho*(bet2-1)+b2/bet2+(rho^2*(bet2-1)^2+2*rho*(bet2-
1)*b2/bet2+(1-b2)^2/(bet1 -bet2)+b2^2/bet2)^.5);
k=0;
for the=themin :increment:themax
%*********************************************************************
% Alpha & Mu Calculation
%*********************************************************************
% For phase 0
```

```
if (0<=the & the<=the01)
alp = 0;
mu = the;
cod = 0;
% For phase I
elseif(the01<the & the<=the12)
bi= 1;
beti = bet1;
alp = 1-bet1-((1-bet1)*((1-rho)/the-bet1))^.5;
mu = 4*(1-3*alp+3*alp^2-alp^3/(1-bet1))*the+(6*alp-3)*(1-rho);
cod = s*ft/E*(1-bi+2*alp*the)/(1-beti);
% For phase II
elseif(the12<the & the<=the23)
bi = b2;
beti = bet2;
alp  =1-bet2-(1-b2)/(2*the)-((  1-bet2)*((  1-b2)^2/(4*the^2)/(bet1  -
bet2)-bet2+(b2-rho)/the))^.5;
mu  =  4*(1-3*alp+3*alp^2-alp^3/(1-bet2))*the+(6*alp-3)*(1-rho)-(((1-
b2)*(3*alp^2-(c/(2*the))^2))/(1-bet2));
cod = s*ft/E*(1-bi+2*alp*the)/(1-beti);
% For phase III
elseif(the23<the)
bi =0;
beti = 0;
alp    =    1    -1    /(2*the)*(1+((1-b2)^2/(bet1-bet2)+b2^2/bet2-
4*rho*the)^.5);
mu         =         4*(1-3*alp+3*alp^2-alp^3)*the+(6*alp-3)*(1-rho)-
3*alp^2+1/(4*the^2)*(1-b2/bet2)*(1-b2/bet2+c)*(1+bet1*c/(1-
bet1))+(c/(2*the))^2;
cod = s*ft/E*(1-bi+2*alp*the)/(1-beti);
end
k=k+1;
pp(k) = 2/3*ft*h^2*t/L*mu;
m = pp(k)*L/4;
sigm = 6*m/(t*db^2);
cod0  =  4*sigm*a0/E*(0.76-2.28*alp0+3.87*alp0^2-2.04*alp0^3+0.66/(1-
alp0)^2);
CMOD(k) = cod + cod0;
end
AA = [CMOD;pp]';
x = AA(:,1); % the x value
y = AA(:,2); % the y value
% select either spline fit or polyfit (choose one option as shown)
%*****************************************************************
% spline fit option
ff=interp1(x,y,xq,'spline');
%*****************************************************************
% poly fit option
% p = polyfit(x,y,polyfitOrder);
% f = polyval(p,x);
% ff = polyval(p,xq);
%*****************************************************************
%Check the maximum differences in theoretical and experimental peak
%load
%*****************************************************************
H1=max(ff);
H2=max(C);
H3=(H2-H1)/H2*100;
if(-2<=H3 && H3<=2)
clear Error
[mm nn]= size(xq);
```

```
for ii = 1:nn
Error(ii,2) = (ff(1,ii)-C(ii,1))^2;
Error(ii,1) = xq(1,ii);
end
SumError(count,1) = sum (Error(:,2))/nn;
SumError(count,2) = a1;
SumError(count,3) = a2;
SumError(count,4) = b2;
SumError(count,5) = ft;
SumError(count,6) = E;
count = count +1;
end
end
end
end
end
end
EE=sortrows(SumError,[1 6]);
MinERR=EE(1,1);
a1=EE(1,2);
a2=EE(1,3);
b2=EE(1,4);
ft=EE(1,5);
E=EE(1,6);
w1=(1-b2)/(a1-a2);
w2=b2/a2;
sigmaft=a2*(w2-w1);
Gf06=0.5*ft*1000*(w1+sigmaft*w2);
D=[0 w1 w2];
EEE=[1 sigmaft 0];
KneeCoordinatesSHallow=[D;EEE]';
%*********************************************************************
clearvars -except sigmaft C xq alp0 E ft db h L t s rho a1 a2 b2
themin increment themax KneeCoordinatesDeep w1 w2 Gf01 Gf06 MinERR
SumError polyfitOrder  a0deep KneeCoordinatesSHallow B1
%*********************************************************************
% input a1, a2, b2 values
a0=a0deep;
bet1=ft*a1*s/E;
bet2=ft*a2*s/E;
c =(1-b2)*(1-bet1)/(bet2-bet1);
rho=0;
the01=1-rho ;
the12=.5*(1-rho-c+((1-rho-c)^2+c^2/(bet1-1))^0.5);
the23=.5*(rho*(bet2-1)+b2/bet2+(rho^2*(bet2-1)^2+2*rho*(bet2-
1)*b2/bet2+(1-b2)^2/(bet1 -bet2)+b2^2/bet2)^.5);
k=0;
% input theta values
 for the=themin :increment:themax
%*********************************************************************
% Alpha & Mu Calculation
%*********************************************************************
% For phase 0
if (0<=the & the<=the01)
alp = 0;
mu = the;
cod = 0;
% For phase I
elseif(the01<the & the<=the12)
bi= 1;
beti = bet1;
```

```
alp = 1-bet1-((1-bet1)*((1-rho)/the-bet1))^.5;
mu = 4*(1-3*alp+3*alp^2-alp^3/(1-bet1))*the+(6*alp-3)*(1-rho);
cod = s*ft/E*(1-bi+2*alp*the)/(1-beti);
% For phase II
elseif(the12<the & the<=the23)
bi = b2;
beti = bet2;
alp =1-bet2-(1-b2)/(2*the)-(( 1-bet2)*(( 1-b2)^2/(4*the^2)/(bet1 -
bet2)-bet2+(b2-rho)/the))^.5;
mu = 4*(1-3*alp+3*alp^2-alp^3/(1-bet2))*the+(6*alp-3)*(1-rho)-(((1-
b2)*(3*alp^2-(c/(2*the))^2))/(1-bet2));
cod = s*ft/E*(1-bi+2*alp*the)/(1-beti);
% For phase III
elseif(the23<the)
bi =0;
beti = 0;
alp = 1 -1 /(2*the)*(1+((1-b2)^2/(bet1-bet2)+b2^2/bet2-
4*rho*the)^.5);
mu = 4*(1-3*alp+3*alp^2-alp^3)*the+(6*alp-3)*(1-rho)-
3*alp^2+1/(4*the^2)*(1-b2/bet2)*(1-b2/bet2+c)*(1+bet1*c/(1-
bet1))+(c/(2*the))^2;
cod = s*ft/E*(1-bi+2*alp*the)/(1-beti);
end
k=k+1;
pp(k) = 2/3*ft*h^2*t/L*mu;
m = pp(k)*L/4;
sigm = 6*m/(t*db^2);
cod0 = 4*sigm*a0/E*(0.76-2.28*alp0+3.87*alp0^2-2.04*alp0^3+0.66/(1-
alp0)^2);
CMOD(k) = cod + cod0;
end
AA = [CMOD;pp]';
x = AA(:,1); % the x value
y = AA(:,2); % the y value
% select either spline fit or polyfit (choose one option as shown)
%*****************************************************************
% spline fit option
ff=interp1(x,y,xq,'spline');
%*****************************************************************
*******
% poly fit option
% p = polyfit(x,y,polyfitOrder);
% f = polyval(p,x);
% ff = polyval(p,xq);
%*****************************************************************
W1(:,1)=xq;
W2(:,1)=C;
W3(:,1)=ff;
ModelCurve = [xq;ff]';
TestCurve=[W1,W2];
ModelTestCurveDeep = [W1';W2';W3']';
HeaderNames1='xq,PTest,PModel';
% Preferable output sheet name printed here
fileName1 = 'ModelTest06.csv';
outid = fopen(fileName1, 'w+');
fprintf(outid, '%s', HeaderNames1);
fclose(outid);
dlmwrite(fileName1,ModelTestCurveDeep,'roffset',1,'-append',
'precision', 4); % increased precision to allow all digits to be saved
disp(strcat('Generated report ''',fileName1,''''))
% Preferable output sheet name printed here
```

```
filename = 'Parameters.xlsx';
% Desired parameters to be printed in the output sheet
A                                                                    =
{'a1','a2','b2','w1','w2','Gf06','ft06','E','MinERR';a1,a2,b2,w1,w2,
Gf06,ft,E,MinERR};
sheet = 1;
xlRange = 'L';
xlswrite(filename,A,sheet,xlRange)
filename = 'Parameters.xlsx';
A = {'Xknee','Yknee';0,1;w1,sigmaft;w2,0};
B2=[a1,a2,b2,Gf01,ft,E,MinERR];
parametersstar=(B1+B2)/2;
sheet = 1;
xlRange = 'U';
xlswrite(filename,A,sheet,xlRange)
%*********************************************************************
%*********************************************************************
% this part is to find the unique parameters of hinge model
%*********************************************************************
% Enter constant values
%*********************************************************************
% Input the specific size-independent fracture energy, GF and
% splitting tensile strength, ft values
%*********************************************************************
GF=0.1469; % Experimental simplified boundary effect method, N/m
ft=3.12;% Experimental of splitting tensile strength, MPa
%*********************************************************************
a1star=parametersstar (1);
a2star=parametersstar (2);
b2star=parametersstar (3);
Gfstar=parametersstar (4);
ftstar=parametersstar(5)*1000;
w1star=(1-b2star)/(a1star-a2star)
w2star=b2star/a2star
w1=w1star*GF*ftstar/(Gfstar*ft);
sigmaftstar=(w2star-w1star)*a2star;
sigmaftstar2=1-a1star*w1star;
sigmastar=ftstar*sigmaftstar;
secondside=GF*sigmastar*w2star/(a2star*Gfstar*ft);
w2one=(w1+(w1^2+4*secondside)^0.5)/2
w2two=(w1-(w1^2+4*secondside)^0.5)/2
if(w2one>0)
    w2=w2one
end
if(w2two>0)
    w2=w2two
end
a2=a2star
sigmaft=(w2-w1)*a2;
a1=(1-sigmaft)/w1;
% Desired parameters to be printed in the output sheet
myMatrix=[a1star;a2star;ftstar;Gfstar;w1star;w2star;sigmaftstar;a1;a
2;ft;GF;w1;w2;sigmaft]';
% Preferable output sheet name printed here
fileName = 'Uniqueparameters.csv';
dlmwrite(fileName,myMatrix,'roffset',1,'-append', 'precision', 8);
disp(strcat('Generated report ''',fileName,''''))
%*********************************************************************
%*********************************************************************
```

Appendix G

Visualisation of simulations of SCC mixes by SPH

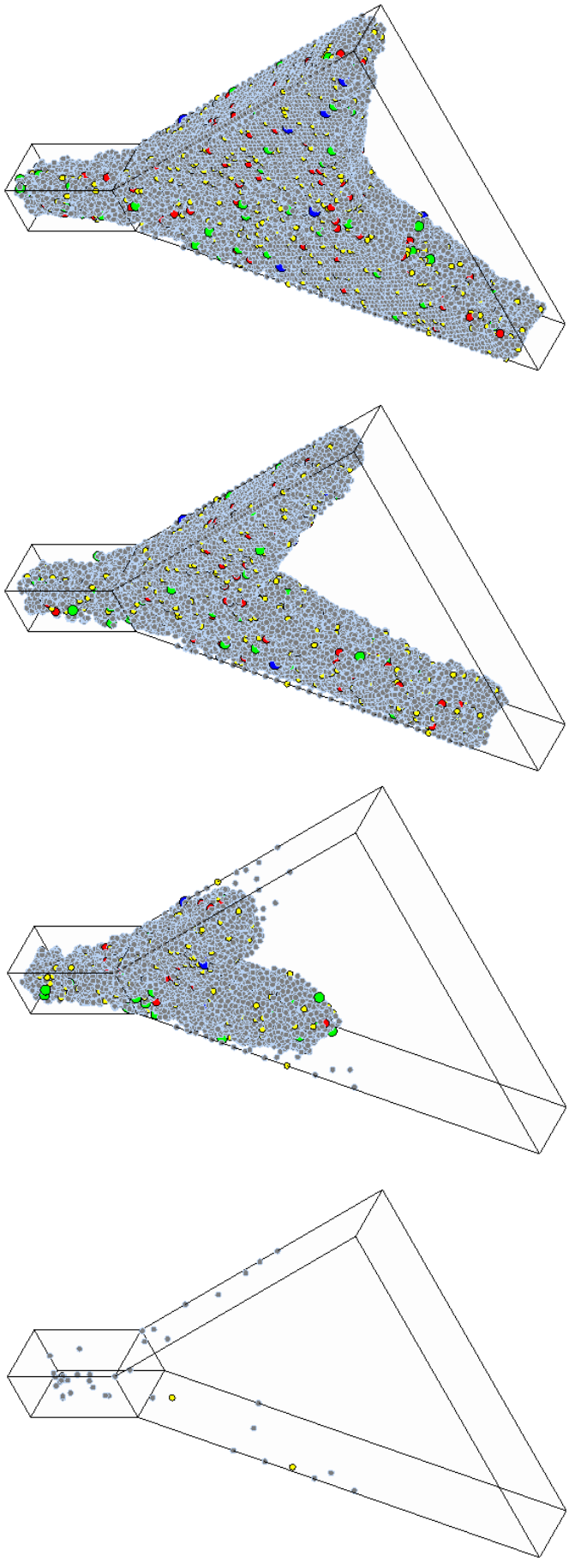

Figure G.1 Visualisation of simulations of 30MPa SCC mix at different times showing the flow pattern as well as the larger aggregate distribution

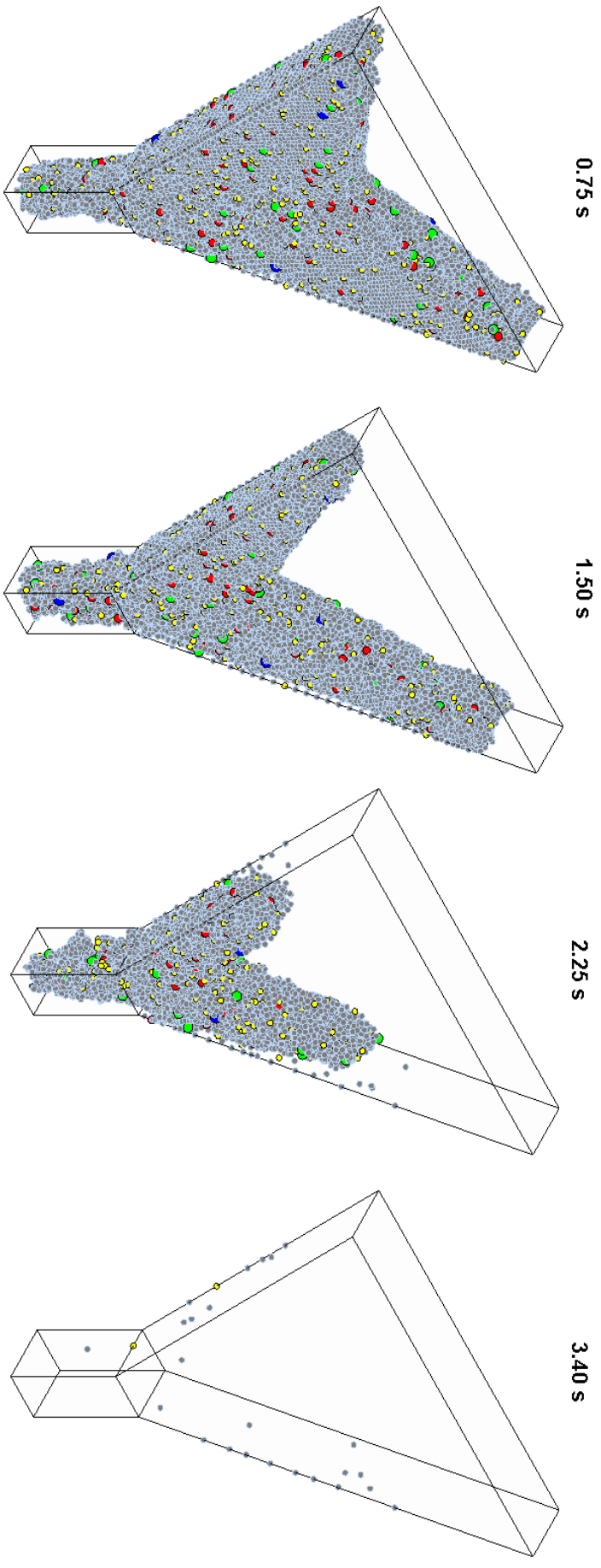

Figure G.2 Visualisation of simulations of 50MPa SCC mix at different times showing the flow pattern as well as the larger aggregate distribution

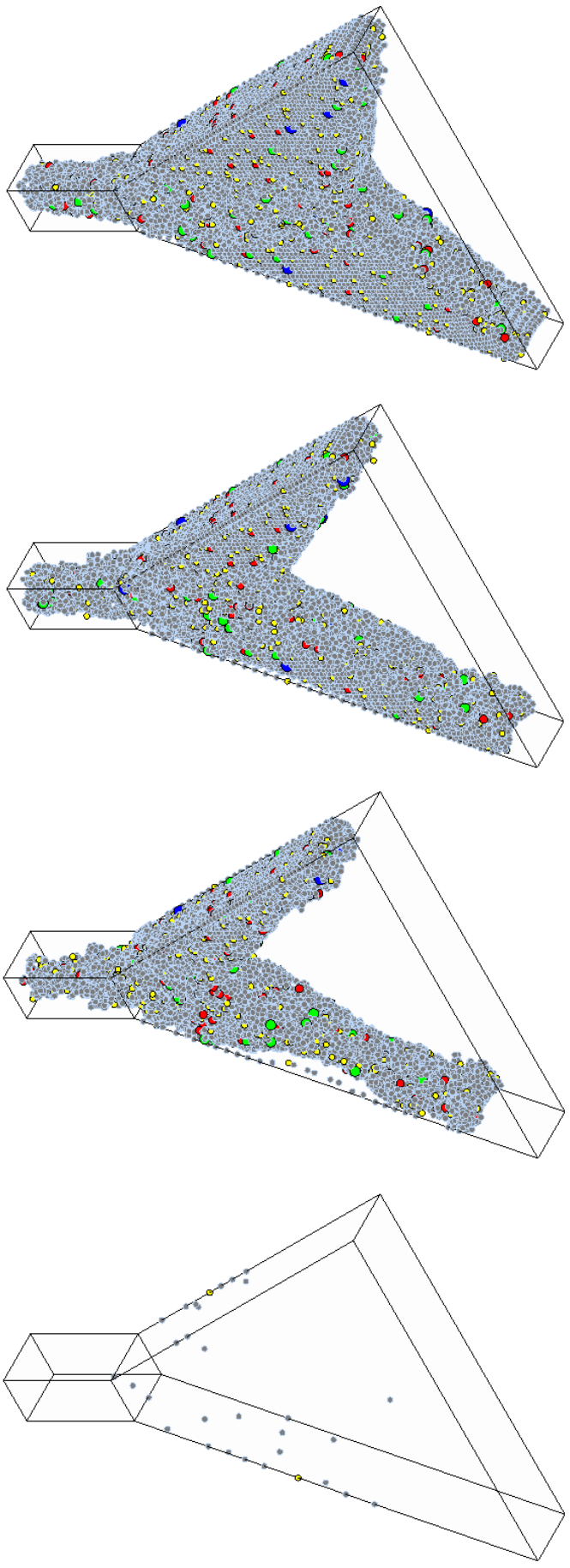

Figure G.3 Visualisation of simulations of 70MPa SCC mix at different times showing the flow pattern as well as the larger aggregate distribution

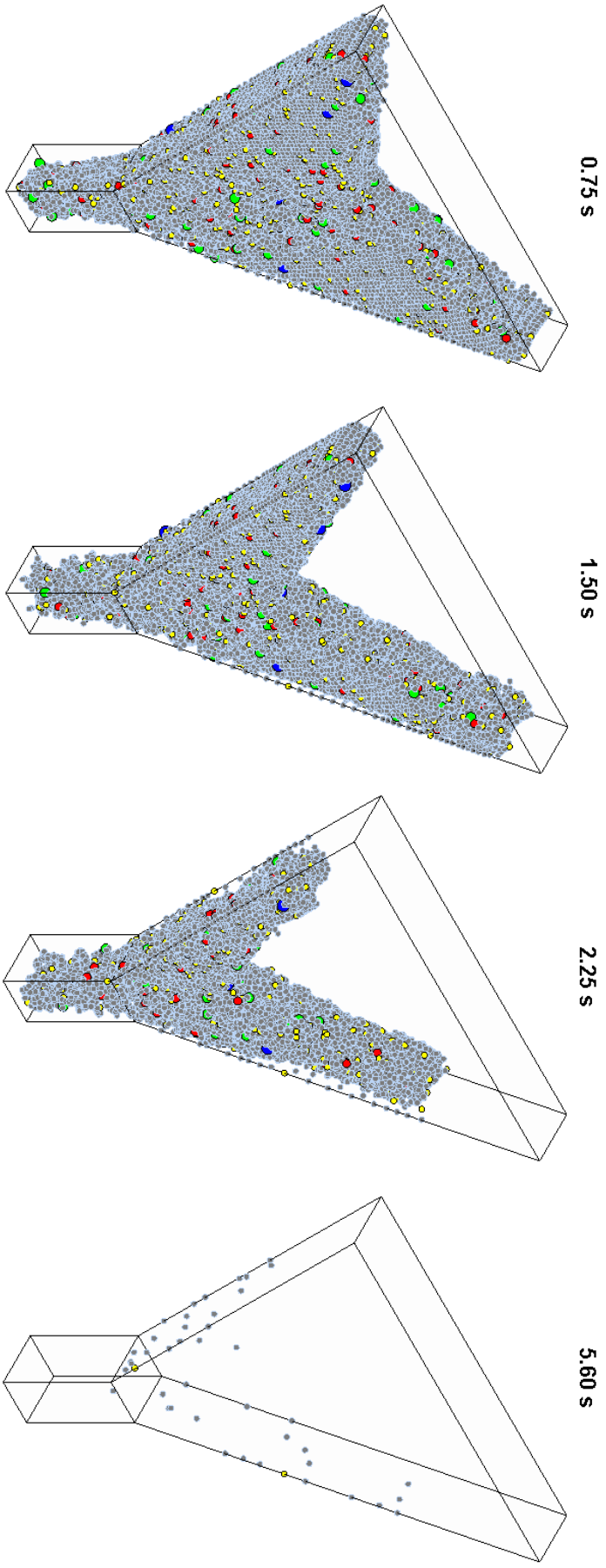

Figure G.4 Visualisation of simulations of 80MPa SCC mix at different times showing the flow pattern as well as the larger aggregate distribution